Bangor University

DOCTOR OF PHILOSOPHY

Finite element analysis of magnetization reversal in granular thin films

Spargo, Adam W.

Award date:
2002

Awarding institution:
University of Wales, Bangor

Link to publication

General rights
Copyright and moral rights for the publications made accessible in the public portal are retained by the authors and/or other copyright owners and it is a condition of accessing publications that users recognise and abide by the legal requirements associated with these rights.

- Users may download and print one copy of any publication from the public portal for the purpose of private study or research.
- You may not further distribute the material or use it for any profit-making activity or commercial gain
- You may freely distribute the URL identifying the publication in the public portal ?

Take down policy
If you believe that this document breaches copyright please contact us providing details, and we will remove access to the work immediately and investigate your claim.

Download date: 10. Apr. 2024

Finite Element Analysis of Magnetization Reversal in Granular Thin Films.

Adam W. Spargo.
School of Informatics,
University of Wales, Bangor.
December 2002.

• PRIFYSGOL CYMRU •
UNIVERSITY OF WALES
BANGOR
1884

Thesis submitted to the University of Wales in
candidature for the degree of
Doctor of Philosophy.

I'W DDEFNYDDIO YN Y
LLYFRGELL YN UNIG
TO BE CONSULTED IN THE
LIBRARY ONLY

LLYFRGELL U.W.B LIBRARY P.C.B

To Jen & Pheobe

Summary

We intoduce the thesis with a discussion of fundemental magnetism, the motivation for our studies and previous theories in the field. Chapter 2 develops the athermal equation of motion for magnetisation first given by Landau and Lifshitz in 1935 and later improved by Gilbert in 1955. We discuss the analysis of the equations given by Kikuchi in 1956 and the points raised by Mallinson in 1986. Simple numerical integration schemes are considered and single spin solutions are presented. Chapter 3 is devoted to the development of our finite element model of magnetisation dynamics. We give a variational formulation of the Gilbert equation with the effective magnetic field taken to be the functional derivative of the systems free energy as derived in chapter 1. Our initial method follows essentially from a paper by Yang and Fredkin in 1998 with some minor modifications. The magnetostatic calculation is a three dimensional generalization of the method given by Ridley *et al.* in 1999. Technical aspects such as sparse matrix storage and the solution of systems of linear algebraic equations are discussed in brief. Some basic examples are given in chapter 4 followed by an analysis of magnetisation reversal in individual cobalt grains. The important differences between grains of longitudinal and perpendicular orientation are established. Chapter 5 describes an attempt to model an open magnetic region using periodic boundary conditions and chapter 6 is concerned with the use of a time-stepping method which naturally conserves the magnitude of magnetisation due to the intrinsic quadratic invariance of the numerical scheme; improved numerical stability is established. The self consistency condition given by Albequerque *et al.* in 2001 is then used to show that the numerical error of our method may be bounded arbitrarily. Chapter 7 is devoted to the consideration of finite temperature magnetisation dynamics. We use the simple energy-barrier model to highlight the importance of thermal fluctuations, giving motivation for a more rigorous analysis. We then derive the stochastic Langevin-Gilbert equation and present single-spin solutions illustrating the superparamagnetic transition of cobalt grains as well as the temperature dependence of coercivity. Our finite element model is then applied to the finite temperature case. In chapter 8 we present some applications of our model. The effects of physical microstructure on magnetisation reversal are investigated as well as the role of energy dissipation and thermal fluctuations. We conclude with an evaluation of both our computational model and the results we have obtained. Further model development is discussed together with some as yet unexplored applications.

Acknowledgements.

I would like to thank my supervisors Dr Gareth Roberts and Prof. Roy Chantrell for giving me the opportunity to study in the field of computational magnetism and for the opportunity to attend various conferences and workshops on magnetism and numerical analysis.

Thanks again go to Roy for initiating the direction of my investigations as well as for his suggestions of topical applications and his assistance in the interpretation of results. I am also grateful for his continued involvement with my work under difficult circumstances.

Special thanks go to Gareth for his help with the numerical formulation of the problem as well as with the practical implementation. His guidance in all aspects of applied mathematics has been invaluable to my development; not least for teaching me the ability to look at a tetrahedron from the inside out!

I would also like to thank the other researchers in computational magnetism during my time at Bangor. In particular Dr Phil Ridley has been wonderfully supportive throughout the course of my PhD and I am grateful for his constructive comments on my work. Conversations with Dr Jonathan Hannay, Dr Huw Vaughan-Jones and Dr Nick Walmsley were also instrumental in my understanding of the relevant Physics.

Thanks to Dr Jose de Toro, Dr James Weston and Dr Francois Bardou for careful attention to my numerous “dumb questions” concerning experimental physics - their dumb answers were gratefully recieved.

Finally I would like to thank Dr Greg Brown, Dr Thomas Schrefl and other memebers of the magnetics group in Vienna, Ms Genevieve Hines, Mr Ricki Walker, Dr Mike Wongsam, Dr Katherine Kirk, Dr Hazel Shute, Dr Andy Goodman, Dr Claudio Serpico, Prof Giorgio Bertotti, Prof Anthony Arrot, Prof Chris Budd and Prof Wolfgang Dahmen; with all of whom I have had useful discussions at some time or another during the course of my postgraduate studies.

I would also like to acknowledge the use of the TRIANGLE mesh generation package written by Jonathan Shewchuk and the CUBIT mesh generation toolsuite made available to us by the Sandia National Laboratory. The financial support of the United Kingdom Engineering and Physical Sciences Research Council is also gratefully acknowledged.

Notation.

Some of the expressions developed during the course of the thesis become quite complex. For clarity we have given a description of our vector and matrix notation below.

Intensity of Magnetisation.

Magnetisation is described by a piecewise linear vector field $\boldsymbol{M}$ with magnitude conserved in space and time

$$|\boldsymbol{M}(t)| = M_s.$$

Reduced units are used throughout the development of our model

$$\boldsymbol{m} = \frac{\boldsymbol{M}}{M_s}$$

the unit vector $\boldsymbol{m}$ then represents the local direction of magnetisation.

Magnetic fields.

The general magnetic field is denoted by uppercase boldface letters $\boldsymbol{H}$ and induction by $\boldsymbol{B}$, with subscripted symbols to denote various contributions to the field
$\boldsymbol{H}_{ex}$ - Exchange field
$\boldsymbol{H}_d$ - Magnetostatic field
$\boldsymbol{H}_{anis}$ - Anisotropy field
$\boldsymbol{H}_z$ - Applied, external, Zeeman field.
The superposition of all contributions is refered to as the effective field

$$\boldsymbol{H}_{eff} = \boldsymbol{H}_{ex} + \boldsymbol{H}_d + \boldsymbol{H}_{anis} + \boldsymbol{H}_z.$$

The effective field is often scaled with respect to the anisotropy field strength

$$\boldsymbol{h}_{eff} = \frac{\boldsymbol{H}_{eff}}{H_k}$$

$\boldsymbol{h}_{eff}$ is then refered to as the reduced effective field.

Energy.

Expressions of energy density are given using an uppercase E and subscripts to denote various contributions correspond to those used for contributions to the effective field. The corresponding energy over a body Ω is expressed using an italic

$$\mathcal{E} = \int_{\Omega} E d\Omega$$

Vectors and Matrices.

To distinguish between vectors and matrices we use different types of boldface font. A matrix is indicated by standard boldface

$$\mathbf{A} = [A_{ij}]$$

whereas a vector is indicated by slanted boldface

$$\boldsymbol{A} = [A_i].$$

A capital letter indicates a global matrix taking contributions from all elements of the finite element mesh, whereas a lower-case letter refers to a local element matrix

$$\mathbf{K} = \sum_e \mathbf{k}^e.$$

A vector taking contributions from the three components of vector valued nodal variables over all N nodes is denoted with an over-arrow

$$\vec{\boldsymbol{m}} = [m_{1,x}, m_{1,y}, m_{1,z}, .., m_{i,x}, m_{i,y}, m_{i,z}, .., m_{N,x}, m_{N,y}, m_{N,z}]$$

Probability.

In chapter 8 some probability theory is used in connection with the treatment of stochastic differential equations. Throughout this chapter the probability of event A is denoted by

$$Prob(A)$$

and a random variable X_i is designated as belonging to a normal distribution of such variables by

$$X_i \backsim N(\bar{X}, \sigma^2)$$

where $\bar{X}$ is the mean of the distribution and σ^2 is the variance.

Contents

1 Introduction. **1**
- 1.1 Fundamental Magnetism. 2
  - 1.1.1 The Atomic Magnetic Dipole Moment. 2
  - 1.1.2 Magnetisation and Response to a Magnetic field. 5
  - 1.1.3 Magnetic Interactions. 8
  - 1.1.4 Magnetic Materials. 11
- 1.2 Motivation for Micromagnetics. 14
  - 1.2.1 Ferromagnetic Domains. 14
  - 1.2.2 Hysteresis. 15
  - 1.2.3 Applications in Magnetic Storage. 16
- 1.3 Theories of Magnetism. 23
  - 1.3.1 Electromagnetism. 23
  - 1.3.2 Weiss Domain Theory. 23
  - 1.3.3 Domain Wall Theory. 24
  - 1.3.4 The Stoner-Wohlfarth Model. 25
  - 1.3.5 Micromagnetics. 27

2 Magnetisation dynamics. **34**
- 2.1 Gyromagnetic Precession. 35
  - 2.1.1 Measuring g. 35
  - 2.1.2 Precession of the Magnetisation. 37
- 2.2 Damped Gyromagnetic Precession. 38
  - 2.2.1 The Landau-Lifshitz Equation. 39
  - 2.2.2 The Gilbert Equation. 41
  - 2.2.3 The Landau-Lifshitz-Gilbert Equation. 43
  - 2.2.4 Discussion. 45
- 2.3 Numerical Integration Schemes. 46
  - 2.3.1 The Euler Method. 46
  - 2.3.2 Improved Euler Methods. 48
  - 2.3.3 Runge-Kutta Methods. 50
- 2.4 A Single Spin System. 53

2.4.1 Reduced Units. 53
2.4.2 Numerical Solution. 54
2.4.3 The Gilbert Damping Mechanism. 55
2.4.4 Field Strength Dependence of the Precession. 56
2.4.5 Anisotropy Induced Hysteresis. 57

3 Finite Element Discretisation. 58
3.1 Finite Element Analysis. 59
3.1.1 The Galerkin Method. 60
3.1.2 Simplex Shape Functions. 61
3.2 The Magnetostatic Field. 68
3.2.1 Scalar Potential Formulation. 69
3.2.2 Galerkin Projection of the Poisson Equation. 70
3.2.3 Magnetostatic Field Calculation. 74
3.3 Micromagnetic Model. 79
3.3.1 Galerkin Projection of the Gilbert Equation. 80
3.3.2 Field Calculations. 81
3.3.3 Spatial Discretisation. 82
3.3.4 Temporal Discretization. 85
3.4 Computer Implementation. 86
3.4.1 Sparse Matrix Technology. 86
3.4.2 Iterative Solvers. 93
3.4.3 Mesh Generation. 95
3.4.4 Code structure. 98
3.4.5 Equilibrium and Tolerance. 99

4 Numerical Examples. 101
4.1 The Magnetostatic field. 102
4.1.1 The Sphere. 102
4.1.2 The Cuboid. 103
4.2 Switching of Cobalt Nano-elements. 104
4.2.1 Remanence States. 104
4.2.2 Switching Mechanisms. 109
4.3 Switching of Individual Cobalt Grains. 112
4.3.1 Longitudinal Orientation. 112
4.3.2 Perpendicular Orientation. 113
4.3.3 Slow reversal. 114
4.3.4 Effects of Grain Size. 114

5 Thin Film Simulations. 116

5.1 Microstructure Model. 117

5.1.1 The Voronoi Tessellation. 117

5.2 The Open Boundary Problem. 122

5.3 Implicit Periodic Boundary Conditions. 124

5.3.1 The Poisson equation on a Torus. 125

5.3.2 Periodic Magnetostatics. 126

5.4 Dynamic Simulations. 132

5.4.1 Uniform Anisotropy. 132

5.4.2 Random Anisotropy. 133

5.4.3 Grain Size Effects. 135

5.4.4 Physical Acceptability. 136

6 Geometric Integration. 139

6.1 Geometric Integration Methods. 140

6.2 A Pointwise Solution. 141

6.3 Finite Element Discretization. 144

6.4 Numerical Stability. 145

6.5 Efficiency. 146

6.6 Error Control. 147

6.7 Adaptivity. 150

7 Finite Temperature Model. 151

7.1 The Energy barrier. 152

7.2 Stochastic Differential Equations. 157

7.2.1 The Wiener process. 157

7.2.2 The Langevin equation. 158

7.2.3 Stochastic Calculus. 161

7.2.4 Numerical Solution of SDE's. 164

7.3 The Langevin-Gilbert Equation. 167

7.3.1 Thermal Field Strength. 168

7.3.2 Reduced Langevin-Gilbert equation. 169

7.3.3 Numerical Integration Scheme. 169

7.3.4 Thermal Relaxation. 172

7.3.5 Stochastic Resonance. 174

7.4 Finite Element Model. 176

7.4.1 Variational Formulation. 178

7.4.2 Implementation. 179

7.4.3 Modelling Thermal Relaxation with Sub-grain Discretisation. 179

8 Applications. 182
8.1 Influence of Material Microstructure. 183
8.1.1 Experimental Comparison. 184
8.1.2 Effects of Grain Size. 186
8.1.3 Effects of Grain Regularity. 187
8.2 Gilbert Damping in Cobalt Thin Films. 191
8.2.1 Single grain simulations 191
8.2.2 Thin film simulations 193
8.2.3 The Nature of Energy Dissipation. 195
8.3 Modelling Superparamagnetism. 198
8.4 Temperature Dependence of Coercivity. 202
8.4.1 Longitudinal Grains. 202
8.4.2 Perpendicular Grains. 203

9 Conclusions. 205
9.1 Evaluation. 206
9.1.1 Micromagnetic Model. 206
9.1.2 Microstructure Model. 208
9.1.3 Applications. 208
9.2 Model Development. 209
9.2.1 Grain Boundary Resolution. 210
9.2.2 BEM Magnetostatic Calculation. 211
9.2.3 Preconditioning. 211
9.2.4 Parallelization. 212
9.3 Further Applications. 212
9.3.1 Magnetic Recording simulation. 213
9.3.2 Rock Magnetism. 213
9.3.3 Superspin-glass Transition in Minute Nano-particles. . 214

Chapter 1

Introduction.

Our introduction leans heavily on two seminal works, "Micromagnetics" by William Fuller Brown, Jr [1] and "Introduction to the theory of Ferromagnetism" by Amikam Aharoni [2] as well as tutorial notes distributed by Giorgio Bertotti at the 10th Biennial Conference on Electromagnetic Field Computation in Perugia, June 2002 [3]. This is inevitable as we agree completely on the statement of the problem. The material is simply stated as concisely as possible in order to establish nomenclature and to allow reference to it in later chapters. We shall introduce the notion of magnetism and discuss it's origin in the atomic magnetic moment. We will also define the magnetic field and the unit system in which we shall be working. We discuss the magnetic interactions which influence the motion of the moment and give a classification of magnetic materials in terms of their susceptibility to an applied magnetic field. The motivation for this study is then illustrated by a discussion of some poorly understood processes in magnetism and the growing demands of the magnetic storage industry which provides the major application of the work. We then give an overview of the historical development of the field and give brief discussions of the pertinant theories. The chapter concludes with an account of the theory of micromagnetics. This theory, which was originally developed by W. F. Brown, Jr and published as a comprehensive text in 1963, will form the basis of our physical model.

1.1 Fundamental Magnetism.

1.1.1 The Atomic Magnetic Dipole Moment.

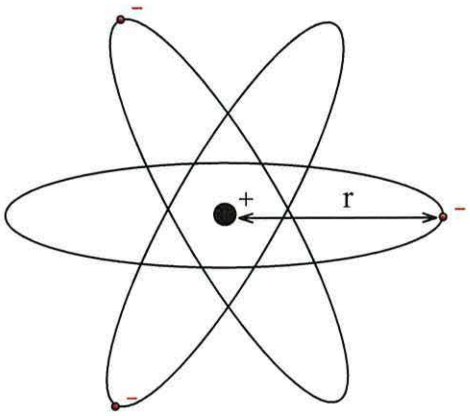

Figure 1.1: The Bohr atom.

Origin of the Magnetic moment.

There are two atomic origins of magnetism. This can be illustrated using the classical model of an atom shown in figure 1.1. An atom posesses a magnetic moment $\boldsymbol{\mu}$ which is the vector sum of an orbital moment $\boldsymbol{\mu}_o$ due to the orbital motion of it's electrons and also a spin moment $\boldsymbol{\mu}_s$ due to the spin of the electrons themselves

$$\boldsymbol{\mu} = \boldsymbol{\mu}_o + \boldsymbol{\mu}_s. \tag{1.1}$$

From figure 1.1 we see that the orbiting electron makes a current loop around the nucleus but also it has a spin motion that can be thought of as rotation around it's own axis. Both of these mechanisms result in the motion of electrical charge giving rise to so-called Amperian currents and a corresponding magnetic moment. We can use the ratio between the net angular momentum and the net atomic magnetic moment to distinguish between a moment which is due to orbital motion or a moment which is due to spin motion.

The Orbital Moment. Assuming that the electron in figure 1.1 is moving with speed v along a circular orbit of radius r with period $2\pi r/v$ we may calculate the resulting magnetic moment. This motion of electrical charge will produce a current of

$$\begin{aligned} i &= \frac{-e}{c}\frac{v}{2\pi r} \\ &= \frac{-ev}{2c\pi r} \end{aligned} \tag{1.2}$$

where e is the electrical charge of the electron and c is the speed of light. From Ampere's law [4] the magnetic moment of a closed current loop is given by the product of the cross-sectional area of the loop and the current. Therefore the moment due to the orbiting electron is given by

$$\begin{aligned} \|\boldsymbol{\mu}_o\| &= \pi r^2 \frac{-ev}{2c\pi r} \\ &= -\frac{evr}{2c}. \end{aligned} \tag{1.3}$$

It is known from quantum mechanics that each electron can exist in various energy levels corresponding to orbits of various r in the Bohr model [5]. As a consequence, on the atomic scale angular momentum is also quantized and is constrained to be an integer multiple of $\hbar = h/2\pi$

$$\|\boldsymbol{P}_o\| = m_e v r = \frac{nh}{2\pi} \tag{1.4}$$

where h is planck's constant and m_e is the electron mass. The orbital moment can then be written

$$\|\boldsymbol{\mu}_o\| = -\frac{enh}{4\pi m_e c}. \tag{1.5}$$

So for $n = 1$ corresponding to one electron in the ground state we have

$$\begin{aligned} \mu_B &= -\frac{eh}{4\pi m_e c} \\ &= -9.27 \times 10^{21} \end{aligned} \tag{1.6}$$

μ_B is known as the Bohr magneton and is the fundamental unit of magnetic moment, measured in ergs/Oe or emu.

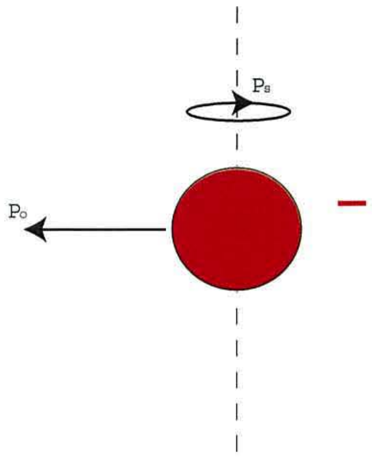

Figure 1.2: Electron spin.

The Spin Moment. The spin of an electron can be thought of as the rotation about it's own axis, figure 1.2. Clearly this rotation also leads to the motion of electrical charge. However, no explanation of the resulting current loops can be given in terms of classical physics primarily due to the fact that the shape and charge distribution of the electron are not classicaly defined, assuming spherical geometry and a uniform charge distribution gives a poor estimate of the observed spin moment [6]. The spin of the electron was first postulated to account for features of the optical spectra of gases subject to a magnetic field and it's value was determined experimentally. The notion of spin has since been given a more concrete interpretation in terms of quantum mechanics [7]. It can be inferred from spectral analysis that the magnetic moment due to electron spin motion is given by

$$\boldsymbol{\mu}_s = -\frac{e}{m_e c}\boldsymbol{P}_s \tag{1.7}$$

where P_s is the spin angular momentum. Since P_s is quantized in units of $\hbar/2$, the spin magnetic moment must also be an integer multiple of the Bohr magneton

$$\begin{aligned} \|\boldsymbol{\mu}\|_s &= -\frac{e}{cm_e}\frac{nh}{4\pi} \\ &= -\frac{neh}{4\pi m_e c} \\ &= n\boldsymbol{\mu}_B \end{aligned} \tag{1.8}$$

The Lande Splitting factor. The orbital moment may also be written in terms of angular momentum

$$\boldsymbol{\mu}_o = -\frac{e}{2m_e c}\boldsymbol{P}_o. \tag{1.9}$$

Here the coefficient of momentum in the expression of orbital moment is half the magnitude of that in the expression of spin moment 1.7. Generally we may write $\boldsymbol{\mu}$ in terms of the Lande splitting factor g and the net angular momentum $\boldsymbol{P}$

$$\begin{aligned} \boldsymbol{\mu} &= -g\frac{e}{2m_e c}(\boldsymbol{P}_o + \boldsymbol{P}_s) \\ &= -g\frac{e}{2m_e c}\boldsymbol{P} \end{aligned} \tag{1.10}$$

where $g \approx 1$ for a moment which is due purely to the orbital angular momentum $\boldsymbol{P}_o$ and $g \approx 2$ for a purely spin moment, an intermediate value of g indicates that both mechanisms contribute to the moment. Contributions to $\boldsymbol{P}_o$ and $\boldsymbol{P}_s$ from closed shells of electrons is always zero due to cancellations. Therefore a magnetic moment is only macroscopically observable in atoms with an incomplete electron shell in the classical model. The magnetic moments in ferromagnetic materials such as iron, cobalt and nickel are predominantly caused by electron spin and the atomic magnetic moment of such materials is therefore often referred to as the spin of the atom.

The classical approach taken above in fact leads to the same results as a more rigorous quantum mechanical description [7].

1.1.2 Magnetisation and Response to a Magnetic field.

Continuum Hypothesis.

In all subsequent chapters we neglect much of the atomic detail in favour of developing a macroscopic model of magnetism which is computationally feasible. To do this we assume a continuum hypothesis, that is we assume that all variables may be specified continuously and absolutely at any given point in space. The variable under consideration, the magnetic moment $\boldsymbol{\mu}$, as we have seen is discrete by nature and is associated with atoms occupying specific regions of space. Further the moments are subject to thermal fluctuations in both their direction and magnitude [1]. To overcome this problem we define a thermodynamically extensive variable. $\boldsymbol{M}$, known as the intensity of magnetisation, or simply as the magnetisation is defined as the net

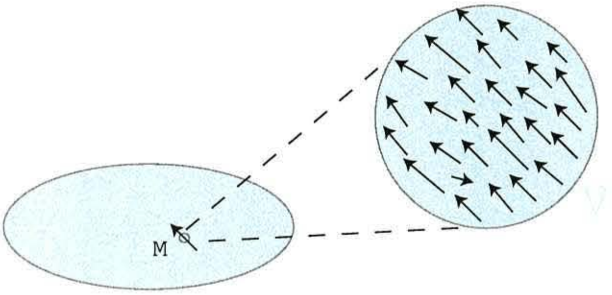

Figure 1.3: The continuum hypothesis.

magnetic moment per unit volume V and measured in units of emu/cm^3

$$\boldsymbol{M} = \frac{\sum_{i \in V} \boldsymbol{\mu}_i}{V}. \tag{1.11}$$

The Magnetic Field.

In physics a field is an abstract quantity defined as the rate of change of energy density with respect to the state variable of a system. For example a magnetic field $\boldsymbol{H}$ may be generated in a medium by a current as described by Ampere's law. The energy of a system can be defined in two ways. The Helmholtz energy is defined as total energy of the system whereas the Gibbs free energy is defined as the internal energy of the system. We therefore define the magnetic field as the functional derivative of the Gibbs free energy density with respect to magnetisation

$$\boldsymbol{H} = \frac{\partial E_G}{\partial \boldsymbol{M}}. \tag{1.12}$$

The magnetisation and the magnetic field are often related to one another through three quantities; permeability μ, susceptibility χ and induction or magnetic flux density $\boldsymbol{B}$. The induction is defined as the response of a medium to an applied magnetic field, it can be thought of as the concentration of magnetic field lines and is measured in units of Gauss

$$\boldsymbol{B} = \boldsymbol{H} + 4\pi \boldsymbol{M}. \tag{1.13}$$

The relation between a magnetic field and the induction in a medium is known as the permeability

$$\boldsymbol{B} = \mu \boldsymbol{H}. \tag{1.14}$$

In free space and in many materials μ is a constant and the relation between $\boldsymbol{B}$ and $\boldsymbol{H}$ is linear. In ferromagnets however μ is a complex function of $\boldsymbol{H}$. Finally when $\boldsymbol{M}$ and $\boldsymbol{H}$ are parallel they may be related by the susceptibility

$$\boldsymbol{M} = \chi \boldsymbol{H}. \tag{1.15}$$

Clearly these parameters are themselves related

$$\begin{aligned} \boldsymbol{B} &= \mu \boldsymbol{H} \\ \boldsymbol{H} + 4\pi \boldsymbol{M} &= \mu \boldsymbol{H} \\ \boldsymbol{H} + 4\pi(\chi \boldsymbol{H}) &= \mu \boldsymbol{H} \\ 1 + 4\pi\chi &= \mu \end{aligned} \tag{1.16}$$

The Gyromagnetic Effect.

We now return to the Bohr model to consider the effect of a magnetic field on the atomic magnetic moments. We define the gyromagnetic ratio γ^{-1} as the ratio between angular momentum and magnetic moment

$$\boldsymbol{\mu} = -\gamma \boldsymbol{P}. \tag{1.17}$$

From the equation 1.10 we see that

$$\gamma = \frac{ge}{2m_e c}. \tag{1.18}$$

By the moment of momentum theorem the torque exerted on a magnetic moment $\boldsymbol{\mu}$ by a magnetic field $\boldsymbol{H}$ is equal to the rate of change of angular momentum

$$\frac{d\boldsymbol{P}}{dt} = \boldsymbol{\mu} \times \boldsymbol{H}. \tag{1.19}$$

We therefore have an equation of motion for the magnetic moment in the presence of an applied magnetic field

$$\frac{d\boldsymbol{\mu}}{dt} = -\gamma \boldsymbol{\mu} \times \boldsymbol{H}. \tag{1.20}$$

The motion of an atomic moment in a magnetic field is often compared to the motion of a spinning top in a gravitational field [6], [8], [9]. The processes have a superficial similarity, however the analogy cannot be pushed too far. If the gravitational field is removed from the spinning top it will carry on spinning for some time under its own momentum. If the magnetic field is removed from the magnetic moment it will stop - instantaneously [10].

1.1.3 Magnetic Interactions.

As well as the effect of an applied magnetic field, the atomic moments and therefore magnetisation are also influenced by the interactions between electrons on neighbouring atoms, interactions between electrons and the crystal lattice and also interactions between the elementary dipoles themselves. These interactions cannot be understood entirely using classical physics. The following explanations of exchange and spin-orbit interactions depend on some quantum mechanical theory which can be found in greater depth elsewhere [5].

Exchange Interactions.

Electrons repel each other as a result of electrostatic forces described by Coulomb's law [4], [11]. The Coulomb interaction arises when the wave functions ψ_i, ψ_j of two electrons i, j overlap in space and is proportional to the product

$$|\psi_i|^2|\psi_j|^2 = \bar{\psi}_i\psi_i\bar{\psi}_j\psi_j. \tag{1.21}$$

where the bar denotes the complex conjugate. Now consider the net electronic wave function of two atoms A, B at positions $\boldsymbol{x}_A$ and $\boldsymbol{x}_B$ respectively. As $d(\boldsymbol{x}_A, \boldsymbol{x}_B) \to 0$ the total electronic wave function is given by

$$\psi_t = \psi_A(\boldsymbol{x}_A)\psi_B(\boldsymbol{x}_B) - \psi_B(\boldsymbol{x}_A)\psi_A(\boldsymbol{x}_B). \tag{1.22}$$

The energy over a volume V containing atoms A and B then includes terms

$$\int_V \bar{\psi}_A(\boldsymbol{x}_A)\bar{\psi}_B(\boldsymbol{x}_B)\psi_A(\boldsymbol{x}_A)\psi_B(\boldsymbol{x}_B)\frac{(e/c)^2}{\rho(\boldsymbol{x}_A, \boldsymbol{x}_B)}dV \tag{1.23}$$

$$-\int_V \bar{\psi}_A(\boldsymbol{x}_B)\bar{\psi}_B(\boldsymbol{x}_A)\psi_A(\boldsymbol{x}_A)\psi_B(\boldsymbol{x}_B)\frac{(e/c)^2}{\rho(\boldsymbol{x}_A, \boldsymbol{x}_B)}dV \tag{1.24}$$

$$-\int_V \bar{\psi}_A(\boldsymbol{x}_A)\bar{\psi}_B(\boldsymbol{x}_B)\psi_A(\boldsymbol{x}_B)\psi_B(\boldsymbol{x}_A)\frac{(e/c)^2}{\rho(\boldsymbol{x}_A, \boldsymbol{x}_B)}dV \tag{1.25}$$

$$+\int_V \bar{\psi}_A(\boldsymbol{x}_B)\bar{\psi}_B(\boldsymbol{x}_A)\psi_A(\boldsymbol{x}_B)\psi_B(\boldsymbol{x}_A)\frac{(e/c)^2}{\rho(\boldsymbol{x}_A, \boldsymbol{x}_B)}dV \tag{1.26}$$

where $\rho(.,.)$ is a metric or distance function. Clearly terms 1.23, 1.26 are of the form 1.21 and derive from the Coulomb interaction. However terms 1.24, 1.25 cannot be explained classically and are quantum mechanical in origin. This phenomenon is known as the exchange interaction and is essentially a consequence of the Pauli exclusion principle which asserts that no two electrons may share all four quantum numbers [11], [5]. It is clear that the exchange interaction occurs only for small inter-atomic distances. Specifically it manifests itself when the distance between neighbouring atoms approaches the spatial support of the respective electronic wave functions. The role of the Coulomb interaction itself is to position the electrons in their respective orbits around the nucleus of each atom. It then has no further influence over the associated magnetic moments.

Spin-Orbit Interactions.

By relativity each electron is perfectly entitled to consider itself at rest. In this scenerio the nucleus of the atom forms a current loop during its orbit around the electron. Consequently there is a coupling between the orbital angular momentum and the spin angular momentum known as Russell-Saunders coupling [11]. In the many-electron atom the net electronic spin vector $\boldsymbol{S} = \sum \boldsymbol{P}_s$ must occupy the maximum value consistent with the Pauli exclusion principle. The same forces act to combine the electronic orbital momentum vectors $\boldsymbol{O} = \sum \boldsymbol{P}_o$ to give a resultant net value for the atom. $\boldsymbol{O}$ too takes the maximum possible value consistent with the exclusion principle. There is in some sense a competition between the spin and orbital momenta to assign consistent quantum numbers which maximize $\boldsymbol{S}$ and $\boldsymbol{O}$ respectively. This is known as the spin-orbit interaction which acts to couple electron spins to the structure of the crystal lattice, consequently the magnetic moments are coupled to a certain crystallographic axes and this results in a prefered direction of the magnetic moments known as the easy-axis [1]. The magnetisation shares the prefered direction of its constituent moments, a phenomenon known as magnetocrystalline anisotropy. The easy-axis or indeed easy-axes depend on the atomic structure of the material. Iron for example has a cubic structure which results in three easy directions coincident with the three crystallographic axes. Whereas cobalt has a hexagonal lattice structure which generally results in a single easy-axis parallel to the c-axis of the crystals. As we shall be mostly concerned with cobalt media we shall discuss only this so-called uniaxial anisotropy here. The energy which results from uniaxial anisotropy depends only on the direction of magnetisation with respect to the easy-axis. Due to symmetry in the ab-plane the energy density may be given as a series in the even powers of $\cos(\theta)$ where θ

---

[1] By prefered direction we mean that it is possible to align magnetic moments in this direction with an applied field of lower magnitude than would be required to align them in other directions. Also in zero applied field they will tend to align to this direction.

is the angle between the c-axis and the magnetic moments

$$E_{anis} = K_1 \cos^2(\theta) + K_2 \cos^4(\theta) + \cdots. \tag{1.27}$$

Alternatively we can expand in terms of a $\sin(\theta)$ series

$$E_{anis} = K_1 \sin^2(\theta) + K_2 \sin^4(\theta) + \cdots. \tag{1.28}$$

The difference between the two expressions is a constant which is meaningless with respect to energy as long as only one or the other expression is applied in the same analysis. Clearly K_1, K_2 take different values in equations 1.27 and 1.28 however it is known from experiment that in both cases that

$$|K_1| >> |K_2| >> |K_3| >> \cdots. \tag{1.29}$$

In particular for cobalt the fourth order terms and higher are negligible and the energy density may be given simply as

$$E_{anis} = K \cos^2(\theta) \tag{1.30}$$

or

$$E_{anis} = K \sin^2(\theta) \tag{1.31}$$

where K is known as the uniaxial anisotropy constant.

Dipole-Dipole Interactions.

The interaction between magnetic moments causes a self demagnetising or magnetostatic energy. This potential energy may be derived by considering a lattice of elementary moments $\boldsymbol{\mu}_i$

$$\mathcal{E} = -\frac{1}{2} \sum_i \boldsymbol{\mu}_i \cdot \boldsymbol{h}_i \tag{1.32}$$

where $\boldsymbol{h}_i$ is the field intensity at lattice point i due to all other moments. In the total summation the interaction of moment i with the field due to moment j is the same as the interaction of moment j with the field due to moment i and each contributions is counted twice. The energy is therefore given by half of the sum [12]. As explained by Aharoni [2] we may generalize to the continuum by replacing the summation with an integral over the sample volume. In equation 1.33 the moments $\boldsymbol{\mu}_i$ are replaced by magnetisation and $\boldsymbol{h}_i$ is replaced by the macroscopic magnetostatic field which may be obtained from Maxwell's equations as we shall see later

$$\mathcal{E} = -\frac{1}{2} \int_V \boldsymbol{M} \cdot \boldsymbol{H}_d. \tag{1.33}$$

Zeeman Interaction.

The application of an external magnetic field increases the energy of a system by definition. When excited atoms emit photons the resulting spectral lines correspond to the quantized energy levels of the atom. The magnetic moment of a sample may be obtained experimentally by spectral analysis of a sample in an external field. The spectral lines are observed to split into three or more distinct lines, this is known as the Zeeman effect [11]. The term Zeeman energy has subsequently been used to denote externally applied magnetic energy. The applied field is also known as the Zeeman field, $\boldsymbol{H}_z$. To obtain the energy density resulting from the Zeeman field we simply take the projection of the field vector onto the magnetisation

$$E_z = -\boldsymbol{H}_z \cdot \boldsymbol{M} = -|\boldsymbol{H}_z| M_s \cos(\theta_{MH}) \tag{1.34}$$

where θ_{MH} is the angle between the field vector and the magnetisation.

Thermal agitations.

In general thermal agitations give rise to fluctuations in both the magnitude and direction of magnetic moments. In ferromagnetic materials the strong exchange forces ensure that fluctuations in magnitude are kept to a minimum. On the other hand fluctuations in direction of the moments is smoothed by considering the statistically averaged quantity of magnetisation. The majority of our work therefore considers the athermal case, the results of which can be applied in most cases. In certain circumstances however the transverse fluctuations become important, especially when considering magnetic particles of reduced dimensions. In this case a phenomenological fluctuating magnetic field is defined with sufficient magnitude to produce the observed fluctuations in the direction of magnetisation. This topic will be investigated in chapter 7 and appropriate modifications to the micromagnetic model are made.

1.1.4 Magnetic Materials.

Magnetic materials may be broadly classified by the five catagories; diamagnetic, paramagnetic, ferromagnetic, anti-ferromagnetic and ferrimagnetic. Their properties are dictated essentially by the number of electrons in the atom, or more precisely by the number of unoccupied orbits in partially filled electron shells and also by interactomic distance which dictates the magnitude of exchange interactions. Also they may be characterized by their susceptibility to an applied magnetic field.

Diamagnetism.

The vast majority of solids have full electron shells and therefore posses negligible magnetic moment. These are characterized by a small negative susceptibility of the order of -10^{-5} and are termed diamagnetic. The characteristic behaviour of diamagnetic materials when placed in an applied field is to acquire a very small magnetic moment which is opposed to the field and hence reduce the induction.

Paramagnetism.

Materials for which χ is small but positive, of the order of 10^{-3} at room temperature, are termed paramagnetic and are characterised by χ being inversely proportional to temperature. Here moments are randomly oriented, except as biased by an applied field, due to weak interactions between the electrons on neighbouring molecules. At low temperature, where we may think of the moments as being frozen, increased interaction between atoms may cause ferromagnetic or anti-ferromagnetic alignment of the moments. However the behaviour of both paramagnetic and diamagnetic materials at ambient temperatures may be well approximated by single atom models.
Materials which have large positive values of χ may be split into three groups.

Ferromagnetism.

In this thesis we shall be concerned with ferromagnetic materials. In these materials strong exchange interactions between atoms cause the elementary magnetic moments to align parallel to each other. This results in a spontaneous magnetisation in bulk samples even where no magnetic field is present. In this case from equation 1.13 the induction is simply equal to $4\pi \boldsymbol{M}$. Ferromagnetic materials undergo a paramagnetic transition at the Curie temperature where the interactions which cause the ferromagnetic alignment become weak in comparison with thermal agitations.

Anti-ferromagnetism.

Anti-ferromagnetism results from strong exchange interactions resulting in an ordered anti-parallel spin configuration. Alternatively the interactions between moments in different sub-lattices may cause them to align anti-parallel to each other. Compounds consisting of two types of atom in which the moments of each sub-lattice precisely cancel, are also known as anti-ferromagnetic. These materials are characterized by zero net magnetisation at all temperatures. The temperature at which anti-ferromagnetic materials undergo a paramagnetic transition is known as the Neel temperature.

Ferrimagnetism.

Variants of anti-ferromagnetism occur when different sub-lattices contain atoms with elementary moments of unequal size, so in the ordered state they don't average to zero, leaving a residual net magnetization. These materials are generally termed ferrimagnetic.

This thesis is solely concerned with the properties of ferromagnetic materials, however paramagnetic behaviour may occur in these media under various conditions. The distinction between the types of magnetism can become rather arbitrary; as well as the 'freezing' of paramagnets and the 'melting' of ferromagnets, further complications exist. When a crystal of ferromagnetic material is very small, the magnitude of its magnetic energy may become smaller than the magnitude of its thermal energy. This phenomenon is known as superparamagnetism and will be discussed further in relation to magnetic storage and will be investigated more thoroughly in chapters 7 and 8.

1.2 Motivation for Micromagnetics.

1.2.1 Ferromagnetic Domains.

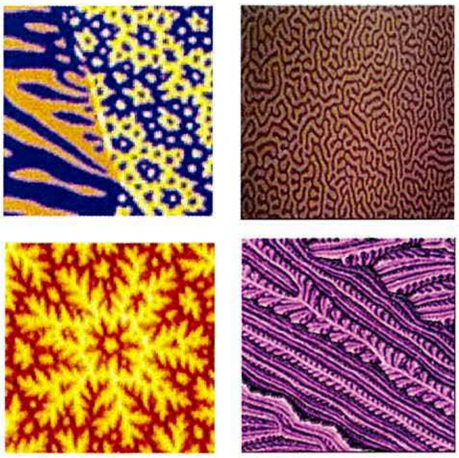

Figure 1.4: Ferromagnetic domain structures in thin film media.

Regions of homogeneous magnetisation are known as magnetic domains. Early investigators of magnetic materials were confused by the fact that ferromagnets which could be magnetized or could acquire a spontaneous magnetisation by virtue of an applied magnetic field could also exist in a state of zero net magnetisation. This was subsequently explained by the existence of magnetic domains which could develop by mutual exclusion into configurations which effectively cancel each other out. Modern experimental imaging techniques have revealed an amazingly rich and beautiful structure of magnetic domain configurations in ferromagnetic materials such as the thin films illustrated in figure 1.4. It should be noted here that domain structures of such complexety are beyond the predictive capability of any current theory in atomic or continuum physics; discussions of the archetypal domain structures for simple geometries may be found in numerous publications elsewhere [6], [8]. The internal magnetostatic field is known to be largely responsible for the formation of domain structures and is highly sensitive to the geometry of the sample. For this reason single-domain ellipsoids of revolution are often used to give a model in which the magnetostatic field can be neglected. The strongest influence on domain propagation is due to exchange interactions. The exchange field favours coherent magnetisation and thus moderates the effect of the magnetostatic field. The rotation of magnetisation within each domain then depends upon the orientation of the magnetisation with respect to the easy-axis. The reversal of single-domain particles is therefore dictated entirely by the magnetocrystalline anisotropy. Although other phenomena have an effect on the dynamics of magnetisation, this thesis will be concerned with the influences of the magnetostatic field, exchange interactions, magnetocrystalline anisotropy and of course external magnetic fields. Clearly a complete description of magnetic domains requires input from electromagnetics, quantum mechanics and thermodynamics. However much of the work in formulating the problem has already been done and it only remains to find the best methods of solution. In section 1.3 we outline theories which best describe the individual aspects of the problem and then give an account of the formalism that underlays ours and most other work in the field.

1.2.2 Hysteresis.

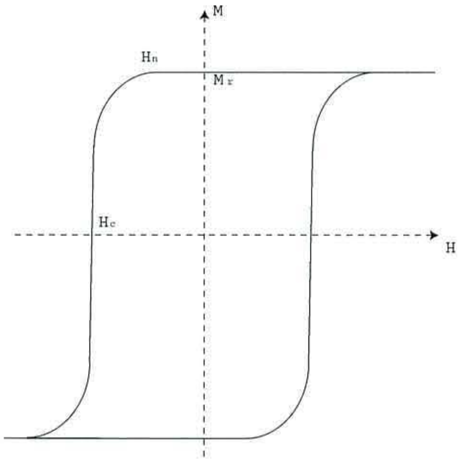

Figure 1.5: The limiting hysteresis or M-H loop.

As a result of magnetic domains as well as material anisotropy all ferromagnetic materials exhibit irreversible dynamics and therefore hysteresis. This phenomenon is best illustrated by use of an M-H loop or hysteresis loop as shown in figure 1.5. Such loops may be obtained experimentally [13] and are used to characterize the magnetic properties of ferromagnetic materials. An accurate hysteresis loop is the fundamental deliverable of any micromagnetic simulation and is a good means by which to obtain experimental verification of numerical results. Starting from an initially demagnetized state, where opposing directions of magnetic domains cause a zero net magnetic moment in the sample, an external magnetic field is applied and steadily increased until the maximum net magnetic moment or saturation magnetisation M_S is reached. Subsequent increases in the field strength result in no further increase in the net magnetic moment because all opposing domains have been annihilated and favourably oriented domains have expanded and rotated into the field direction until the sample consists of one single domain aligned with the field. The field is then slowly reversed until negative saturation is reached, clearly the sample now consists of a single magnetic domain oriented in the opposite direction. If the field is reversed once more the sample will naturally return to positive saturation, however the curve will not in general follow the same path between the two states. The parameter H_c denotes the critical value of the applied field which must be applied in order to switch the magnetisation. Other parameters from the loop reveal further information about the material; the nucleation field H_n if it exists denotes the value of the applied field at which irreversible magnetisation changes first occur, this refers to the creation or nucleation of reversed domains. The remanence M_r is the value of magnetisation when the applied field is exactly zero, this corresponds to the natural macroscopically observable value of magnetisation in the absence of any field. Also the slope of the M-H loop is a characteristic of different materials. Minor loops can be obtained by applying the applied field until any given magnetisation is reached; in fact there is a continuum of such loops. The loop shown in figure 1.5 is known as the limiting hysteresis loop as further increases of field in either direction cannot result in a magnetisation higher than the saturation magnetisation and subsequent cycles of the field will retrace this limiting curve [13].

1.2.3 Applications in Magnetic Storage.

The technology of magnetic storage is pushing the limits of established theory and requires quantitative numerical predictions to enable further development. Although we are not concerned directly with industrially relevent research, the recording industry does provide the major application of work such as ours. We therefore take some time here to describe the recording process itself and to establish what can be gained by the application numerical modelling. Notwithstanding information encoded by reversal of the planetary magnetic moment, the history of magnetic recording begins with the telegraphone in 1898. This was a device invented by Vlademar Poulsen on which he made the first audio recording. Using a microphone connected to an electromagnet he made a recording of his own voice on a thin ferromagnetic wire. By connecting the electromagnet to a speaker and then passing it through the stray field from the magnetized wire he was able to play back the recording. In the last 100 years the magnetic recording industry has been conerned with refining essentially the same process in order to manufacture media for audio, video and now computer information storage. 1927 saw the invention of magnetic tape which consisted of fine ferromagnetic particles embedded in a non-magnetic film. This was advantageous from the point of view of reproducible magnetic properties and also because it enabled the media to be stored on spindles and passed over a read or write head by simple mechanisms. The first audio recorders appeared in 1948 making use of tape media and inductive read-write heads. By the 1950's IBM was developing metallic thin films to act as storage media for the emerging computer technologies. Much of their initial success came on the back of experimental results combined with heuristic computational modelling. More recently however the rise of optical storage media particularly for audio and video applications has put pressure on magnetic recording to justify its existence. Also the demanding operating systems and software packages in use in todays computers require hard disk drives with fast data rates, high storage densities and fast access times. For example the areal storage density of drives is currently approaching 100Gbits/inch^2 and rising at a rate of 60-100 percent a year, see figure 1.6. This astonishing rate of increase is pushing both technological and fundmental limits. For it to be maintained requires a deeper understanding of the magnetisation reversal mechanism in relation to those limits. This requires the use of rigorous numerical modelling.

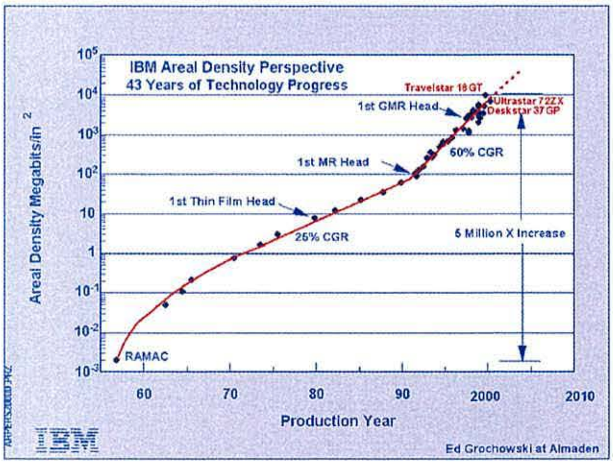

Figure 1.6: The growth of areal storage density in magnetic recording media [14].

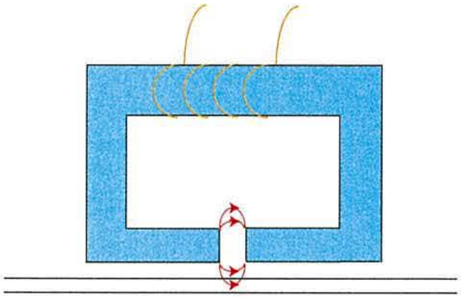

Figure 1.7: The longitudinal writing process.

The Modern Recording Process.

As in Poulsen's device modern magnetic recording relies on the fact that in certain ferromagnetic materials small regions can be magnetised using an external field to form a single magnetic domain aligned in some direction. Provided the remenance magnetisation of the media is high enough this single domain or bit has stored information once the field is removed, namely the direction in which it has been magnetised. The process therefore requires information to be stored as binary digits so that opposing directions of magnetisation can be used to store a zero or a one. The writing process is illustrated in figure 1.7. An inductive write head consists of a toroidal ferromagnet with a fine gap, when the head is magnetised a strong magnetostatic field or fringe field forms around the head gap which may be used as the external writing field with respect to the media. The exact geometry of the head can be optimized to achieve a strong field near the gap. An electric coil around the head is used to change the direction of magnetisation in the head and therefore the direction of the fringe field in order to write bits of opposite orientation. Once bits are written the storage media is then moved passed the head, thus transforming the temporal changes in write current into spatial bit patterns in the media. This processes is known as longitudinal recording reflecting the orientation of the written bits with respect to the plane of the media. Obvious technological limitations come from the minimum feature size obtainable in the fabrication of such heads, more fundamental is the intrinsic rate at which magnetisation in the head can be reversed. In older

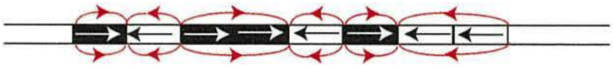

Figure 1.8: Written bits storing the binary string ...10110100...

systems the playback process was simply the reverse of the writing process, the stray field from the written bits shown in figure 1.8 was used to induce a magnetisation in the head which could be read by the changes in the current of electric coils around the head [15], [16]. In many cases the same head was used for reading and writing. It later became clear that different material and geometric properties are important for read and write heads respectively. This lead to the replacement of inductive read heads with magnetoresistive or MR heads [15], [16], [17], [18] which cause a change in the resistance of the head when a change of magnetisation occurs. These have quite recently been superseeded by heads making use of the Giant Magnetoresistance property or GMR [19]. In general heads are manufactured from soft magnetic materials and although micromagnetic methods are an appropriate means with which to investigate such materials we are concerned in this thesis with the magnetisation reversal of hard polycrystalline materials. Our work therefore has more immediate application in modelling magnetic storage media.

Magnetic Storage Media.

Thin films for magnetic recording are created by sputter deposition or similar processes. After deposition, drying commences at nucleation points throughout the melt; this proceeds at equal speed from each "seed" until a crystallographic structure has formed by mutual obstruction of neighbouring grains. The grains form a stochastic geometry dependent on the relative position of seed points. In general the film is very thin, $\leq$ 20nm and the grain structure is continuous through its thickness. Each grain adopts it's distinct atomic structure resulting in a lattice mis-match at grain boundaries. The grain boundary, consisting of a "few" atomic layers in which the atoms switch from the orientation of one grain to the next, has a surface tension because its atoms have a higher free energy than those within the grains. During post deposition annealing, where the material is held at high enough temperatures for atoms to migrate from one grain to the next, energy will be minimised with the straightening of curved boundaries and the reduction of grain area. In cobalt in particular, this results in a strongly hexagonal grain structure. On any one recording track it would seem sensible to manufacture films with an easy axis parallel to the direction of the written bits, however the media is manufactured in the form of a disk to enable the location of individual bits by rotation of the disk combined with radial movements of the head. The films are therefore manufactured so that easy-axes of the grains in the plane of the film but with random orientation in the plane. This results in an anisotropy which is locally strong, preventing erasure but globally averages to zero. The straight-forward approach to increasing storage density has been to use bits consisting of ever fewer grains. However a fundemental limit of signal to noise ratio is soon reached [15]. As illustrated in figure 1.9, when the number of grains per bits is reduced the transitions between bits becomes indistinct resulting in low signal quality. This limits the increase in density by reducing the number of constituent grains. To further increase density it is therefore necessary to reduce the size of the constituent grains. We now encounter the superparamagnetic limit, this occurs when the strength of magnetic energy is reduced to the level of thermal energy in each grain. In this grain size regime it becomes impossible to store information because the magnetisation is subject to thermally activated reversals.

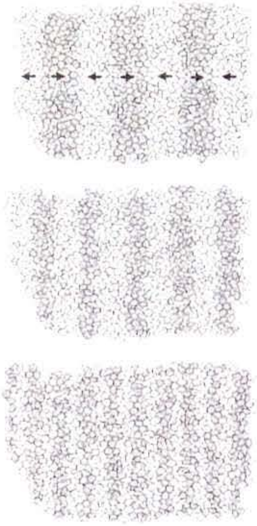

Figure 1.9: Reduction in signal quality with decreasing bit size[96].

Recording Technologies.

We have already illustrated the longitudinal recording technology which is used in today's commercially available hard disks. There are however three viable alternatives to this technology. The first is perpendicular recording in which the written bits are oriented perpendicular to plane of the film [20]. This has been shown experimentally to result in thinner transitions between bits and it is thought that perpendicular grains will show greater thermal stability and therefore reduce size constraints imposed by the super-paramagnetic limit. The most difficult obstacle in the development of such technology is the design of a write head that can produce the desired fringe

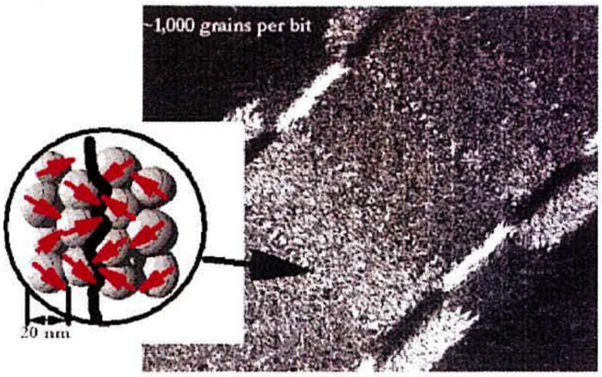

Figure 1.10: A written bit from a commercially available hard disk.

field without erasing adjacent bits. The most promising solution is to manufacture films with a soft magnetic underlayer. This underlayer then acts as part of the write head, closing the flux from the pole head itself as illustrated in figure 1.11. The second alternative is the use of patterned storage

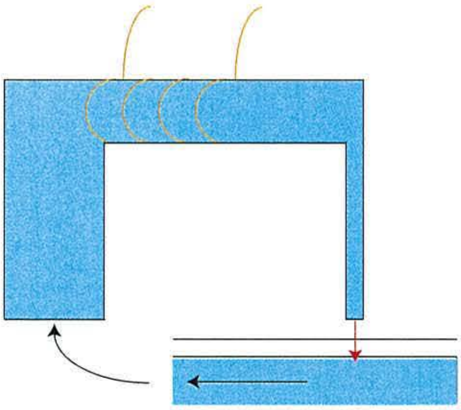

Figure 1.11: Perpendicular magnetic recording.

media, this would consist of arrays of nano-scale magnetic elements or nano-elements with each storing an individual bit. Since there is no transition between bits, this technology is fundamentally limited only by the superparamagnetic limit of a single grain. This technology is also being developed as a form of non-volatile random access memory or MRAM which could replace the conventional hard disk altogether. Nano-elements with rectangular in plane geometry are showing most promise at present as shape anisotropy results in two anti-parallel equilibrium magnetisation configurations along the long axis of the element. Finally density could be increased by the use of thermally assisted magnetic recording. Here the media is heated by a laser at the time of writing, lowering the coercivity. This would enable the use of very high anisotropy materials, hence increasing the magnetic energy of the grains and reducing the superparamagnetic limit.

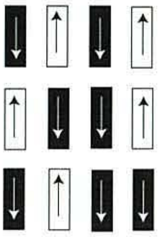

Figure 1.12: Patterned magnetic recording.

Applications of Micromagnetics.

Heuristic micromagnetics has helped in the development of tape media and with resolving the fields produced by write heads. Now that technology has almost reached the superparamagnetic limit there is a clear need for quantitative numerical modelling which can produce reliable predictions concerning the magnetic reversal mechanism. Our model has many potential applications. Firstly there is a need to understand the switching characteristics of MRAM elements. As well as understanding ways of obtaining the desired properties it will also be useful in understanding how to obtain reproducible switching properties. There is also still much to be learned about the fundamental differences between magnetic grains of longitudinal and perpendicular orientation. Micromagnetic simulations are vital in exploring magnetisation structure in the regime below experimental resolution. With the incorporation of temperature into the model we will also be able to investigate thermal stability as well as thermally assisted reversal. Finally with efficient numerical methods we hope it will be possible to develop a full-scale model of the recording process with subgrain resolution. This will help in the optimization of conventional media and in the development of new technologies.

1.3 Theories of Magnetism.

1.3.1 Electromagnetism.

In 1845 James Clerk Maxwell published his "Treatise on Electricity and Magnetism" which formed the basis of his theory of the electromagnetic field [21]. The theory can be summarized by the set of eponymous field equations

$$\begin{aligned} \nabla \cdot \boldsymbol{D} &= \rho \\ \nabla \cdot \boldsymbol{B} &= 0 \\ \nabla \times \boldsymbol{E} &= -\frac{\partial \boldsymbol{B}}{\partial t} \\ \nabla \times \boldsymbol{H} &= \frac{\partial \boldsymbol{D}}{\partial t} + \boldsymbol{J}. \end{aligned} \tag{1.35}$$

These equations are sufficient to describe the relationship between the electric field $\boldsymbol{E}$, electric flux density $\boldsymbol{D}$, the magnetic field $\boldsymbol{H}$ and magnetic flux density or induction $\boldsymbol{B}$ in a self-contained way and have found a multitude of applications. Maxwell's theory of electromagnetism is however insufficient to describe nano-scale phenomena in ferromagnetic materials because it does not take into account the intrinsic material properties of the media. Although electromagnetism can be used to describe macroscopically observable effects such as the magnetostatic field, to give a complete description of the magnetisation reversal process a deeper level of understanding is required. The behaviour of the magnetic moments within such materials, which manifests itself macroscopically as electromagnetism, depends strongly on the atomic interactions described previously. Clearly a complete description of any macroscopic system cannot be given in terms of the individual atoms. The problem is then to decide on an appropriate length-scale at which atomic effects are important and yet tractable mathematical formulations can be given.

1.3.2 Weiss Domain Theory.

The first theories of magnetism to incorporate material properties and temperature dependence into the description emerged in the late 1800's and early 1900's. After extensive studies of magnetic properties in a wide range of materials Curie published results on the susceptibility of diamagnets and paramagnets. It was shown that the meager susceptibility of diamagnets is independent of temperature whereas that of paramagnets is governed by an inverse proportionality to temperature

$$\chi = \frac{C}{T} \tag{1.36}$$

where C is the Curie constant for the relevent material [6]. Later Weiss postulated the existence of a molecular field which acted to align magnetisation in ferromagnets

$$\boldsymbol{H}_{Weiss} = \lambda \boldsymbol{M} \tag{1.37}$$

where λ is another material dependent constant [6], [11]. This led to a generalization of 1.36 to the ferromagnetic case

$$\chi = \frac{C}{T - \theta}. \tag{1.38}$$

Here $\theta = C\lambda M_s$ is known as the paramagnetic Curie temperature. This theory had some success in accounting for the paramagnetic transition but ultimatley failed to account for the demagnetisation of ferromagnets in zero field. Accordingly in 1907 Weiss postulated the existence of magnetic domains as an explanation [22]. His explanation has since been shown to be essentially correct but was complete conjecture at the time. The theory was partially validated by Barkhausen in 1915. Using an experimental apparatus of an iron sample within a coil which was then connected to an amplifier and speaker Barkhausen showed that audible clicks now known as Barkhausen noise were emitted during the magnetic reversal of the iron sample. These noises were interpreted as the reversal of individual Weiss domains. By application of the magnetic Kerr and Faraday effects the existence of ferromagnetic domains soon became visibly verified in experiments by Bitter [23] and Kittel [24] in particular. However Weiss's theory of the molecular field was later rejected in favour of the theory put forward by Heisenberg in 1931 [25], which first described ferromagnetic order in terms of exchange interactions.

1.3.3 Domain Wall Theory.

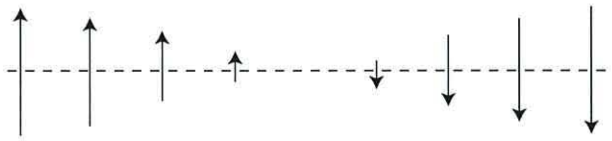

Figure 1.13: The Bloch domain wall.

Once the existence of magnetic domains was established attention turned to understanding their nucleation and propagation, and specifically to investigating the properties of the domain wall. The domain wall is defined as the transition region between adjacent domains. The idea that domain motion depended in a non-trivial way on the properties of the wall was first put forward in 1931 by Sixtus and Tonks [26]. They conjectured that the wall should posses its own free energy in analogy with the interface between liquids of different properties, oil and water for example. The first complete theory of the domain wall was derived by Bloch in 1932. He established a calculation for both the free energy and the corresponding wall thickness [27]. A bloch wall is illustrated in figure 1.13. The theory of course has one fatal error; the magnetisation cannot reduce to zero at the center of the wall because its magnitude is conserved everywhere by definition. The correct interpretation was given by Landau and Lifshitz in 1935 [28]. They showed that only the direction of $\boldsymbol{M}$ changes across the wall and that $|\boldsymbol{M}| = M_s$ is retained as in figure 1.14. Clearly the bloch wall is the correct interpretation of the tangential component of magnetisation only. The 1935 Landau-Lifshitz paper gives calculations for the $\boldsymbol{M}$ vectors across the wall as well as a calculation for the free energy. With slight developments by Neel in 1945 [29] and Kittel in 1949 [30] these results are still accepted today.

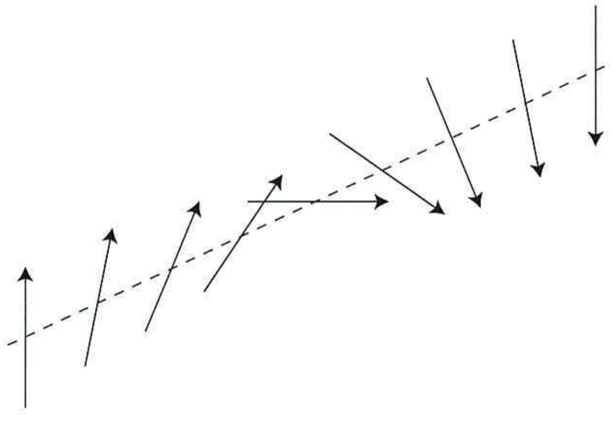

Figure 1.14: The Landau-Lifshitz domain wall.

1.3.4 The Stoner-Wohlfarth Model.

The Stoner-Wohlfarth model came about in the 1940's because of interest in single domain magnetic particles. At the time it was beginning to become apparant that many commercial alloys consisted of a dispersion of strongly ferromagnetic segregates set within a weakly ferromagnetic or non-magnetic matrix. The macroscopic ferromagnetic behaviour of these alloys was seen to be a product of the fine particle dipoles. Studies of the domain wall

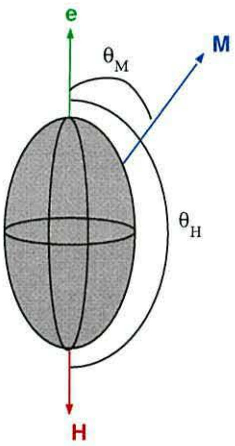

Figure 1.15: The Stoner-Wohlfarth particle.

by researchers such as Becker and Doring [31] were proving to give a good understanding of hysteresis in homogeneous materials. However the fine ferromagnetic particles of many alloys are below the critical dimensions for which domain nucleation is energetically feasible. The reversal of magnetisation must then occur by coherent rotation of the single domain as a whole. In their 1948 paper Stoner and Wohlfarth develop a theory of this reversal mechanism and proceed to develop results on the single domain limit of such particles [32]. Here we simply recreate the essential energy minimization approach which leads to the prediction of anisotropy induced hysteresis below the single domain limit. This has since become known as the Stoner-Wohlfarth model. The particle under consideration is illustrated in figure 1.15 where the easy-axis $\hat{\boldsymbol{e}}$ is along the z-axis, θ_M is the angle between $\boldsymbol{M}$ and $\hat{\boldsymbol{e}}$ and θ_H is the angle between the applied field and $\hat{\boldsymbol{e}}$. The energy due to uniaxial magnetocrystalline anisotropy and the Zeeman energy of the applied field are found by integrating their respective energy densities given in section 1.1.3 over the sphere

$$\begin{aligned} \mathcal{E}_{anis} &= \int_V K \sin^2(\theta_M) dV \qquad (1.39) \\ \mathcal{E}_z &= -\int_V M_s H \cos(\theta_H - \theta_M) dV \end{aligned}$$

where V is the volume of the particle, H is the magnitude of the applied field and M_s is the magnitude of magnetisation. The assumption of single domain behaviour eliminates exchange energy, this together with the ellipsoidal geometry results in a magnetostatic energy which can be expressed as a constant demagnetising factor [2], [32], [3]

$$\begin{aligned} \mathcal{E}_{ex} &= 0 \\ \mathcal{E}_d &= -\int_V \mathbf{N} M_s dV. \end{aligned} \tag{1.40}$$

To obtain equilibrium states of the magnetisation for given θ_H the total energy is minimized with respect to θ_M

$$\begin{aligned} \mathcal{E} &= \int_V K\sin^2\theta_M - \int_V HM_s\cos(\theta_H - \theta_M) - \int_V NM_s dV \\ &= KV\sin^2\theta_M - M_sVH\cos(\theta_H - \theta_M) - M_sNV. \\ \frac{d\mathcal{E}}{d\theta_M} &= 2KV\sin\theta_M\cos\theta_M - M_sVH\sin(\theta_H - \theta_M). \end{aligned} \tag{1.41}$$

We then have an energy minimum at

$$\begin{aligned} \frac{d\mathcal{E}}{d\theta_M} &= 0 \\ \frac{d^2\mathcal{E}}{d\theta_M^2} &> 0. \end{aligned} \tag{1.42}$$

This may then be used to obtain a minimum for all θ_H between 0 and π, hence plotting a hysteresis loop for given easy-axis directions. The original results from the Stoner-Wohlfarth paper are shown in figure 1.16

1.3.5 Micromagnetics.

Although specific aspects of ferromagnetic reversal may be accounted for by the theories outlined above, each describes only a facet of the underlying magnetisation processes. A need clearly exists to develop a numerical model which is able to predict hysteretic properties and realistic domain structures of ferromagnetic media from given material parameters. Micromagnetics was the first theory of magnetism which had the power to investigate magnetisation properties within any conceivable geometry and yet to take into account the material properties of the medium. No simplifying assumptions are required and in principal the theory can be applied numerically to any magnetic system provided that the discretization cells satisfy the restrictions given by

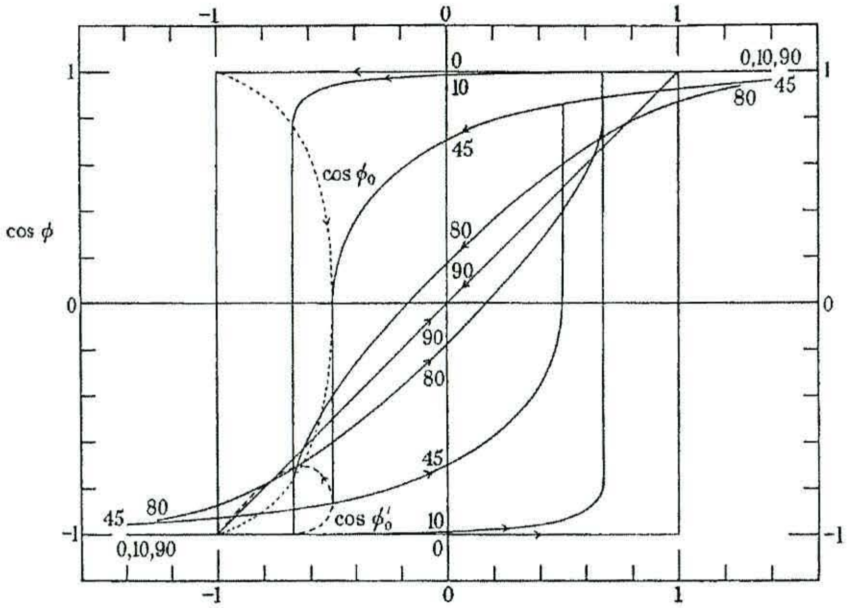

Figure 1.16: Results from Stoner and Wohlfarth's 1948 paper [32].

the definition of magnetisation. The idea is simple, all that is required to obtain an equilibrium configuration in any system is to minimize that system's free energy with respect to the appropriate state variable, see figure 1.17. In magnetism the state variable is the magnetisation configuration with a state space consisting of all such configurations. The Gibbs free energy must then be derived in terms of the magnetisation in order to perform the minimization. As in Brown's original work we assume that the energy takes contributions from exchange energy, anisotropy energy, magnetostatic energy and applied zeeman energy. Other terms such as magnetostriction and thermal energy are regarded as negligible in the first instance. This model essentially strips away the simplifying restrictions of the Stoner-Wohlfarth model and applies energy minimization in the general case.

Exchange Energy.

The wave function analysis of the exchange interaction discussed in section 1.1.3.1 leads to an expression for the exchange energy of atoms A, B of the form

$$E_{ex} = -2J_{ex}\boldsymbol{S}_A \cdot \boldsymbol{S}_B \tag{1.43}$$

where J_{ex} is the exchange integral, which is always positive for ferromagnetic materials [11], and $\boldsymbol{S}_A$, $\boldsymbol{S}_B$ are the net electronic spin vectors of atoms

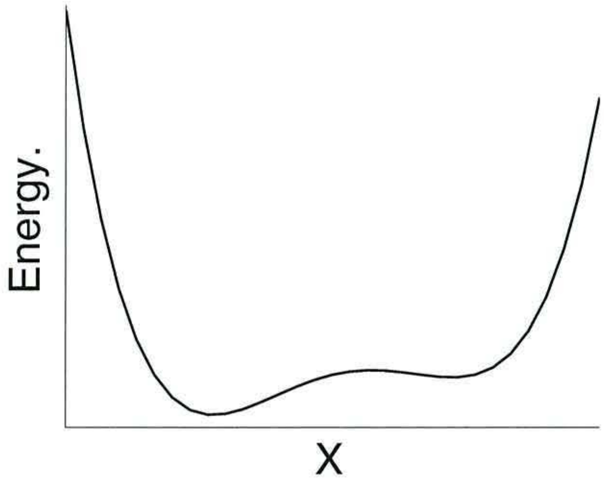

Figure 1.17: The energy functional.

A, B. By virtue of the dot product in 1.43 the exchange energy is minimized for ferromagnets when $\boldsymbol{S}_A$ and $\boldsymbol{S}_B$ are parallel. For anti-ferromagnets the exchange integral is negative and E_{ex} is minimized by anti-parallel spin vectors. Naturally $J_{ex} = 0$ for atoms with full electron shells. This optimal orientation of spin vectors results in a corresponding orientation of the atomic magnetic moments. Ferromagnetic exchange energy is therefore minimized when magnetisation is homogeneous. Generalizations of 1.43 to the many atom case give a means by which to calculate the exchange energy. However these are only valid in *ab initio* calculations in which all atoms are considered. Corresponding macroscopic approximations [2], [9], [33] usually involve the distance between evaluation points and result in the severe mesh dependency of numerical solutions. Instead we note that E_{ex} is zero when the magnetisation is homogeneous and increases with increased irregularity of the magnetisation. Such spatial variation is appropriatley measured by $\nabla \boldsymbol{M}$. Consequently the most straight-forward expression of the exchange energy is given by

$$\mathcal{E}_{ex} = \int_V \frac{A}{M_s^2} |\nabla \boldsymbol{M}|^2 dV. \tag{1.44}$$

The exchange constant A may then be obtained experimentally. Aharoni gives a derivation of $\mathcal{E}_{ex}$ in terms of atomic spin vectors which arrives at the same expression as that in 1.44 [2]. His derivation relys on a small angle approximation for the orientation of moments and their neighbours, this shows that to remain valid the magnetisation should change by only small angles between evaluation points. As a result discretization cells should be no larger in any direction than the intrinsic exchange length of the material

$$l_{ex} = \sqrt{\frac{A}{2\pi M_s}}. \tag{1.45}$$

Clearly the exchange energy is independent of the local orientation of $\boldsymbol{M}$ but depends on the homogeneity of magnetisation.

Anisotropy Energy.

The term anisotropy refers to any mechanism by which measurements depend on the direction in which they are taken. As well as that due to the spin-orbit interaction there are other forms of anisotropy at work in ferromagnetic materials. A prefered direction of magnetisation is often dictated by the geometry of the sample, this is known as shape anisotropy and although it is often important it requires no new energy term as it is a product of the magnetostatic interaction which is calculated separately. Anisotropy due to the coupling of magnetisation and internal stresses is known as magnetostriction and may be regarded as negligible in our initial applications. We are left with just the magnetocrystalline anisotropy which may be calculated for uniaxial materials from the energy density given in section 1.1.3. We require the expression in terms of the magnetisation which may be obtained using the properties of the scalar product

$$\begin{aligned} \mathcal{E}_{anis} &= \int_V K\cos^2(\theta)dV \qquad (1.46) \\ &= \int_V K(\frac{\boldsymbol{M}}{M_s}\cdot\hat{\mathbf{e}})^2 dV \\ &= \int_V \frac{K}{M_s^2}(\boldsymbol{M}\cdot\hat{\mathbf{e}})^2 dV \end{aligned}$$

where $\hat{\mathbf{e}}$ is a unit vector along the easy-axis direction. Magnetocrystalline anisotropy energy is in general far lower than the exchange energy and therefore has negligible effect on the magnitude of M_s. However in the absence of an applied field the direction of local magnetisation is determined entirely by the easy-axis direction.

Magnetostatic Energy.

The magnetostatic energy is given simply by

$$\mathcal{E}_d = -\frac{1}{2}\int_V \boldsymbol{M}\cdot\boldsymbol{H}_d dV. \tag{1.47}$$

The derivation is given by Brown [1] and Aharoni [2] as the potential energy of a distribution of elementary dipoles over V using the Lorentz local field approximation. Before the development of modern numerical methods with which to solve the Maxwell equations for arbitrary geometry it was the calculation of $\boldsymbol{H}_d$ which prevented the general application of micromagnetics. The field may be expressed using the integral equation

$$\boldsymbol{H}_d = -\int_V \nabla \cdot \boldsymbol{M}(\boldsymbol{r}') \frac{(\boldsymbol{r}-\boldsymbol{r}')}{|\boldsymbol{r}-\boldsymbol{r}'|^3} dV' + \int_S \hat{\boldsymbol{n}}' \cdot \boldsymbol{M}(\boldsymbol{r}') \frac{(\boldsymbol{r}-\boldsymbol{r}')}{|\boldsymbol{r}-\boldsymbol{r}'|^3} dS' \tag{1.48}$$

where $\boldsymbol{r}$ and $\boldsymbol{r}'$ are distributed field sources and the points of evaluation respectively. However problems occur with the evaluation of singular integrals when $\boldsymbol{r}' = \boldsymbol{r}$. The calculation is simplified when considering uniformly saturated samples, in that case the field may be given in terms of a demagnetising factor

$$\boldsymbol{H}_d = -\mathbf{N} \cdot \boldsymbol{M}. \tag{1.49}$$

In particular for symmetric bodies with symmetry axes coincident with the coordinate axes $\mathbf{N}$ is simply a diagonal matrix. When diagonal elements are equal due to symmetry $\mathbf{N}$ reduces to a scalar N, for example in the case of the sphere

$$N_{sphere} = \frac{4\pi M_s}{3}, \tag{1.50}$$

simple expressions can also be obtained for the general ellipsoid and used in conjunction with Stoner-Wohlfarth type models.

Brown's Equations.

Superposing the terms derived above with the Zeeman energy due to an applied field we may form the free energy functional

$$\mathcal{E}_G = \int_V (\frac{A}{M_s^2} |\nabla \boldsymbol{M}|^2 + K \sin^2 \theta - \frac{1}{2} \boldsymbol{M} \cdot \boldsymbol{H}_d - \boldsymbol{M} \cdot \boldsymbol{H}_z) dV. \tag{1.51}$$

These are known as Brown's equations after William Fuller Brown, Jr [1]. The first two terms incorporate the essentially quantum mechanical and thermodynamical material dependent information into the problem, while the third and fourth terms are material independent Maxwellian terms. The minimization of this functional gives equilibrium configurations of $\boldsymbol{M}$ for any given set of parameters, geometry and applied field. Simulations of a hysteresis experiment may then be performed by calculating the equilibrium configuration at each of the required field steps. This process yields a plot of the hysteresis loop itself as well as the intermediate domain configurations at each field-step. However the method does have two fundamental limitations. The first is that the dynamic behaviour of the magnetisation between field steps is not resolved. This is becoming increasingly important in applications to magnetic recording where the resolution of magnetisation over very short time intervals is extremely valuable. Secondly and more fundamentally, magnetisation reversal often occurs via an irreversible switching mechanism at the critical applied field strength H_c. This is known as a Barkhausen jump, see figure 1.18. There is often ambiguity in energy minimization methods as a multiplicity of local energy minima my exist in the free energy functional. The problem is further complicated by the fact that more than one jump may occur during the same reversal corresponding to the reversal of individual domains. From a configuration in advance of a Barkhausen jump 1.18 (a), obtained from the initial saturation by means of reversible magnetisation changes, there are many possible equilibrium states 1.18 (b) corresponding to local energy minima. Energy minimization methods can be used to obtain all such states but, in relation to the first point, a dynamic visualization of the magnetisation is required to understand the transition from state (a) to state(s) (b). It is the aim of this thesis to show

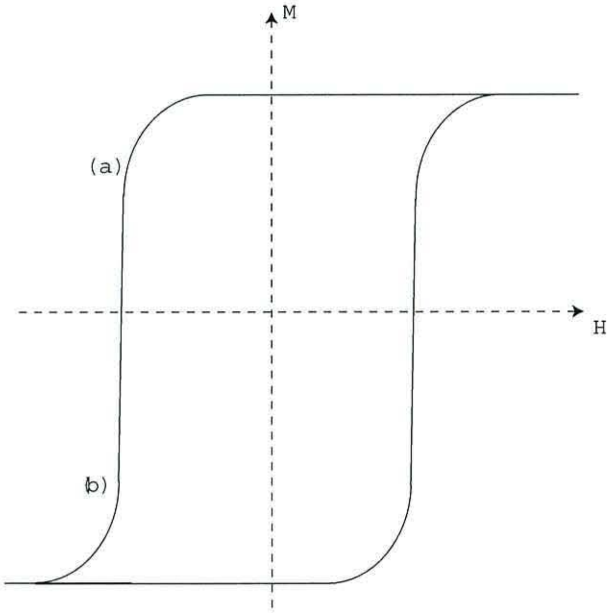

Figure 1.18: The Barkhausen Jump.

that this problem can be addressed by dynamic finite element analysis on the micromagnetic length-scale. Micromagnetics is not yet a feasible design tool for magnetic storage and engineering applications. We hope to develop a numerical model incorporating all the fundemental aspects of magnetisation reversal with resolution of magnetisation in both space and time. Further we will investigate the computational efficiency and numerical stability of the model in order to establish both the region of applicability as well as our level of confidence in the results.

Chapter 2

Magnetisation dynamics.

In this chapter we develop the ideas from chapter 1 and give a brief discussion of gyromagnetic precession and ferromagnetic resonance of magnetic moments and the gyromagnetic effect is then generalized to the magnetisation. We subsequently introduce the Landau-Lifshitz and Gilbert equations of motion for magnetisation and discuss their relative merits in modelling the damped gyromagnetic precession of magnetisation about an externally applied field. We find in favour of the Gilbert equation and proceed to consider suitable numerical integration methods. The dynamics of a single-spin system are then investigated with discussions of how the damping parameter and the strength of the applied field influence the precession. Finally we introduce the notion of an effective field and show that inclusion of the anisotropy field term yields solutions of the Gilbert equation which agree exactly with Stoner-Wohlfarth theory.

2.1 Gyromagnetic Precession.

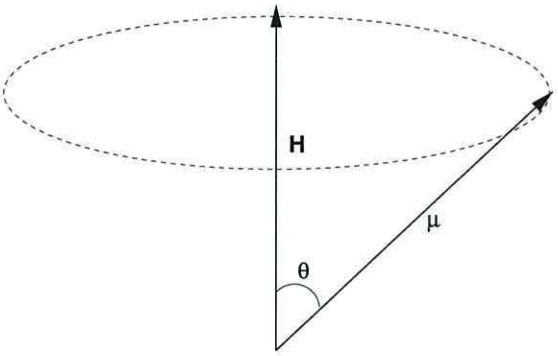

Figure 2.1: The Larmor precession.

From section 1.1.2 we have

$$\frac{d\boldsymbol{\mu}}{dt} = -\gamma\boldsymbol{\mu} \times \boldsymbol{H} \tag{2.1}$$

where

$$\gamma = \frac{ge}{2m_e c}. \tag{2.2}$$

Solving this equation of motion for individual moments $\boldsymbol{\mu}$, gives infinitely precessional trajectories at constant angle θ around the applied field as shown in figure 2.1. Notwithstanding thermal fluctuations the frequency of the precession is given by the Larmor frequency

$$\begin{aligned} v_L &= \frac{\gamma|\boldsymbol{H}|}{2\pi} \\ &= \frac{ge|\boldsymbol{H}|}{4\pi m_e c}. \end{aligned} \tag{2.3}$$

2.1.1 Measuring g.

As mentioned in section 1.1.2, by considering the ratio of spin-angular momentum to orbital angular momentum we may establish whether a magnetic moment is due essentially to spin motion, orbit motion or a combination of the two. This problem, like the problem of computing the Larmor frequency, reduces to the problem of measuring the Lande splitting factor g. This can be achieved in a number of ways, most common are two indirect methods which exploit the coupling of magnetic moment and angular momentum. Both indirect methods rely on a quantity known as the magnetomechanical factor g^*

$$\frac{1}{g} + \frac{1}{g^*} = 1. \tag{2.4}$$

The Einstein-de Haas method involves inducing a rotation by magnetisation, conversely the Barret method involves inducing a magnetisation by rotation. Alternatively g may be measured directly using equation 2.3.

Einstein-de Haas Method.

A rod of the material in question may be suspended in an applied magnetic field, the field is then suddenly reversed. In consequence the atomic moments of the rod align accordingly. This results in corresponding re-alignment of the atomic angular momentum vectors which must be balanced by an opposite increase in the macroscopic angular momentum of the rod. This small angle of rotation which occurs upon reversal of the field may be measured and used to compute g in terms of g^*.

Barnett Method.

Proceeding by rapidly rotating the rod around its longitudinal axis in zero field produces the reciprocal effect. The angular momentum vectors align with the axis of rotation which causes a corresponding alignment of the magnetic moments. This manifests itself as an increased magnetisation component along the axis of the rod. Again allowing g to be computed in terms of g^*.

Ferromagnetic Resonance.

Direct measurement of g is made possible by equation 2.3. The sample is placed in a powerful constant applied field $\boldsymbol{H}_{cf}$ and subject to a weak transverse field $\boldsymbol{H}_{af}$ which alternates rapidly at frequency v. The precession of moments in the sample is primarily dependent on g and $|\boldsymbol{H}_{cf}|$, although energy is absorbed from $\boldsymbol{H}_{af}$. Slow variation of $|\boldsymbol{H}_{cf}|$ and v allows the resonant frequency to be found. This is when the state of maximum energy absorption is reached and v is equal to the frequency of precession. Using 2.3 we have

$$v = v_L = \frac{ge|\boldsymbol{H}_{cf}|}{4\pi m_e c} \tag{2.5}$$

and so

$$g = \frac{4\pi m_e c v}{e|\boldsymbol{H}_{cf}|}. \tag{2.6}$$

This is known as the ferromagnetic resonance or FMR experiment.

2.1.2 Precession of the Magnetisation.

In our micromagnetic model we assume a continuum hypothesis, that is we assume that the magnetization or the net magnetic moment per unit volume is a continuous quantity which may be specified at any point in space. Similarly we follow the assumptions of micromagnetic theory that all magnetic fields may be specified exactly at a point as the functional derivative of the Gibbs free energy with respect to the magnetization. Although we take account of atomistic effects, the atomic structure is not explicitly represented in the micromagnetic model. We therefore require an equation of motion which applies to magnetisation rather than to individual atomic moments. This presents no difficulty as the individual atomic moments appear on both sides of equation 2.1, we may therefore generalize to the magnetisation. For all lattice sites i in an elementary volume V we have

$$\frac{d\boldsymbol{\mu_i}}{dt} = -\gamma\boldsymbol{\mu_i} \times \boldsymbol{H}; \quad i \in V \tag{2.7}$$

we may then take the sum over all sites in V while still preserving the equality

$$\sum_{i\in V}\left(\frac{d\boldsymbol{\mu_i}}{dt}\right) = \sum_{i\in V}\Big(- \gamma\boldsymbol{\mu_i} \times \boldsymbol{H}\Big). \tag{2.8}$$

Dividing both sides by the volume V we obtain the precession equation in terms of magnetisation

$$\begin{aligned} \frac{\sum_{i\in V}\frac{d\boldsymbol{\mu_i}}{dt}}{V} &= \frac{\sum_{i\in V} -\gamma\boldsymbol{\mu_i} \times \boldsymbol{H}}{V} \\ \frac{d(\sum_{i\in V}\boldsymbol{\mu_i}/V)}{dt} &= -\gamma(\sum_{i\in V}\boldsymbol{\mu_i}/V) \times \boldsymbol{H} \\ \frac{d\boldsymbol{M}}{dt} &= -\gamma\boldsymbol{M} \times \boldsymbol{H}. \end{aligned} \tag{2.9}$$

We note here that this equation refers to the motion of magnetisation at a single point in space and no longer applies to the single atomic moment. All subsequent reference to a single-spin model refers to a single spin in this sense and not to a single atom model.

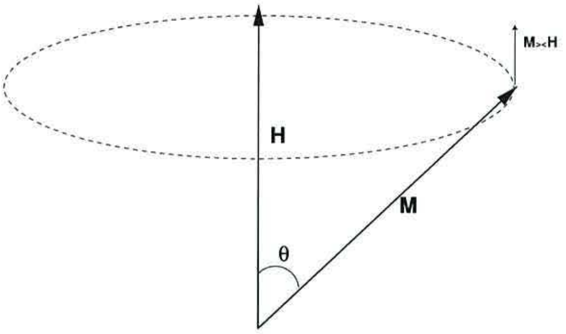

Figure 2.2: Precession of magnetisation.

2.2 Damped Gyromagnetic Precession.

We have seen that magnetic moments will precess around an applied magnetic field ***H*** at the Lamour frequency if they are not subject to any other forces. Further that this relation (equation 2.7) generalizes to the magnetization, provided that the applied field may be assumed to be homogeneous over each unit volume. However 2.9 implies that the magnetisation should precess eternally at a constant angle θ around the field vector as shown in figure 2.2, this does not fully describe the macroscopically observed magnetic relaxation. If this were the case then the reversal of a magnetic bit by application of a writing head field would be impossible and the hard disk in my computer would not be able to store this information. We know from experience that ferromagnetic moments do indeed align with an applied magnetic field and therefore must be subject to some action other than gyromagnetic precession. We may gain further insight by cautiously returning to the analogy with a spinning top. The top will precess around the direction of the gravitational field in the same way as an atomic moment around a magnetic field. However the top will eventually lose energy due to frictional forces and fall into alignment with the gravitational field. A similar mechanism is at work during the precession of the magnetic moment. To align with a magnetic field, a magnetic moment must lose or dissipate energy. This damping occurs through the spin-spin and spin-orbit interactions. However the precise mechanism by which energy is dissipated during these interactions is not well understood. The damping mechanism has been interpreted essentially in three different ways. One interpretation is that energy is lost basically in the form of heat [3]. Others support the idea that damping represents a lag between the atomic interactions and the response time of the moments [10]. Finally damping may be seen as a result of thermal agitations.

We feel that the real dissipation mechanism is probably a combination of all three of the above, in any case these interactions occur on a time and length scale that we cannot hope to model macroscopically. For the same reasons as we are forced to work with magnetisation rather than individual magnetic moments, we are forced to consider damping in a phenomenologically manner rather than in terms of the underlying physics.

In deriving an equation of motion for damped magnetisation dynamics we note that any vector may be decomposed into three orthogonal basis vectors, for example

$$\begin{pmatrix} a \\ b \\ c \end{pmatrix} = a \begin{pmatrix} 1 \\ 0 \\ 0 \end{pmatrix} + b \begin{pmatrix} 0 \\ 1 \\ 0 \end{pmatrix} + c \begin{pmatrix} 0 \\ 0 \\ 1 \end{pmatrix}. \tag{2.10}$$

In the same way we may decompose the vector $d\boldsymbol{M}/dt$ into three orthogonal components in terms of $\boldsymbol{M}$ and $\boldsymbol{H}$ to give an equation of motion

$$\frac{d\boldsymbol{M}}{dt} = a\boldsymbol{M} + b\boldsymbol{M} \times \boldsymbol{H} + c\boldsymbol{M} \times (\boldsymbol{M} \times \boldsymbol{H}) \tag{2.11}$$

these three terms are orthogonal by virtue of the vector product. As a consequence of the fact that $|\boldsymbol{M}|$ must be conserved, a cannot be anything other than zero. To ensure that the undamped case is modelled effectively b is naturally given by $-\gamma$, thereby recovering equation 2.9 when $c = 0$.

2.2.1 The Landau-Lifshitz Equation.

Landau and Lifshitz were the first to suggest a model of damped gyromagnetic precession in 1935 [28]. Their method was to derive a damping term by linking the magnetic relaxation with the expected equilibrium, namely that the magnetization $\boldsymbol{M}$ will align with an applied external field $\boldsymbol{H}$. As well as the precession term which follows from first principles they assumed that $d\boldsymbol{M}/dt$ should have a component which is perpendicular to both the current magnetization and the direction of the precession $\boldsymbol{M} \times \boldsymbol{H}$ as in 2.11. The vector perpendicular to both $\boldsymbol{M}$ and $\boldsymbol{M} \times \boldsymbol{H}$ is simply $\boldsymbol{M} \times (\boldsymbol{M} \times \boldsymbol{H})$ as shown in figure 2.3. This component must be negative to ensure that the

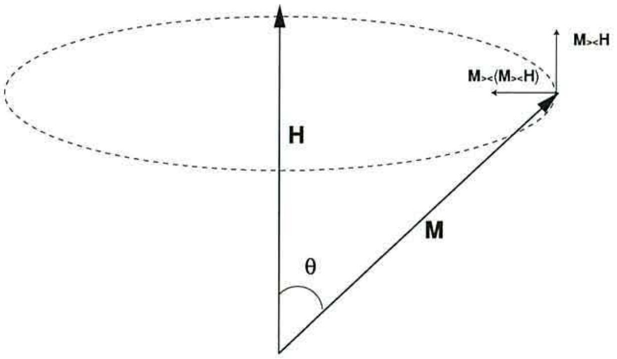

Figure 2.3: The Landau-Lifshitz damping mechanism.

desired equilibrium is achieved. The phenomenological damping constant $c = \lambda/M_s$ is then introduced to give

$$\frac{d\boldsymbol{M}}{dt} = -\gamma(\boldsymbol{M} \times \boldsymbol{H}) - \frac{\lambda}{M_s}(\boldsymbol{M} \times (\boldsymbol{M} \times \boldsymbol{H})). \tag{2.12}$$

As shown by Kikuchi [34] and more recently by Mallinson [35] it is convenient

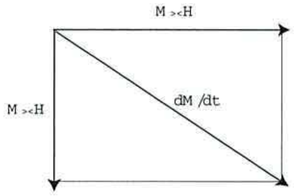

Figure 2.4: Spherical components of the Landau-Lifshitz equation.

to visualize the solution of such equations on the surface of a sphere of radius $|\boldsymbol{M}|$. Applying the cross-product right-hand rule to 2.12 we have two $\frac{d\boldsymbol{M}}{dt}$ components of $\gamma(\boldsymbol{M} \times \boldsymbol{H})$ and $\lambda(\boldsymbol{M} \times \boldsymbol{H})$ in the azimuthal direction and the polar direction respectively. The azimuthal component corresponds to undamped precession and the polar component to alignment with the applied field as depicted in figure 2.4. With $\lambda = 0$, $d\boldsymbol{M}/dt$ points in the azimuthal direction and we recover the precession equation 2.9. At small values of λ, $d\boldsymbol{M}/dt$ acquires a polar component and the tip of the magnetisation vector takes a spiral path around the sphere until the magnetisation has aligned with the field. As λ is increased the azimuthal component is unchanged. The increased polar component however results in both an increase in the magnitude of $d\boldsymbol{M}/dt$ and a more direct path around the sphere. With a greater change in $\boldsymbol{M}$ for each increment of time dt, the alignment of the magnetisation with the applied field becomes faster with increased λ. As can be seen from figure 2.5 there is no limiting behaviour and so $|d\boldsymbol{M}/dt|$ increases, and the time taken for $\boldsymbol{M}$ to align with $\boldsymbol{H}$ decreases, indefinitely with increased λ.

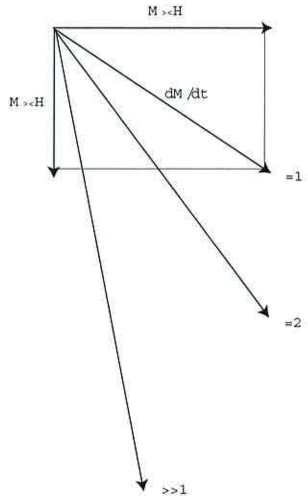

Figure 2.5: Asymptotic behaviour of the Landau-Lifshitz equation.

2.2.2 The Gilbert Equation.

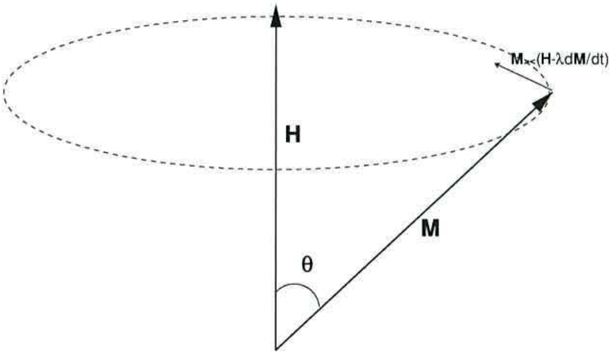

Figure 2.6: The Gilbert damping mechanism.

In 1955 Gilbert [36], in subtle contrast to Landau and Lifshitz, proposed that the relaxation of a magnetic moment should be linked to the energy

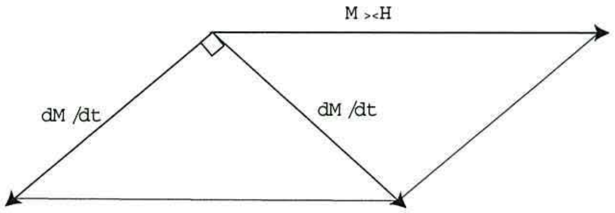

Figure 2.7: Precession and damping components of the Gilbert equation.

dissipation of the system rather than the expected equilibrium. Although his approach is still a phenomenological one, it does highlight a marked difference in thinking. Gilbert asserted that the equation should model the physical behaviour of the system and not simply be tailored to arrive at the anticipated solution. To this end the Gilbert equation takes the form of the standard precession equation 2.9 with the field term $\boldsymbol{H}$ augmented by a damping term which is proportional to the rate of change of magnetisation

$$\frac{d\boldsymbol{M}}{dt} = -\gamma(\boldsymbol{M} \times (\boldsymbol{H} - \frac{\lambda}{M_s}\frac{d\boldsymbol{M}}{dt})). \tag{2.13}$$

The magnitude of the field components in the cross product is then reduced. Damping is thus incorporated implicitly as the precession direction is no longer perpendicular to $\boldsymbol{H}$. We may then write the Gilbert equation in its more familliar form with seperated precession and damping terms

$$\frac{d\boldsymbol{M}}{dt} = -\gamma(\boldsymbol{M} \times \boldsymbol{H}) + \frac{\gamma\lambda}{M_s}(\boldsymbol{M} \times \frac{d\boldsymbol{M}}{dt}). \tag{2.14}$$

In the language of the Landau-Lifshitz equation, the damping term is now perpendicular to both the magnetisation and the dynamic gradient of the magnetisation. The Gilbert damping constant is then written as $\alpha = \gamma\lambda$ to give

$$\frac{d\boldsymbol{M}}{dt} = -\gamma(\boldsymbol{M} \times \boldsymbol{H}) + \frac{\alpha}{M_s}(\boldsymbol{M} \times \frac{d\boldsymbol{M}}{dt}). \tag{2.15}$$

We proceed as before and apply the cross-product right-hand rule to give two $d\boldsymbol{M}/dt$ components of $\gamma(\boldsymbol{M} \times \boldsymbol{H})$ and $\alpha d\boldsymbol{M}/dt$ in the azimuthal and polar directions respectively. Now in contrast to the Landau-Lifshitz equation, the Gilbert damping term contains both azimuthal and polar components and the damping mechanism is acting on the total resultant motion $d\boldsymbol{M}/dt$ of the magnetisation. For small α we see similar behaviour, but now as α increases past a critical value we see that the magnitude of $d\boldsymbol{M}/dt$ must decrease to remain at right-angles to the damping term, see figure 2.7. As a result, in highly damped systems the magnetisation takes longer to align with the applied field. In agreement with Mallinson [35] we feel that this limiting behaviour is more physically plausable than the situation implied by the Landau-Lifshitz equation. The possible situations arising from Gilbert damping are summarised in figure 2.8.

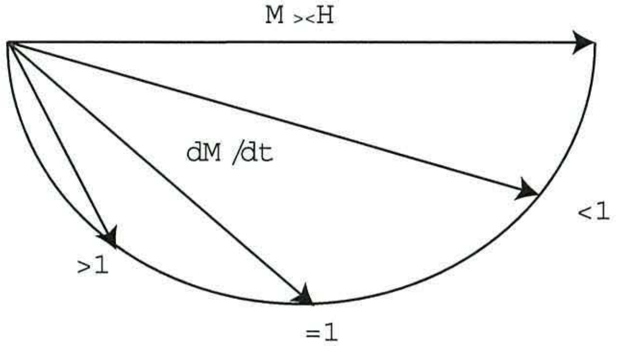

Figure 2.8: Asymptotic behaviour of the Gilbert equation.

2.2.3 The Landau-Lifshitz-Gilbert Equation.

The fact that the Landau-Lifshitz equation has dominated over the Gilbert equation in the literature until recently is due to computational efficiency rather than physical plausability. The Landau-Lifshitz equation is, in a trivial sense, easier to solve than the Gilbert. This is due to the fact that $d\boldsymbol{m}/dt$ appears in only the left-hand side of the equation as the dependent variable. Although the right-hand side of the Gilbert equation poses no problem in general, if a pointwise solution is required, it is simpler to cast this equation in so called Landau-Lifshitz form; resulting in the Landau-Lifshitz-Gilbert equation. If we take the vector product of $\boldsymbol{M}$ with both sides of 2.15 we have

$$\boldsymbol{M} \times \frac{d\boldsymbol{M}}{dt} = -\gamma(\boldsymbol{M} \times (\boldsymbol{M} \times \boldsymbol{H})) + \frac{\alpha}{M_s}(\boldsymbol{M} \times (\boldsymbol{M} \times \frac{d\boldsymbol{M}}{dt})) \tag{2.16}$$

Since the magnitude of the magnetisation is conserved $\boldsymbol{M} \cdot d\boldsymbol{M}/dt = 0$. This together with the vector identity

$$\boldsymbol{Q} \times (\boldsymbol{Q} \times \frac{d\boldsymbol{Q}}{dt}) = (\boldsymbol{Q} \cdot \frac{d\boldsymbol{Q}}{dt})\boldsymbol{Q} - |\boldsymbol{Q}|^2 \frac{d\boldsymbol{Q}}{dt} \tag{2.17}$$

gives

$$\boldsymbol{M} \times \frac{d\boldsymbol{M}}{dt} = -\gamma(\boldsymbol{M} \times (\boldsymbol{M} \times \boldsymbol{H})) - \alpha M_s \frac{d\boldsymbol{M}}{dt} \tag{2.18}$$

substituting back into the right-hand side of 2.15 we have

$$\begin{aligned} \frac{d\boldsymbol{M}}{dt} &= -\gamma(\boldsymbol{M} \times \boldsymbol{H}) + \frac{\alpha}{M_s}(-\gamma(\boldsymbol{M} \times (\boldsymbol{M} \times \boldsymbol{H})) \qquad (2.19) \\ &\quad -\alpha M_s(\frac{d\boldsymbol{M}}{dt}) \\ &= -\gamma(\boldsymbol{M} \times \boldsymbol{H}) - \frac{\gamma\alpha}{M_s}(\boldsymbol{M} \times (\boldsymbol{M} \times \boldsymbol{H})) - \alpha^2(\frac{d\boldsymbol{M}}{dt}) \\ \frac{d\boldsymbol{M}}{dt}(1+\alpha^2) &= -\gamma(\boldsymbol{M} \times \boldsymbol{H}) - \frac{\gamma\alpha}{M_s}(\boldsymbol{M} \times (\boldsymbol{M} \times \boldsymbol{H})) \\ \frac{d\boldsymbol{M}}{dt} &= -\frac{\gamma}{(1+\alpha^2)}(\boldsymbol{M} \times \boldsymbol{H}) - \frac{\gamma\alpha}{M_s(1+\alpha^2)}(\boldsymbol{M} \times (\boldsymbol{M} \times \boldsymbol{H})). \end{aligned}$$

At this point many authors conclude that we have obtained the Landau-Lifshitz equation from the Gilbert equation and that the two equations are therefore equivalent provided

$$\gamma_L = \frac{\gamma_G}{1+\alpha^2} \tag{2.20}$$

and

$$\lambda = \frac{\gamma_G \alpha}{1+\alpha^2}. \tag{2.21}$$

However we recall that γ represents the reciprocal of the gyromagnetic ratio, which is proportional to the ratio of electron charge to electron mass. Equation 2.20 is therefore meaningless since a constant cannot be a function of itself. In the above derivation we may have shown that the two equations belong to the same family of damped gyromagnetic precession equations as explained by Podio-Guidugli [37], however the proviso shows that they are not at all equivalent. To quote Mallinson [35] "The arguement that, with appropriate substitutions of the constants, the two forms are equivalent is a sophism; they express different physics." Indeed an extra line of reasoning in the above such as "But $\gamma_L = \gamma_G = \gamma = \frac{ge}{2m_e c}$." constitutes a proof by contradiction that the Gilbert and Landau-Lifshitz equations are distinct, excepting the case of zero damping of course where $\alpha = 0$ implies that $\gamma_L = \gamma_G$ and $\lambda = 0$.

2.2.4 Discussion.

We have shown that due to the physical meaningfulness of the parameters involved that the Landau-Lifshitz and Gilbert equations are not equivalent, either mathematically or physically.

The difference lies in the fact that Gilbert takes his damping term to be perpendicular to the left-hand side of the precession equation 2.9 whereas Landau and Lifshitz take theirs from the right-hand side. Once the right-hand side is augmented by the damping term, these two approaches are no longer equivalent except in the case of zero damping. In the Gilbert equation $d\boldsymbol{M}/dt$ is damped in a self-consistent manner. In the Landau-Lifshitz equation however, the $\boldsymbol{M} \times \boldsymbol{H}$ which is present in the damping term is no longer equivalent to $d\boldsymbol{M}/dt$.

Considering the Landau-Lifshitz-Gilbert form of the Gilbert equation we again see that in the Gilbert formalism the damping parameter influences the precession term as well as the dissipation term. This is not the case with the Landau-Lifshitz formalism.

We also reinforce the point that the Landau-Lifshitz equation is only truely valid for the case of zero damping and it's use for a damping parameter of $\lambda < 1$ which is assumed to be acceptable by many authors, is not in fact physically acceptable. Due to the non-linear behaviour of the system under consideration we therefore conclude that the Gilbert equation is to be preferred in all circumstances.

It has often been commented that these two equations are not the only members of the family [34], [35]. The semi-circle in figure 2.8 could be replaced by many concievable curves, and among them there are many which would give the desired limiting behaviour of the Gilbert equation, such as the parabola mentioned by Mallinson [35]. It has also been shown [37] that the standard Gilbert equation incorporates only relativistic dissipation, while a generalized form of the equation may be derived to incorporate exchange dissipation [38], dry-friction dissipation [39] and others. However in light of the fact that very little experimental evidence exists to verify such formalisms we opt to model magnetisation dynamics using the standard Gilbert equation, with other phenomenon incorporated via the standard effective field method of dynamic micromagnetics.

2.3 Numerical Integration Schemes.

If no spatial derivatives are present in the expression of magnetic field, then the Gilbert equation is in fact a system of three coupled ordinary differential equations (ODE's) for the three components of $\boldsymbol{M}$. We first consider the variation of a scalar variable x with respect to independent variable t

$$\frac{dx}{dt} = f(t, x). \tag{2.22}$$

In general, numerical methods of solving such equations divide the domain of x into finite sections Δt. In dynamic systems these correspond to increments of time from some time t_0 which is considered as the origin. The existence and uniqueness of solutions for such initial value problems is well established [43]. If we wish to solve for x over some fixed time interval t_0 to t_1, then a finite element or finite difference method is appropriate. In that case we would use our knowledge of the relation between x_i and x_{i+1} in terms of t_i and t_{i+1} to form an equation for each increment or element Δt and solve the resulting global matrix equation subject to suitable conditions at t_0 and t_1; this is known as a boundary value problem. In predictive simulations however, were x at t_1 is unknown, this method cannot be applied in a straightforward way. Indeed in our work we have no knowledge of where t_1 will fall on the t-axis. Rather we use our knowledge of the function $f(t, x)$ to make an approximation of x_{i+1} from the known value of x_i, starting at some initial state $x_0 = x(t_0)$ we iterate until the system reaches equilibrium, i.e. $x_{i+1} = x_i$. In practice we iterate until our given tolerence ϵ is reached

$$|x_{i+1} - x_i| < \epsilon. \tag{2.23}$$

This is known as an initial value problem. We now discuss some elementary solution schemes in the general case.

2.3.1 The Euler Method.

Considering the graph of $x(t)$ in 2.9 we see that over the interval Δt we may approximate the gradient of the tangent to $x(t)$ by the gradient of the line connecting (t_i, x_i) and (t_{i+1}, x_{i+1}), that is

$$\frac{dx}{dt} \approx \frac{\Delta x}{\Delta t} = \frac{(x_{i+1} - x_i)}{(t_{i+1} - t_i)} \tag{2.24}$$

We see by the definition of a derivative

$$\frac{dx}{dt} = \lim_{\Delta t \to 0} \frac{\Delta x}{\Delta t} \tag{2.25}$$

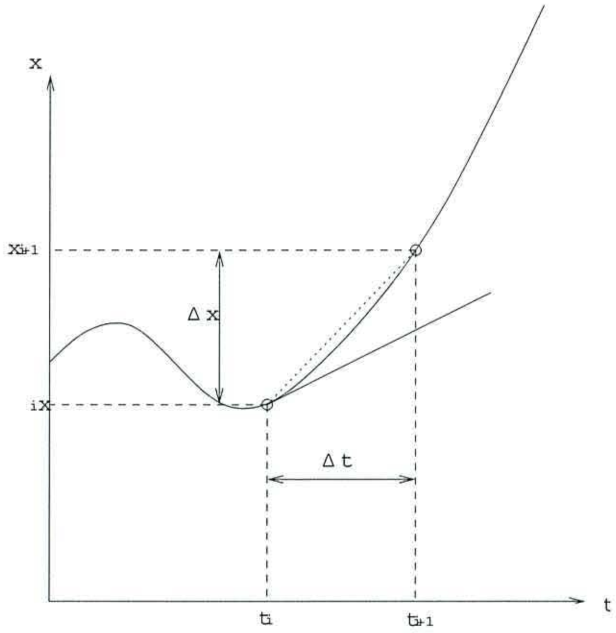

Figure 2.9: The tanget at t_i and the chord (t_i, x_i) to (t_{i+1}, x_{i+1})

that this approximation converges to the true derivative with decreasing Δt. We may now use these facts to give an approximation for x_{i+1}

$$\frac{dx}{dt} \approx \frac{(x_{i+1} - x_i)}{\Delta t} \tag{2.26}$$

implies that

$$f(t, x) \approx \frac{(x_{i+1} - x_i)}{\Delta t} \tag{2.27}$$

and so

$$x_{i+1} \approx x_i + \Delta t f(t_i, x_i) \tag{2.28}$$

So starting with $x = x_i$ at $t = t_i$, we assume that over the time increment Δt, x will be incremented by $\Delta t f(t_i, x_i)$. This is the simplest form of numerical integration known as the forward or explicit Euler method. Graphically we can see that there is some discretization error. In figure 2.10 (a) the shaded area corresponds to the exact area under the curve $f(t, x)$. This solution may be obtained by integration

$$\int_{x_i}^{x_{i+1}} dx \;=\; \int_{t_i}^{t_{i+1}} f(t, x) dt \tag{2.29}$$

$$\begin{aligned} x_{i+1} - x_i &= \int_{t_i}^{t_{i+1}} f(t,x)dt \\ x_{i+1} &= x_i + \int_{t_i}^{t_{i+1}} f(t,x)dt \end{aligned}$$

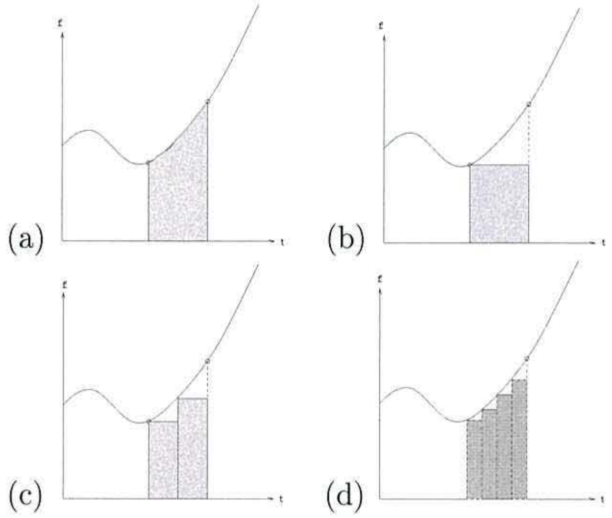

Figure 2.10: (a) The true integral of $f(t,x)$, (b) The forward Euler approximation, (c) halving the time-step and (d) further refinement.

In figure 2.10 (b) we see that in general the approximation under-estimates the area under $f(t,x)$ between t_i and t_{i+1} for an increasing function f. However this method is very cheap computationally and upon halving Δt as in figure 2.10 (c) the error is greatly reduced. With further refinement (d) we may achieve an arbitrarily close approximation. Fine discretization is often only required in those areas where the solution is varying rapidly. The placing of mesh points in order to obtain an optimal solution for a given computational cost is in general a non-trivial task and is currently a very active field of research [40].

2.3.2 Improved Euler Methods.

Taking a second look at exact solution 2.29 we see that in principle it was an arbitrary choice to take $f(t,x) = f(t_i,x_i)$ as this is no more likely to reflect the mean derivative over the interval than the value of f at any other point t. In practice the value of the function is taken at this point because we already know the value of f at (x_i,t_i). We may have chosen to take our value of f

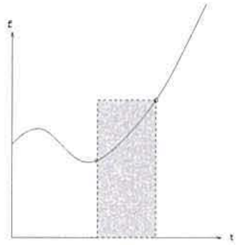

Figure 2.11: The backward Euler method.

at time t_{i+1} to give the approximation

$$\begin{aligned} x_{i+1} &= x_i + \int_{t_i}^{t_{i+1}} f(t,x)dt \\ x_{i+1} &\approx x_i + \Delta t f(t_{i+1}, x_{i+1}) \end{aligned} \tag{2.30}$$

This scheme is known as the implicit or backward Euler method and as can be seen from figure 2.11, makes an over estimate of the integral for an increasing function f. This is known as an implicit scheme since the unknown x_{i+1} is present on both the left-hand side and the right-hand side of the approximation. In general implicit schemes have the advantage of increased numerical stability at the expense of greater computational effort in evaluating x_{i+1} on the right-hand side. We may however use an explicit Euler scheme to obtain an estimate of x_{i+1} on the right-hand side. So we may predict that

$$\tilde{x}_{i+1} = x_i + \Delta t f(t_i, x_i) \tag{2.31}$$

and then correct using

$$x_{i+1} = x_i + \Delta t f(t_{i+1}, \tilde{x}_{i+1}) \tag{2.32}$$

This is a basic example of a predictor-corrector scheme known as the Heun method, more advanced predictor-corrector schemes [41] are often used in dynamic micromagnetic simulations [33], [42]. From figure 2.12 we see that a much better approximation can clearly be achieved by using a trapezoid rather than a rectangular area as shown in figure 2.12

$$\int_{t_i}^{t_{i+1}} f(t,x)dt \approx \frac{\Delta t}{2}\Big(f(x_i,t_i) + f(t_{i+1}, x_{i+1})\Big). \tag{2.33}$$

This leads to a scheme known as the improved Euler, trapezoidal or midpoint rule

$$x_{i+1} \approx x_i + \frac{\Delta t}{2}\Big(f(t_i,x_i) + f(t_{i+1}, x_{i+1})\Big) \tag{2.34}$$

This method can be thought of as giving a better average of the function

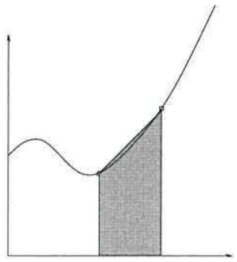

Figure 2.12: The improved Euler method.

x over the interval and indeed gives the true mean for a linear function. As with the implicit Euler scheme a Heun method can be used to evaluate the implicit contribution. We shall return to the problem of evaluating the implicit x_{i+1} term in chapter 6.

2.3.3 Runge-Kutta Methods.

We now take a more rigorous perspective on the problem. Let $x(t)$ be the exact solution of the initial value problem

$$\begin{aligned} \frac{dx}{dt} &= f(t,x) && (2.35)\\ x(t_0) &= x_0 && (2.36) \end{aligned}$$

and take the Taylor series for $x(t)$ about the point t_i

$$\begin{aligned} x(t) &= x(t_i) + \Delta t x'(t_i) + \frac{\Delta t^2}{2} x''(t_i) + \ldots && (2.37)\\ & \ldots + \frac{\Delta t^p}{p!} x^{(p)}(t_i) + O(\Delta t^{p+1}) \end{aligned}$$

where $\Delta t = t - t_i$. Truncating the Taylor series after the linear term in Δt we have

$$x(t) \approx x(t_i) + \Delta t x'(t_i). \tag{2.38}$$

Since $x(t)$ is known to satisfy the initial value problem we recover the forward Euler approximation

$$x_{i+1} \approx x_i + \Delta t f(t_i, x_i). \tag{2.39}$$

From this perspective we see that we have incurred a truncation error of $O(\Delta t^2)$, further we see that we may reduce this error by taking more terms from the Taylor series. For example truncating after the second order term we have

$$x(t) \approx x(t_i) + \Delta t x'(t_i) + \frac{\Delta t^2}{2} x''(t_i) \tag{2.40}$$

and since we know $x'(t_i) = f(t_i, x_i)$, we have $x''(t_i) = f'(t_i, x_i)$ to give

$$x_{i+1} \approx x_i + \Delta t f(t_i, x_i) + \frac{\Delta t^2}{2} f'(t_i, x_i) \tag{2.41}$$

with error $O(\Delta t^3)$ and so on. So we may construct Taylor methods as a generalization of the Euler method to arbitrary order p with rate of convergence $O(\Delta t^{p+1})$.

$$\begin{aligned} x_{i+1} &\approx x_i + \sum_{n=1}^{p} \frac{\Delta t^n}{n!} f^{(n)}(t_i, x_i). \qquad (2.42) \\ &\quad +O(\Delta t^{p+1}) \qquad (2.43) \end{aligned}$$

High order schemes using this method soon become cumbersome as the pth derivatives of f must be computed at each time-step. To obtain higher order methods with less complexity we note that 2.41 may be said to have the form

$$x_{i+1} = x_i + \Delta t F(t_i, x_i; \Delta t) \tag{2.44}$$

where F depends on the order of approximation p. To find an approximation scheme with convergence $O(\Delta t^{p+1})$ it is sufficient to find F such that its Taylor expansion agrees with that of the Taylor method of order p as $\Delta t \to 0$. In general this may be achieved without the use of derivatives of the function f and such schemes are known as Runge-Kutta methods. For example to obtain a second order method we may choose F such that

$$F(t, x; \Delta t) = f(t + \alpha \Delta t, x(t) + \beta \Delta t f(t, x)) \tag{2.45}$$

where α and β are chosen so that 2.44 converges at $O(\Delta t^3)$. We therefore require that its Taylor expansion agrees with that of the Taylor method of order 2. This may be achieved with $\alpha = \beta = 1/2$ [41] to give

$$x_{i+1} = x_i + \Delta t f(t_i + \frac{\Delta t}{2}, x_i + \frac{\Delta t}{2} f(t, x)) \tag{2.46}$$

This is also a form of midpoint method which reduces to the improved Euler method when f is linear. The fourth order Runge-Kutta method may be derived in a similar manner by working with the Taylor method of order 4 to give

$$x_{i+1} = x_i + \frac{1}{6}(K_1 + 2K_2 + 2K_3 + K_4) \tag{2.47}$$

where

$$\begin{aligned} K_1 &= \Delta t f(t, x) \\ K_2 &= \Delta t f(t + \frac{\Delta t}{2}, x + \frac{K_1}{2}) \\ K_3 &= \Delta t f(t + \frac{\Delta t}{2}, x + \frac{K_2}{2}) \\ K_4 &= \Delta t f(t + \Delta t, x + K_3). \end{aligned} \tag{2.48}$$

2.4 A Single Spin System.

We now develop a simple integration scheme for the Gilbert equation at a single point in space. To simplify matters we will neglect exchange and magnetostatic energy in the first instance and consider only the effects of an externally applied field and anisotropy energy; thus removing spatial variation from the effective magnetic field. Alternatively the results of this section can be thought of as referring to the magnetisation of a single domain spherical particle. This essentially bestows dynamic visualization upon the Stoner-Wohlfarth model. The anisotropy term is incorporated into the model using the effective magnetic field

$$\begin{aligned} \boldsymbol{H}_{eff} &= \frac{dE_G}{d\boldsymbol{M}} \qquad (2.49) \\ &= \frac{d\left(\frac{K}{M_s^2}\left(\boldsymbol{M}\cdot\hat{\mathbf{e}}\right)^2\right)}{d\boldsymbol{M}} + \boldsymbol{H}_z \\ &= \frac{2K}{M_s^2}(\boldsymbol{M}\cdot\hat{\mathbf{e}})\hat{\mathbf{e}} + \boldsymbol{H}_z. \end{aligned}$$

2.4.1 Reduced Units.

We have developed the assumption that magnetisation is identical at all points of a homogeneous medium and that changes in macroscopic magnetisation occur via in changes in direction and not via changes in magnitude of the local magnetisation. To remove the magnitude from consideration entirely we work in reduced units. This simplifies the definition of the problem and presents the equations in a more suitable format for computer programming. We re-scale the magnetisation in terms of the saturation magnetisation, we may then talk of magnetisation in arbitrary units or reduced magnetisation

$$\boldsymbol{m} = \frac{\boldsymbol{M}}{M_s}. \qquad (2.50)$$

Substituting $\boldsymbol{H} = \boldsymbol{H}_{eff}$ and $\boldsymbol{M} = M_s\boldsymbol{m}$ into 2.15 we have

$$\begin{aligned} M_s\frac{d\boldsymbol{m}}{dt} &= -\gamma M_s(\boldsymbol{m}\times\boldsymbol{H}_{eff}) + \frac{\alpha M_s^2}{M_s}(\boldsymbol{m}\times\frac{d\boldsymbol{m}}{dt}) \qquad (2.51) \\ \frac{d\boldsymbol{m}}{dt} &= -\gamma(\boldsymbol{m}\times\boldsymbol{H}_{eff}) + \alpha(\boldsymbol{m}\times\frac{d\boldsymbol{m}}{dt}). \end{aligned}$$

Dividing by γ we have

$$\frac{d\boldsymbol{m}}{d\tilde{t}} = -(\boldsymbol{m}\times\boldsymbol{H}_{eff}) + \alpha(\boldsymbol{m}\times\frac{d\boldsymbol{m}}{d\tilde{t}}). \qquad (2.52)$$

where $d\tilde{t} = \gamma dt$ is a reduced time increment. In terms of $\boldsymbol{m}$ the effective field is now given by

$$\boldsymbol{H}_{eff} = \frac{2K}{M_s}(\boldsymbol{m} \cdot \hat{\boldsymbol{e}})\hat{\boldsymbol{e}} + \boldsymbol{H}_z. \tag{2.53}$$

Finally we divide 2.52 by the anisotropy field strength $H_k = 2K/M_s$ which may then be given in terms of the reduced effective field

$$\boldsymbol{h}_{eff} = (\boldsymbol{m} \cdot \hat{\boldsymbol{e}})\hat{\boldsymbol{e}} + \frac{\boldsymbol{H}_z}{H_k}. \tag{2.54}$$

The Gilbert equation may then be written in dimensionless form as

$$\frac{d\boldsymbol{m}}{d\tau} = -(\boldsymbol{m} \times \boldsymbol{h}_{eff}) + \alpha(\boldsymbol{m} \times \frac{d\boldsymbol{m}}{d\tau}). \tag{2.55}$$

where $d\tau = \gamma dt H_k$ is now the reduced time increment. Similarly the reduced Landau-Lifshitz-Gilbert equation may be written as

$$\frac{d\boldsymbol{m}}{d\tau} = -\frac{1}{1+\alpha^2}(\boldsymbol{m} \times \boldsymbol{h}_{eff}) + \frac{\alpha}{1+\alpha^2}(\boldsymbol{m} \times (\boldsymbol{m} \times \boldsymbol{h}_{eff})). \tag{2.56}$$

2.4.2 Numerical Solution.

We now apply an explicit Euler method to the solution of the Landau-Lifshitz-Gilbert equation. The left-hand side of 2.56 is approximated by

$$\frac{d\boldsymbol{m}}{d\tau} = \frac{\boldsymbol{m}^{t+1} - \boldsymbol{m}^t}{\Delta\tau} \tag{2.57}$$

where the superscripts t and $t+1$ refer to the start and end points of $\Delta\tau$, the time-step in reduced time or simulation time τ. Simulation time is converted to real time in seconds by the formula

$$\begin{aligned} \Delta\tau &= \gamma H_k \Delta t \\ \Delta t &= \frac{\Delta\tau}{\gamma H_k} \\ t &= \frac{T\Delta\tau}{\gamma H_k} \end{aligned} \tag{2.58}$$

where T is the number of time-steps taken. The right-hand side of 2.56 is approximated over the interval $[\tau^t, \tau^{t+1}]$ by its value at τ^t giving the discretization

$$\begin{aligned} \frac{\boldsymbol{m}_{t+1} - \boldsymbol{m}_t}{\Delta\tau} &= -\frac{1}{1+\alpha^2}(\boldsymbol{m}^t \times \boldsymbol{h}^t_{eff}) + \frac{\alpha}{1+\alpha^2}(\boldsymbol{m}^t \times (\boldsymbol{m}^t \times \boldsymbol{h}^t_{eff})) \\ \boldsymbol{m}_{t+1} &= \boldsymbol{m}_t + \Delta\tau\Big(-\frac{1}{1+\alpha^2}(\boldsymbol{m}^t \times \boldsymbol{h}^t_{eff}) + \frac{\alpha}{1+\alpha^2}(\boldsymbol{m}^t \times (\boldsymbol{m}^t \times \boldsymbol{h}^t_{eff}))\Big). \end{aligned} \tag{2.59}$$

Starting with some initial magnetisation state $\boldsymbol{m}_0$ we may evolve the system for a given time period or until equilibrium is reached

$$\frac{|\boldsymbol{m}^{t+1} - \boldsymbol{m}^t|}{\Delta\tau} < \epsilon. \tag{2.60}$$

At this stage to ensure that $|\boldsymbol{m}| = 1$ is conserved we must renormalize $\boldsymbol{m}$ to a unit vector at every time-step

$$\boldsymbol{m}^{t+1} \cdot \boldsymbol{m}^{t+1} = \boldsymbol{m}^t \cdot \boldsymbol{m}^t = 1. \tag{2.61}$$

2.4.3 The Gilbert Damping Mechanism.

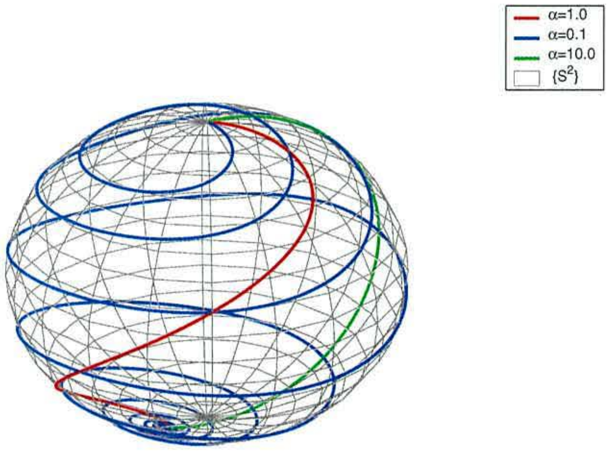

Figure 2.13: Magnetisation trajectories for $\alpha < 1$, $\alpha = 1$ and $\alpha > 1$.

To illustrate the damping mechanism we iterate 2.59 until $|\boldsymbol{m}^{t+1} - \boldsymbol{m}^t|/\Delta\tau < 10^{-6}$ with initial magnetisation $\boldsymbol{m}_0 = (0,0,1)$, reduced external field $\boldsymbol{h}_z = (0,0,-1)$ and easy axis $\hat{\boldsymbol{e}} = (1/\sqrt{2}, 0, 1/\sqrt{2})$. This results in a reversal of the magnetisation with the trajectory and therefore the switching time dependent on the damping parameter α. In figure 2.13 the trajectories are plotted on the surface of the unit sphere. For $\alpha < 1$ gyromagnetic precession dominates the reversal resulting in a large switching time. For $\alpha = 1$ the damping has more effect and the path to equilibrium is more direct. Finally for $\alpha > 1$ the path takes a geodesic across the sphere. This seems at odds with our earlier analysis which predicted that as α increased above unity the switching time should increase. However we recall that in this regime the magnitude of $d\boldsymbol{m}/dt$ becomes very small. Consequently, although the trajectory takes a shorter route across the sphere, it is composed of many very much smaller increments. Switching time versus α for this system is plotted in figure 2.14, confirming that $\alpha = 1$ gives the minimum switching time in agreement with Mallinson [35] and the much earlier work by Kikuchi [34].

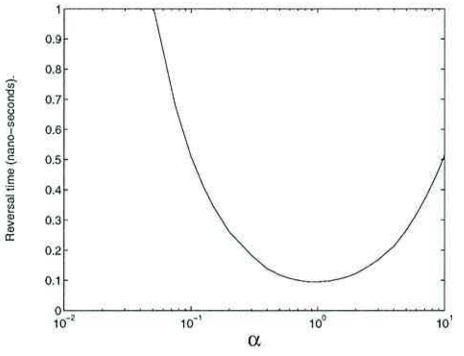

Figure 2.14: Switching time versus α.

2.4.4 Field Strength Dependence of the Precession.

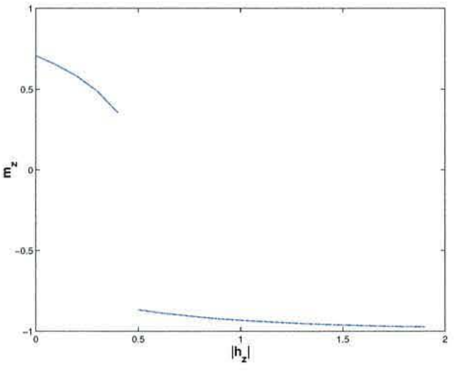

Figure 2.15: Equilibrium magnetisation versus $|\boldsymbol{h}_z|$.

One suprising result of the single spin model is that for an isotropic system, any applied field of finite magnitude is sufficient to switch the magnetisation. Although the switching time will vary according to $|\boldsymbol{h}_z|$, the trajectory of the magnetisation vector is invariant for given material parameters. In the more realistic anisotropic system an energy barrier is created by the anisotropy energy and only an applied field of $|\boldsymbol{h}_z| \geq 0.5$ is sufficient to switch the magnetisation for the system described in section 2.4.3.

This is illustrated in figure 2.15, clearly $|\boldsymbol{h}_z| \geq 0.5$ results in an equilibrium magnetisation which may be regarded as reversed. Figure 2.16 shows the corresponding switching times.

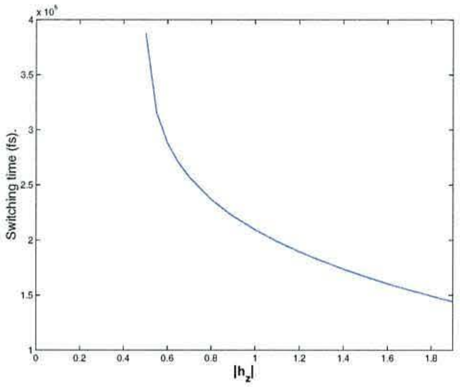

Figure 2.16: Switching time versus $|\boldsymbol{h}_z|$.

2.4.5 Anisotropy Induced Hysteresis.

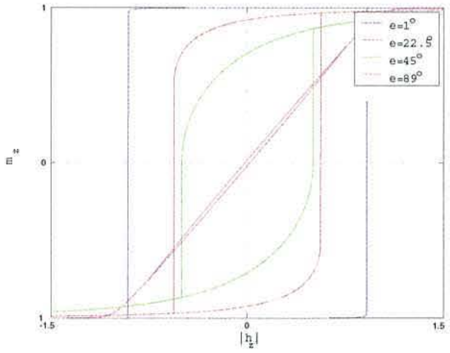

Figure 2.17: Hysteresis simulations for a single spin.

The height of the energy barrier depends of the orientation of magnetisation with respect to the easy-axis $\hat{\boldsymbol{e}}$. This results in hysteresis and as can be seen from figure 2.17 this model may used to generate hysteresis loops which are in exact agreement with the Stoner-Wolhfarth model. We will discuss the energy barrier further in chapter 7 in relation to finite temperature dynamics.

Chapter 3

Finite Element Discretisation.

This chapter will be devoted to the development of our finite element model of magnetization dynamics. We have considered the numerical integration with respect to time or the temporal discretisation in the previous chapter; we now consider spatial resolution of the system. We give a brief discusion of finite element analysis in general. The derivation of the magnetostatic field as a magnetic scalar potential is then described, followed by details of the finite element solution. We then proceed with the Galerkin formulation of the Gilbert equation which leads to our numerical model of magnetisation dynamics. Finally technical aspects of the solver are discussed.

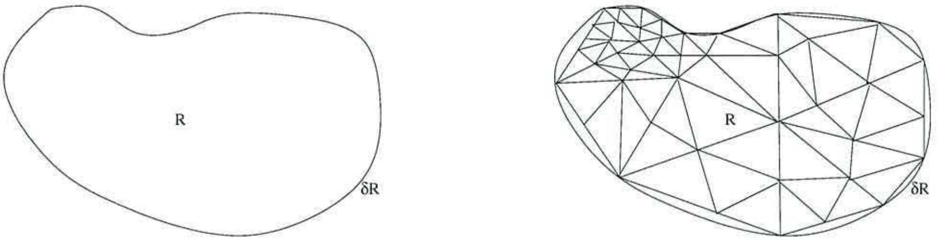

Figure 3.1: Discretisation of the problem domain.

3.1 Finite Element Analysis.

This section will serve as an introduction to the variational finite element techniques that we shall employ in the subsequent development of our micromagnetic model. The finite element method was first developed to solve problems in structural engineering in the 1950's and 60's. The region of interest was subdivided into a finite set of components or finite elements which were connected by a set of nodes. The structural behavior was considered in each of these elements independently and then the over-all equilibrium equations were assembled. This was the first step in approximating an infinite dimensional problem with a finite dimensional problem or discrete problem with essentially the same properties. The analysis was based on the theory of minimum potential energy. From its origins in structural mechanics the finite element method was rapidly developed into a rigorous mathematical tool for the solution of field problems by piecewise discretization of variational methods. The method may be summarized as follows. A set of functions Ψ must be identified which are both sufficiently differentiable and satisfy any boundary conditions of the problem. A so called $n-$term solution ϕ_n is then sought of the form

$$\phi_n = \sum_{i=1}^{n} c_i \psi_i \tag{3.1}$$

where $\psi_i \in \Psi$ and the n parameters c_i are to be determined. The domain of the problem is divided into simple sub-domains or elements as shown in figure 3.1. Each element then has its own set of trial functions Ψ which are the restriction of the global trial funcntions and the global solution is simply the sum of the local solutions. In finite element literature the trial functions may be referred to as basis functions, test functions, shape functions, interpolation functions or may be interpreted as local coordinates depending on context and the variational method under discussion. We will use the term shape function throughout the rest of this thesis as this intuitively describes their role in controlling the functional form of the solution.

3.1.1 The Galerkin Method.

The Galerkin method is one of a family of methods known as the minimum residual methods. For self-adjoint elliptic partial differential equations such as the Poisson equation it is equivalent to the Rayleigh-Ritz method which seeks to find a solution as the minimum of a corresponding energy functional. The Galerkin method is however more general and may also be applied to problems in which no such functional exists. Consider the boundary value problem specified by

$$L\phi = f; \quad (x, y, z) \in R \tag{3.2}$$

where L is a differential operator on ϕ and $f = f(x, y, z)$ is a function of position with ϕ subject to suitable conditions at the boundary of the region ∂R. In general an approximation will not satisfy 3.2 exactly; the distance between the approximate solution ϕ and the exact solution ϕ_0 is formally defined as the residual $r(\phi)$ associated with the approximate solution ϕ.

$$r(\phi) = L\phi - f \tag{3.3}$$

and naturally for the exact solution we have

$$\begin{aligned} r(\phi_0) &= L\phi_0 - f \\ &= 0. \end{aligned} \tag{3.4}$$

To minimize the residual we take the orthogonal-projection or L_2-projection [43] onto our chosen set of shape functions ψ_i

$$\int_R r(\phi)\psi_i \, dV = 0; \quad i = 1, n. \tag{3.5}$$

Then assuming a solution of the form 3.1 we have

$$\begin{aligned} \int_R (L\phi - f)\psi_i \, dV &= 0 \\ \int_R (L\phi)\psi_i \, dV &= \int_R f\psi_i \, dV \\ \int_R (L\sum_{j=1}^{n} c_j\psi_j)\psi_i \, dV &= \int_R f\psi_i \, dV \\ \sum_{j=1}^{n} c_j \int_R (L\psi_j)\psi_i \, dV &= \int_R f\psi_i \, dV \end{aligned} \tag{3.6}$$

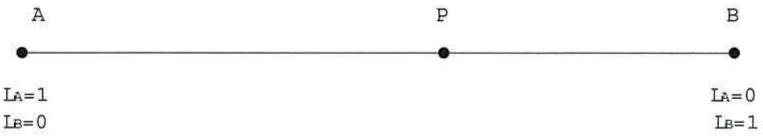

Figure 3.2: One dimensional finite element.

this gives a system of n linear algebraic equations for the n unknown parameters c_j. The solution of which gives the minimum residual for a given set of shape functions $\Psi = \psi_1, .., \psi_n$ satisfying the necessary boundary conditions. The essence of the method is that we may solve a partial differential equation simply by performing the differential operator L on a set of functions which may be chosen to be easily differentiable. The integrations in 3.6 may then be performed numerically if necessary. The problem of integrating the operator L has thus been reduced to the problem of solving a system of linear algebraic equations. Within a finite element context the shape functions are chosen to be interpolatory over each element so that ψ_i^e takes the value of unity at node i of element e and zero elsewhere i.e. $\psi_i^e(x_j, y_j, z_j) = \delta_{ij}$. The values of the c_j then correspond to the local values of ϕ at each node j. In practice each element of the mesh is mapped to a simple parent cell so that the shape functions take the same form over each element. The solution may then be written simply as

$$\phi = \sum_e \phi_e \tag{3.7}$$

where

$$\phi_e = \sum_i \phi_i \psi_i^e. \tag{3.8}$$

3.1.2 Simplex Shape Functions.

Consider the point P on line AB of figure 3.2. This line is a one dimensional simplex. It is often the case that we are not interested in the coordinate of P with respect to an origin but merely in specifying it's position on the line relative to the vertices A and B. This may be accomplished with the use of two local coordinates L_A and L_B defined as

$$\begin{aligned} L_A &= \frac{\rho(P,B)}{\rho(A,B)} = \frac{(x_B - x_P)}{(x_B - x_A)} \\ L_B &= \frac{\rho(A,P)}{\rho(A,B)} = \frac{(x_P - x_A)}{(x_B - x_A)}. \end{aligned} \tag{3.9}$$

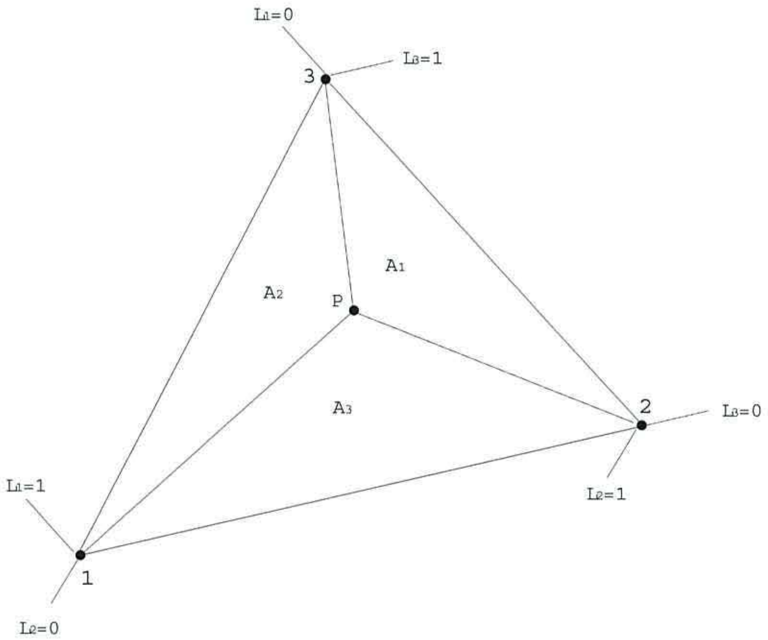

Figure 3.3: Two dimensional finite element.

These are clearly equivalent to the coefficients of Lagrange's linear interpolating polynomial [41], [44], [45] and may therefore be used to interpolate over AB. We also note that the functions are linearly dependent

$$L_A + L_B = \frac{\rho(A,P) + \rho(B,P)}{\rho(A,B)} = 1. \tag{3.10}$$

A two dimensional simplex is a triangle 123 as shown in figure 3.3. Again we may specify the location of a point P within the triangle relative to its vertices as $P(L_1, L_2, L_3)$, where

$$L_1 = \frac{A_1}{A} \tag{3.11}$$

$$L_2 = \frac{A_2}{A} \tag{3.12}$$

$$L_3 = \frac{A_3}{A} \tag{3.13}$$

here A_i are the areas of triangles Pjk, where j, k are the nodes $j, k \neq i$ and A is the area of the whole triangle. As in the one dimensional case these simplex coordinates are interpolatory and linearly dependent

$$L_i(x_j, y_j) = \delta_{ij} \tag{3.14}$$

$$L_1 + L_2 + L_3 = \frac{A_1 + A_2 + A_3}{A} = 1.$$

The relations to the global cartesian coordinates however are now more complex. Over the triangle 123 we have

$$\begin{aligned} 1 &= L_1 + L_2 + L_3 \\ x &= L_1 x_1 + L_2 x_2 + L_3 x_3 \\ y &= L_1 y_1 + L_2 y_2 + L_3 y_3 \end{aligned} \tag{3.15}$$

or in matrix form

$$\begin{aligned} \begin{pmatrix} 1 \\ x \\ y \end{pmatrix} &= \begin{pmatrix} 1 & 1 & 1 \\ x_1 & x_2 & x_3 \\ y_1 & y_2 & y_3 \end{pmatrix} \begin{pmatrix} L_1 \\ L_2 \\ L_3 \end{pmatrix} \\ \boldsymbol{X} &= \mathbf{C}\boldsymbol{L} \\ \boldsymbol{L} &= \mathbf{C}^{-1}\boldsymbol{X}, \end{aligned} \tag{3.16}$$

which gives

$$L_i = \frac{a_i + b_i x + c_i y}{2A} \tag{3.17}$$

where $2A$ is equal to twice the area of the triangle and is given by the determinant of the coefficient matrix $\mathbf{C}$. The a_i,b_i,c_i are given by its cofactors

$$\begin{aligned} 2A &= \begin{vmatrix} 1 & 1 & 1 \\ x_1 & x_2 & x_3 \\ y_1 & y_2 & y_3 \end{vmatrix} \\ a_i &= x_j y_k - x_k y_j, \\ b_i &= y_j - y_k, \\ c_i &= x_k - x_j \end{aligned} \tag{3.18}$$

where i, j, k is a cyclic permutation of $1, 2, 3$. Finally, a three dimensional simplex is the tetrahedron 1234 as shown in figure 3.4. The location of a point P within the tetrahedron relative to it's vertices may be specified as $P(L_1, L_2, L_3, L_4)$ where

$$\begin{aligned} L_1 &= \frac{V_1}{V} \\ L_2 &= \frac{V_2}{V} \\ L_3 &= \frac{V_3}{V} \\ L_4 &= \frac{V_4}{V}. \end{aligned} \tag{3.19}$$

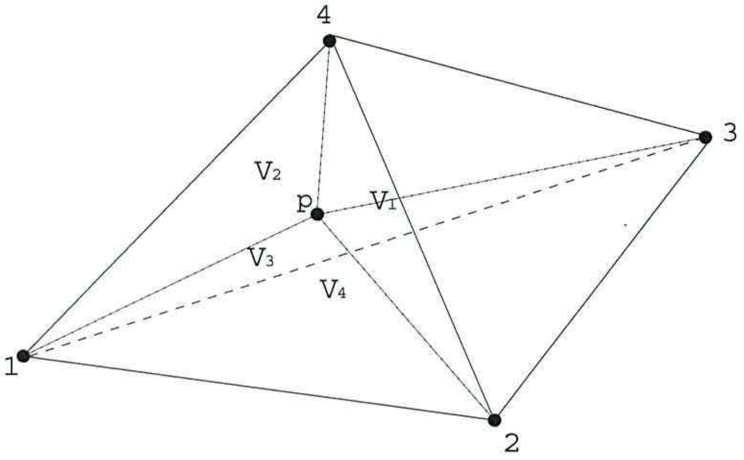

Figure 3.4: Three dimensional finite element.

Again these are interpolatory and linearly dependent

$$\begin{aligned} L_i(x_j, y_j) &= \delta_{ij} \\ L_1 + L_2 + L_3 + L_4 = \frac{V_1 + V_2 + V_3 + V_4}{V} &= 1. \end{aligned} \tag{3.20}$$

The relations to cartesian coordinates are a generalization of the lower dimensional cases

$$L_i = \frac{a_i + b_i x + c_i y + d_i z}{6V}. \tag{3.21}$$

Here the determinant $6V$ is equal to six times the volume of the tetrahedron and the a_i,b_i,c_i,d_i are again given by the cofactors of the coefficient matrix

$$6V = \begin{vmatrix} 1 & 1 & 1 & 1 \\ x_1 & x_2 & x_3 & x_4 \\ y_1 & y_2 & y_3 & y_4 \\ z_1 & z_2 & z_3 & z_4 \end{vmatrix} \tag{3.22}$$

$$a_i = \begin{vmatrix} x_j & y_j & z_j \\ x_k & y_k & z_k \\ x_l & y_l & z_l \end{vmatrix} \qquad b_i = -\begin{vmatrix} 1 & y_j & z_j \\ 1 & y_k & z_k \\ 1 & y_l & z_l \end{vmatrix}$$

$$c_i = -\begin{vmatrix} x_j & 1 & z_j \\ x_k & 1 & z_k \\ x_l & 1 & z_l \end{vmatrix} \qquad d_i = -\begin{vmatrix} x_j & y_j & 1 \\ x_k & y_k & 1 \\ x_l & y_l & 1 \end{vmatrix}$$

where the i, j, k, l are not a cyclic permutation of $1, 2, 3, 4$ as is quoted by many authors. For given i, the j, k, l are any consistent ordering of the other 3 three vertices looking through the tetrahedron from vertex i. We adopt a right-hand convention which results in an anticlockwise ordering. This is important as the direction of the ordering dictates the direction of the normal vector to each surface of the tetrahedron.

The simplex coordinates derived above are clearly equivalent to Lagrangian interpolation polynomials of order 1 [41], [44] [45]. They also form a linearly dependent basis for the discrete function spaces given by splitting the problem domain into the corresponding line, triangle or tetrahedron elements. Moreover they are easily differentiated and enable straight forward integration over each element. They are therefore identified as suitable linear shape functions for our purposes. We now concentrate on the tetrahedron as this will be used as the standard parent element in most of our subsequent work. Analogous results are given for triangle elements in the introductory text on the finite element method by A. J. Davies [46]. Partial derivatives of the shape functions are given by

$$\begin{aligned}\frac{\partial L_i}{\partial x} &= \frac{b_i}{6V} \\ \frac{\partial L_i}{\partial y} &= \frac{c_i}{6V} \\ \frac{\partial L_i}{\partial z} &= \frac{d_i}{6V}.\end{aligned} \tag{3.23}$$

Integrations over each element are likewise straight-forward to perform using the integral formula [46]

$$\int_V L_1^m L_2^n L_3^p L_4^q \, dV = \frac{6V m!n!p!q!}{(m+n+p+q+3)!}. \tag{3.24}$$

Since integrals may usually be reformulated so that only products of shape functions or their derivatives appear in the integrand; they may be evaluated analytically using 3.24 in almost all circumstances.

$$\int_V \phi \, dV = \int_V \sum_{i=1}^{4} L_i \phi_i \, dV = \sum_{i=1}^{4} \phi_i \int_V L_i \, dV, \tag{3.25}$$

$$\int_V \frac{\partial \phi}{\partial x} \, dV = \int_V \sum_{i=1}^{4} \frac{\partial L_i \phi_i}{\partial x} \, dV \tag{3.26}$$

$$\begin{aligned} &= \sum_{i=1}^{4} \int_V \frac{\partial L_i}{\partial x} \phi_i \, dV \\ &= \sum_{i=1}^{4} \frac{b_i \phi_i}{6V} \int_V dV \\ &= \sum_{i=1}^{4} \frac{b_i \phi_i}{6} \end{aligned}$$

Alternatively numerical quadrature can be used in all cases [47], [48]. Second order or quadratic elements are easily generated in terms of the linear elements by considering nodes at the mid-side of each edge of the tetrahedron and noting that the linear shape functions corresponding to adjacent corner nodes are equal to 1/2 there, as shown in figure 3.5. Suitable quadratic shape functions are then given by

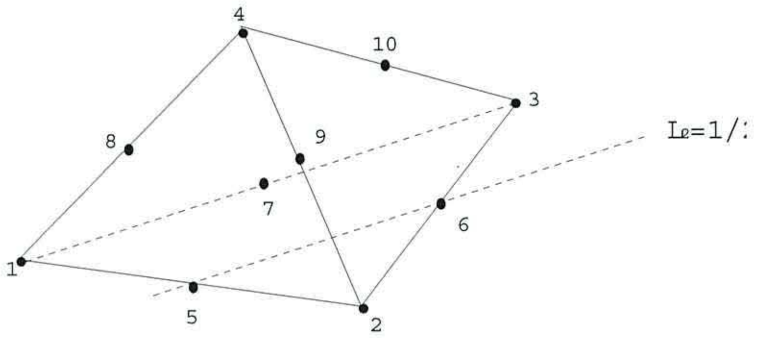

Figure 3.5: Second order two dimensional finite element.

$$N_i = \begin{cases} L_i(2L_i - 1); & i = 1, .., 4 \\ 4L_j L_k; & i = 5, .., 10 \end{cases} \tag{3.27}$$

where j,k are adjacent corner nodes to mid-side node i. Partial derivatives are given by

$$\begin{aligned} \frac{\partial N_i}{\partial x} &= \frac{b_i}{6V}(4L_i - 1) \\ \frac{\partial N_i}{\partial y} &= \frac{c_i}{6V}(4L_i - 1) \\ \frac{\partial N_i}{\partial z} &= \frac{d_i}{6V}(4L_i - 1); \quad i = 1, .., 4 \end{aligned} \tag{3.28}$$

and

$$\begin{aligned}
\frac{\partial N_i}{\partial x} &= \frac{2}{3V}(b_j L_k + b_k L_j) \\
\frac{\partial N_i}{\partial y} &= \frac{2}{3V}(c_j L_k + c_k L_j) \\
\frac{\partial N_i}{\partial z} &= \frac{2}{3V}(d_j L_k + d_k L_j); \quad i = 5, .., 10.
\end{aligned} \tag{3.29}$$

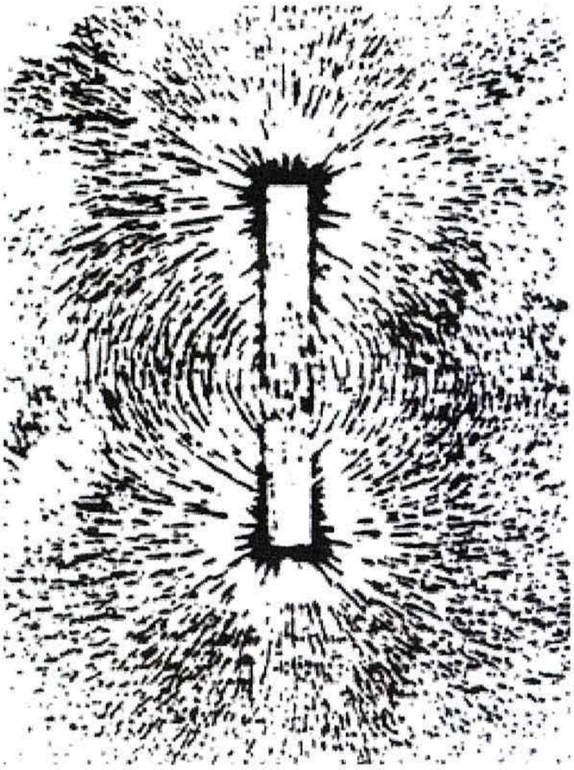

Figure 3.6: The iron filings experiment.

3.2 The Magnetostatic Field.

The magnetostatic field or self-demagnetizing field results from the classical interaction between magnetic dipoles. Famously the field can be visualized by sprinkling iron fillings around a saturated and hence polarized ferromagnet. As shown in figure 3.6 the filings align with the field lines exterior to the magnet to form a characteristic pattern. The interior of the magnet experiences a field which is directly opposed to the direction of magnetisation in most circumstances. However the field is highly geometry dependent. Boundary features such as holes or corners can have a strong effect on the configuration of field lines. Indeed for some geometries such as a re-entrant corner the field develops a singularity [49]. In this section we shall apply the theory outlined in section 3.1 to describe our finite element solution of the magnetostatic problem. We first formulate the problem as a magnetic scalar potential necessitating the solution of Poisson's equation. We then describe the Galerkin projection of the Poisson equation in general followed by relevent modifications to the case in point.

3.2.1 Scalar Potential Formulation.

The field may be calculated using *ab initio* calculations of the interactions between atomic moments [12], however within our continuum model it is more straight forward to apply Maxwell's equations 1.35. In the absence of electric fields $\boldsymbol{E}$ and free currents $\boldsymbol{J}$ we have simply

$$\nabla \cdot \boldsymbol{B} = 0 \tag{3.30}$$

and

$$\nabla \times \boldsymbol{H} = \boldsymbol{0}. \tag{3.31}$$

With zero Zeeman energy the magnetic field consists solely of the magnetostatic field $\boldsymbol{H} = \boldsymbol{H}_d$. We may therefore define the magnetic scalar potential ϕ such that

$$\boldsymbol{H}_d = -\nabla\phi \tag{3.32}$$

where $\boldsymbol{H}_d$ is a general solution of 3.31. Recalling that the magnetic flux density is given by

$$\boldsymbol{B} = \boldsymbol{H} + 4\pi\boldsymbol{M} \tag{3.33}$$

and substituting into 3.30 we see that ϕ must satisfy Poisson's equation

$$\begin{aligned} \nabla \cdot (\boldsymbol{H_d} + 4\pi\boldsymbol{M}) &= 0 \\ \nabla \cdot ((-\nabla\phi) + 4\pi\boldsymbol{M}) &= 0 \\ \nabla \cdot (-\nabla\phi) &= -\nabla \cdot (4\pi\boldsymbol{M}) \\ \nabla^2\phi &= 4\pi\nabla \cdot \boldsymbol{M}. \end{aligned} \tag{3.34}$$

Naturally in the region exterior to the magnetic body where $\boldsymbol{M} = \boldsymbol{0}$, ϕ satisfies Laplace's equation

$$\nabla^2\phi = 0. \tag{3.35}$$

To ensure continuity, so called jump conditions must be enforced at the interface between magnetic and non-magnetic regions. Finally the potential must be bounded at infinity. So for a bounded magnetic region Ω_{int} surrounded by an exterior non-magnetic region Ω_{ext} with interface $\partial\Omega$ having outward normal $\hat{\boldsymbol{n}}$; the problem can be stated by the following set of equations

$$\begin{aligned} \nabla^2\phi &= 4\pi\nabla \cdot \boldsymbol{M}; \quad (x, y, z) \in \Omega_{int} \\ \nabla^2\phi &= 0; \quad (x, y, z) \in \Omega_{ext} \\ \frac{\partial\phi_{int}}{\partial\hat{\boldsymbol{n}}} - \frac{\partial\phi_{ext}}{\partial\hat{\boldsymbol{n}}} &= 4\pi\boldsymbol{M} \cdot \hat{\boldsymbol{n}}; \quad (x, y, z) \in \partial\Omega \\ \phi_{int} &= \phi_{ext}; \quad (x, y, z) \in \partial\Omega \\ \phi &\to 0; \quad x \to \infty,\ y \to \infty,\ z \to \infty. \end{aligned} \tag{3.36}$$

3.2.2 Galerkin Projection of the Poisson Equation.

The Poisson equation

$$-\nabla^2\phi = f; \quad (x, y, z) \in R \tag{3.37}$$

is a self-adjoint and positive-definite elliptic partial differential equation and as such, together with suitable conditions at the domain boundary ∂R, can be shown to have a unique solution [46], [47], [48]. This is due to the fact that the positive-definite form has a single minimum. The boundary conditions usually fall into one of three categories; either

the Dirichlet type

$$\phi = f(s), \tag{3.38}$$

the Neumann type

$$\frac{\partial\phi}{\partial n} = g(s), \tag{3.39}$$

or the mixed type

$$\frac{\partial\phi}{\partial n} + \sigma(s)\phi = h(s) \tag{3.40}$$

where s is the length along ∂R from some fixed point on ∂R and $\partial/\partial n$ is the partial derivative along the outward normal to ∂R. For an elliptic operator such as ∇^2, the problem is said to be properly posed if only one type of condition holds at each point along ∂R. In our subsequent work we will consider only the homogeneous form of the Dirichlet condition $\phi = 0$ at the exterior mesh boundary. Putting $L = \nabla^2$ into equation 3.6 the Galerkin projection onto the shape functions ψ_i is given by

$$\begin{aligned} \int_R (\nabla^2\phi - f)\psi_i \, dV &= 0 \qquad (3.41) \\ \int_R (\nabla^2\phi)\psi_i \, dV &= \int_R \psi_i f \, dV; \quad i = 1, n. \end{aligned}$$

Using Green's theorem [43], [46] we have

$$\int_V \psi_i(\nabla^2\phi)dV = -\int_V \nabla\psi_i \cdot \nabla\phi dV + \int_S \psi_i \nabla\phi \cdot d\boldsymbol{S}. \tag{3.42}$$

The shape functions ψ_i are chosen to satisfy the homogeneous Dirichlet boundary conditions so that the boundary integral in 3.42 vanishes. Substituting back into the Galerkin projection we have

$$-\int_R \nabla\psi_i \cdot \nabla\phi dV = \int_R \psi_i f \; dV. \tag{3.43}$$

The integration may then be performed separaley over each element e where the ψ_i are the quadratic shape functions N_i^e and ϕ takes the form

$$\phi^e = \sum_{j=1}^{10} N_j^e \phi_j \tag{3.44}$$

so for every node $i \in e$ we have

$$\begin{aligned} -\int_R (\nabla N_i^e \cdot \nabla(\sum_{j=1}^{10} N_j^e \phi_j) \; dV &= \int_R f N_i^e \; dV && (3.45) \\ \sum_{j=1}^{n_e} \phi_j \int_R \nabla N_i^e \cdot \nabla N_j^e \; dV &= \int_R f N_i^e \; dV && (3.46) \end{aligned}$$

or in matrix form

$$\mathbf{k}^e \boldsymbol{\phi} = \boldsymbol{f}^e \tag{3.47}$$

where

$$k_{ij}^e = \int_R \nabla N_i^e \cdot \nabla N_j^e \; dV \tag{3.48}$$

and

$$f_i^e = \int_R f N_i^e \; dV. \tag{3.49}$$

For historical reasons $\mathbf{k}^e$ is known as the element stiffness matrix and $\boldsymbol{f}^e$ is known as the element force vector. The solution over the whole of R is then obtained by accumulating these equations over all elements e to form the global matrix equation

$$\mathbf{K}\boldsymbol{\phi} = \boldsymbol{F}. \tag{3.50}$$

Here we list some properties of $\mathbf{K}$ that apply to all such formulations.

- **K** is a sparsely populated matrix. K_{ij} is only non-zero if nodes i and j are connected in the finite element mesh.
- **K** is symmetric. The relation or stiffness between nodes i and j is the same as the stiffness between j and i, therefore $K_{ij} = K_{ji}$.
- If the differential operator of the problem is positive definite then, assuming properly posed boundary conditions, **K** is a positive definite matrix.

We now obtain a closed form expression for the integral 3.48 The element stiffness matrix for the three dimensional Poisson problem may be expressed as

$$\mathbf{k^e} = \int_{V^e} \boldsymbol{\alpha}^T \boldsymbol{\alpha} \, dV \tag{3.51}$$

where

$$\boldsymbol{\alpha} = \begin{pmatrix} \frac{\partial}{\partial x} \\ \frac{\partial}{\partial y} \\ \frac{\partial}{\partial z} \end{pmatrix} (N_1, ..., N_{10}).$$

Using the relation $L_1 + L_2 + L_3 + L_4 = 1$, a factorization of $\boldsymbol{\alpha}$ may be found by inspection such that

$$\boldsymbol{\alpha} = \frac{1}{6V} \boldsymbol{\omega} \mathbf{B} \tag{3.52}$$

where

$$\boldsymbol{\omega} = \begin{pmatrix} L_1 & L_2 & L_3 & L_4 & 0 & 0 & 0 & 0 & 0 & 0 & 0 & 0 \\ 0 & 0 & 0 & 0 & L_1 & L_2 & L_3 & L_4 & 0 & 0 & 0 & 0 \\ 0 & 0 & 0 & 0 & 0 & 0 & 0 & 0 & L_1 & L_2 & L_3 & L_4 \end{pmatrix}$$

and

$$\mathbf{B} = \begin{pmatrix} 3b_1 & -b_2 & -b_3 & -b_4 & 4b_2 & 0 & 4b_3 & 4b_4 & 0 & 0 \\ -b_1 & 3b_2 & -b_3 & -b_4 & 4b_1 & 4b_3 & 0 & 0 & 4b_4 & 0 \\ -b_1 & -b_2 & 3b_3 & -b_4 & 0 & 4b_2 & 4b_1 & 0 & 0 & 4b_4 \\ -b_1 & -b_2 & -b_3 & 3b_4 & 0 & 0 & 0 & 4b_1 & 4b_2 & 4b_3 \\ 3c_1 & -c_2 & -c_3 & -c_4 & 4c_2 & 0 & 4c_3 & 4c_4 & 0 & 0 \\ -c_1 & 3c_2 & -c_3 & -c_4 & 4c_1 & 4c_3 & 0 & 0 & 4c_4 & 0 \\ -c_1 & -c_2 & 3c_3 & -c_4 & 0 & 4c_2 & 4c_1 & 0 & 0 & 4c_4 \\ -c_1 & -c_2 & -c_3 & 3c_4 & 0 & 0 & 0 & 4c_1 & 4c_2 & 4c_3 \\ 3d_1 & -d_2 & -d_3 & -d_4 & 4d_2 & 0 & 4d_3 & 4d_4 & 0 & 0 \\ -d_1 & 3d_2 & -d_3 & -d_4 & 4d_1 & 4d_3 & 0 & 0 & 4d_4 & 0 \\ -d_1 & -d_2 & 3d_3 & -d_4 & 0 & 4d_2 & 4d_1 & 0 & 0 & 4d_4 \\ -d_1 & -d_2 & -d_3 & 3d_4 & 0 & 0 & 0 & 4d_1 & 4d_2 & 4d_3 \end{pmatrix}$$

To give

$$\begin{aligned}
\mathbf{k^e} &= \int_{V^e} \boldsymbol{\alpha}^T \boldsymbol{\alpha}\, dV \qquad (3.53)\\
&= \frac{1}{36V^2} \int_{V^e} (\boldsymbol{\omega}\mathbf{B})^T (\boldsymbol{\omega}\mathbf{B})\, dV\\
&= \frac{1}{36V^2} \int_{V^e} \mathbf{B}^T \boldsymbol{\omega}^T \boldsymbol{\omega} \mathbf{B}\, dV\\
&= \frac{1}{36V^2} \mathbf{B}^T \Big(\int_{V^e} \boldsymbol{\omega}^T \boldsymbol{\omega}\, dV \Big) \mathbf{B}.
\end{aligned}$$

Integration of $\boldsymbol{\omega}^T\boldsymbol{\omega}$ may now be performed using the formula 3.24 to give

$$\int_{V^e} \boldsymbol{\omega}^T \boldsymbol{\omega}\, dV = \begin{pmatrix} \boldsymbol{\Lambda} & 0 & 0 \\ 0 & \boldsymbol{\Lambda} & 0 \\ 0 & 0 & \boldsymbol{\Lambda} \end{pmatrix} = \mathbf{D}$$

where

$$\boldsymbol{\Lambda} = \frac{V}{20} \begin{pmatrix} 2 & 1 & 1 & 1 \\ 1 & 2 & 1 & 1 \\ 1 & 1 & 2 & 1 \\ 1 & 1 & 1 & 2 \end{pmatrix}.$$

So $\mathbf{k^e}$ is given by

$$\mathbf{k^e} = \frac{1}{36V^2} \mathbf{B}^T \mathbf{D} \mathbf{B}. \qquad (3.54)$$

To test our Poisson solver we compare our solution for the boundary value problem over the unit cube with that given by the NAG routine D03FAF. This is a standard seven point finite difference solver for the Helmholtz equation

$$\frac{\partial^2 \phi}{\partial x^2} + \frac{\partial^2 \phi}{\partial y^2} + \frac{\partial^2 \phi}{\partial z^2} + \lambda \phi = f(x, y, z) \qquad (3.55)$$

which of course becomes the Poisson equation when $\lambda = 0$. We use D03FAF with 64,000,000 mesh nodes to obtain a solution which may be regarded as exact. We solve the boundary value problem with a homogeneous Dirichlet condition enforced on all the boundary surfaces. A plot of the convergence of our solution with mesh refinement is shown in figure 3.7.

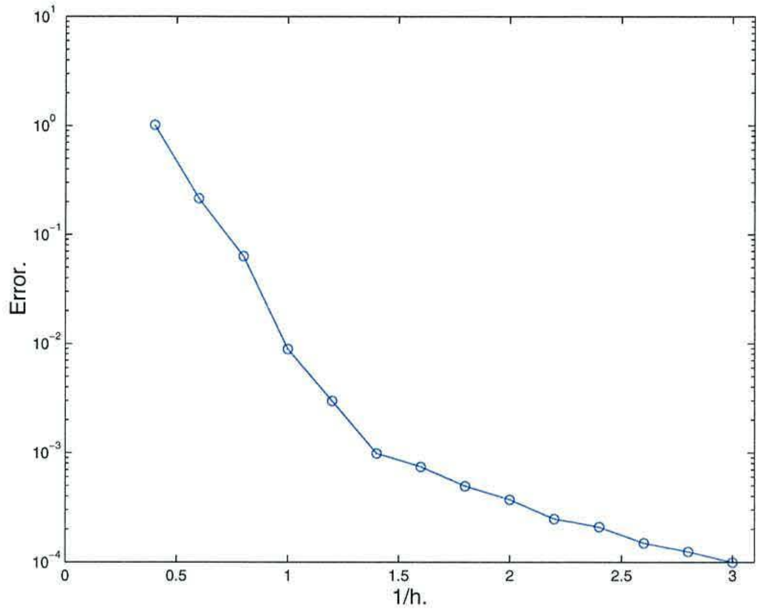

Figure 3.7: Convergence of the three dimensional Poisson solver.

3.2.3 Magnetostatic Field Calculation.

We now consider the more complex problem posed by equations 3.36 and the associated conditions. As it stands this system should be solved over all space with the open non-magnetic region extending to infinity. Following previous work [33] we overcome this problem by enforcing a homogeneous Dirichlet condition at a truncated outer boundary ∂R far from the magnetic region. This method has been shown to give satisfactory results provided that ∂R extends over 5 times the extent of the largest dimension of the magnetic region. The resulting difficulty of generating a conforming finite element mesh over the two regions is acknowledged as a non-trivial problem [50]. However this method preserves the sparsity of the stiffness matrix which is lost by using alternative techniques such as a hybrid finite element - boundary element method [51]. We reduce the number of unknowns by ensuring that the mesh in the non-magnetic region is as coarse as possible. The system of equations to be solved can be written as

$$\begin{aligned} \nabla^2 \phi &= 4\pi \nabla \cdot \boldsymbol{M}; \quad (x,y,z) \in \Omega_{int} \\ \nabla^2 \phi &= 0; \quad (x,y,z) \in \Omega_{ext} \\ (\nabla \phi_{int} - \nabla \phi_{ext}) \cdot \hat{\boldsymbol{n}} &= 4\pi \boldsymbol{M} \cdot \hat{\boldsymbol{n}}; \quad (x,y,z) \in \partial\Omega \\ \phi &= 0; \quad (x,y,z) \in \partial R. \end{aligned} \tag{3.56}$$

As described elsewhere it is important that the potential is of higher order than the magnetisation to reflect the physics of the system [52]. Using quadratic shape functions $\boldsymbol{N}^e$ over each element $e \in \Omega_{int}$ the contribution to the Galerkin residual is given by

$$\begin{aligned} R^e_{int} &= -\int_{V^e} \nabla N^e_i \cdot \nabla \phi dV^e - \int_{V^e} N^e_i (4\pi \nabla \cdot \boldsymbol{M}) dV^e \\ &\quad + \int_{S^e} N^e_i \nabla \phi \cdot d\mathbf{S}^e \\ &= -\int_{V^e} \nabla N^e_i \cdot \nabla \phi dV^e - \int_{V^e} N^e_i (4\pi \nabla \cdot \boldsymbol{M}) dV^e \\ &\quad + \int_{S^e} N^e_i \nabla \phi \cdot \hat{\boldsymbol{n}} dS^e. \end{aligned} \tag{3.57}$$

Similarly for elements $e \in \Omega_{ext}$ the residual takes contributions

$$R^e_{ext} = -\int_{V^e} \nabla N^e_i \cdot \nabla \phi dV^e + \int_{S^e} N^e_i \nabla \phi \cdot \hat{\mathbf{n}} dS^e. \tag{3.58}$$

Here we note that the normal directions for the interface integrals are opposite so that the direction of integration is opposite for elements in Ω_{int} and Ω_{ext}

$$\begin{aligned} &\int_{\circlearrowleft} N^e_i \nabla \phi_{int} \cdot \hat{\mathbf{n}} dS^e + \int_{\circlearrowright} N^e_i \nabla \phi_{ext} \cdot \hat{\mathbf{n}} dS^e \\ &\qquad = \int_{\circlearrowleft} N^e_i (\nabla \phi_{int} - \nabla \phi_{ext}) \cdot \hat{\mathbf{n}} dS^e. \end{aligned} \tag{3.59}$$

Making a substitution we may include the interface condition $(\nabla \phi_{int} - \nabla \phi_{ext}) \cdot \hat{\mathbf{n}} = (4\pi \mathbf{M}) \cdot \hat{\mathbf{n}}$ implicitly within the calculation

$$\int_{\circlearrowleft} N^e_i (\nabla \phi_{int} - \nabla \phi_{ext}) \cdot \hat{\mathbf{n}} dS^e = \int_{\circlearrowleft} N^e_i (4\pi \mathbf{M}) \cdot \hat{\mathbf{n}} dS^e. \tag{3.60}$$

Summing the residual over all elements we have

$$R = \sum_{e \in \Omega_{int}} R^e_{int} + \sum_{e \in \Omega_{ext}} R^e_{ext}. \tag{3.61}$$

The solution is then obtained by setting $R = 0$ and solving the resulting system of linear algebraic equations

$$\mathbf{K}\phi = \boldsymbol{F} + \bar{\boldsymbol{F}} \tag{3.62}$$

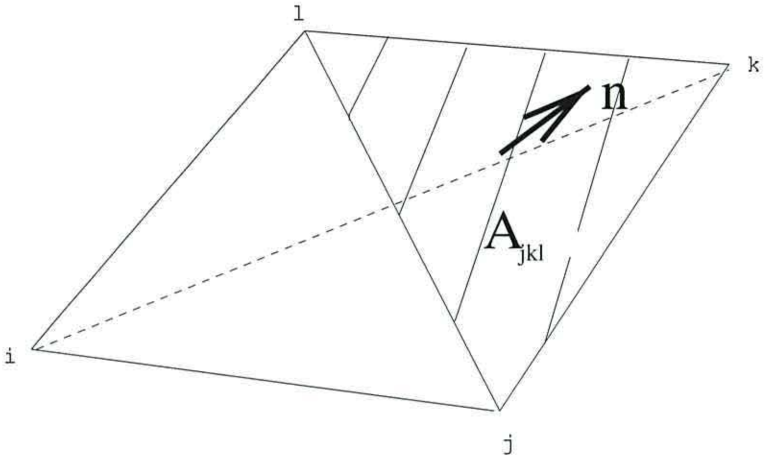

Figure 3.8: Interface condition enforced at element faces which coincide with $\partial\Omega$.

where **K** takes contributions from each element e

$$k^e_{ij} = \int_{V^e} \nabla N^e_i \cdot \nabla N^e_j \; dV^e \tag{3.63}$$

which can be calculated using the closed form matrix expression 3.54 and $\boldsymbol{F}$ takes contributions from elements e within Ω_{int}

$$f^e_i = -\int_{V^e} N^e_i (4\pi\nabla \cdot \boldsymbol{M}) \; dV^e \tag{3.64}$$

Using linear interpolation of $\boldsymbol{M}$ over each element we have

$$\begin{aligned} f^e_i &= -\int_{V^e} N^e_i (4\pi\nabla \cdot \boldsymbol{M}) dV^e \qquad (3.65)\\ &= -4\pi \int_{V^e} N^e_i \Bigg(\nabla \cdot \Bigg(\sum_{j=i}^{4} L_j \boldsymbol{M}_j\Bigg)\Bigg) dV^e \\ &= -4\pi \int_{V^e} N^e_i \Bigg(\Bigg(\sum_{j=i}^{4} \Big(\nabla \cdot L_j\Big) \boldsymbol{M}_j\Bigg)\Bigg) dV^e. \end{aligned}$$

Contributions to $\bar{\mathbf{F}}$ then come from the boundary integral enforced along the interface

$$\bar{f}^e_i = \int_{A^e} N_i 4\pi \boldsymbol{M} \cdot \hat{\mathbf{n}} dA^e; \quad i \in \partial\Omega \tag{3.66}$$

where A^e refers to faces of element e which coincide with the interface. Again the integrals can be performed analytically. To illustrate our method consider the element in figure 3.8 as an example. Face jkl is on $\partial\Omega$ with node i inside Ω_{int}. Over face jkl $L_i = 0$, so $L_j + L_k + L_l = 1 \Rightarrow L_l = 1 - L_k - L_j$. So

$$\begin{aligned} x &= L_j(x_j - x_l) + L_k(x_k - x_l) + x_l \\ y &= L_j(y_j - y_l) + L_k(y_k - y_l) + y_l \\ z &= L_j(z_j - z_l) + L_k(z_k - z_l) + z_l. \end{aligned} \tag{3.67}$$

Therefore

$$\mathbf{r}(L_j, L_k) = \begin{pmatrix} (L_j(x_j - x_l) + L_k(x_k - x_l) + x_l) \\ (L_j(y_j - y_l) + L_k(y_k - y_l) + y_l) \\ (L_j(z_j - z_l) + L_k(z_k - z_l) + z_l) \end{pmatrix} \tag{3.68}$$

gives a parameterization of the surface A_{jkl}. The direction of the tangents to the surface are given by

$$\begin{aligned} \mathbf{r}_j &= \frac{\partial \mathbf{r}}{\partial L_j} = \begin{pmatrix} (x_j - x_l) \\ (y_j - y_l) \\ (z_j - z_l) \end{pmatrix} \\ \mathbf{r}_k &= \frac{\partial \mathbf{r}}{\partial L_k} = \begin{pmatrix} (x_k - x_l) \\ (y_k - y_l) \\ (z_k - z_l) \end{pmatrix} \end{aligned} \tag{3.69}$$

The surface area differential is then given by

$$dA_{jkl} = |\mathbf{r}_j \times \mathbf{r}_k| dL_j dL_k \tag{3.70}$$

which on expansion can be expressed in terms of the coefficients of shape function L_i

$$dA_{jkl} = (b_i^2 + c_i^2 + d_i^2)^{\frac{1}{2}} dL_j dL_k. \tag{3.71}$$

The unit outward normal to the surface is given by

$$\begin{aligned} \hat{\mathbf{n_{jkl}}} &= -\frac{\mathbf{r}_j \times \mathbf{r}_k}{|\mathbf{r}_j \times \mathbf{r}_k|} \\ &= (b_i^2 + c_i^2 + d_i^2)^{-\frac{1}{2}} \begin{pmatrix} -b_i \\ -c_i \\ -d_i \end{pmatrix}. \end{aligned} \tag{3.72}$$

So the contribution from corner nodes j on the interface to $\bar{\mathbf{f}}^e$ is then

$$\begin{aligned}
\bar{\mathbf{f}}_j^e &= 4\pi \int_{A_{jkl}} N_j \boldsymbol{M} \cdot \hat{\mathbf{n_{jkl}}} dA_{jkl} \qquad (3.73)\\
&= -4\pi \int_0^1 \int_0^{1-L_k} L_j(2L_j - 1)\boldsymbol{M} \cdot \begin{pmatrix} b_i \\ c_i \\ d_i \end{pmatrix} dL_j dL_k \\
&= -\frac{4\pi}{120} \begin{pmatrix} (b_i(2M_{xj} - M_{xk} - M_{xl}) \\ +c_i(2M_{yj} - M_{yk} - M_{yl}) \\ +d_i(2M_{zj} - M_{zk} - M_{zl}) \end{pmatrix}
\end{aligned}$$

and the contribution from midside nodes q is

$$\begin{aligned}
\bar{\mathbf{f}}_q^e &= 4\pi \int_{A_{jkl}} N_q \boldsymbol{M} \cdot \hat{\mathbf{n_{jkl}}} dA_{jkl} \qquad (3.74)\\
&= -4\pi \int_0^1 \int_0^{1-L_k} 4L_j L_k \boldsymbol{M} \cdot \begin{pmatrix} b_i \\ c_i \\ d_i \end{pmatrix} dL_j dL_k \qquad (3.75)\\
&= -\frac{4\pi}{30} \begin{pmatrix} (b_i(2M_{xj} + 2M_{xk} + M_{xl}) \\ +c_i(2M_{yj} + 2M_{yk} + M_{yl}) \\ +d_i(2M_{zj} + 2M_{zk} + M_{zl}) \end{pmatrix} \qquad (3.76)
\end{aligned}$$

where j, k refer to adjacent corner nodes to midside node q.

As we shall be working with reduced magnetisation $\boldsymbol{m} = \boldsymbol{M}/M_s$ in our micromagnetic model the magnetostatic field will be calculated as a function of $\boldsymbol{m}$ at each timestep. We therefore require the magnitude of the field to be scaled by M_s

$$\begin{aligned}
-\nabla\phi(\boldsymbol{M}) &= -\nabla\phi(M_s\boldsymbol{m}) \qquad (3.77)\\
&= -M_s\nabla\phi(\boldsymbol{m}).
\end{aligned}$$

3.3 Micromagnetic Model.

Our computational model is based on the reduced Gilbert equation of motion given in chapter 2

$$\begin{aligned} \frac{d\boldsymbol{m}}{d\tau} &= -\boldsymbol{m} \times \boldsymbol{h}_{eff} + \alpha\left(\boldsymbol{m} \times \frac{d\boldsymbol{m}}{d\tau}\right) \quad (3.78) \\ \alpha\left(\boldsymbol{m} \times \frac{d\boldsymbol{m}}{d\tau}\right) - \frac{d\boldsymbol{m}}{d\tau} &= \boldsymbol{m} \times \boldsymbol{h}_{eff} \end{aligned}$$

with $d\tau = \gamma H_k dt$ as before. The effective field now takes contributions froms all terms in the Gibb's free energy, i.e. exchange energy, magnetostatic energy, anisotropy energy and applied Zeeman enegy

$$\mathcal{E} = \int_V \frac{A}{M_s^2}|\nabla \boldsymbol{M}|^2 - \frac{1}{2}\boldsymbol{H}_d \cdot \boldsymbol{M} - \frac{K}{M_s^2}(\boldsymbol{M} \cdot \hat{\boldsymbol{e}})^2 - \boldsymbol{H}_z \cdot \boldsymbol{M} \; dV. \quad (3.79)$$

Again the effective field is defined as the derivative of internal free energy with respect to the magnetisation

$$\begin{aligned} \boldsymbol{H}_{eff} &= \frac{\partial \mathcal{E}}{\partial \boldsymbol{M}} \quad (3.80) \\ &= \frac{2A}{M_s^2}\nabla^2 \boldsymbol{M} + \boldsymbol{H}_d(\boldsymbol{M}) + \frac{2K}{M_s^2}(\boldsymbol{M} \cdot \hat{\boldsymbol{e}})\hat{\boldsymbol{e}} + H_z. \end{aligned}$$

In terms of reduced magnetisation $\boldsymbol{m} = \boldsymbol{M}/M_s$ we have

$$\boldsymbol{H}_{eff} = \frac{2A}{M_s}\nabla^2 \boldsymbol{m} + M_s \boldsymbol{H}_d(\boldsymbol{m}) + \frac{2K}{M_s}(\boldsymbol{m} \cdot \hat{\boldsymbol{e}})\hat{\boldsymbol{e}} + H_z. \quad (3.81)$$

Finally we scale the effective field with respect to the anisotropy field strength $\boldsymbol{h}_{eff} = \boldsymbol{H}_{eff}/H_k$, $H_k = 2K/M_s$ to give

$$\begin{aligned} \boldsymbol{h}_{eff} &= \frac{A}{K}\nabla^2 \boldsymbol{m} - \frac{M_s^2}{2K}\nabla\phi(\boldsymbol{m}) + (\boldsymbol{m} \cdot \hat{\boldsymbol{e}})\hat{\boldsymbol{e}} + \frac{\boldsymbol{H}_z}{H_k} \quad (3.82) \\ &= \boldsymbol{h}_{ex} + \boldsymbol{h}_d + \boldsymbol{h}_{anis} + \boldsymbol{h}_z. \end{aligned}$$

This problem now involves both spatial and temporal discretization, provided that all terms of h_{eff} can be evaluated at each node, a pointwise solution is reasonably straight forward. However the exchange field cannot be easily evaluated at a point due to the second order spatial derivative of magnetisation which vanishes under linear interpolation. Rather than using a more computationally intensive higher order basis for $\boldsymbol{m}$ we implement a variational formulation of the problem.

3.3.1 Galerkin Projection of the Gilbert Equation.

This section highlights the power of the Galerkin method over other variational formulations. Although no underlaying quadratic form exists from which to extract a minimum corresponding to the solution, we may still utilize the Galerkin projection in order to obtain a solution. Taking the Galerkin projection of 3.78 onto a set of linear basis functions $\Psi = \{\psi_i,\ i = 1,..,N\}$ we have an expression for each of the N nodes of the spatial mesh

$$\begin{aligned} \int_V \psi_i\left(\alpha\left(\mathbf{m}\times\frac{d\mathbf{m}}{d\tau}\right)-\frac{d\mathbf{m}}{d\tau}\right) dV &= \int_V \psi_i(\mathbf{m}\times\mathbf{h}_{eff})\ dV \\ i &= 1,..,N. \end{aligned} \tag{3.83}$$

here the ψ_i refer to global basis functions which vanish at all nodes $j \neq i$

$$\psi_i(x_j, y_j, z_j) = \delta ij \tag{3.84}$$

with support over all elements containing node i

$$supp(\psi_i) = \{e : i \in e\}. \tag{3.85}$$

These global basis functions are nothing more than the accumulation of the local shape functions L_i^e of elements $e \in supp(\psi_i)$. In fact the support of ψ_i is equivalent to the union of support of the L_i^e for elements e containing node i

$$supp(\psi_i) = \bigcup_{e:i\in e} supp(L_i^e). \tag{3.86}$$

Coversly the support of each L_i^e is equivalent to the common support of the ψ_j for nodes $j \in e$

$$supp(L_i^e) = \bigcap_{j\in e} supp(\psi_j). \tag{3.87}$$

This can be visualized in a straight forward manner by considering the example of a one dimensional mesh in figure 3.9, with nodes $i = 1,..,N$ and elements e_j, $j = 1,..,N-1$. The support of ψ_i contains elements e_{j-1} and e_j. The global basis function ψ_i is then clearly equivalent to the accumulation of local shape functions $L_i^{e_{j-1}}$ and $L_i^{e_j}$. The projection onto Ψ is therefore equivalent to the accumulated projections onto the L_i^e, $i = 1, 2, 3, 4$ for all elements e of the spatial mesh

$$\begin{aligned} \int_{V^e} L_i^e\left(\alpha\left(\boldsymbol{m}\times\frac{d\boldsymbol{m}}{d\tau}\right)-\frac{d\boldsymbol{m}}{d\tau}\right) dV^e &= \int_V L_i^e(\boldsymbol{m}\times\boldsymbol{h}_e f f)\ dV^e. \\ i &= 1, 2, 3, 4 \\ e &= 1,..,E \end{aligned} \tag{3.88}$$

The accumulation of local projections results in duplicate contributions from each node, with $supp(\psi_i)$ contributions for each node (i). Because $\psi_i \in [0,1]$ by definition, ψ_i is not the direct sum of the L_i^e

$$\psi_i \neq \sum_{e \in supp(\psi_i)} L_i^e. \tag{3.89}$$

However by considering figure 3.9 we realize that it is true to say that integrals of ψ_i are given by the direct sum of integrals of the L_i

$$\int_V \psi_i \, dV = \sum_{e \in supp(\psi_i)} \int_{V^e} L_i^e \, dV. \tag{3.90}$$

For each i the equality in 3.83 is preserved and no averaging to preserve $\psi \in [0,1]$ is required. Clearly the i contribution from all nodes $j \notin supp(i)$ is zero. This build-up of the projection integrals from elemental contributions was implicit in our previous Galerkin formulation of the Poisson equation. By expressions of the form 3.88 in future working we will always mean the accumulation of such expressions over $supp(\psi_i)$ and the superscript e will be dropped.

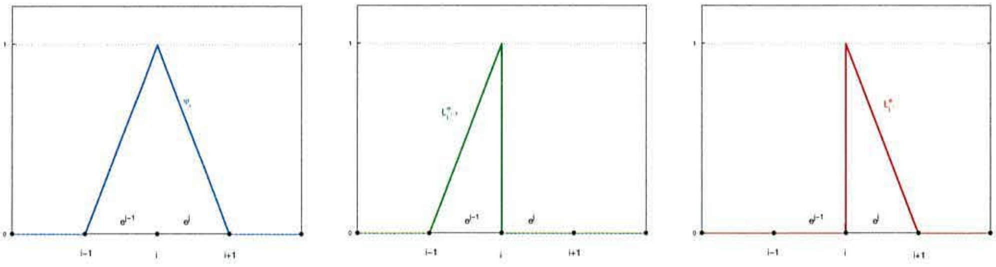

Figure 3.9: (a) Global basis function ψ_i, (b) local shape function $L_i^{e_{j-1}}$ and (c) local shape function $L_i^{e_j}$.

3.3.2 Field Calculations.

The right hand side of equation 3.88 takes contributions from the four terms of $\boldsymbol{h}_{eff}$

$$\begin{aligned} \int_V L_i \boldsymbol{m} \times \boldsymbol{h}_{eff} \, dV &= \frac{A}{K} \int_V L_i \boldsymbol{m} \times \nabla^2 \boldsymbol{m} \, dV \\ &\quad + \int_V L_i \boldsymbol{m} \times \boldsymbol{h}_d \, dV \end{aligned} \tag{3.91}$$

$$+\int_V L_i \boldsymbol{m} \times (\boldsymbol{m} \cdot \hat{\boldsymbol{e}})\hat{\boldsymbol{e}}\, dV$$
$$+\int_V L_i \boldsymbol{m} \times \boldsymbol{h}_z\, dV.$$

The integral for the exchange term may be evaluated using Green's theorem [53]

$$\begin{aligned} \int_V L_i \boldsymbol{m} \times \nabla^2 \boldsymbol{m}\, dV &= \int_{\partial V} L_i \boldsymbol{m} \times (\hat{\boldsymbol{n}} \cdot \nabla)\boldsymbol{m}\, dS \\ &\quad - \int_V \boldsymbol{m} \times (\nabla L_i \cdot \nabla)\boldsymbol{m}\, dV. \end{aligned} \tag{3.92}$$

The Galerkin projection effectively reduces the order of differentiation on $\boldsymbol{m}$, enabling the integral to be evaluated after discretization using the linear interpolation scheme. Contributions from the magnetostatic field are evaluated using data from the scalar potential calculation described previously

$$\begin{aligned} \int_V L_i \boldsymbol{m} \times \boldsymbol{h}_d\, dV &= \frac{M_s^2}{2K} \int_V L_i \boldsymbol{m} \times (-\nabla\phi)\, dV \\ &= -\frac{M_s^2}{2K} \int_V L_i \boldsymbol{m} \times \nabla\phi\, dV \\ &= \frac{M_s^2}{2K} \int_V L_i \nabla\phi \times \boldsymbol{m}\, dV. \end{aligned} \tag{3.93}$$

Contributions from anisotropy and applied field terms are then straight forward.

3.3.3 Spatial Discretisation.

The final step in developing our variational formulation of the model is to expand the magnetisation and contributions to the effective field in terms of the local shape functions and nodal values

$$\boldsymbol{m} = \sum_{i=1}^{4} L_i \boldsymbol{m}_i \tag{3.94}$$

$$\frac{d\boldsymbol{m}}{d\tau} = \sum_{i=1}^{4} L_i \frac{d\boldsymbol{m}_i}{d\tau} \tag{3.95}$$

$$\nabla\phi = \nabla\Big(\sum_{i=1}^{10} N_i \phi_i\Big) \tag{3.96}$$

$$
\begin{aligned}
&= \sum_{i=1}^{10}\Big(\nabla N_i\Big)\phi_i \\
\boldsymbol{h}_z &= \sum_{i=1}^{4} L_i \boldsymbol{h}_{z,i}.
\end{aligned} \tag{3.97}
$$

Over each element we have

$$
\begin{aligned}
&\int_V L_i\alpha\Big(\sum_{j=1}^{4}L_j\boldsymbol{m}_j\Big)\times\Big(\sum_{k=1}^{4}L_k\frac{d\boldsymbol{m}_k}{d\tau}\Big)\,dV-\int_V L_i\Big(\sum_{j=1}^{4}L_j\frac{d\boldsymbol{m}_j}{d\tau}\Big)\,dV \\
&=\frac{A}{K}\int_{\partial V}L_i\Big(\sum_{j=1}^{4}L_j\boldsymbol{m}_j\Big)\times(\hat{\boldsymbol{n}}\cdot\nabla)\Big(\sum_{k=1}^{4}L_k\boldsymbol{m}_k\Big)\,dS \\
&-\frac{A}{K}\int_V\Big(\sum_{j=1}^{4}L_j\boldsymbol{m}_j\Big)\times(\nabla L_i\cdot\nabla)\Big(\sum_{i=1}^{4}L_k\boldsymbol{m}_k\Big)\,dV \\
&+\frac{M_s^2}{2K}\int_V L_i\Big(\sum_{j=1}^{10}(\nabla N_j)\phi_j\Big)\times\Big(\sum_{k=1}^{4}L_k\boldsymbol{m}_k\Big)\,dV \\
&+\int_V L_i\Big(\sum_{j=1}^{4}L_j\boldsymbol{m}_j\Big)\times\Big(\sum_{k=1}^{4}L_k\boldsymbol{m}_k\cdot\hat{\boldsymbol{e}}\Big)\hat{\boldsymbol{e}}\,dV \\
&+\int_V L_i\Big(\sum_{j=1}^{4}L_j\boldsymbol{m}_j\Big)\times\Big(\sum_{k=1}^{4}L_k\boldsymbol{h}_{z,k}\Big)\,dV.
\end{aligned} \tag{3.98}
$$

Since the nodal values are constants these integrals may then be reformulated with only the local shape functions appearing within each integrand

$$
\begin{aligned}
&\alpha\sum_{j=1}^{4}\sum_{k=1}^{4}\boldsymbol{m}_j\times\frac{d\boldsymbol{m}_k}{d\tau}\int_V L_iL_jL_k\,dV-\sum_{j=1}^{4}\frac{d\boldsymbol{m}_j}{d\tau}\int_V L_iL_j\,dV \\
&=\frac{A}{K}\sum_{j=1}^{4}\sum_{k=1}^{4}\boldsymbol{m}_j\times(\hat{\boldsymbol{n}}\cdot\nabla L_k)\boldsymbol{m}_k\int_{\partial V}L_iL_j\,dS \\
&-\frac{A}{K}\sum_{j=1}^{4}\sum_{i=1}^{4}(\nabla L_i\cdot\nabla L_k)\boldsymbol{m}_j\times\boldsymbol{m}_k\int_V L_j\,dV \\
&+\frac{M_s^2}{2K}\sum_{j=1}^{10}\sum_{k=1}^{4}\phi_j\int_V L_iL_k\begin{bmatrix}\frac{\partial N_j}{\partial x}\\ \frac{\partial N_j}{\partial y}\\ \frac{\partial N_j}{\partial z}\end{bmatrix}\,dV\times\boldsymbol{m}_k
\end{aligned} \tag{3.99}
$$

$$+\sum_{j=1}^{4}\sum_{k=1}^{4}\boldsymbol{m}_j \times (\boldsymbol{m}_k \cdot \hat{\boldsymbol{e}})\hat{\boldsymbol{e}} \int_V L_i L_j L_k \, dV$$
$$+\sum_{j=1}^{4}\sum_{k=1}^{4}\boldsymbol{m}_j \times \boldsymbol{h}_{z,k} \int_V L_i L_j L_k \, dV.$$

Evaluation of each integral is then straight forward using the integral formula 3.24. For each node i we have a linear equation with $3N$ unknowns, namely the three components of $d\boldsymbol{m}/d\tau$ at each of the N nodes, in terms of the known components of $\boldsymbol{m}$ and the calculated components of $\boldsymbol{h}_{eff}$. These equations may then be formulated as the matrix equation

$$\begin{aligned}\mathbf{A}(\boldsymbol{m})\frac{d\vec{\boldsymbol{m}}}{d\tau} &= \mathbf{G}(\boldsymbol{h}_{eff})\vec{\boldsymbol{m}} \qquad (3.100)\\ &= \boldsymbol{G}(\boldsymbol{h}_{eff}, \boldsymbol{m})\end{aligned}$$

where

$$\frac{d\vec{\boldsymbol{m}}}{d\tau} = \begin{pmatrix} \frac{dm_x^1}{d\tau} \\ \frac{dm_y^1}{d\tau} \\ \frac{dm_z^1}{d\tau} \\ \vdots \\ \frac{dm_x^i}{d\tau} \\ \frac{dm_y^i}{d\tau} \\ \frac{dm_z^i}{d\tau} \\ \vdots \\ \frac{dm_x^N}{d\tau} \\ \frac{dm_y^N}{d\tau} \\ \frac{dm_z^N}{d\tau} \end{pmatrix} \qquad (3.101)$$

and

$$\vec{m} = \begin{pmatrix} m_x^1 \\ m_y^1 \\ m_z^1 \\ \vdots \\ m_x^i \\ m_y^i \\ m_z^i \\ \vdots \\ m_x^N \\ m_y^N \\ m_z^N \end{pmatrix} . \tag{3.102}$$

The bilinear forms, mass matrix $\mathbf{A}(\boldsymbol{m})$ and force vector coefficient matrix $\mathbf{G}(\boldsymbol{h}_{eff})$ take contributions from the left hand side and the right hand side of 3.99 respectively.

3.3.4 Temporal Discretization.

Solving the matrix equation yields pointwise values for $d\boldsymbol{m}/d\tau$. We are then free to use any of the numerical integration schemes outlined in chapter 2 to obtain values of $\boldsymbol{m}$ at the subsequent time-step. For example our initial applications of the model used an explicit Euler method which may be implemented as follows

$$\begin{aligned} \left(\frac{d\boldsymbol{m}_i}{d\tau}\right)^t &= \frac{\boldsymbol{m}_i^{t+1} - \boldsymbol{m}_i^t}{\Delta\tau} \\ \boldsymbol{m}_i^{t+1} &= \boldsymbol{m}_i^t + \Delta\tau\left(\frac{d\boldsymbol{m}_i}{d\tau}\right)^t . \end{aligned} \tag{3.103}$$

So solving the system of linear equations 3.99 and performing an Euler integration at each node takes the system from simulation time τ^t to τ^{t+1}. We may therefore evolve the entire system from any initial configuration $\boldsymbol{m}_0$ in the same way as a standard initial value problem. Hysteresis simulations can be performed by allowing the system to reach equilibrium at each field step in the same way as the example for a single spin in chapter 2.

3.4 Computer Implementation.

We now discuss some technical aspects of the model. The calculations have been implemented using the both the Fortran 90 and C++ programming languages and run on Dec alpha and Pentium 4 machines. Our methods of storing and manipulating sparse matrices, iteratively solving systems of linear equations, mesh generation as well as the structure of the computer program itself require further explanation. Using sparse column format to store the large matrices we encounter uses memory efficiently but more importantly allows us to build-up the mass matrix **A** symbolically at the start of the program and assign numerical contributions from each element directly to the correct global index at each time-step of the simulation. Use of the GMRES [54] iterative solver enables efficient solution of the linear equations, using the magnetisation configuration from the previous time-step as input. We discuss some problems encountered during the meshing of the "two-region" geometry and the effects of mesh quality on our solutions. Finally we give schematic illustrations of how the code is structured and discuss the importance of user-defined tolerances in relation to the definition of equilibrium.

3.4.1 Sparse Matrix Technology.

The stiffness matrix and mass matrix of our magnetostatic and dynamic calculation will be very large; n^2 and $(3N)^2$ where n is the total number of quadratic nodes in the mesh and N is the number of linear nodes within the magnetic region respectively. For large systems with more than a few hundred nodes this makes our computations impossible, within our available computing facilities, without the use sparse matrix technology. Taking the stiffness matrix for the three dimensional Poisson problem as an example, each element matrix has 100 entries. This gives an upper limit on the number of non-zero entries in the global matrix of 100 times the number of elements. With a typical mesh for a small magnetostatic problem of say 900 nodes and 600 elements, the stiffness matrix will have $900^2 = 810,000$ entries while less than $100 \times 600 = 60,000$ of these will be non-zero. So even in this small problem only around 7.5% of the allocated memory is storing anything other than zero's. This percentage drops still further for larger problems and finer meshes. Various sparse matrix formats have been developed which store only the non-zero elements of the matrix and usually two other arrays containing directions to their position in the matrix.

Triad Format.

This simple sparse format consists of three linear arrays A, IA and JA which completely specify any given matrix. Each non-zero entry is stored in array A, the corresponding row number is stored at the same index of IA and the corresponding column number is stored at the same index of JA. For example the matrix

$$A_{full} = \begin{pmatrix} 11 & 12 & 0 & 0 & 15 \\ 21 & 22 & 0 & 0 & 0 \\ 0 & 0 & 33 & 0 & 35 \\ 0 & 0 & 0 & 44 & 0 \\ 51 & 0 & 53 & 0 & 55 \end{pmatrix}$$

may be stored as

$$\begin{aligned} A &= (51, 12, 11, 33, 15, 53, 55, 22, 35, 44, 21) \\ IA &= (5, 2, 1, 3, 1, 5, 5, 2, 3, 4, 2) \\ JA &= (1, 1, 1, 3, 5, 3, 5, 2, 5, 4, 1) \end{aligned}$$

Although we have not saved memory in this example as $5^2 < (3 \times 11)$, the saving is great for all but the smallest systems. This is clear from figure 3.4.1 where we have assumed that the number of elements is 2/3 the number of nodes in a given mesh. It can be seen from the above example that the entries need not be ordered, which is sometimes useful when building up a matrix with contributions from each element.

Row Format.

This format again consists of three arrays A, IA and JA which completely specify the matrix. The non-zero elements are stored in A counting down the rows. IA holds the column index for each non-zero entry and JA holds the offsets into IA and A for the beginning of each row. So for

$$A_{full} = \begin{pmatrix} 11 & 12 & 0 & 0 & 15 \\ 21 & 22 & 0 & 0 & 0 \\ 0 & 0 & 33 & 0 & 35 \\ 0 & 0 & 0 & 44 & 0 \\ 51 & 0 & 53 & 0 & 55 \end{pmatrix}$$

we have

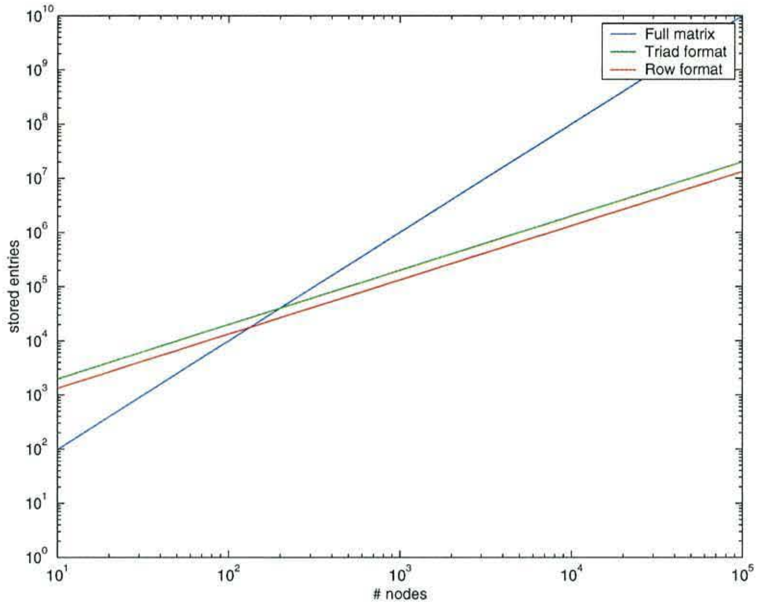

Figure 3.10: Full versus sparse matrix formats.

$$\begin{aligned} A &= (11, 12, 15, |21, 22, |33, 35, |44, |51, 53, 55) \\ IA &= (1, 2, 5, |1, 2, |3, 5, |4, |1, 3, 5) \\ JA &= (1, 4, 6, 8, 9, 12) \end{aligned}$$

We now have a slight improvement in memory allocation over the triad format; instead of 3×number of non-zero's we use 2×number of non-zero's+number of rows+1 [1]. The benefit of this format comes with improved computational efficiency, as instead of searching the whole list to find a given entry $A_{i,j}$, we only have to search row i which we know to begin at $JA(i)$. Here the rows must appear in order but the ordering of the elements of each row is unimportant in general.

Sparse Matrix Addition.

In formulating the matrix equation in finite element calculations the global stiffness matrix must be accumulated over all e elements of the mesh; this is equivalent to performing the addition of e sparse matrices. It is straightforward to perform the addition of matrices in triad format, if we have two such matrices A and B, then $C = A + B$ may be written simply as

---

[1] Note that JA has a length of the number of row + 1, as the last entry is used to mark the end of the list

$$\begin{aligned} C &= (A, B) \\ IC &= (IA, IB) \\ JC &= (JA, JB) \end{aligned}$$

However this may result in more than one entry for any given position the matrix. This is a further waste of memory, if contributions from many element matrices are required for example in the Poisson problem, then the full 100×number of elements must be allocated. Further, if the matrix is to be passed to another package which will not accept duplicate entries in the specification, then these duplicates must be removed, which is a laborious task - even for a computer! For each entry we must loop over all remaining entries to see if a duplicate exists that must be added and the saving of memory has become very costly in CPU time. The addition of two matrices in row format is performed by two algorithms: a symbolic algorithm which determines the resulting structure and a numerical algorithm which determines the values of the non-zero entries in the resulting matrix, taking advantage of the previous knowledge of their positions. It is possible to perform the addition numerically in a single step, but little is gained by doing so. On the other hand, splitting the procedure into two steps introduces an additional degree of freedom into the program, which is very useful when, as in our case, duplicate entries must be removed. Also for our dynamic calculations the structure is fixed and only the numerical values of the matrix change at each time-step.

The Multiple Switch Method.

We illustrate this method by performing the addition of two matrices in row format

$$\begin{aligned} A_{full} &= \begin{pmatrix} 6 & 0 & 0 & 1 \\ 3 & 0 & 5 & 0 \\ 7 & 2 & 0 & 0 \\ 0 & 0 & 0 & 3 \end{pmatrix} \\ A &= (6, 1, 3, 5, 7, 2, 3) \\ IA &= (1, 4, 1, 3, 1, 2, 3) \\ JA &= (1, 3, 5, 7, 8) \end{aligned}$$

and

$$\begin{aligned}
B_{full} &= \begin{pmatrix} 0 & 8 & 2 & 0 \\ 0 & 5 & 0 & 3 \\ 1 & 0 & 2 & 0 \\ 6 & 0 & 0 & 1 \end{pmatrix} \\
B &= (8,2,5,3,1,2,6,1) \\
IB &= (2,3,2,4,1,3,1,4) \\
JB &= (1,3,5,7,9)
\end{aligned}$$

Symbolic algorithm. The resulting matrix $\boldsymbol{C} = \boldsymbol{A}+\boldsymbol{B}$ has four columns, we therefore define the multiple switch vector to be an integer array IX with four positions, initialized to zero; this array is used to keep track of contributions to each position in the row under consideration. The first part of the addition is to form $\boldsymbol{IC}$ by merging $\boldsymbol{IA}$ and $\boldsymbol{IB}$ row by row. For the first row this implies merging $1,4$ and $2,3$. These numbers are sequentially added to $\boldsymbol{IC}$; when 1 is added to $\boldsymbol{IC}$, the row index 1 is also stored in $\boldsymbol{IX(1)}$. Then 4 is added to $\boldsymbol{IC}$ and 1 is stored in $\boldsymbol{IX}(4)$. In order to avoid repeating elements in $\boldsymbol{IC}$, before adding each element we check $\boldsymbol{IX}$ for the value 1, i.e. to see if the switch is 'on', this doesn't occur for row 1. Once row 1 is processed we have

$$\begin{aligned}
\boldsymbol{IC} &= (1,4,2,3) \\
\boldsymbol{IX} &= (1,1,1,1)
\end{aligned}$$

Here we see that row 1 of $\boldsymbol{C}$ is fully populated as there is a 1 in all positions of $\boldsymbol{IX}$. $\boldsymbol{JC}$ is easily constructed with the help of a pointer, which points to the first empty position of $\boldsymbol{IC}$, in this case

$$\begin{aligned}
\boldsymbol{JC}(1) &= 1 \\
\boldsymbol{JC}(2) &= 5
\end{aligned}$$

Now we have to merge the second row; $1,3$ and $2,4$. The row index is now 2 and we store 2 in $\boldsymbol{IX}$ and check $\boldsymbol{IX}$ for the value 2. After processing row 2 we have

$$\begin{aligned}
\boldsymbol{IC} &= (1,4,2,3,1,3,2,4) \\
\boldsymbol{IX} &= (2,2,2,2) \\
\boldsymbol{JC} &= (1,5,9)
\end{aligned}$$

and $\boldsymbol{IX}$ is ready to process row 3

$$\begin{aligned}\boldsymbol{IC} &= (1,4,2,3,1,3,2,4,1,2,3)\\ \boldsymbol{IX} &= (3,3,3,2)\\ \boldsymbol{JC} &= (1,5,9,12).\end{aligned}$$

Finally

$$\begin{aligned}\boldsymbol{IC} &= (1,4,2,3,1,3,2,4,1,2,3,4,1)\\ \boldsymbol{IX} &= (4,3,3,4)\\ \boldsymbol{JC} &= (1,5,9,12,14).\end{aligned}$$

Numerical algorithm. To perform the numerical part of the algorithm we define an array $\boldsymbol{X}$, of length the number of columns, to accumulate the values of the non-zero's in each row of $\boldsymbol{A}$ and $\boldsymbol{B}$. Again taking the only sensible option of starting at row 1

(i) we first use $\boldsymbol{IC}$ to set to zero the positions $1, 4, 2$ and 3 of $\boldsymbol{X}$.

$$\boldsymbol{X} = (0,0,0,0)$$

(ii) We then use $\boldsymbol{IA}(\boldsymbol{JI}(1)..\boldsymbol{JI}(2)-1) = 1,4$ to store the first two values of $\boldsymbol{A}$ in positions 1 and 4 respectively, of $\boldsymbol{X}$.

$$\boldsymbol{X} = (6,0,0,1)$$

(iii) Next we use $\boldsymbol{IB}$ and $\boldsymbol{B}$ to accumulate the values 8 and 2 in positions 2 and 3 of $\boldsymbol{X}$ respectively.

$$\boldsymbol{X} = (6,8,2,1)$$

(iv) Finally we use $\boldsymbol{IC}$ to retrieve from positions $1, 4, 2$ and 3 of $\boldsymbol{X}$ the final values to be stored in $\boldsymbol{C}$.

$$\boldsymbol{C} = (6,1,8,2)$$

The remaining rows are processed sequentially in the same way

Row 2:

$$\begin{aligned} (i)\ \boldsymbol{X} &= (0,0,0,0) \\ (ii)\ \boldsymbol{X} &= (3,0,5,0) \\ (iii)\ \boldsymbol{X} &= (3,5,5,3) \\ (iv)\ \boldsymbol{C} &= (6,1,8,2,3,5,5,3) \end{aligned}$$

Row 3:

$$\begin{aligned} (i)\ \boldsymbol{X} &= (0,0,0,3) \\ (ii)\ \boldsymbol{X} &= (7,2,0,3) \\ (iii)\ \boldsymbol{X} &= (8,2,2,3) \\ (iv)\ \boldsymbol{C} &= (6,1,8,2,3,5,5,3,8,2,2) \end{aligned}$$

Row 4:

$$\begin{aligned} (i)\ \boldsymbol{X} &= (0,2,2,0) \\ (ii)\ \boldsymbol{X} &= (0,2,2,3) \\ (iii)\ \boldsymbol{X} &= (6,2,2,4) \\ (iv)\ \boldsymbol{C} &= (6,1,8,2,3,5,5,3,8,2,2,4,6) \end{aligned}$$

To give

$$\begin{aligned} \boldsymbol{C} &= (6,1,8,2,3,5,5,3,8,2,2,4,6) \\ \boldsymbol{IC} &= (1,4,2,3,1,3,2,4,1,2,3,4,1) \\ \boldsymbol{JC} &= (1,5,9,12,14). \end{aligned}$$

It is interesting to note that the symbolic section of the procedure has no knowledge of the actual numerical values of the elements. If zero's are present in the sparse representation of $\boldsymbol{A}$ or $\boldsymbol{B}$, due to imposing a Dirichlet condition for example, then these will be processed as if they were non-zero entries and cause no problems. It is clear that these methods are very easily extended to add more than two sparse matrices together and are therefore appropriate for accumulating contributions to a global stiffness matrix from individual element matrices. The improvement in computational efficiency is now clear, as to remove duplicate entries we only have to check entries in the same row, leading to at most n operations per entry instead of n^2.

SLAP column format.

More sophisticated methods exist for sparse matrix representation, but the desired efficiency for our work is achieved using a variant of the row format described above, this is the most common advanced sparse matrix format [55]. Our chosen Sparse Linear Algebra Package uses a sparse column format with the diagonal entry appearing first in each column and the other entries ordered by row number. The solver will accept matrices in the triad format, however computational efficiency is further compromised as the format is converted internally by the routine at every time-step of the simulation. So for optimal efficiency we present the matrix in column format by using the methods outlined above but with the roles of rows and columns interchanged. Some additional work is then required to order the columns but this only amounts to a heap-sort over each column.

3.4.2 Iterative Solvers.

In both the magnetostatic and dynamic calculations we are required to solve matrix equations of the form

$$\mathbf{A}\boldsymbol{x} = \boldsymbol{b} \tag{3.104}$$

The large number of unknowns in finite element calculations not only has an impact on memory requirements, the methods we use to solve the systems of linear equations must also be chosen carefully. Direct methods such as Gaussian elimination are not at all suitable because the sparsity of the matrices is not exploited. The computational effort required grows with every step of a standard Gaussian elimination as more entries become non-zero.

Matrix decomposition Methods.

For this reason various forms of iterative solver have been developed. The simplest of these is the fixed point method. Here $\mathbf{A}$ is decomposed

$$\mathbf{A} = \mathbf{M} - \mathbf{N} \tag{3.105}$$

where $\mathbf{M}$ is chosen to be an easily invertible matrix. Substituting into 3.104, we then have

$$\mathbf{M}\boldsymbol{x} = \mathbf{N}\boldsymbol{x} + \boldsymbol{b}. \tag{3.106}$$

This leads to the so-called fixed point iteration

$$\begin{aligned} \mathbf{M}\boldsymbol{x}^{k+1} &= \mathbf{N}\boldsymbol{x}^{k} + \boldsymbol{b} \qquad (3.107) \\ \boldsymbol{x}^{k+1} &= \mathbf{M}^{-1}(\mathbf{N}\boldsymbol{x}^{k} + \boldsymbol{b}) \\ &= (\mathbf{I} - \mathbf{M}^{-1}\mathbf{A})\boldsymbol{x}^{k} + \mathbf{M}^{-1}\boldsymbol{b}. \end{aligned}$$

Since $\mathbf{N}$ no longer appears explicitly in this expression, iterations may be performed using any easily invertible matrix $\mathbf{M} \neq \mathbf{I}$. The true solution $\boldsymbol{x}$ is clearly a fixed point of the system and these iterations will converge for all $\boldsymbol{x}^0 \in \mathbb{R}$ provided that the spectral radius of $\mathbf{A}$ is strictly less than 1 [56].

Alternatively we may perform a diagonal decomposition of $\mathbf{A}$ as follows

$$\mathbf{A} = \mathbf{D} - \mathbf{L} - \mathbf{U} \tag{3.108}$$

where $\mathbf{D}$ is a diagonal matrix, $\mathbf{L}$ is a lower triangular matrix, $\mathbf{U}$ is an upper triangular matrix. This can result in two types of iteration scheme.

$$\begin{aligned} \mathbf{D}\boldsymbol{x}^{k+1} &= (\mathbf{L}+\mathbf{U})\boldsymbol{x}^k + \boldsymbol{b} \\ \boldsymbol{x}^{k+1} &= \mathbf{D}^{-1}(\mathbf{L}+\mathbf{U})\boldsymbol{x}^k + \mathbf{D}^{-1}\boldsymbol{b} \\ &= \mathbf{G}\boldsymbol{x}^k + \boldsymbol{d} \end{aligned} \tag{3.109}$$

where

$$\begin{aligned} G_{ij} &= \begin{cases} -\frac{a_{ij}}{a_{ii}}; & i \neq j \\ 0; & i = j \end{cases} \\ d_i &= \frac{b_i}{a_{ii}}. \end{aligned}$$

If the components of $\boldsymbol{x}^{k+1}$ are computed sequentially this is known as the Jacobi method whereas if $\boldsymbol{x}^k$ is updated with the known values of $\boldsymbol{x}^{k+1}$ at each stage we have an improved scheme known as the Gauss-Seidel method. This method may be further improved by weighting the change in the value of each x_i, a technique known as overrelaxation or underrelaxation depending on the value of the weighting factor [56].

Gradient Methods.

The methods described above are all essentially modifications of the fixed point method. Alternatively we may consider the solution of $\mathbf{A}\boldsymbol{x} = \boldsymbol{b}$ as a minimizer of the functional

$$f(\boldsymbol{x}) = \frac{1}{2}\boldsymbol{x}^T\mathbf{A}\boldsymbol{x} - \boldsymbol{b}^T\boldsymbol{x}. \tag{3.110}$$

We may now choose some initial guess $\boldsymbol{x}^0 \in \mathbb{R}^n$ and compute successive directions towards the minimum

$$\boldsymbol{d}_k = -\nabla f(\boldsymbol{x}^k) \tag{3.111}$$

and

$$\alpha_k = \frac{\boldsymbol{d}_k^T \boldsymbol{d}_k}{\boldsymbol{d}_k^T \mathbf{A} \boldsymbol{d}_k} \tag{3.112}$$

until we obtain a minimum of f at

$$\boldsymbol{x}^{k+1} = \boldsymbol{x}^k + \alpha_k d_k. \tag{3.113}$$

This method is efficient for well-conditioned matrices, however successive direction may become almost parallel for a matrix $\mathbf{A}$ of large condition number $\kappa(\mathbf{A})$. This results in very slow convergence.

To ensure that successive direction do not become nearly-parallel we may choose them to be orthogonal in the metric dictated by $\mathbf{A}$. Directions $\boldsymbol{d}_k$ and $\boldsymbol{d}_{k+1}$ are $\mathbf{A}$-orthogonal if

$$\boldsymbol{d}_k^T \mathbf{A} \boldsymbol{d}_{k+1} = 0. \tag{3.114}$$

This conjugate gradient method ensures that the solution $\boldsymbol{x} = \mathbf{A}^{-1}\boldsymbol{b}$ for $\boldsymbol{x} = (x_1, x_2, ..., x_n)$ is obtained after at most n iterations. With a rate of convergence which depends on $\kappa(\mathbf{A}^2)$ Finally we may replace scalar products $\boldsymbol{u}^T\boldsymbol{v}$ by $\boldsymbol{u}^T\mathbf{A}\boldsymbol{v}$. This minimizes errors in the norm

$$||\boldsymbol{x}^k - \boldsymbol{x}||_A. \tag{3.115}$$

This is known as the minimum residual method and can be shown to converge with a rate proportional to $\kappa(\mathbf{A})$. In our calculations we use a generalized minimum residual method (GMRES), this relies on the fact that optimal convergence would be achieved if successive directions d_k were $\mathbf{A}$-orthogonal to all previous directions. The space of all such directions is known as the Krylov subspace [57]. In practice it is inefficient to orthogonalize against the whole Krylov space of dimension k and a maximum dimension is set a priori. We have used a freely available version of the GMRES solver which employs preconditioning and diagonal scaling [58]. We have so far used right preconditioning with the identity as a scaling marix. The maximum dimension of the Krylov space has been set in accordance with optimal values for micromagnetic calculations outlined in the work of other researchers [59].

3.4.3 Mesh Generation.

To generate our finite element meshes we the Triangle mesh generation package [60] in two dimensions and the Cubit mesh generation toolsuite [61] for three dimensional problems. Triangle is run from the command line and takes a planar line segment graph as input whereas cubit allows the creation of geometry by Boolean operations on primitives. Due to the fact that domain nucleation is intrinsically a consequence of magnetostatic energy, the quality of our simulations in multi-domain systems hinges on the quality of our magnetostatic calculation. This in turn is dictated by the quality of the finite element discretisation.

Mesh Quality.

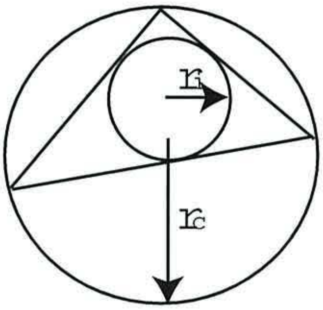

Figure 3.11: The beta aspect ratio of a triangular element.

Assuming the use of simplex elements, mesh quality in finite element models can be measured by the beta aspect ratio of the elements β. Which can be defined as the ratio of the radius of the circumcircle/circumsphere r_c to three times the radius of the inscribed circle/sphere r_i as depicted in figure 3.11.

$$\beta = \frac{r_i}{r_c}. \tag{3.116}$$

Acceptable values of β range between 1 and 3 [62], [63]. This is a consequence of the fact that *a priori* error estimators for the Poisson equation can always be derived directly in terms of β [43], [62]. As we have already discussed, due to the magnetostatic calculation we require a fine discretization within the magnetic region coupled to a coarse discretisation in the surrounding non-magnetic region if possible. The size of elements are constrained to be smaller than the exchange length within the magnetic region and unconstrained in the exterior. Also we constrain β to be between 1 and 3 in the magnetic region. In two dimensions a natural grading of the element size from the fine to coarse region was obtained directly from the mesh generator. This enabled us to obtain a good solution of ϕ with relatively few exterior elements. However our method became problematic in three dimensions. Here meshes obtained directly from the generator often contained large or long-thin elements spanning the exterior region and containing nodes from both the interface and the exterior boundary. This resulted in unacceptable errors in the scalar potential. As a remedy we introduced one or more mesh grading shells at intervals across the exterior region enabling us to stagger the transition between fine and coarse discretization and improve exterior mesh quality with respect to β. Thus we were able to obtain acceptable solutions, albeit at the expense of increasing the number of elements.

Mesh Topolgy.

The numerical values associated with the mesh, known as the mesh topology are stored in three files. The first is a list of nodes such as

1	0.001	0.001	0.001	1
2	0.001	0.001	−0.001	1
3	0.00073654	0.00062543	0.00074354	0
⋮	⋮	⋮	⋮	⋮

the lines are indexed by a global node number and each line consists of the cartesian coordinates for that node. The final column is used to store markers which denote nodes at which the Dirichlet condition is to be enforced. The second file consists of a list of elements such as

1	67	68	69	70	253	255	354	756	534	543	1
2	69	70	72	73	255	354	425	534	535	865	1
3	71	72	73	74	425	672	673	176	353	223	1
⋮	⋮	⋮	⋮⋮	⋮	⋮	⋮⋮	⋮	⋮			

here the lines are indexed by a global element number and each line consists of a list of quadratic nodes contained in that element, for the tetrahedron they are listed according to the ordering shown in figure 3.5. The final column is used to store a 1 or a 0 depending on whether the element is part of the magnetic or non-magnetic region. In simulations of polycrystalline media a non-zero value indicates an element within the magnetic region with the value identifying the grain number. Finally a list of boundary faces which comprise the interface between the magnetic and non-magnetic regions is stored in a third file. To remove any ambiguity the interior element to which the face belongs as well as the number of that face within the element must be stored.

3.4.4 Code structure.

This program takes an initial magnetisation configuration and evolves the system to equilibrium subject to given field and material parameters.

Equilibrium

1. Initialize
   - Read and store finite element mesh.
   - Compute element shape functions and store coefficients.
   - Set parameters from an input file: $\hat{\boldsymbol{e}}$, $\boldsymbol{h}_z$, A, M_s, K, α, ϵ.
   - Set GMRES parameters.
   - Initialize time $T = 0$
2. Assign magnetisation
   - Assign or read in the initial magnetisation configuration.
3. Matrix Build-up
   - Build-up stiffness matrix for the Poisson solver and assign coefficients to a static array.
   - Symbolic Build-up of the mass matrix for the Gilbert solver.
   - Store markers for elemental contributions to Gilbert matrix coefficients.
4. Dynamic loop
   - Build-up force vector for the Poisson solver.
   - Solve the Poisson equation.
   - Calculate coefficients of the Gilbert matrix and pass to dynamic array using markers.
   - Build-up force vector for the Gilbert solver.
   - Solve the Gilbert equation.
   - Output new magnetisation configuration.
   - Update time $T = T + 1$, $t = T\Delta t$.
   - If $d\boldsymbol{m}/dt > \epsilon$ return to 4.

5. End

Hysteresis simulations are performed using essentially the same code with an extra loop over the field steps.

Hysteresis

1. Initialize
2. Assign magnetisation.
3. Matrix Build-up.
4. Saturate magnetisation
    - $\boldsymbol{h}_z = 1.5$.
    - Dynamic loop.
5. Hysteresis loop
    - Reduce applied field.
    - Dynamic loop.
    - If $\boldsymbol{h}_z > -1.5$ return to 5.
6. End

3.4.5 Equilibrium and Tolerance.

Thermodynamic Equilibrium.

As we shall see in chapter 7 the notion of a magnetisation configuration at equilibrium is somewhat naive as magnetic moments are always subject to thermal fluctuations. However even in the athermal case the notion is problematic. We may define the equilibrium in a number of ways, firstly the configuration of the magnetisation may be regarded as stationary if $d\boldsymbol{m}/dt = 0$ everywhere. Alternatively no further change can occur if the torque $\boldsymbol{m} \times \boldsymbol{h}_{eff}$ vanishes. For simplicity we have considered the vanishing derivative to signal equilibrium. However it can be seen from a simple single-spin simulation that the spin will precess ever closer to the field but will never actually align with it exactly. By considering an ever greater number of decimal places in our value of the derivative we may continue to observe precession of the moment. This is because the notion of equilibrium is analogous to the mathematical notion of infinity, it is something to be approached rather than something to be reached. We therefore need to define a tolerance at which we can say that the derivative is negligible. From trial and error we have found that in all cases no significant change in magnetisation will occur once the maximum value of $d\boldsymbol{m}/d\tau$ at any node has fallen below 10^{-6}. This then serves as our value of ϵ above.

GMRES Tolerance.

We have found that to achieve convergence of the magnetisation to this equilibrium requires a tighter constraint on the tolerance of the GMRES solver. This is the value at which the residual can be regarded as minimized. Often we require it to be as low as 10^{-10} in order for sensible results to be obtained.

Chapter 4

Numerical Examples.

We now present some examples of calculations which can be performed using the method developed in the previous chapter. None of the following represents any new physics, we simply aim to show the diversity of problems which can be investigated and establish agreement with previous results. We give solutions of the magnetostatic calculation for three different geometries. That of the sphere gives agreement with the analytical solution whereas the cube and the general nano-element are calculations which can only be performed numerically. We then present some well known remenance states of a rectangular cobalt nano-element and proceed to investigate possible switching mechanisms. Finally we simulate the reversal of an individual cobalt grain and compare the properties of longitudinal versus perpendicular orientation.

4.1 The Magnetostatic field.

4.1.1 The Sphere.

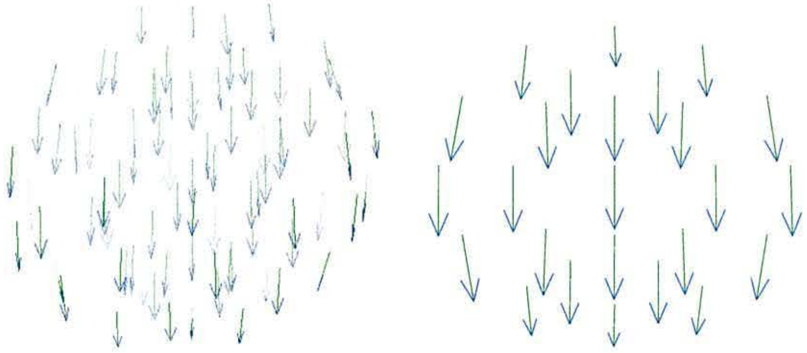

Figure 4.1: Magnetostatic field of a uniformly saturated sphere, calculated using a very coarse mesh $\Delta x \approx 500$nm. A Three dimensional image is shown on the left and a horizontal cross-section on the right.

From chapter 1 we know that the magnetostatic field within a uniformly saturated sphere is given by the scalar relation

$$H_d^{sphere}(\boldsymbol{M}) = \frac{4\pi M_s}{3} \tag{4.1}$$

within our model we solve for $\boldsymbol{H}_d = -\nabla\phi(\boldsymbol{m})$ and therefore expect

$$H_d^{sphere}(\boldsymbol{m}) = \frac{4\pi}{3}. \tag{4.2}$$

Due to this scalar relation we also expect that H_d^{sphere} will be uniform within the sphere. We now show some results of the magnetostatic calculation for a sphere of radius 1μm. The vector field calculated over a very coarse mesh is shown in figure 4.1. The calculation was performed with $\boldsymbol{m}$ uniformly saturated along the z-axis. It appears from the three dimensional image on the left that $\boldsymbol{H}_d$ is infact uniform, however on closer inspection we see that significant divergence exists near the boundary. Refining the mesh we obtain the images shown in figure 4.2. Clearly we have convergence towards a uniform state even with mesh sizes $1-2$ orders of magnitude less than those required for micromagnetic calculations. As well as field configuration it is also important that we calculate the magnitude of the field correctly. In figure 4.3 we plot the average magnitude of H_d^{sphere} for these calculations and for those with further mesh refinement.

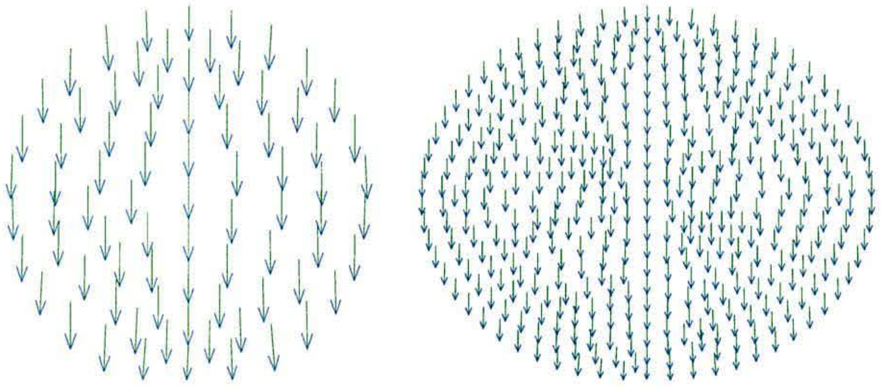

Figure 4.2: Repeated calculations with mesh refinement. $\Delta x \approx 250$nm (left) and $\Delta x \approx 100$nm.

4.1.2 The Cuboid.

Non-ellipsoidal geometry results in magnetostatic fields which are non-unifrom in both direction and magnitude as shown in figure 4.4. Here we show the calculated field for a 1μm cube. The field curls at the corners of the cube and can be seen to be much stronger there than in the interior. In the next section we will see that the field is in fact strong enough to cause magnetisation to rotate out of the easy-axis direction. This results in the so-called flower state. Here we see that the magnetostatic field is also dependent on the aspect ratio in cuboidal geometries. We see from rectangular cuboid on the right in figure 4.4 that the magnitude of field becomes very small at the center of the cuboid at an aspect ratio of $4:1$. In fact $\boldsymbol{H}_d$ at the center approches zero as the length of the long axis approaches infinity. An error analysis for the analogous two dimensional problem is given by Ridley *et al.* [64].

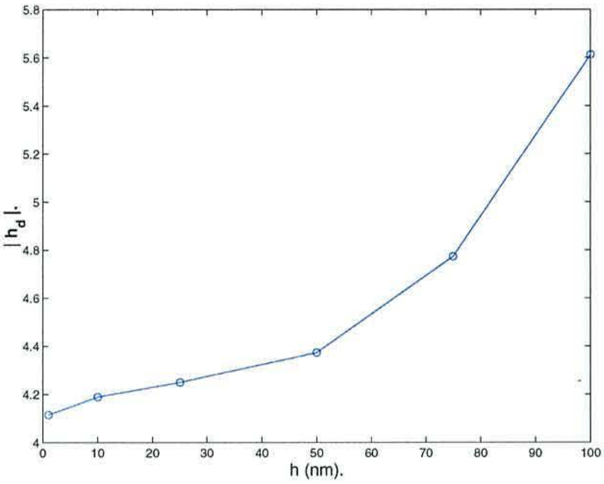

Figure 4.3: Convergence of the magnitude of H_d^{sphere} with mesh refinement.

4.2 Switching of Cobalt Nano-elements.

The investigation of so-called nano-elements is technologically important as they provide the basic memory elements of the patterned magnetic recording media discussed in chapter 1. The greatest technological challenge in developing such media is the manufacture of elements with a consistent remenance state which can be used to indicate whether a 0 or a 1 is being stored. Further the switching characteristics must be reproducible over many reversals and also consistent over the many elements of a memory array.

4.2.1 Remanence States.

As we saw in chapter 1 a strong remanece state must exist within a memory element in order for information to be re-read once it has been written. For this reason elements with a long aspect ratio are used in order to obtain two well defined equilibrium states which are anti-parallel along the length of the element. As shown in figure 4.5 the remanence value increases with increased aspect ratio. In this section we investigate some possible remenance states for a cobalt nano-element of dimensions $80 \times 25 \times 10\text{nm}^3$ surrounded by non-magnetic material. The remanence states are obtained by saturating the element along its long axis and then allowing the magnetisation to relax in zero field.

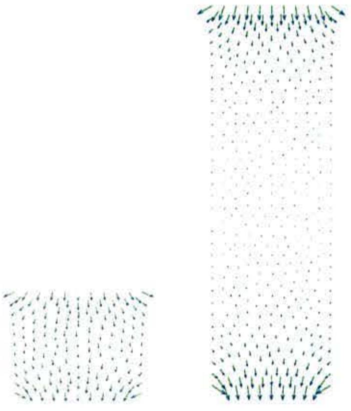

Figure 4.4: Magnetostatic field for a uniformly saturated cube (left) and rectangular cuboid (right).

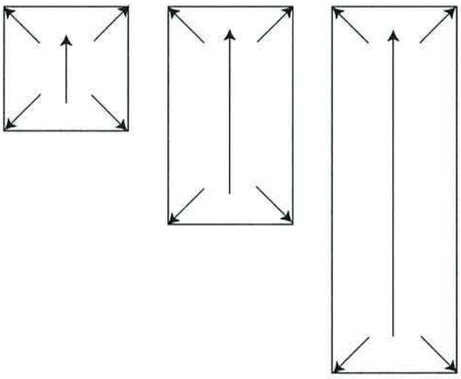

Figure 4.5: Remanence states of rectangular nano-elements.

The Flower State.

First we simulate an element which has an easy-axis aligned with the long axis. The three components of magnetisation are plotted in figure 4.6. Due to symmetry the magnetisation curls in a similar manner at all the corners of the element. This curling is due essentially to the magnetostatic field which is minimized when magnetisation is aligned with boundary surfaces, this results in the so-called flower state shown on the left in figure 4.7. This is a snap-shot of the magnetisation along a horizontal cross-section after 0.01ns of the relaxation. Eventually symmetry is broken and an anti-symmetric state is formed known as an S-state. This state is observed on the right in figure 4.7 at 0.1ns, here an equilibrium has been reached and no further

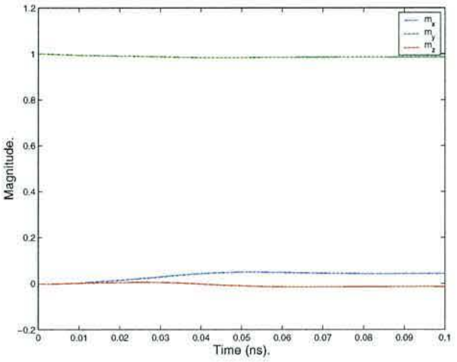

Figure 4.6: Components of magnetisation during relaxation to the flower state.

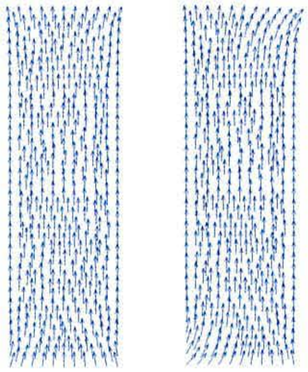

Figure 4.7: The flower state on the left and the S-state on the right.

change in magnetisation occurs. This is physically meaningful as the S-state has a lower energy than the flower state for this geometry; however it is not entirely clear how symmetry is broken within the numerical model.

The Curling State.

We now consider the case of a similar nano-element with an easy-axis perpendicular to the long axis. The relaxation now sees a far greater change in magnetisation with significant domain structures emerging. We see from figure 4.8 that precession of the magnetisation now has more of an effect, both the x and z component make an over-relaxation before returning to an equilibrium. The final equilibrium configuration is shown in figure 4.9. This sort of structure is known as magnetisation ripple and is attributed to conflict

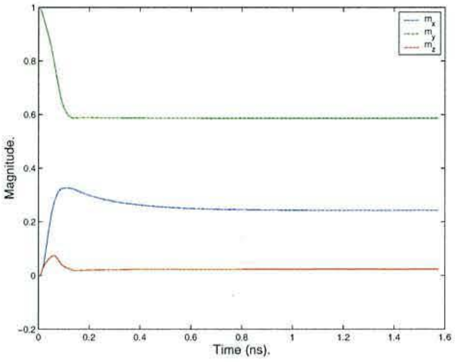

Figure 4.8: Components of magnetisation during relaxation to the curling state.

between shape anisotropy which would tend to make the magnetisation align with the long axis and magnetocrystalline anisotropy which would encourage alignment with the short axis.

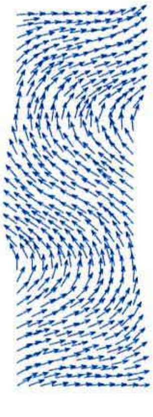

Figure 4.9: The curling state.

Breaking Symmetry.

Finally we consider the effects of artificially breaking the symmetry of the flower state. To achieve this we perform the relaxation from a slightly skewed initial saturation. These results are obtained with only a 1° skew over the element length. From average components of magnetization shown in figure 4.10 and the equilibrium configuration shown in figure 4.11 it seems that this makes little difference to the relaxation. However on closer inspection

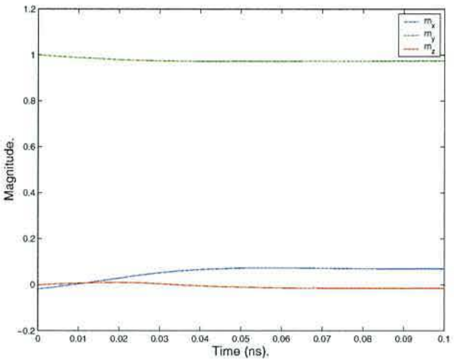

Figure 4.10: Relaxation from a skewed initial saturation.

it can be seen that the magnetisation at the ends of the particle are now slightly more aligned with the short axis than the S-state shown in figure 4.7. By inspecting the magnitude of $d\boldsymbol{m}/d\tau$ during the three relaxations in figure 4.12 we see that there is a substantial difference between relaxations from the symmetric and skewed initial saturations. With the symmetric saturation the flower state forms and the system approaches a metastable state until approximately 0.02ns when symmetry is broken and $d\boldsymbol{m}/d\tau$ rises once more. The skewed saturation on the other hand has a more direct path to equilibrium and consequently reaches an energy minimum some 50ps more quickly than the symmetric case. Since in applications the sides of the nano-element could never be made perfectly parallel with current fabrication

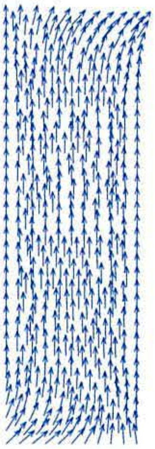

Figure 4.11: A stronger S-state.

techniques, the relaxation obtained from skewed saturation must be regarded as more realistic. The relaxation of the particle with easy-axis perpendicular to the saturation shows far more structure in the $dm/d\tau$ plot reflecting the more complex energy surface.

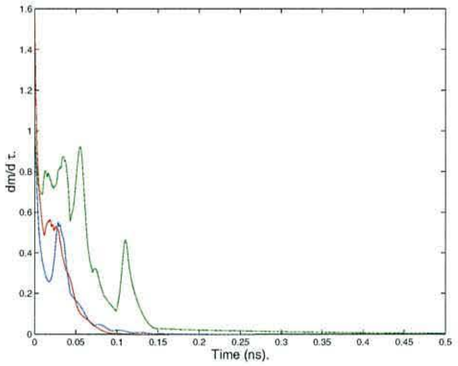

Figure 4.12: $dm/d\tau$ for the three states, that obtained from the symmetric parallel saturation in blue, the skewed parallel saturation in red and the perpendicular saturation in green.

4.2.2 Switching Mechanisms.

Numerical reversal experiments were then performed by the application of an external field of 9000Oe along the long axis of the particle starting from the three remanence states calculated in the previous section. By flower state we refer to the final equilibrium configuration of the symmetric saturation and by S-state we mean the state obtained from the skewed saturation. By observing the magnetisation configuration during the course of these three reversals we shall see domain nucleation and subsequent magnetisation reversal by the three most important switching mechanisms namely domain wall motion, coherent rotation and vortex motion. The easy-axis during these reversals remains the same as that used to obtain the remanence state in each case.

Switching from the Flower State.

The reversal from the flower state is shown in figure 4.13. Reversed domains nucleate at anti-symmetric corners of the element, separated from the remaining interior domain by magnetic swirls or vortices. At the center of these vortices a large out of plane component develops in the magnetisation. The vortices then pass through the width of the element leaving a so-called

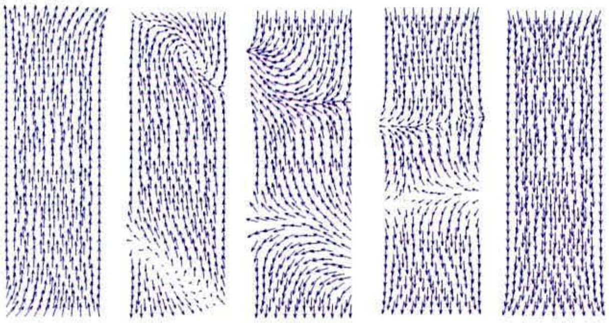

Figure 4.13: Switching from the flower state.

head to head domain wall in their wake. However it can be seen that this wall is nonuniform across the nano-element, during the motion of the wall a saddle structure passes along its length. Finally the walls meet at the center of the nano-element as the reversed domains expand at the expense of the interior domain.

Switching from the curling State.

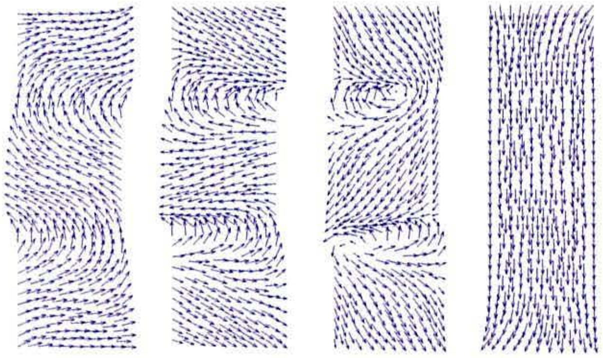

Figure 4.14: Switching from the curling state.

A markedly different mechanism is at work in the reversal experiment with transverse anisotropy. Here the magnetisation ripple observed at remenance develops into two vortices which nucleate at the edges of the nano-element and then migrate towards the center. The vortices which remain stationary at the center of the nano-element for some time form the boundaries between three domains. These domains remain coherent throughout the reversal and rotate into the direction of the applied field. By which time the vortices have passed through the width of the element.

Switching from the S-State.

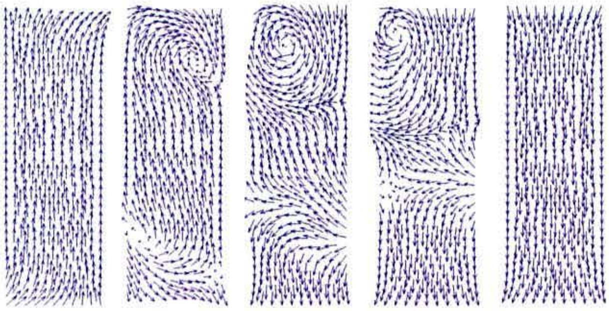

Figure 4.15: Switching from the S-state.

Figure 4.15 shows the reversal from the S-state. We now see further effects of the break in symmetry during relaxation. As with the flower state the reversal commences with the nucleation of anti-symmetric vortices near the ends of the nano-element. However due to slight skew (...very slight!) in magnetisation, the lower vortex migrates far more quickley across the nano-element. This leaves a head-to-head wall which begins to travel up the length of the nano-element while the upper vortex still occupies the central region. This example highlights the sensitivity of the reversal mechanism and illustrates the challenges in the development of MRAM elements with consistent switching properties.

4.3 Switching of Individual Cobalt Grains.

The results presented so far are important for validation of our computer model as they give agreement with previous numerical results for such idealized systems [65] and we have qualitative agreement with experimental results. The results are idealized in two fundamental ways. Firstly in applications cobalt is usually polycrystalline in nature made up of many irregular grains. Secondly our assumption of a uniform easy axis direction over the sample is unrealistic; in reality each grain has a distinct easy-axis with the orientations varying randomly from grain to grain in longitudinal media. As a first step in modelling such media we consider the reversal of an individual cobalt grain. In thin film cobalt media such as that used for magnetic recording the polycrystalline structure is generally continuous in the out of plane direction with an irregular lattice in the plane. Each grain can therefore be modelled by a deformed hexagonal prism, this is particularly realistic for cobalt which has a strongly hexagonal structure as we shall discuss in the next chapter. We consider a grain with a 20nm diameter and 20nm thickness which is typical of the grain size for the magnetic layer of hard disk media in current drives. The finite element discretization of the grain is shown in figure 4.16, again the size of the elements is constrained such that no element edge is longer than 2.5nm.

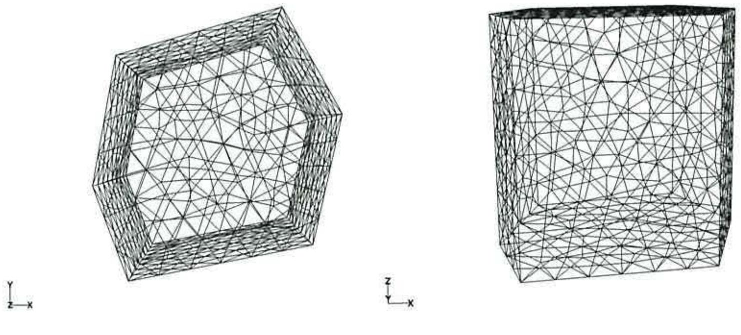

Figure 4.16: Spatial discretization of the cobalt grain. Showing a plan view (left) and front elevation (right).

4.3.1 Longitudinal Orientation.

In longitudinal recording media granular orientations, and therefore easy-axis directions, are randomly distributed in the plane. The combined easy directions then average to zero over the many grains which constitute a written bit. To model the reversal of a single grain we assume that bits are written along the y-axis and we define the easy-axis to be $\hat{\boldsymbol{e}} = (\sqrt{1/2}, \sqrt{1/2}, 0)$ so that the magnetisation is saturated half way between the hard and easy-axis. In a real film any orientation is equally likely, but this is a fair represenation of the general case. As before we allow the sample to relax in zero field and then apply a field of -9000Oe along the direction of initial saturation. In the remanence state on the left of figure 4.17 we see that the magnetisation has aligned with the easy axis direction in the interior of the grain with some curling at the corners due to magnetostatics. This gives a remenance of $m_r = 0.72$, this low value is due to the fact that the initial saturation is misaligned with both the easy-axis direction and with most of the edges of the grain. The reversal then proceeds by coherent rotation as shown in horizantal cross-section in figure 4.17.

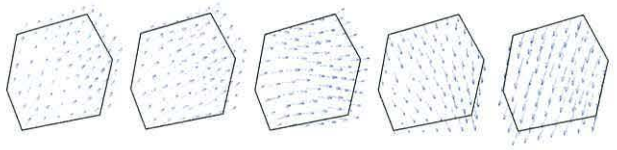

Figure 4.17: Switching mechanism of the longitudinal grain.

4.3.2 Perpendicular Orientation.

To model the reversal in a grain of perpendicular orientation we use the same mesh with both the initial saturation and easy-axis direction along the z-axis. Again the reversing field is applied anti-parallel to the initial saturation. In the perpendicular grain we have a stronger remanence state of $m_r = 0.96$ due to the fact that magnetisation is initially aligned with both the easy-axis direction as well as most physical axes of the grain. The greater stability of magnetisation in perpendicular grains is one of the major advantages of perpendicular magnetic recording media. The reversal mechanism is illustarted in vertical cross-section in figure 4.18. Again the reversal occurs by coherent rotation but we now see more pronounced curling of the magnetisation. This indicates that the grain is only just below the single domain limit for perpendicular orientation. These results are in qualitative agreement with those of Suess *et al.* where the single domain behaviour is observed in perpendicular of diameter 12nm when the grain height falls below 40nm [66].

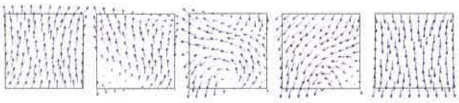

Figure 4.18: Switching mechanism of the perpendicular grain.

4.3.3 Slow reversal.

In order to obtain coercivity values for the grain in its respective orientations we perform simulations of the hysteresis experiment for both the longitudinal and perpendicular case. As explained in great detail elsewhere [15], [16], the square loop obtained from the perpendicular grain indicates much greater suitability as a magnetic recording media. However at this grain-size the perpendicular grain exhibits a lower coercivity value than the longitudinal case. This is explained by the less coherent magnetisation configurations in figure 4.18 as opposed to figure 4.17.

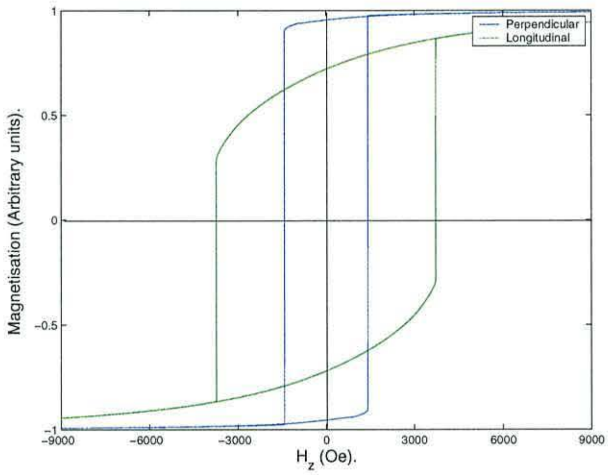

Figure 4.19: Hysteresis loops for the longitudinal and perpendicular grain of diameter 20nm.

4.3.4 Effects of Grain Size.

Finally we demonstrate a well known feature of polycrystalline thin films, namely the grain size dependence of coercivity. This result is the basis for much of the development in high density storage media. Figure 4.20 compares the hysteresis loops for the same grains as figure 4.19 but here the mesh has

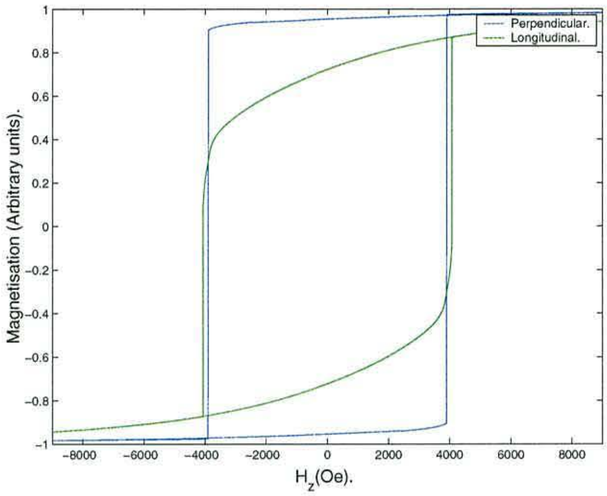

Figure 4.20: Hysteresis loops for a longitudinal and perpendicular grain of diameter 15nm.

been scaled to realize a reduction in grain diameter from 20 to 15nm while maintaining geometry and aspect ratio. As expected from previous numerical and experimental work this reduction in grain size results in an increase in coercivity in both cases. This increase is marginal in the longitudinal case but substantial in the perpendicular case. The grain size is now below the critical single domain limit for both perpendicular as well as longitudinal orientations resulting in comparable values of the coercivity. Perpendicular grains below the single domain limit therefore possess both the sort after qualities of high remenance and high coercivity. This is a good example of the manner in which micromagnetics may be used in order to investigate the switching properties of magnetic media, paving the way for experimental investigations and assisting in the interpretation of experimental results. The challenge is now to perform simulations of thin film media consisting of many thousands of such grains. Development and optimization of the magnetic properties for applications can then be performed computationally as well as experimentally.

Chapter 5

Thin Film Simulations.

In this chapter we apply the method derived in chapter 3 and illustrated in chapter 4 to the simulation of magnetisation dynamics within a continuous thin film. First we develop an algorithm with which to generate a realistic physical model of the microstructure of polycrystalline thin film. This model is based on the Voronoi tessellation of a random planar point set. We then discuss methods of solving open boundary problems and illustrate the use of implicit periodic boundary conditions for the Poisson problem. Progressing to the open boundary problem we consider solutions of the magnetostatic calculation on an infinite periodic extension of a two dimensional array of cobalt grains. Solving the Gilbert equation over this region then gives a model of magnetisation dynamics within an infinite thin film. Solutions for uniformly oriented grains recover those of the Stoner-Wohlfarth model. This is to be expected since within a uniformly saturated infinite two dimensional film no surface charges exist and therefore the magnetostatic field is everywhere zero. Likewise the vanishing exchange energy allows the spins to act independently, which of course means they act coherently for uniform anisotropy. Repeating the simulations with random granular orientations results in realistic magnetisation ripple structures at remanence and hysteresis curves which are qualitatively in agreement with experiment. Interesting questions are raised as to how big the parent ensemble of the periodic region should be in order obtain quantitative agreement with experiment.

5.1 Microstructure Model.

Having developed our micromagnetic model we wish to apply our work in the simulation of polycrystalline thin film media. The imaging of such films has been the subject of much recent work [67]. Consequently we have a very good idea of how the films form and the geometry of the resulting grain structure. It has also become clear from experimental work that magnetic properties of thin films are closely related to the microscopic physical structure. As discussed in chapter 1, once thin films are deposited drying commences from random nucleation points forming a stochastic geometry in the plane. Post-deposition annealing then results in a straightening of grain boundaries to give a roughly hexagonal polycrystalline grain structure. To simulate this geometry we employ the Voronoi tessellation which is a common model for stochastic geometries and arrival time dependent partitions.

5.1.1 The Voronoi Tessellation.

The Voronoi tessellation or Voronoi diagram is defined as a partitioning of R^n associated with a given set of points $P \subset \mathbb{R}^n$ [68]. Each Voronoi partition or Voronoi cell $V(p_i)$ is defined as the region of $\mathbb{R}^n$ which is closer to point p_i than any other point in P. In two dimensions it may also be defined as the dual of the Delauney triangulation of the given point set. This simple tessellation has a multitude of applications; for example the British post office use such a tessellation in the allocation of post codes. Our application is to generate the in-plane structure of polycrystalline thin films such as those discussed above. Before discussing the generation of the point-set or seed set $P = \{p_i\}$ we give a more formal definition of the planar Voronoi tessellation.

Planar Ordinary Voronoi Diagrams.

Let $P = \{p_1, p_2, ..., p_n\}$ be a set of n distinct points in the plane. With $2 \leq n < \infty$ and $\boldsymbol{x}_i \neq \boldsymbol{x}_j$ for $i \neq j$, where $\boldsymbol{x}_i$ is the position vector of p_i. Then the (ordinary) Voronoi polygon associated with p_i is formally defined as the region given by

$$V(p_i) = (\boldsymbol{x} : ||\boldsymbol{x} - \boldsymbol{x}_i|| \leq ||\boldsymbol{x} - \boldsymbol{x}_j||,\ i \neq j) \tag{5.1}$$

Also, when $P \subset \mathbb{R}$ the planar ordinary Voronoi diagram generated by P is the set given by

$$\mathcal{V}(P) = \{V(p_1), V(p_2), ..., V(p_n)\}.$$

Some observations concerning this type of structure are listed below

- Under this definition all $V(p_i)$ are closed sets.
- Some points are elements of more than one Voronoi polygon, these points form the boundaries of the polygons.
- Polygons only overlap at their boundary, $\partial V(p_i)$.
- The set of polygons is collectively exhaustive and mutually exclusive apart from at boundaries i.e. $\mathcal{V}$ forms a tessellation.
- Voronoi edges may be line segments, a half line or an infinite line shared by two Voronoi polygons i.e.

  $$e(p_i, p_j) = V(p_i) \bigcap V(p_j).$$

  This set may be empty or may degenerate into a point, otherwise we say that $V(p_i)$ and $V(p_j)$ are adjacent.
- A Voronoi vertex q_i may be defined as a point shared by three or more Voronoi polygons.

Degeneracy. A Voronoi diagram is said to be degenerate when there exists at least one vertex at which four or more Voronoi edges meet. A degenerate Voronoi diagram often appears when the generator points are regularly spaced. We shall assume that every vertex in the Voronoi diagram has exactly three edges. This is known as the non-degeneracy assumption. In practice this can always be achieved when generating a lattice for purposes such as ours.

Planar ordinary Voronoi diagram defined with half-planes. Let $P = \{p_1, p_2, ..., p_n\} \subset \mathbb{R}^2$, with $2 \leq n < \infty$ and $\boldsymbol{x}_i \neq \boldsymbol{x}_j$ for $i \neq j$. Then the ordinary Voronoi polygon associated with p_i is given by

$$V(p_i) = \bigcap_{j \neq i} \mathcal{H}(p_i, p_j)$$

where $\mathcal{H}(p_i, p_j)$, the dominance region of p_i over p_j, is given by

$$\mathcal{H}(p_i, p_j) = (\boldsymbol{x} : \|\boldsymbol{x} - \boldsymbol{x}_i\| \leq \|\boldsymbol{x} - \boldsymbol{x}_j\|, \quad j \neq i).$$

This is the region to one side of the bisector of p_i and p_j

$$b(p_i, p_j) = (\boldsymbol{x} : \|\boldsymbol{x} - \boldsymbol{x}_i\| = \|\boldsymbol{x} - \boldsymbol{x}_j\|).$$

Again the planar ordinary Voronoi diagram generated by P is the set

$$\mathcal{V}(P) = \{V(p_1), \ldots\ldots, V(p_n)\}.$$

The equivalence of the two definitions is clear, for $i \neq j$

$$\|\boldsymbol{x} - \boldsymbol{x}_i\| \leq \|\boldsymbol{x} - \boldsymbol{x}_j\| \iff \boldsymbol{x} \in \mathcal{H}(p_i, p_j).$$

This definition is more suitable for implementation as a computer program. However a naive algorithm constructed from the definitions given above would be computationally costly as well as prone to ambiguities at vertices caused by numerical errors. However, due to the multitude of applications for this tessellation there has been substantial research into efficient algorithms with which to generate them. The most widely used are the incremental method, the divide-and-conquer method and the plane sweep method [69]. Our Voronoi generator uses a version of the sweep method.

Edge-effects. Assuming that an algorithm has been developed for generating a large, suitably dense, number of points inside a bounded region, we still have a further complication. No matter how large $\mathcal{V}(P)$ is, allowance must be made for edge-effects introduced by those cells on the boundary. All such cells are either infinite in area with two edges which are infinitely long rays or they consist of truncated versions of the above intersecting with the boundary. One way around this is to exclude from consideration any cells for which a circle, centered at any vertex of a cell and passing through the three seed points which are equidistant from that vertex, intersects the boundary. Alternatively, if the boundary region is a rectangle, additional points may be created outside of each boundary edge which are translates of elements of P inside the opposite edge of the rectangle. The translated points can then be used to complete the polygons of those points of $\mathcal{V}(P)$ whose polygons intersect the boundary. The later method, which is equivalent to converting the rectangular region into a torus, is usually referred to as a periodic boundary condition. It has the advantage that an infinity of computational platelets may be interlocked to give a region which extends indefinitely in all directions. Since we will be employing periodic boundary conditions within our micromagnetic model, we require a periodic geometry and the second method is naturally applied.

Computational Algorithm.

We shall be concerned with modelling the grains of a pure cobalt thin film and therefore require a strongly hexagonal grain structure. After generating

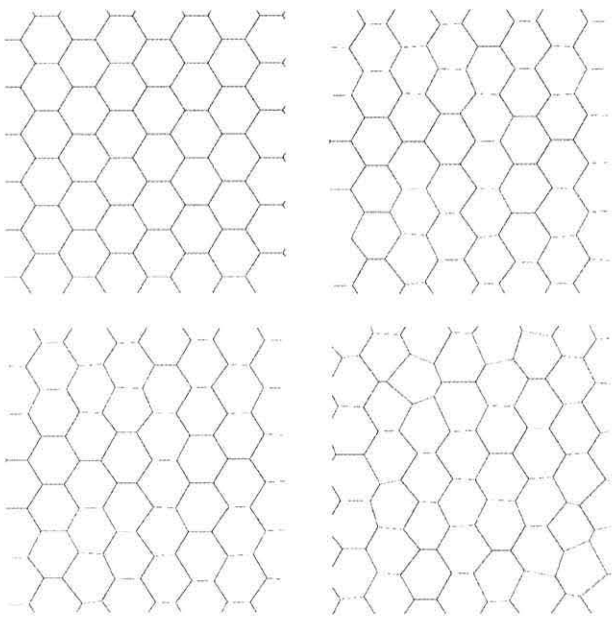

Figure 5.1: Examples of grain structure with increasing irregularity.

Voronoi diagrams from a standard Poisson point process we found that very irregular and unrealistic structures were obtained. We therefore developed a simple algorithm with which to generate a geometry which consists of a deformed hexagonal lattice. The algorithm is outlined below:

1. Store a set of points whose Voronoi diagram is a planar hexagonal array.
2. Take a random walk from each point in the set.
3. Apply periodic boundary conditions if required.
4. Recompute the Voronoi diagram of the deformed point set.
5. Store the Voronoi cells whose seed points fall inside the chosen geometry.

By controlling the time and step size of the random walk grain structures of arbitrary irregularity may be generated. Four such structures are illustrated in figure 5.1, ranging from the hexagonal array with zero deviation in grain size to a pseudo random Voronoi structure as would be obtained from a Poisson point set. The mean grain size is maintained in all four examples since the area is partitioned into the same number of cells in each case. An example with periodic boundary conditions is shown in figure 5.2. A unique

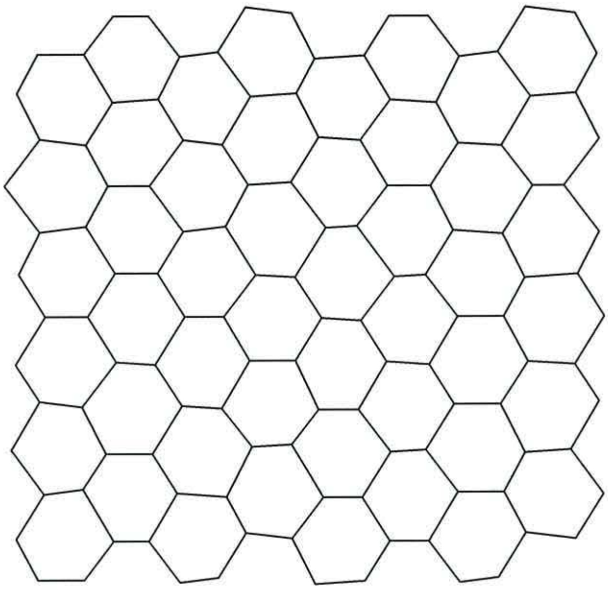

Figure 5.2: An example of grain structure with periodic boundary conditions.

randomly chosen orientation of the easy-axis is assigned to each grain in the micromagnetic model.

Grain Boundaries.

Our model has one distinct limitation, namely the description of the grain boundaries. These are modelled as the edges of the Voronoi cells which have no thickness whereas in real thin films the grain boundary has a finite thickness of several atomic layers over which the lattice orientation changes from that of one grain to the next. Although the grains could be physically separated as in other micromagnetic models [42], [70] it was decided that meshing within a finite grain boundary would not be computationally feasible. We therefore decided that all boundary integrals of the micromagnetic formulation should be evaluated at the grain boundary and the easy-axes of adjacent grains should be averaged there.

5.2 The Open Boundary Problem.

Numerical simulation of magnetisation dynamics in thin film media is nontrivial due to the fact that numerical methods such as finite element analysis require a bounded computational region over which to perform calculations in finite dimensional space. Appropriate boundary conditions must then be enforced depending on the physics of the system, mathematically they are also necessary in order to remove indeterminacies which correspond to rigid body motions or deformations of the system. These otherwise manifest themselves as matrix singularities which prevent us from solving the system of linear equations. Accordingly a non-magnetic interface is usually defined at the boundary of the discretization which allows suitable conditions to be enforced. The more complex problem of studying magnetisation dynamics in continuous thin films has received little rigorous attention. At the relevant length scale, the computational region in such systems may be regarded as infinitely far from the boundary of the magnetic region. The problem is sometimes resolved using replicas of the computational region surrounding the central cell to create effective periodic boundary conditions [9]. The imaged regions are used to calculate the interaction fields acting upon the central region. The magnetic moments in the replica cells are then updated after every time step in the dynamic simulation. This approach has been very successful in modelling the magnetisation dynamics in polycrystalline thin films where the magnetisation is assumed homogeneous within each grain and may therefore be represented by a single magnetic moment. However it has recently become apparent that quantitative micromagnetic modelling requires discretization at the sub-grain level [71], [72]. It is therefore difficult to see how these methods could be applied to formal numerical calculations. To enforce appropriate boundary conditions, the magnetisation over the whole region must be resolved at each time-step and this becomes computationally intensive for systems of a reasonable size. The minimum image convention adopted by [9], although successfully applied to arrays of Stoner-Wolhfarth particles, appears meaningless in the context of a finite element calculation.

Methods for solving open boundary problems via the finite element method are well established [73]. Indeed various methods exist for the calculation of electromagnetic fields exterior to a magnetic region. (i) The exterior region may be truncated to approximate the infinite domain by a sufficiently large closed domain which is the method we have successfully employed in the calculation of magnetostatic fields. (ii) The use of infinite or mapped elements [74]. (iii) Hybrid finite element/boundary element methods have been used to calculate magnetostatic fields within a magnetic region without the need to perform a discretization of the exterior region [51]; this method has the advantage of significantly reducing the computational region, although it does lead to a fully populated stiffness matrix. (iv) Finally transformations may be used to map the infinite open region to a closed domain [75], [76]. All these methods provide a means to deal with the infinite external region in electromagnetic computations, but cannot in general be applied to modelling an open magnetic region. We now develop a simple method with which to model the micromagnetic behaviour of an infinite thin film using implicit periodic boundary conditions.

5.3 Implicit Periodic Boundary Conditions.

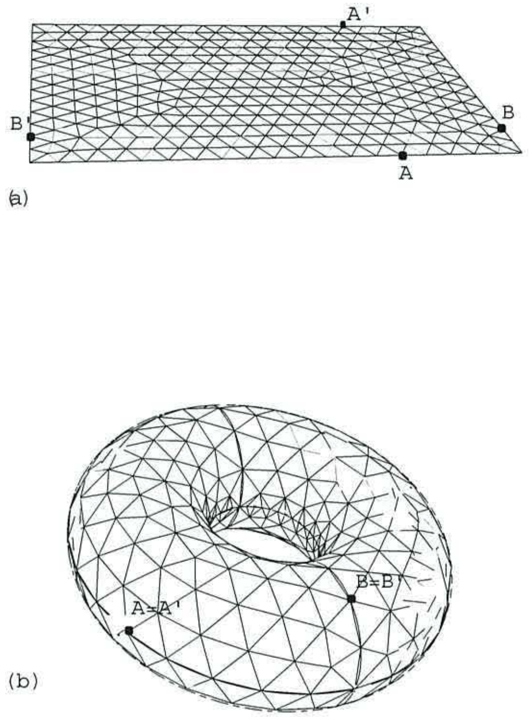

Figure 5.3: (a) Finite element discretization and (b) periodic mesh topology.

In this chapter we employ a two dimensional discretization with triangular elements, again with linear interpolation of magnetisation and quadratic interpolation of the scalar potential

$$\boldsymbol{m} = \sum_{i=1}^{3} L_i \boldsymbol{m}_i \tag{5.2}$$

$$\phi = \sum_{i=1}^{6} N_i \phi_i \tag{5.3}$$

The calculation follows essentially the same method as that outlined for the three dimensional element in chapter 3. First consider the magnetostatic calculation. To obtain an infinite periodic extension of Ω_{int} we enforce implicit periodic boundary conditions at $\partial\Omega$ which is achieved by associating geometrically opposite nodes on $\partial\Omega$ with the same linear equation in the variational formulation of the Poisson equation. These are then effectively the same node and the linear equation corresponding to one of them may be removed. With no explicit enforcment of any boundary conditions we enforce $\phi_i = \phi_{i'}$ for all nodes $i, i' \in \partial\Omega$ such as A, A' and B, B' in figure 5.3. Similarly $\boldsymbol{m}_i = \boldsymbol{m}_{i'}$ is implicitly enforced in the dynamic calculation. As we can see from figure 5.3, this is topologically equivalent to working on a torus, a finite two dimensional region with no external boundary. The dynamic calculations may then proceed as before and the magnetostatic calculation consists simply of a Galerkin minimization of the Poisson equation over Ω_{int}. Although no explicit boundary conditions have yet been enforced the periodicity will clearly constrain the solution in some way. In fact the periodic boundary conditions are sufficient to remove indeterminacies or equivalently to remove matrix singularities corresponding to deformation and spatial translation from the resulting linear equations. The remaining matrix singularity, corresponding to rigid body motion of the solution along the ϕ axis, may be removed by enforcing a Dirichlet condition $\phi = \phi_D$ at a single node of the discretization. This allows the linear equations to be solved and effectively fixes the solution. The value we choose is unimportant as we require the gradient of the potential rather than the potential itself and clearly $\boldsymbol{H}_d = -\nabla\phi$ is invariant with respect to ϕ_D so for simplicity we choose $\phi_D = 0$.

5.3.1 The Poisson equation on a Torus.

To investigate the convergence of the Poisson solver we take a hypothetical periodic magnetisation distribution with sinusoidal divergence of period 2π, so that ϕ satisfies

$$-\nabla^2\phi = \sin(x)\sin(y) \tag{5.4}$$

over $[0, 2\pi] \times [0, 2\pi]$. Enforcing $\phi_D = 0$ at (π, π), the potential may then be compared with the exact solution

$$\hat{\phi} = \frac{1}{2}\sin(x)\sin(y). \tag{5.5}$$

Figure 5.4 illustrates the point that for our magnetostatic calculation the value of ϕ_D is irrelevant because the gradient of the potential is the same in all cases. The solution is merely shifted up or down the ϕ-axis accordingly. Plots

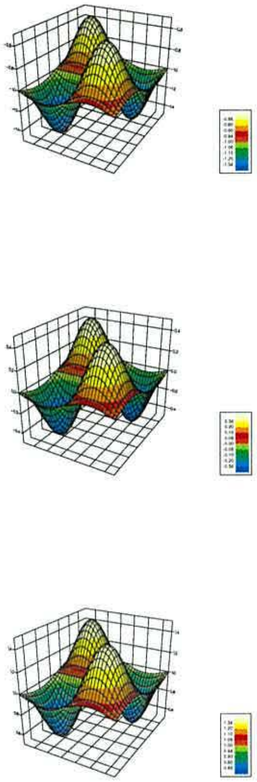

Figure 5.4: Solutions of $-\nabla^2\phi = \sin(x)\sin(y)$ for $\phi_D = -1$ (top), $\phi_D = 0$ (middle) and $\phi_D = 1$ (bottom).

of the error in the L_2 and energy norm versus mesh size are shown in figure 5.5 for $\phi_D = 0$ fixed at (π, π). This solution is naturally periodic and since we have chosen a domain to coincide with the period and boundaries $(x, 0)$, $(x, 2\pi)$, $(0, y)$, $2\pi, y)$ at which ϕ is naturally zero; the periodic boundary conditions should have no effect. Indeed for the meshes we have considered these curves are indistinguishable from those obtained by a conventional Poisson solver with $\phi = 0$ enforced at all nodes on the boundary.

5.3.2 Periodic Magnetostatics.

It is then straight-forward to employ the periodic Poisson solver in our magnetostatic calculation. For a uniformly saturated two dimensional film we

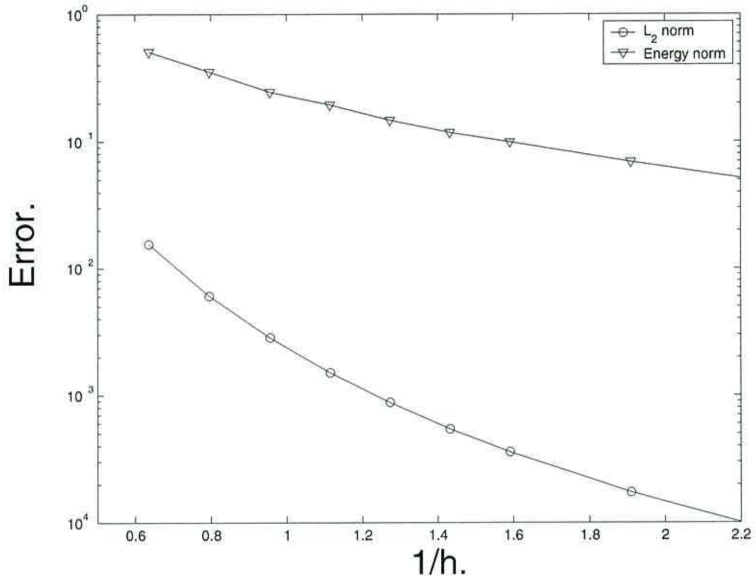

Figure 5.5: Convergence of periodic Poisson solver.

have no surface charges and as expected the magnetostatic field is zero everywhere. This is a fair asymptotic representation of the field which naturally tends to zero as the extent of the film tends to infinity. For non-uniform magnetisation configurations we observe the familiar dipole configuration. Figure 5.6 shows $\boldsymbol{h}_d$ for negatively saturated grain embedded in a film which is otherwise saturated in the positive direction. Figure 5.7 shows the effect of saturating the grain perpendicular to the surrounding film. Here the field aligns at 45° between the magnetisation inside the grain and that outside, giving closure of the flux lines $\boldsymbol{B} = \boldsymbol{H}_d + 4\pi\boldsymbol{M}$. By instead saturating the bottom left grain in the reverse direction we can better see the transparency of the periodic boundary, the corresponding $\boldsymbol{h}_d$ configuration is shown in figure 5.8. Finally figure 5.9 shows $\boldsymbol{h}_d$ for two mis-aligned grains in an otherwise saturated film, resulting in dipole-dipole interactions between grains as expected.. The closure of the flux lines is again clear and so too is the transparency of the periodic boundary.

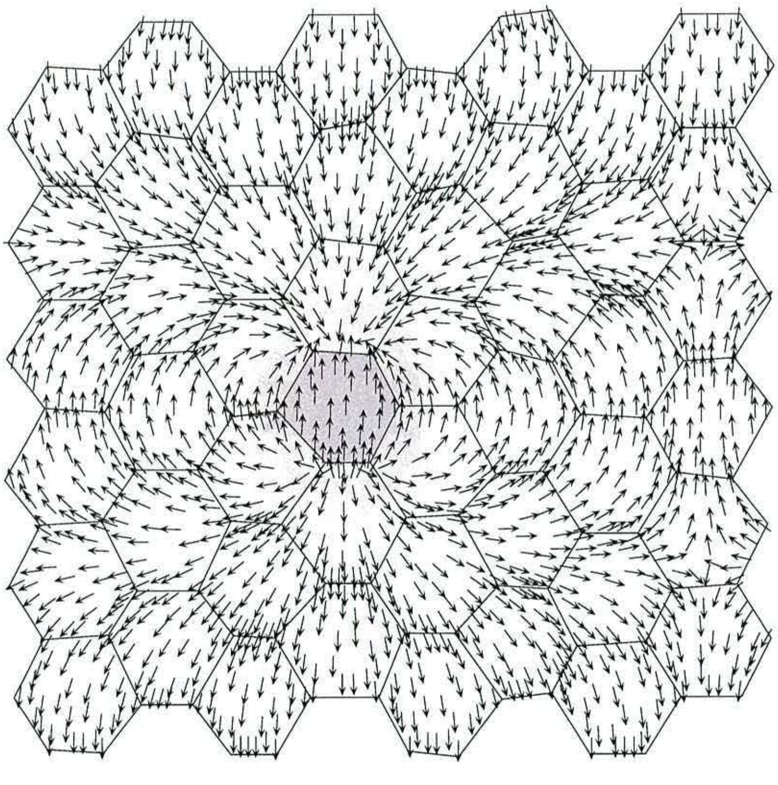

Figure 5.6: $\boldsymbol{h}_d$ for a grain of anti-parallel magnetisation in an otherwise saturated film.

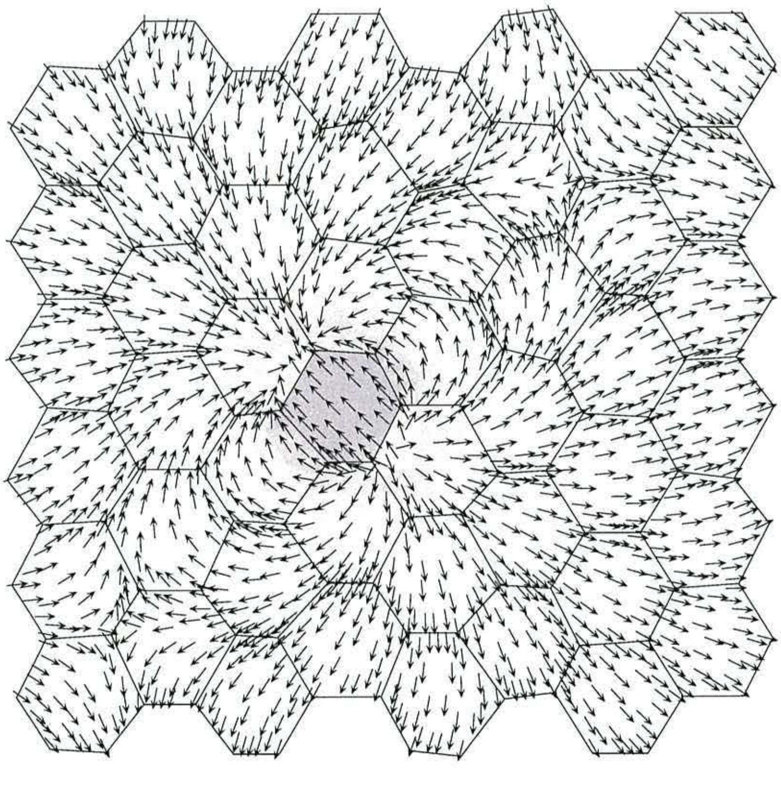

Figure 5.7: $\boldsymbol{h}_d$ for a grain of perpendicular magnetisation in an otherwise saturated film.

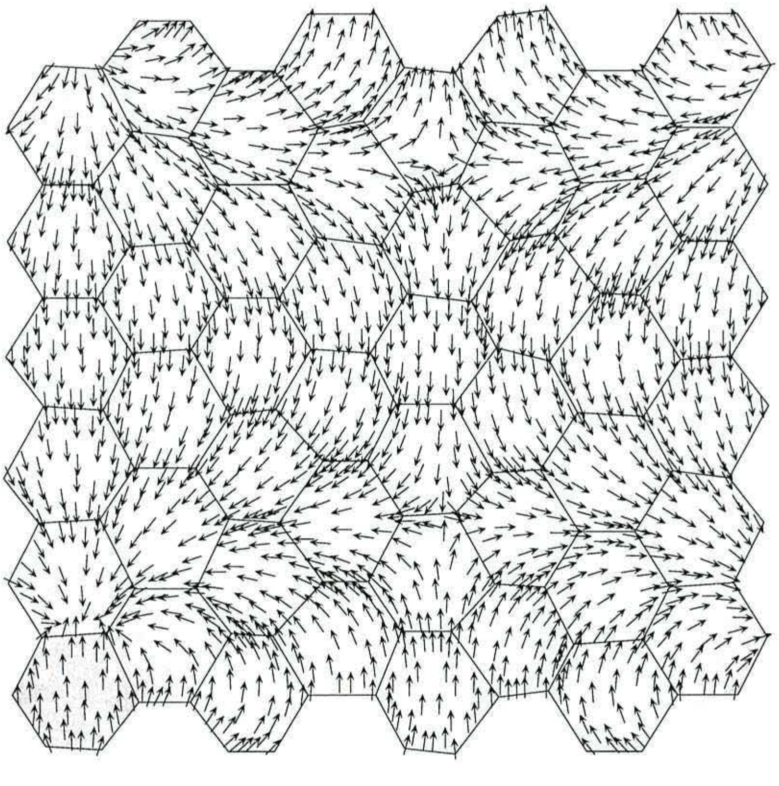

Figure 5.8: The effect of assigning a reverse saturation to the grain in the bottom-left corner of the computational region.

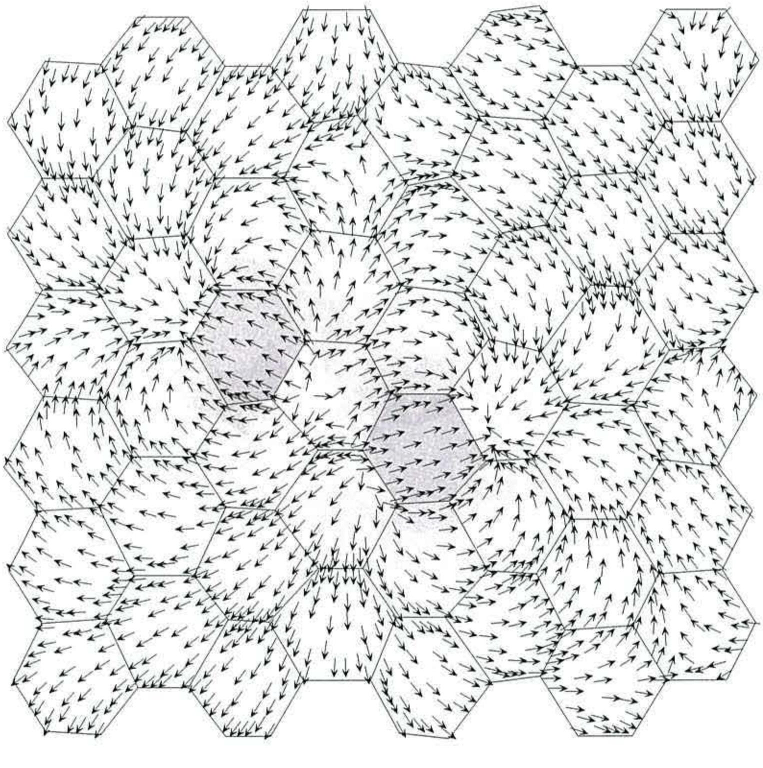

Figure 5.9: Dipole-dipole interaction between two mis-aligned grains.

5.4 Dynamic Simulations.

5.4.1 Uniform Anisotropy.

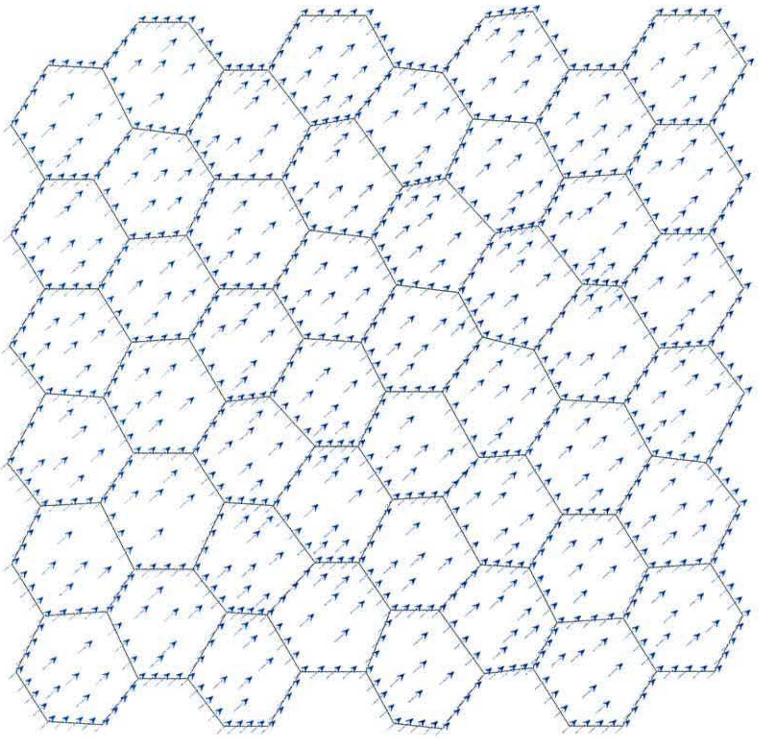

Figure 5.10: Remanence configuration with $\hat{\boldsymbol{e}} = (\sqrt{1/2}, \sqrt{1/2})$.

The dynamic computation is unaffected by the periodic boundary; nodes on the boundary are no different from nodes in the interior of the computational region. As a simple test of the code we consider magnetisation dynamics over the array of 20nm grains shown previously with uniform granular orientations. This admits the simple prediction that performing a relaxation from a uniform saturation along the y-axis with uniform anisotropy will result in $\boldsymbol{h}_d$ and $\boldsymbol{h}_{ex}$ remaining at zero throughout the simulation. Magnetisation at each node will therefore act independently. Since they will all experience the same anisotropy field, they will therefore act coherently. With $\hat{\boldsymbol{e}} = (\sqrt{1/2}, \sqrt{1/2})$ we observe the remanence configuration shown in figure 5.10. With nothing to cause inhomogeneities in the magnetisation, the spins simply align with the easy-axis direction. Figure 5.11 shows hysteresis loops of the same film for various orientaions of $\hat{\boldsymbol{e}}$. In each case the reversal occurs by coherent rotation of the magnetisation from the saturated state. Again the magnetostatic and exchange interactions remain negligible during these simulations and we recover hysteresis curves as predicted by the single-spin Stoner-Wohlfarth model [32].

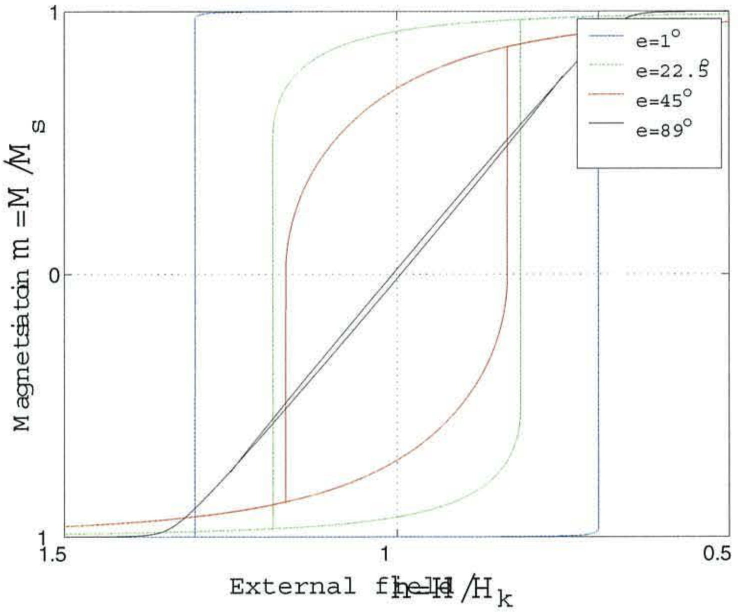

Figure 5.11: Hysteresis curves of a uniformly oriented thin film for various $\hat{e}$.

5.4.2 Random Anisotropy.

In reality of course, polycrystalline thin films are known to have randomly oriented grains. We therefore assign a unique easy axis to each grain, randomly chosen from a uniform distribution across the half-circle. Over the film the easy-axes then cancel each other and the net anisotropy is zero. As before we have used a Gilbert damping parameter of $\alpha = 1$ in these results, a discussion of variable damping will be given in chapter 8. Saturating the film along the y-direction and allowing the magnetisation to relax in zero field we obtain the remanence configuration shown in figure 5.12. As expected from experimental images of the remanent state in such films the magnetisation relaxes to a wave-like structure known as magnetisation ripple. This structure must be attributed to the net effects of exchange interactions which encourage the magnetisation to remain in the saturated state and the local magnetocrystalline anisotropy which favours relaxation to the

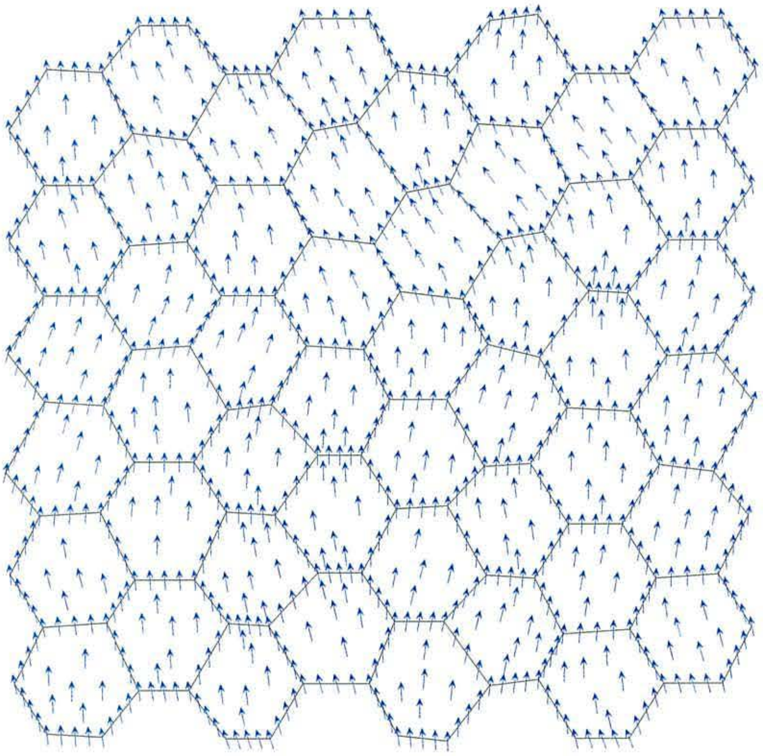

Figure 5.12: Remenance configuration with $\hat{\boldsymbol{e}}$ randomly assigned in each grain.

easy-axis within each grain. Once the homogeneity of magnetisation is broken the magnetostatic field becomes non-zero and causes shape anisotropy within each grain. Performing a hysteresis simulation in the usual manner we observe a reversal by vortex nucleation and subsequent expansion of reversed domains. This contests the often quoted assumption that domains must nucleate at defects in the sample or at edge irregularities on the sample boundary. Here we have no defects and no boundary yet vortices may be observed in the magnetisation configuration at coercivity illustrated in figure 5.13. As we saw in figure 5.9 dipole-dipole interactions exist between the grains and in figure 5.12 we see that non-uniform magnetisation exists at remanence. Curling of the magnetisation due to the magnetostatic field is then the only explanation of vortex nucleation in this model. The hysteresis loop is plotted in figure 5.14. Here we see further evidence of nucleation with the curve falling below the saturation magnetisation well before the coercive field is reached, indicating that irreversible magnetisation processes are occuring prior to switching.

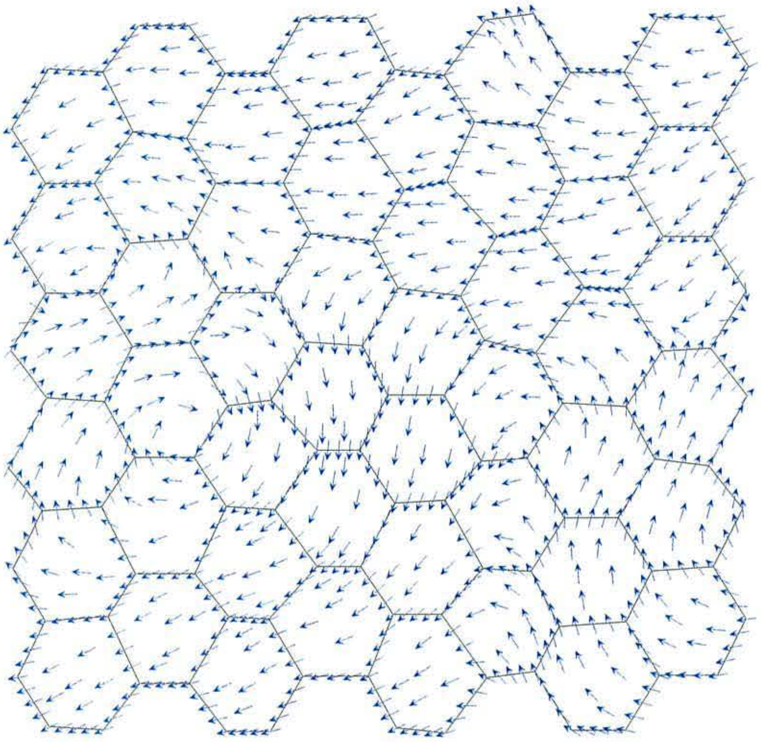

Figure 5.13: Magnetisation configuration at coercivity with $\hat{\boldsymbol{e}}$ randomly assigned in each grain.

5.4.3 Grain Size Effects.

Subsequently hysteresis simulations were performed with films of lower grain sizes. These were performed by geometric scaling of the finite element mesh to achive the desired grain size as in the previous chapter. Coercive states of the magnetisation for grain diameters of 10nm and 15nm are shown in figures 5.16 and 5.15. Here we see a transition to more coherent magnetisation as grain size decreases. This can be explained by noticing that magnetisation was less homogeneous within individual grains in the 20nm case. As grain size decreases the magnetisation is more strongly pinned because the smaller grains aproaching the single domain limit ensure that a vortex or domain wall cannot pass without reversing the grain as a whole. This is reflected in the increasing squareness of the hysteresis loops with decreasing grain size as shown in figures 5.18 and 5.17

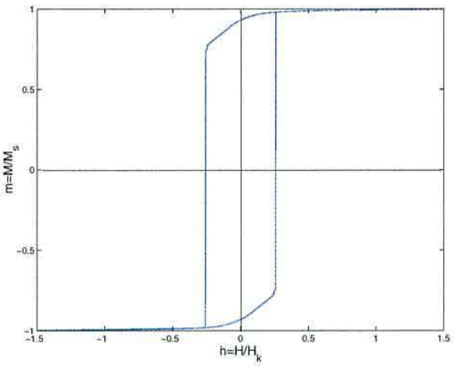

Figure 5.14: Hysteresis loop for randomly oriented 20nm grains.

5.4.4 Physical Acceptability.

With this model we have been successful in predicting a transition to increased uniformity of magnetisation with decreasing grain size as well as increased loop-squareness. Although these predictions are in agreement with experiment [77], there are two fundamental flaws in these results. Firstly we have predicted that $\boldsymbol{h}_c$ will decrease with decreasing grain size. This is in contradiction to accepted experimental findings [77] and indeed contradicts our results from the previous chapter. Secondly all of the calculated coercivities are rather lower than would be expected [78]. This second point may be explained by the fact that grains are strongly exchange coupled whereas at physical grain boundaries the exchange decoupling may be more severe. This is a possibly recoverable modelling error. The incorrect prediction of coercivity dependence on grain size is however more of a problem. This suggests that scaling the mesh to achieve smaller grain size is instrumental in lowering $\boldsymbol{h}_c$ and hence that our model is sensitive to the size of the computational region under consideration. Experimental results can be found to support such behaviour [79], however we feel that this is the exception that proves the rule. Although we are clearly modelling an infinite film, the constraints imposed on the magnetisation by the periodic boundary conditions appear to be too restrictive. Although this could be rectified by using a much larger ensemble of grains, deciding on the number necessary to remove this artifact could form the basis of an entire PhD project in its own right. A decision was therefore made to pursue the modelling of individual cobalt grains and nano-particles where our model has had more success. Thus giving us time to investigate the numerical stability of the problem and to consider the incorporation of thermal effects into the model.

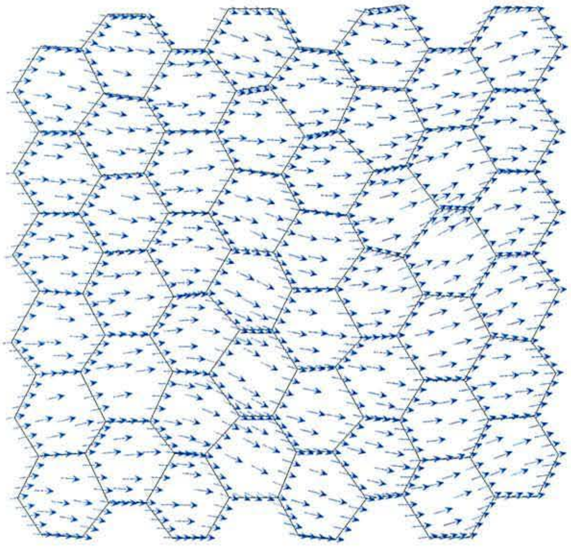

Figure 5.15: Magnetisation configuration at coercivity with $\hat{e}$ randomly assigned in each 15nm grain.

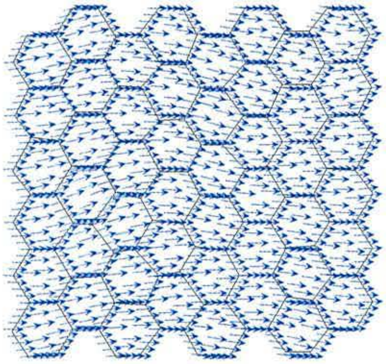

Figure 5.16: Magnetisation configuration at coercivity with $\hat{e}$ randomly assigned in each 10nm grain.

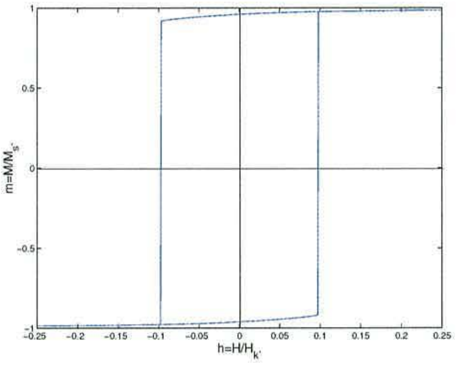

Figure 5.17: Hysteresis loop for randomly oriented 15nm grains.

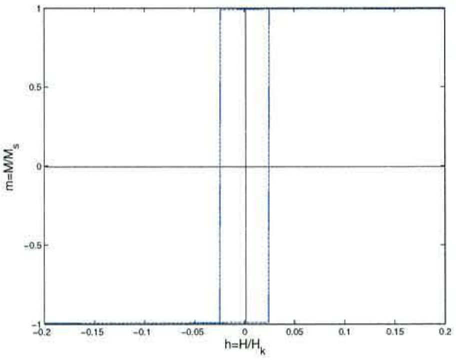

Figure 5.18: Hysteresis loop for randomly oriented 10nm grains.

Chapter 6

Geometric Integration.

In this chapter we go on to consider the most appropriate time-stepping scheme to implement in the model. Several such schemes were outlined in chapter 2 which were the basic schemes obtained by truncation of the Taylor series for the solution. These have many adaptations and generalizations. For example the idea of a predictor corrector scheme illustrated by the Heun method may be generalized to higher order. So out of the myriad of possible solution schemes, which one do we choose? Does it matter? The classical answer is that we choose the highest order scheme permitted by our computational facillities, thus minimizing the truncation error. The practical answer is often that we use Euler and refine our time-step until our error falls below the given tolerence and perhaps increase it again if the error gets very small on subsequent time-steps. Neither of these philosophies is particularly efficient and neither makes any attempt to incorporate the physical properties of the problem into the properties of the solution scheme. However the "third-way" of geometric integration is making a very strong case for the opinion that intrinsic phenomenon or invariants of a system are in fact the most important feature of a given problem and that truncation error is of secondary importance [80]. These methods have found particular applications in long time scale problems such as meteorology and stellar dynamics where a numerical error, no matter how small, is likely to accumulate exponentially and eventually swamp the solution. Whereas a scheme which respects the intrinsic properties of the solution will often evolve in a manner that agrees well over time with the real system, even though the local truncation error may be quite large. The definition of suitable intrinsic properties is often a non-trivial task, however from chapter 2 we know that the gyromagnetic precession modelled by the Gilbert equation has one important invariant, namely that the solutions should all lie on the surface of a sphere of radius $|\boldsymbol{M}| = M_s$; we therefore require a scheme which is quadratically invariant.

6.1 Geometric Integration Methods.

In general numerical methods for ordinary differential equations such as the Runge-Kutta scheme seek to minimize local errors incurred by the Taylor series truncation of the solution. Over any finite time interval the correct solution is then obtained in the limit as the time-step approaches zero. However the qualitative and geometrical structure of the problem is often lost. In this case, for problems involving long integration times, the build-up of local errors is inevitable. Geometric integration is an emerging paradigm which aims to preserve the underlying structure of a differential equation after discretization. This structure may take the form of conservation laws associated with the manifold on which the solution evolves such as the conservation of energy in planetary motion or the conservation of vorticity in atmospheric problems. Alternatively conservation laws may be associated with the phase space such as the conservation of volume in divergence-free problems. Deeper invariants are often found such as Galilean, reversal, scaling or Lie group symmetries. Discretization schemes which are also invariant under such symmetries are therefore identified as appropriate numerical methods [80]. In dynamic micromagnetics the magnetisation vector $\boldsymbol{M}$ represents a statistical average of magnetic moments, the magnitude of which should be conserved in time $|\boldsymbol{M}(t)| = M_s$. We work in reduced units $\boldsymbol{m} = \boldsymbol{M}/M_s$ and so local solutions are constrained to evolve on the unit sphere. Any numerical scheme which is intrinsically quadratically invariant is therefore identified as an appropriate method. This simply means that solutions are constarined to lie on the sphere quite naturally due to the structure of the scheme in the same way as exact solutions must lie on the sphere due to the structure of the differential equation. For a general three dimensional vector valued variable $\boldsymbol{x} = \boldsymbol{x}(t)$ satisfying some differential equation; quadratic invariance of a numerical solution scheme can be defined as any method such that

$$\sum_{i=1}^{3} x_i^{t+1} = \sum_{i=1}^{3} x_i^{t} = C \tag{6.1}$$

where C is a constant over every time-step $[t, t+1]$. As shown by Budd *et al.* this criterion is satisfied by an implicit midpoint rule. It is important in this context that the scheme is truely implicit, that is we deal with implicit terms directly and not approximate them using a nested or iterated explicit method. This rules out the use of any predictor-corrector type schemes.

6.2 A Pointwise Solution.

The midpoint method has been successfully implemented by various authors within a finite difference formulation of magnetisation dynamics. Serpico *et al.* [81] have used a midpoint rule to integrate the Landau-Lifshitz eqution while Albuquerque *et al.* [82] have used a variant of the Crank-Nicholson scheme in their discretization of the Landau-Lifshitz-Gilbert equation. Here we employ the method described by Serpico *et al.* to obtain pointwise solutions of the reduced Landau-Lifshitz-Gilbert equation. The symmetry of a midpoint rule is most straight-forward to illustrate if we write the equation in terms of a damped field $\tilde{\boldsymbol{h}}$.

$$\begin{aligned}
(1+\alpha^2)\frac{d\boldsymbol{m}}{d\tau} &= -\boldsymbol{m}\times\tilde{\boldsymbol{h}} && (6.2)\\
\tilde{\boldsymbol{h}} &= \boldsymbol{h}_{eff}+\alpha(\boldsymbol{m}\times\boldsymbol{h}_{eff}) && (6.3)\\
\boldsymbol{h}_{eff} &= \frac{A}{K}\nabla^2\boldsymbol{m}+\boldsymbol{h}_d+(\boldsymbol{m}\cdot\hat{\boldsymbol{e}})\hat{\boldsymbol{e}}+\boldsymbol{h}_z && (6.4)
\end{aligned}$$

where $\boldsymbol{h}_{eff}$ is the sum of exchange, magnetostatic, anisotropy and applied field terms, scaled with respect to the anisotropy field strength H_k as usual. Using the $O(\Delta\tau^2)$ approximations

$$\begin{aligned}
\frac{d\boldsymbol{m}^{t+1/2}}{d\tau} &\approx \frac{\boldsymbol{m}^{t+1}-\boldsymbol{m}^{t}}{\Delta\tau} && (6.5)\\
\boldsymbol{m}^{t+1/2} &\approx \frac{\boldsymbol{m}^{t+1}+\boldsymbol{m}^{t}}{2} && (6.6)
\end{aligned}$$

we have an implicit midpoint scheme which yields a straight-forward pointwise solution obtained from the system of three linear equations

$$\begin{aligned}
\mathbf{A}\boldsymbol{m}^{t+1} &= \mathbf{A}^T\boldsymbol{m}^{t}\\
\boldsymbol{m}^{t+1} &= \mathbf{A}^{-1}\mathbf{A}^T\boldsymbol{m}^{t} && (6.7)
\end{aligned}$$

where

$$\mathbf{A}=\begin{pmatrix} \frac{1+\alpha^2}{\Delta\tau} & \frac{1}{2}\tilde{h}_z & -\frac{1}{2}\tilde{h}_y\\ -\frac{1}{2}\tilde{h}_z & \frac{1+\alpha^2}{\Delta\tau} & \frac{1}{2}\tilde{h}_x\\ \frac{1}{2}\tilde{h}_y & -\frac{1}{2}\tilde{h}_x & \frac{1+\alpha^2}{\Delta\tau}\end{pmatrix}^{t+1/2} . \tag{6.8}$$

Intuitively we see that $|\boldsymbol{m}|$ cannot grow because

$$||A|| = ||A^T|| \tag{6.9}$$

and therefore over any time-step $[t, t+1]$, both $\boldsymbol{m}^{t+1}$ and $\boldsymbol{m}^t$ have coefficients of equal size; a more rigorous proof is given by Serpico *et al.* [81]. Values of $\tilde{\boldsymbol{h}}^{t+1/2}$ are calculated from previous timesteps using an $O(\Delta\tau^2)$ extrapolation formula

$$\tilde{\boldsymbol{h}}^{t+1/2} = \frac{3}{2}\tilde{\boldsymbol{h}}^{t} - \frac{1}{2}\tilde{\boldsymbol{h}}^{t-1}. \tag{6.10}$$

This causes a problem at $t = 0$ because $\tilde{\boldsymbol{h}}^{t-1}$ is not defined, this so called starting problem is overcome by using an iterated Euler method for the first time-step. Solutions for a single point, neglecting magnetostatic and exchange

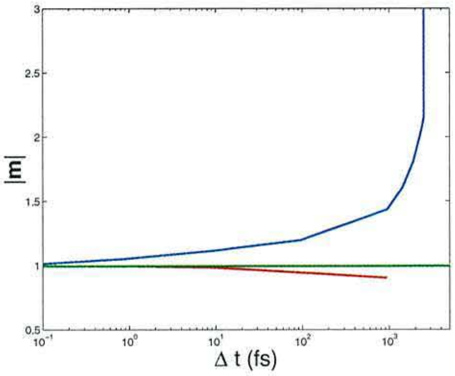

Figure 6.1: Convergence of single spin solutions using an implicit Euler method (red), an explicit Euler method (blue) and an implicit midpoint method (green).

interactions, are summarised in figure 6.1 for initial magnetisation $\boldsymbol{m}_0 = (0, 0, 1)$, applied field $\boldsymbol{h}_z = (0, 0, -1.5)$ and easy-axis $\hat{\boldsymbol{e}} = (\sqrt{1/2}, 0, \sqrt{1/2})$. In general an explicit Euler scheme shown by the blue line will over-estimate the magnitude of $\boldsymbol{m}$ and an implicit Euler method shown by the red line will make an under estimate, whereas the midpoint scheme shown by the green line ensures that the solution is constrained to lie upon the unit sphere. The graph shows the magnitude of $\boldsymbol{m}$ at equilibrium versus time-step for the three methods. Clearly intolerable errors build up with the Euler schemes for all but the smallest time-steps. It must be emphazied that this applies to any Taylor method, no matter how high the order of local approximation achieved, any finite errors will accumulate and eventually swamp the solution over long integration times. Figure 6.2 depicts the evolution of solutions using the explicit Euler (dashed) and midpoint (solid) methods for a time-step of Δt = 10fs. Although $\boldsymbol{m}$ comes to equilibrium along the same direction in both cases there is a clear departure of the Euler solution from the unit sphere. Also a marked difference in the direction of $\boldsymbol{m}$ can be seen at intermediate stages of the reversal. In a multi-spin system where the magnetisation is interacting, such errors may well be propagated through the system. This is our major objection to simply normalizing the solution from a Taylor scheme at every timestep by enforcing $\boldsymbol{m} \cdot \boldsymbol{m} = 1$.

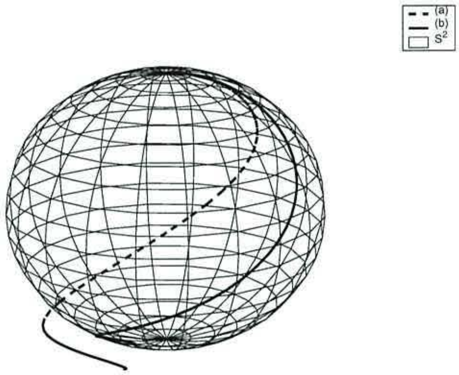

Figure 6.2: The evolutions of solutions with $\Delta t = 10fs$ for an explicit Euler method (dashed line) and an implicit midpoint method (solid line).

6.3 Finite Element Discretization.

Returning to the Galerkin projection of the standard reduced Gilbert equation onto a set of linear basis functions

$$\int_V \psi_i(\alpha(\boldsymbol{m} \times \frac{d\boldsymbol{m}}{d\tau}) - \frac{d\boldsymbol{m}}{d\tau})\, dV = \int_V \psi_i(\boldsymbol{m} \times \boldsymbol{h}_{eff})\, dV. \tag{6.11}$$

We use the temporal discretization given in equations 6.5 and 6.6 with an extrapolated effective field at the midpoint

$$\boldsymbol{h}_{eff} = (3/2)\boldsymbol{h}_{eff}^{t} - (1/2)\boldsymbol{h}_{eff}^{t-1}, \tag{6.12}$$

to build up the variational formulation from elemental contributions over three dimensional mesh

$$\begin{aligned}
\int_V \frac{L_i\alpha}{\Delta\tau}\boldsymbol{m}^t \times \boldsymbol{m}^{t+1}\, dV - \int_V \frac{L_i}{\Delta\tau}\boldsymbol{m}^{t+1}\, dV & & -\int_V \frac{L_i}{\Delta\tau}\boldsymbol{m}^{t}\, dV \\
-\int_V \frac{3L_i}{4}\boldsymbol{m}^{t+1} \times \boldsymbol{h}_{eff}^{t}\, dV &= & +\int_V \frac{3L_i}{4}\boldsymbol{m}^{t} \times \boldsymbol{h}_{eff}^{t}\, dV \\
+\int_V \frac{L_i}{4}\boldsymbol{m}^{t+1} \times \boldsymbol{h}_{eff}^{t-1}\, dV & & -\int_V \frac{L_i}{4}\boldsymbol{m}^{t} \times \boldsymbol{h}_{eff}^{t-1}\, dV.
\end{aligned} \tag{6.13}$$

The L_i are local shape functions over each tetrahedron as before. Local spatial discretization $\boldsymbol{m} = \sum_{j=1}^{4} L_j \boldsymbol{m}_j$ and $\boldsymbol{h}_{eff} = \sum_{k=1}^{4} L_k \boldsymbol{h}_{eff,k}$ over each finite element then allows the integrals to be performed analytically. This yields a system of linear algebraic equations for $\boldsymbol{m}^{t+1}$ over the whole domain, which is solved iteratively by the GMRES algorithm as before.

The following numerical results are obtained by performing a reversal of the cobalt nano-element from skewed saturation as in chapter 4. Comparisons are made between the midpoint scheme outlined above and the Euler scheme described in chapter 3.

6.4 Numerical Stability.

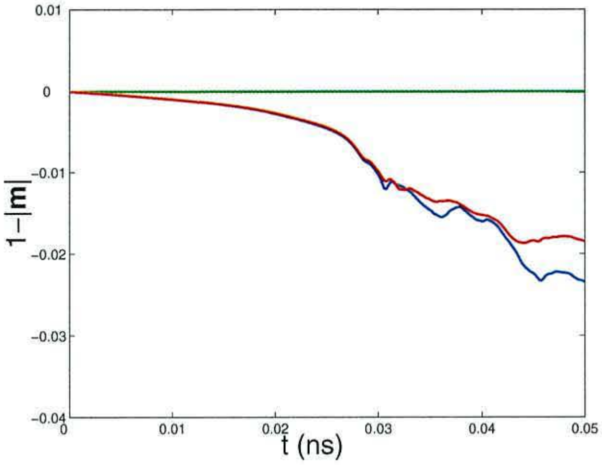

Figure 6.3: Magnitude of the average magnetisation vector during the early stages of reversal using an explicit Euler method with Δt = 10fs (red), an explicit Euler method with Δt = 20fs (blue) and a midpoint method with Δt = 20fs (green).

We now consider the build-up of numerical errors in an Euler scheme in comparison with our midpoint method. In figure 6.3 we plot $1 - |\boldsymbol{m}|$ during the the early stages of the calculation. The midpoint scheme with Δt = 20fs is shown in green, the Euler method with Δt = 20fs is shown in blue and the Euler method with Δt = 10fs is shown in red. The errors in the Euler solutions can be seen to accumulate very quickly. Whereas the midpoint scheme conserves $|\boldsymbol{m}|$ to reasonable precision as in the single-spin case. It is often assumed that using a Taylor scheme with very small time-steps will overcome the problem of numerical instability. Indeed in this case halving the time-step results in some improvement after a period of 0.04ns. However we also see that in the initial stages of the simulation the errors accumulate just as quickly in real time independent of Δt. Consequently simulations are flawed from the outset despite later improvements due to the reduced time-step. It must be emphasized here that although truncation errors would be smaller for a higher order Taylor method, such error accumulation would still occur given long enough simulation time [80].

6.5 Efficiency.

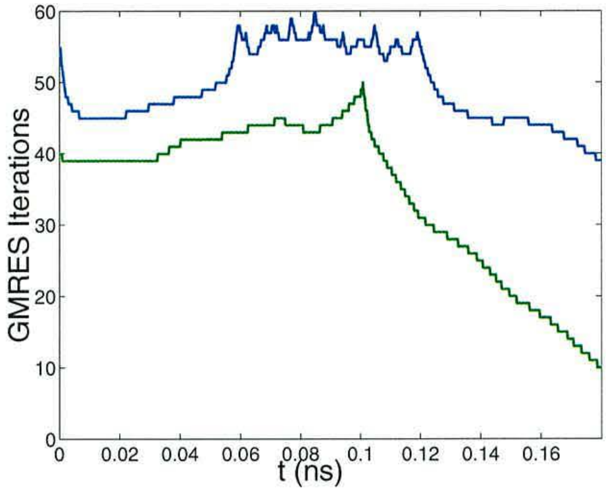

Figure 6.4: Comparison of GMRES iterations over the whole simulation for the Euler method with normalization (blue) and the midpoint method (green), both with $\Delta t = 20\text{fs}$.

Normalization of the magnetisation vector at every time-step is a common method of avoiding the error build-up, however this merely masks the numerical instability that exists. Further, normalization has a negative impact on computational efficiency. As can be seen from figure 6.4, normalization of the Euler scheme requires far more iterations of the GMRES algorithm. This is because normalization effectively discards part of the solution at each time-step. This in turn makes minimization of the residual using values from the previous time-step as an initial value more computationally intensive. Integrating the area between these curves corresponds to a significant amount of cpu time for long simulations such as the calculation of a hysteresis loop for a large system.

6.6 Error Control.

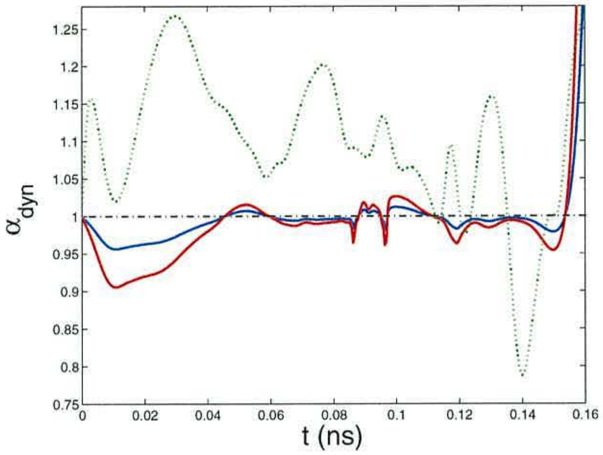

Figure 6.5: Recalculated α values during the reversal, using the midpoint method with $\Delta t = 20$fs and $\Delta x = 2.5$nm (blue), $\Delta t = 40$fs and $\Delta x = 2.5$nm (red), $\Delta t = 20$fs and $\Delta x = 5$nm (dotted green).

With a numerically stable method, such as the midpoint scheme outlined above, $|\boldsymbol{m}|$ becomes redundant as an error estimator. As even at large time-steps where accuracy is impossible $|\boldsymbol{m}|$ will be conserved. This highlights the fact the $|\boldsymbol{m}|$ should be thought of as an indicator of numerical stability rather than of truncation error. A useful alternative is the self-consistency based control scheme described by Albuquerque *et al.* [82]. Re-calculating the value of the damping parameter α at each time-step gives a measure of self-consistency of the discretization. This may then be used as an estimate of the error which causes any change in the system's total energy. The re-calculated α is derived from the Landau-Lifshitz-Gilbert equation in terms of the rate of change of the system's free energy

$$\alpha_{dyn} = \frac{\int_V \boldsymbol{h}_{eff} \cdot \frac{d\boldsymbol{m}}{d\tau} dV}{\int_V (\frac{d\boldsymbol{m}}{d\tau})^2 dV}. \tag{6.14}$$

This value may be calculated by expansion in terms of the global basis functions $\psi_i,\ i = 1, .., N$

$$\alpha_{dyn} = \frac{\int_V \left(\sum_{i=1}^N \psi_i \boldsymbol{h}_{eff,i}\right) \cdot \left(\frac{\sum_{j=1}^N \psi_j d\boldsymbol{m}_j}{d\tau}\right) dV}{\int_V \left(\sum_{k=1}^N \psi_k \frac{d\boldsymbol{m}_k}{d\tau}\right) \cdot \left(\sum_{l=1}^N \psi_l \frac{d\boldsymbol{m}_l}{d\tau}\right) dV} \tag{6.15}$$

$$= \frac{\left(\sum_{i,j} \boldsymbol{h}_{eff,i} \cdot \frac{d\boldsymbol{m}_j}{d\tau}\right) \int_V \psi_i \psi_j dV}{\left(\sum_{k,l} \frac{d\boldsymbol{m}_k}{d\tau} \cdot \frac{d\boldsymbol{m}_l}{d\tau}\right) \int_V \psi_k \psi_l dV}.$$

Due to the long range magnetostatic interactions α_{dyn} is a global quantity and cannot be evaluated locally. To perform the calculation using local shape functions the numerator and denominator of 6.16 must be evaluated separately over each element and contributions must be accumulated over the whole region before the division is performed.

$$\alpha_{dyn} = \frac{\sum_e I^e_{numerator}}{\sum_e I^e_{denominator}} \tag{6.16}$$

where

$$I^e_{numerator} = \left(\sum_{i,j=1}^{4} \boldsymbol{h}_{eff,i} \cdot \frac{d\boldsymbol{m}_j}{d\tau}\right) \int_{V^e} L_i L_j dV^e \tag{6.17}$$

and

$$I^e_{denominator} = (\sum_{k,l=1}^{4} \frac{d\boldsymbol{m}_k}{d\tau} \cdot \frac{d\boldsymbol{m}_l}{d\tau}) \int_{V^e} L_k L_l dV^e \tag{6.18}$$

As shown in figure 6.5, α_{dyn} is sensitive to both spatial and temporal discretisation error. First consider the red and blue lines, these both refer to simulations with spatial discretization size $\Delta x = 2.5$nm but with temporal discrestisation sizes of $\Delta t = 20$fs shown in blue and $\Delta t = 40$fs shown in red. We see that the model is convergent in some sense as the time-step is reduced, with a halving of the time-step resulting in a halving of the maximum error. With a time-step of $\Delta t = 20$fs the error is bounded at 5 percent and with $\Delta t = 40$fs the error is bounded at 10 percent. We note however that even with the larger time-step, α_{dyn} remains below 5 percent for the most part of the simulation.

Now compare the blue and green lines. These both represent simulations with $\Delta t = 20$fs but we now consider the effects of spatial discretisation size. The dotted green line represents a simulation with a doubling of the average element size. As we can see this has a drastic effect on numerical error, in fact it is true to say that we are no longer performing the same simulation. This justifies our earlier assumption that elements should be no larger than the exchange length of the material.

We conclude that α_{dyn} provides an excellent error indicator during the dynamic reversal. However we have found in all cases that its value rises exponentially as the system comes to equilibrium. This is inevitably due to the fact that $(d\boldsymbol{m}/d\tau)^2$ vanishes more quickly than $\boldsymbol{h}_{eff} \cdot d\boldsymbol{m}/d\tau$ in our model. This problem is not addressed in the original publication of the α_{dyn} calculation [82].

6.7 Adaptivity.

We have seen that large time-steps can give an acceptable solution during certain parts of the simulation. Also we have seen that the time-step may at times need to be quite small if better than 5 percent accuracy is required. It is therefore appropriate to apply the model adaptively in time with appropriate adjustment of the extrapolation formula for $\boldsymbol{h}_{eff}$. For example if $|\alpha - \alpha_{dyn}|$ is greater than the prescribed tolerance then the time-step may be halved and equation 6.13 will take contributions from

$$\boldsymbol{h}_{eff} = \frac{5}{4}\boldsymbol{h}^{t}_{eff} - \frac{1}{4}\boldsymbol{h}^{t-1}_{eff} \tag{6.19}$$

or alternatively if the time-step is doubled when the error falls well below tolerance we have

$$\boldsymbol{h}_{eff} = \frac{3}{2}\boldsymbol{h}^{t}_{eff} - \frac{1}{2}\boldsymbol{h}^{t-2}_{eff}. \tag{6.20}$$

A doubling of the spatial discretization size has been shown to have a more dramatic effect resulting in unacceptable error. For this reason spatial adaptivity would not be beneficial. Due to the global nature of α_{dyn} we do not have a spatial error indicator on which to base such adaptivity and further de-refinement of the mesh is limited by the constraint that elements should be smaller than l_{ex}. This is well below the element size needed to achieve a good solution of the magnetostatic problem in any case.

Chapter 7

Finite Temperature Model.

Before embarking on a finite element analysis of finite temperature dynamics we will return to the Stoner-Wohlfarth model of a single domain particle. This model may be used to illustrate the motivation behind a more rigorous formulation. A brief discussion of the necessary stochastic calculus will then be given followed by the Langevin formulation of the Gilbert equation. Single-spin solutions will then be presented giving simple examples of thermal relaxation and stochastic resonance. Our finite element discretization of the Gilbert equation will then be adapted to the finite temperature case.

7.1 The Energy barrier.

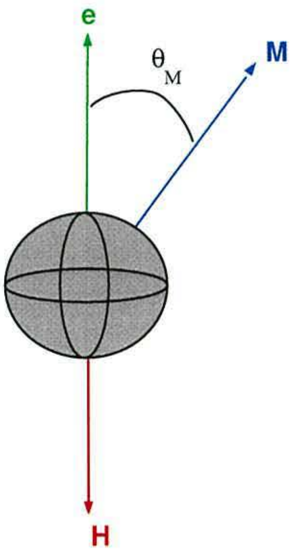

Figure 7.1: Stoner-Wohlfarth particle with easy-axis $\hat{\boldsymbol{e}} = (0, 0, 1)$ and magnetisation at angle θ_M to the z-axis.

Consider a non-interacting spherical Stoner-Wohlfarth particle of volume $V = 4\pi r^3/3$ as shown in figure 7.1 in an applied magnetic field in the negative z-direction. With easy-axis $\hat{\boldsymbol{e}} = (0, 0, 1)$ and magnetisation $|\boldsymbol{M}| = M_s$ at angle $\theta_M$rad to the z-axis. The particle clearly has two equilibrium states at $\boldsymbol{M} = (0, 0, M_s)$ and $\boldsymbol{M} = (0, 0, -M_s)$. Recall from chapter 1 that for applied field $\boldsymbol{H} = (0, 0, -H)$ the total energy of the system is given by

$$\mathcal{E}(\theta_M) = KV\sin^2(\theta_M) + M_sVH\cos(\theta_M) \tag{7.1}$$

with stationary point given by

$$\sin(\theta_M)(2KV\cos(\theta_M) - M_sVH) = 0 \tag{7.2}$$

$\sin(\theta_M) = 0$ gives two minima at $\theta_M = 0$ and $\theta_M = \pi$, $\cos(\theta_M) = M_sH/2K$ gives a single maxima at $\theta_M = \pi/2$. The minimum energy of the system is therefore $\pm M_sVH$ and the maximum energy is given by $KV(1 + (M_sH/2K)^2)$. The significant parameter in this problem is the energy barrier

$$\Delta E = E_{max} - E_{min} \tag{7.3}$$

which by the use of some simple mathematics determines the energy required for the system to make a transition from one stable equilibrium or energy minimum to another.

$$\begin{aligned} \Delta E &= KV\Big(1 + (\frac{M_s H}{2K})^2\Big) \pm M_s V H \qquad (7.4) \\ &= KV\Big(1 + (\frac{H}{H_k})^2 \pm 2\frac{H}{H_k}\Big) \\ &= KV\Big(1 \pm \frac{H}{H_k}\Big)^2 \end{aligned}$$

where $H_k = 2K/M_s$ as usual. The energy functional is visualized in figure 7.2 for different applied field strengths H. In zero-field the energy barrier is KV with symmetric energy minima at $\theta_M = 0$ and $\theta_M = \pi$. For an applied field of $H = H_k/2$ symmetry is broken and $\Delta E = KV(1 \pm 1/2)$, so that the energy barrier now differs by a factor of KV depending on which equilibrium state the system occupies. Finally for fields $H \geq H_k$ the energy barrier vanishes leaving a single equilibrium state. This corresponds to a field associated with sufficient Zeeman energy to rotate the magnetisation out of the easy axis. This model is rather limited. Firstly real magnetic grains are not spherical meaning that the magnetostatic field cannot be neglected. Secondly as we shall see, the state of thermodynamic equilibrium is never actually realized due to thermal agitation. The Stoner-Wohlfarth model does enable us however to see that, with these idealized conditions, in zero field there exists an energy barrier of height KV between two stable magnetisation states. The thermal energy associated with the particle is given by $E_{thm} = K_B T$ where $K_B = 1.38065 \times 10^{-16}$ is Boltzmann's constant and T is temperature on the Kelvin scale. Clearly if T is large or V is small the thermal energy may become greater than the energy barrier that exists between equilibrium magnetisation states. The magnetisation may then reverse due to thermal energy alone in the abscence of any applied field. As discussed in chapter 1 the point at which ferromagnets become dominated by thermal agitation is known as the Curie temperature, above which they behave paramagnetically. The recipricol situation where the particle volume becomes so small that $KV < K_B T$ at ambient temperature is known as superparamagnetism and again results in the particle becoming dominated by thermal agitations. This phenomenon is particularly important in magnetic storage technology where the grains of thin film recording media are already close to this size regime and approaching what has become known as the superparamagnetic limit. The estimation of this critical grain size is a difficult task as it is very sensitive to a vast number of parameters. We may at least illustrate the problem and give a crude estimate by using the Stoner-Wohlfarth par-

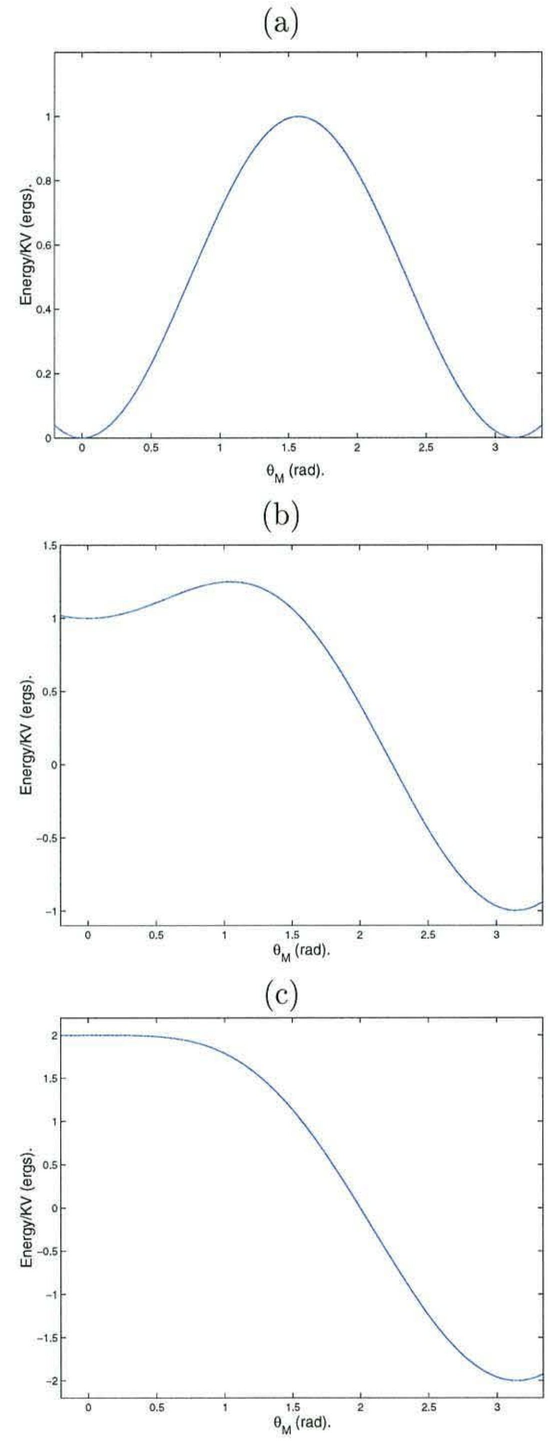

Figure 7.2: Energy functional for a Stoner-Wohlfarth particle with (a) $H = 0$ field, (b) $H = H_k/2$ and (c) $H = H_K$.

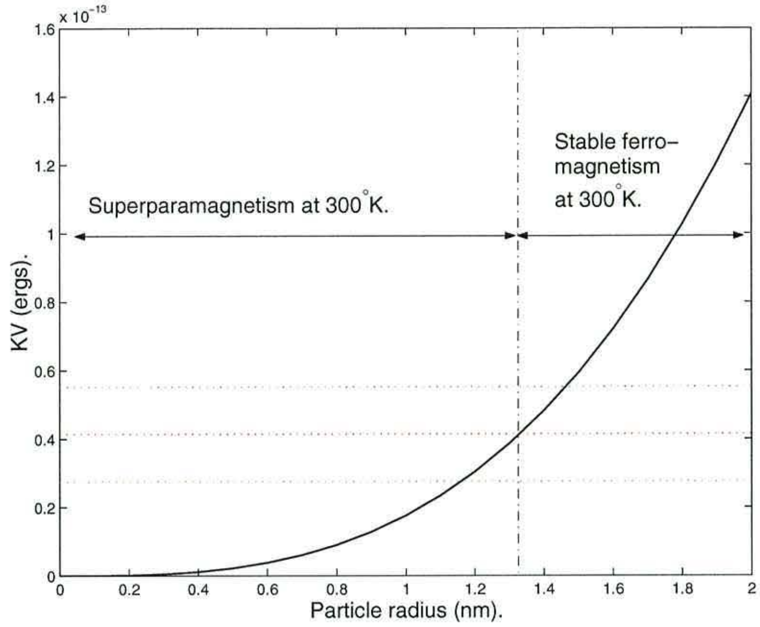

Figure 7.3: Temperature dependence of the superparamagnetic limit.

ticle. We may say that the particle will become superparamagnetic, that is susceptible to random switching in zero field, when $K_BT/KV > 1$. At $T = 300$°K and assuming a spherical cobalt particle we have $K_BT > KV$ when the particle radius $r < 1.33$nm. The dependence of KV on r is plotted in figure 7.3. Also plotted is K_BT at $T = 200$°K (green), $T = 300$°K (red) and $T = 400$°K (blue) to indicate the superparamagnetic limit at those temperatures. Finally we may appeal to the Stoner-Wohlfarth model to illustrate thermally assisted magnetisation reversal. This is a process which has been proposed to overcome the superparamagnetic limit. Even with small V we may retain $K_BT/KV < 1$ by increasing the uniaxial anisotropy constant K. In figure 7.4 $\sigma = K_BT/KV$ is plotted against K for the cobalt particle of radius $r = 1.33$nm. Clearly as K increases the stability ratio σ descends below unity and the particle is once more within the stable ferromagnetic region at $T = 300$°K. The increase in K may be achieved in storage media by alloying of the cobalt to achieve harder magnetic properties. This possiblity has recieved little attention until recently due to problems of writing information on such high anisotropy media. This problem may however be resolved by heating the media with a laser to lower H_c for writing. With increased T, σ is taken above unity once more where the application of a field $H \ll H_k$ will be sufficient to switch the magnetisation. When the media has returned to

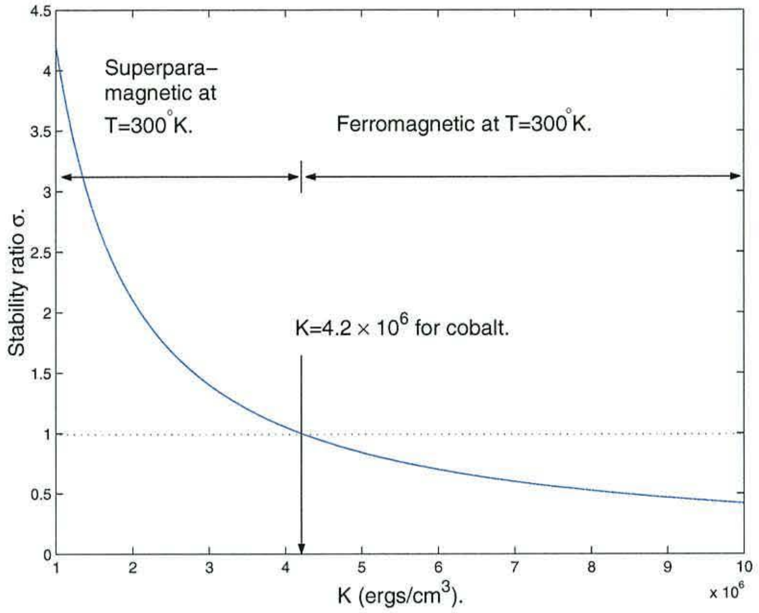

Figure 7.4: Stability ratio versus uniaxial anisotropy constant for the Stoner-Wohlfarth partical of radius $r = 1.33$nm at $T = 300°$K.

ambient temperature the thermal stability properties are naturally restored.

As mentioned previously this model is very limited due to its simplifying assumptions. This together with the need for dynamic resolution of magnetisation motivates us to formulate a stochastic differential equation of motion.

7.2 Stochastic Differential Equations.

Thermal agitations in magnetic media have correlation times much shorter than the response time of the system which is typically of the order of 10^{-7}s. According to the quantum mechanical Nyquist formula [83] the spectrum of thermal fluctuations may be regarded as Gaussian or white up to a frequency of order $K_B T/h$ which is approximatly 10^{-13}s^{-1} at $T = 300°\text{K}$. This is due essentially to the central limit theorem or law of large numbers. We may therefore apply the theory of Langevin dynamics [84] and regard the thermal agitations as being driven by a Markov process with normal distribution and mean zero; commonly known as a Wiener process. Since the Wiener process is nowhere differentiable, its derivative is not classically defined and we may not use the theory of deterministic calculus to derive an equation of motion. Instead we must appeal to the theory of stochastic calculus which was first made rigorous by Ito [85] in the 1940's and independently by Gikhman [86] at around the same time. A more straight-forward interpretation of the stochastic integral was later given by Stratonovich in 1966 [87]. In general stochastic calculus may be regarded as the generalization of deterministic theory to incorporate the statistical features of the real world such as noise, diffusion and thermal agitations. In fact a deterministic differential equation may legitimately be defined as a degenerate form of the associated stochastic differential equation where the Wiener process has zero variance. To give a full derivation of stochastic calculus requires the use of probability and measure theory largely beyond the scope of this thesis. In the following therefore we give only a brief outline of the way in which the stochastic integral should be interpreted and the subsequent impact of one's interpretation on appropriate methods of numerical solution. All the points raised in this section are covered with far greater detail and rigour in the comprehensive book on the subject by Kloeden and Platen [88].

7.2.1 The Wiener process.

We define the one dimensional Wiener process as any path $W(t)$ which is continuous on $[0, T]$ and satisfying conditions (i) to (iii) below.

(i) $Prob(W(0) = 0) = 1$

(ii) For all $0 \leq t_1 \leq t_2 \leq T$,

$$(W(t_2) - W(t_1)) \backsim N(0, t_2 - t_1)$$

or equivalently

$$(W(t_2) - W(t_1)) \backsim \sqrt{(t_2 - t_1)}N(0,1)$$

(iii) For all $0 \leq t_1 \leq t_2 \leq t_3 \leq t_4$,

$$(W(t_2) - W(t_1)) \text{ and } (W(t_4) - W(t_3)) \text{ are independent.}$$

The process is vectorized by defining each of the i components as an independent Wiener process with $Prob(\mathbf{W}(0) = \mathbf{0}) = 1$ and $W_i(t)$ independent of $W_j(t)$ for all components i, j at $t \in [0, T]$. We may define a discrete Wiener process by dividing the time interval into N sub-intervals of length Δt separated by $N + 1$ discretization nodes

$$\begin{aligned} \Delta t &= T/N && (7.5) \\ W(t_i) &= W(t);\ t = i\Delta t && (7.6) \\ &= W(t_{i-1}) + \Delta W(t_i);\ i = 1, .., N && \end{aligned}$$

where $\Delta W(t_i)$ is an independent Gaussian increment

$$\begin{aligned} \Delta W(t_i) &\backsim N(0, \Delta t) && (7.7) \\ &\backsim \sqrt{(\Delta t)}N(0,1). && \end{aligned}$$

Three such discrete Wiener processes, or equivalently one three dimensional Wiener process is shown in figure 7.5. The independent Gaussian variables $\Delta W_j(t_i)$, $j = 1, .., 3$, $i = 1, .., N$ are generated using a lagged Fibonacci generator with two Marsaglia shifts to give uniformly distributed input for the Box-Muller generator which then outputs standard Gaussian deviates [89].

7.2.2 The Langevin equation.

The first stochastic differential equation (SDE) was used to describe Brownian motion by Langevin in 1908 [90]. Using Newton's second law he arrived at the following description of a solid particle in fluid suspension

$$M\frac{dv(t)}{dt} = -av(t) + f(t) \qquad (7.8)$$

where the state variable is the velocity of the particle v, M is the mass of the particle, a is the viscous drag coefficient and f is a stochastic process

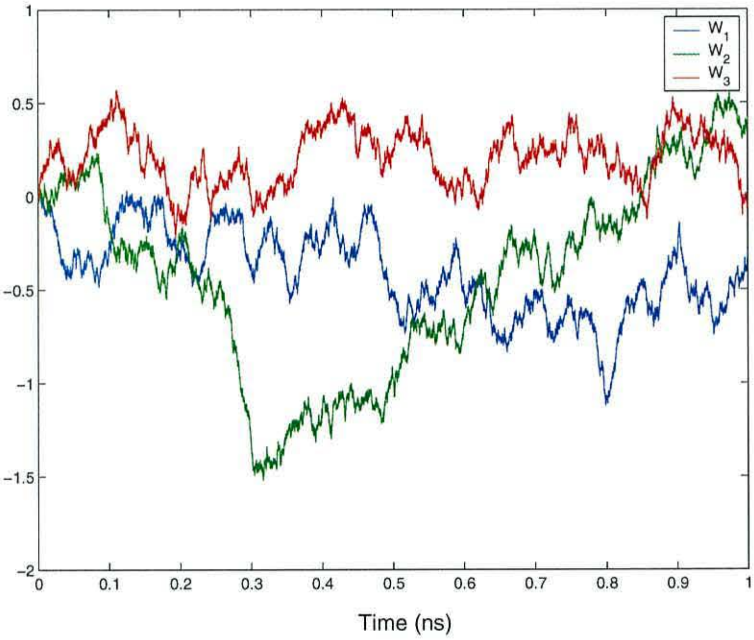

Figure 7.5: Three dimensional Wiener process with Gaussian deviates generated by the Box-Muller method.

representing the impacts of fluid molecules. The moments of f are naturally

$$\begin{aligned} \langle f(t)\rangle &= 0 \\ \langle f(t_1)f(t_2)\rangle &= \sigma_s^2\delta(t_2-t_1). \end{aligned} \tag{7.9}$$

where σ_s is the strength of the impacts from fluid molecules and $\delta(t_2-t_1)$ is the Dirac delta function. The first moment ensures that the effect of collisions averages to zero over time while the second moment represents the high frequency of the collisions with respect to the time-scale of the particle's velocity. Equations of this type are now generally known as the family of Langevin equations and expressed for state variable $X(t)$ as

$$\frac{dX(t)}{dt} = a(t,X(t)) + b(t,X(t))\xi(t) \tag{7.10}$$

where a is a deterministic or 'drift' term and $b(t,X(t))\xi(t)$ is a stochastic diffusion or 'noise' term, with space-time independent noise intensity factor b and Gaussian random variables $\xi(t)$ for each t. If $b=b(t)$ is independent of the state variable the drift term is said to be perturbed by additive noise whereas if $b=b(t,X(t))$ is a function of both t and $X(t)$ as in the case of finite temperature magnetisation dynamics we have multiplicative noise. Clearly for $b=0$ a deterministic differential is recovered. The above equation may then be written as a symbolic differential

$$dX(t) = a(t,X(t))dt + b(t,X(t))\xi(t)dt \tag{7.11}$$

to be interpreted as the integral equation

$$X(t) = X(0) + \int_0^T a(t,X(t))dt + \int_0^T b(t,X(t))\xi(t)dt. \tag{7.12}$$

For the special case $a=0$, $b=1$; $\xi(t)$ should be the derivative of a Wiener process $W(t)$, suggesting that the integral equation may be written

$$\begin{aligned} X(t) &= X(0) + \int_0^T a(t,X(t))dt + \int_0^T b(t,X(t))\frac{dW(t)}{dt}dt \\ &= X(0) + \int_0^T a(t,X(t))dt + \int_0^T b(t,X(t))dW(t). \end{aligned} \tag{7.13}$$

As mentioned earlier however the Wiener process is nowhere differentiable and therefore the white noise process $\xi(t)$ does not strictly exist as a conventional function of t. As with the original Langevin equation representing Brownian motion, for any Gaussian noise term $\xi(t)$, the covariance function is a constant multiple of the Dirac delta function. Hence the integral with respect to $dW(t)$ cannot be evaluated in the conventional Riemann or Lebesgue sense. Since a Wiener process is not of bounded variation over time interval $[0,T]$, the integral cannot be evaluated as a Riemann-Stieltjes integral either.

7.2.3 Stochastic Calculus.

The problem of interpreting a stochastic differential equation therefore lies in the interpretation of the integral

$$\int_0^T b(t, X(t))dW(t). \tag{7.14}$$

We first make the simplifying assumption that $b(t, X(t)) = b$ is constant over some small interval $[t_i, t_{i+1}]$. No-matter how the integral is defined over this interval, provided that $t_{i+1} - t_i$ is small, we would demand that

$$\int_{t_i}^{t_{i+1}} b\ dW(t) = b\{W(t_{i+1}) - W(t_i)\}. \tag{7.15}$$

We now assume that over the interval $[0, T]$, b is a step function comprised of constant functions over each small interval $[t_i, t_{i+1}]$ as illustrated in figure 7.6. So we have $b(t, X(t)) = b(t) = b_i$ on $t_i \leq t < t_{i+1}$ for $i = 0, .., n-1$ where $0 = t_0 < t_1 < ..... < t_i < t_{i+1} < ... < t_n = T$ and b_i are constants. We may then say that with probability 1

$$\int_0^T b^{(n)}(t)dW(t) = \sum_{1=0}^{n-1} b_i(W(t_{i+1}) - W(t_i)). \tag{7.16}$$

Relaxing the assumption of a step function we may then consider the full set of continuous, differentiable functions on $[0, T]$. The general integrand $b(t, X(t))$ may always be written as the limit of step functions $b^{(n)}$ and therefore the problematic integral 7.14 may be defined as the limit of integrals 7.16

$$\begin{aligned} \int_0^T b(t, X(t))dW(t) &= \lim_{n\to\infty} \int_0^T b^{(n)}(t, X(t))dW(t) \qquad (7.17) \\ &= \lim_{n\to\infty} \sum_{i=0}^{n-1} b_i\{W(t_{i+1}) - W(t_i)\}. \end{aligned}$$

The problem now comes down to determining the proper mode of convergence by which the step functions $b^{(n)}$ approach the function $b(t, X(t))$ in the limit as $n \to \infty$. The pioneering work of Ito [85] was to establish, due to the well behaved mean-squared properties of the Wiener process [88],[91], that 7.18 exists and is unique with probability 1 in the sense of a mean-squared limit.

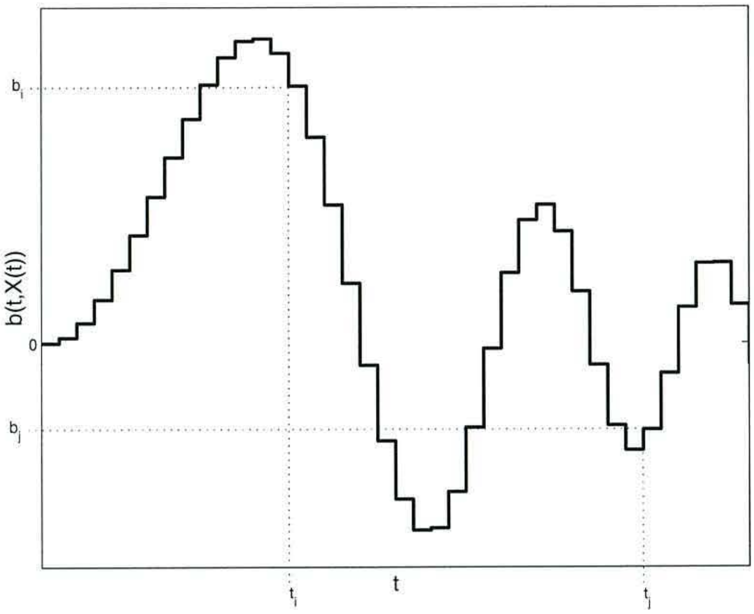

Figure 7.6: $b(t, X(t)) = b_i$ on $t_i \leq t < t_{i+1}$ for $i = 0, .., n-1$.

This definition of the stochastic integral obeys rules of deterministic calculus such as linearity and additivity

$$\begin{aligned}&\int_0^T \Big(\alpha\{b(t, X(t))\} + \beta\{b(t, X(t))\}\Big)\, dW(t) \\ =\ &\alpha \int_0^T b(t, X(t))dW(t) + \beta \int_0^T b(t, X(t))dW(t)\end{aligned} \tag{7.18}$$

$$\begin{aligned}\int_{t_0}^{t_2} b(t, X(t))dW(t) &= \int_{t_0}^{t_1} b(t, X(t))dW(t) \\ &+ \int_{t_1}^{t_2} b(t, X(t))dW(t).\end{aligned} \tag{7.19}$$

However the interpretation leads to a more peculiar form of the chain rule. In deterministic calculus we are used to the fact that

$$\int_0^T W(t)dW(t) = \frac{1}{2}W(T)^2 \tag{7.20}$$

when $w(0) = 0$. This is not the case with the Ito integral. Due to the properties of the mean square limit we have

$$\sum_{i=0}^{n-1}\Big(W(t_{i+1})-W(t_1)\Big)^2 = T. \tag{7.21}$$

Hence in Ito calculus the integral is evaluated as

$$\begin{aligned}\int_0^T W(t)dW(t) &= \sum_{i=0}^{n-1} W(t_i)\Big(W(t_{i+1})-W(t_1)\Big) \qquad (7.22)\\ &= \frac{1}{2}W(T)^2-\frac{1}{2}\sum_{i=0}^{n-1}\Big(W(t_{i+1})-W(t_1)\Big)^2\\ &= \frac{1}{2}W(T)^2-\frac{1}{2}T\end{aligned}$$

This extra term results from the fact that in Ito calculus the Taylor series and therefore the chain rule are fundamentally different from deterministic calculus. Classically for a function

$$U(t) = b(t, X(t)) \tag{7.23}$$

where $b(t, X(t))$ has continuous second order partial derivatives and $X(t)$ is defined as $dX(t) = f dW(t)$ we would expect that

$$dU(t) = \frac{\partial b}{\partial t}(t, X(t))dt + \frac{\partial b}{\partial x}(t, X(t))dx. \tag{7.24}$$

This comes from the Taylor expansion for $b(t, X(t))$ with second order terms and higher in Δt and Δx to be regarded as negligible. In contrast when $X(t)$ is a stochastic process we must take account of the fact that $d(X(t))^2 = f^2(dW(t))^2$ is non-negligible [88]. This gives

$$\begin{aligned}dU(t) &= \Big(\frac{\partial b}{\partial t}(t, X(t)) + \frac{1}{2}f^2\frac{\partial^2 b}{\partial x^2}(t, X(t))\Big)dt \qquad (7.25)\\ &\quad +\frac{\partial b}{\partial x}(t, X(t))dx.\end{aligned}$$

This is known as the Ito theorem and is essentially a consequence of the fact that in the definition of the Ito integral, b is evaluated at the beginning of each time interval in the sum

$$b_i = b(t_i, X(t_i)). \tag{7.26}$$

There was no justification for this decision other than the assumption that the beginning is usually a good place to start. Clearly we could have adopted a convention in which b was evaluated at the end of each interval

$$b_i = b(t_{i+1}, X(t_{i+1})). \tag{7.27}$$

Or indeed each b_i could be evaluated at any other point in the interval

$$\begin{aligned} b_i &= b\Big((1-\lambda)t_i + \lambda t_{i+1}, \\ &\quad X((1-\lambda)t_i) + X(\lambda t_{i+1})\Big), \quad 0 \le \lambda \le 1. \end{aligned} \tag{7.28}$$

It can be shown [88] that in this interpretation

$$\int_0^T W(t)dW(t) = \frac{1}{2}W(T)^2 + (\lambda - \frac{1}{2})T. \tag{7.29}$$

Clearly when $\lambda = 0$ we recover the Ito interpretation, whereas when $\lambda = 1/2$ the irksome extra term vanishes and we recover the classical result. It was first shown by Stratonovich in 1966 [87] that this interpretation in fact obeys all the transformation laws of deterministic calculus without exception. The convention of using $\lambda = 1/2$ became known as the Stratonovich interpretation with the integral of $f(t)$ with respect to W denoted

$$\int_0^T f(t) \circ dW(t) \tag{7.30}$$

It has become popular in the numerical treatment of stochastic differential equations due to the fact that the Stratonovich-Taylor series takes the same form as the classical Taylor series. Numerical integration schemes are therefore more straight-forward to develop. The Ito interpretation is often preferred in analytical treatments due to the martingale properties associated with stochastic integrals of this type only [88].

7.2.4 Numerical Solution of SDE's.

There has been much debate over the merits of the various interpretations of stochastic integrals. As the different interpretations will clearly converge to different solutions for a given Wiener process. In this work we are not interested in investigating stochastic calculus for its own sake but merely seeking a convenient method by which to develop a stochastic form of the Gilbert equation. We therefore adopt the Stratonovich interpretation in order to take advantage of the simpler form of its Taylor expansion. The numerical methods based on truncation of the Taylor series described in chapter 2 may then be generalized to the stochastic case. We give brief examples of two such schemes below. Again a more detailed discussion is given by Kloeden and Platen [88]. Also discussions related to the Stratonovich interpretation and subsequent numerical solution of the stochastic Gilbert and Landau-Lifshitz equations are given by Hannay [9] and Scholz [92] respectively.

The Euler-Maruyama method.

This method is a generalization of the deterministic Euler method. Given the symbolic differential

$$dX(t) = a(t, X(t))dt + b(t, X(t))dW(t) \tag{7.31}$$

we proceed with a first order time discretization

$$\Delta X = a(t, X(t))\Delta t + b(t, X(t))\Delta W \tag{7.32}$$

where

$$\begin{aligned}\Delta X &= \int_{t_n}^{t_{n+1}} dX(t) = X(t_{n+1}) - X(t_n)\\ \Delta t &= \int_{t_n}^{t_{n+1}} dt = t_{n+1} - t_n\\ \Delta W &= \int_{t_n}^{t_{n+1}} dW(t) = W(t_{n+1}) - W(t_n)\end{aligned}$$

So that ΔW is the $\sqrt{\Delta t}N(0,1)$ distributed increment of the Weiner process over $[t_n, t_{n+1}]$. Evaluating a and b at t_n then gives the stochastic counterpart of the deterministic explicit Euler method, known as the Euler-Maruyama method

$$X(t_{n+1}) = X(t_n) + a(t_n, X(t_n))\Delta t + b(t_n, X(t_n))\Delta W. \tag{7.33}$$

Since we have evaluated integrals at the lower end of $[t_n, t_{n+1}]$, this scheme will naturally converge to the Ito solution. However a so-called noise-induced drift term may be used to ensure convergence to the stratonovich solution if required [88], [9].

The Heun method.

As in the deterministic case we may improve the Euler method by attempting to evaluate a and b at the upper end of the time interval or at the midpoint. For example a midpoint scheme would take the form

$$\begin{aligned} X(t_{n+1}) &= X(t_n) + \frac{1}{2}\Big(a(t_n, X(t_n))\Delta t + b(t_n, X(t_n))\Delta W\Big) \\ &\quad + \frac{1}{2}\Big(a(t_{n+1}, X(t_{n+1}))\Delta t + b(t_{n+1}, X(t_{n+1}))\Delta W\Big). \end{aligned} \tag{7.34}$$

This scheme naturally converges to the Stratonovich solution because 7.35 approximates the corresponding Stratonovich integral by definition. Here we may convert back to the Ito integral using a recipricol correction term [88], [9]. Approximating the implicit contributions using an explicit Euler approximation we have a Stochastic Heun method

$$\begin{aligned} X(t_{n+1}) &= X(t_n) + \frac{1}{2}\Big(a(t_n, X(t_n))\Delta t + b(t_n, X(t_n))\Delta W\Big) \\ &\quad + \frac{1}{2}\Big(a(t_{n+1}, \tilde{X}(t_{n+1}))\Delta t + b(t_{n+1}, \tilde{X}(t_{n+1}))\Delta W\Big) \\ \tilde{X}(t_{n+1}) &= X(t_n) + a(t_n, X(t_n))\Delta t + b(t_n, X(t_n))\Delta W. \end{aligned} \tag{7.35}$$

However stronger convergence is obtained by using a fully implicit method or by iterating calculation of the implicit contribution $\tilde{X}(t_{n+1})$ until convergence is reached at each time-step.

7.3 The Langevin-Gilbert Equation.

Having developed the rudiments of stochastic calculus we are now in a position to discuss the derivation of a stochastic differential equation of motion for magnetisation dynamics. To take account of thermal agitations we recall that not only the magnitude but also the direction of the magnetisation vector should be regarded as a statistical average. Superposed upon the mean trajectory of magnetisation given by the Gilbert equation are spontaneous fluctuations in $\boldsymbol{M}$ as described by the fluctuation-dissipation theorem [84], [93]. To achieve this the effective field of deterministic magnetisation dynamics is augmented by a randomly fluctuating field $\boldsymbol{H}_{thm}$. The thermal field is a formal concept, introduced for convenience, which is defined as the field necessary to produce the observed fluctuations in $\boldsymbol{M}$ from the deterministic path predicted by the Gilbert equation. This leads to a definition of the Langevin-Gilbert equation in reduced units as

$$\frac{d\boldsymbol{m}}{d\tau} = -\boldsymbol{m} \times (\boldsymbol{h}_{eff} + \boldsymbol{h}_{thm}) + \alpha(\boldsymbol{m} \times \frac{d\boldsymbol{m}}{d\tau}) \tag{7.36}$$

re-arranging we have

$$\alpha(\boldsymbol{m} \times \frac{d\boldsymbol{m}}{d\tau}) - \frac{d\boldsymbol{m}}{d\tau} = \boldsymbol{m} \times \boldsymbol{h}_{eff} + \boldsymbol{m} \times \boldsymbol{h}_{thm} \tag{7.37}$$

or written as a symbolic differential

$$\alpha(\boldsymbol{m} \times d\boldsymbol{m}) - d\boldsymbol{m} = \boldsymbol{m} \times \boldsymbol{h}_{eff} d\tau + \boldsymbol{m} \times \boldsymbol{h}_{thm} d\tau. \tag{7.38}$$

Now $\boldsymbol{H}_{thm}$ is a random fluctuating three dimensional vector quantity and may therefore be defined as the time derivative of a three dimensional Wiener process

$$\begin{aligned} \boldsymbol{H}_{thm} &= \frac{d\boldsymbol{W}}{dt} \\ \boldsymbol{W} &= (W_x, W_y, W_z) \end{aligned} \tag{7.39}$$

where W_x, W_y, W_z are space and time independent Wiener processes satisfying the conditions outlined in section 7.2.1. We then scale with respect to H_k in order to remain consistent with the reduced units of the equation

$$\boldsymbol{h}_{thm} = \boldsymbol{H}_{thm}/H_k \tag{7.40}$$

also taking account of the reduced time increment $d\tau = \gamma H_k dt$

$$\begin{aligned} \boldsymbol{h}_{thm} &= \frac{1}{H_k}\frac{d\boldsymbol{W}}{d\tau}\gamma H_k \\ &= \frac{d\boldsymbol{W}}{d\tau}\gamma \end{aligned} \tag{7.41}$$

So finally we have

$$\begin{aligned} \alpha(\boldsymbol{m}\times d\boldsymbol{m}) - d\boldsymbol{m} &= (\boldsymbol{m}\times\boldsymbol{h}_{eff})d\tau + \gamma(\boldsymbol{m}\times\frac{d\boldsymbol{W}}{d\tau})d\tau \qquad (7.42)\\ &= (\boldsymbol{m}\times\boldsymbol{h}_{eff})d\tau + \gamma(\boldsymbol{m}\times d\boldsymbol{W}) \end{aligned}$$

which is to be interpreted as the integral equation

$$\begin{aligned} \alpha\int_0^T \boldsymbol{m}(\tau)\times d\boldsymbol{m}(\tau) &= \int_0^T \boldsymbol{m}(\tau)\times\boldsymbol{h}_{eff}(\tau,\boldsymbol{m}(\tau))d\tau \qquad (7.43)\\ -\int_0^T d\boldsymbol{m}(\tau) \qquad & \quad +\gamma\int_0^T \boldsymbol{m}(\tau)\otimes d\boldsymbol{W}(\tau) \end{aligned}$$

where $\otimes$ denotes a vector product within a Stratonovich interpretation of the stochastic integral. The moments of $d\boldsymbol{W}(\tau)$ follow from the Langevin theory referenced earlier [83], [90], [84] for fluctuations of frequency orders of magnitude higher than the response time of the system

$$\begin{aligned} \langle d\boldsymbol{W}(\tau)\rangle &= \boldsymbol{0} \qquad (7.44)\\ \langle d\boldsymbol{W}(\tau_i)d\boldsymbol{W}(\tau_j)\rangle &= \sigma^2\delta(\tau_j-\tau_i) \qquad (7.45) \end{aligned}$$

where δ is again the Dirac delta function and σ is the strength of thermal fluctuations.

7.3.1 Thermal Field Strength.

The purpose of the work in this chapter is to enable a quantitative investigation of temperature dependence in magnetic materials and subsequently to allow investigations into superparamagnetism and thermally assisted magnetisation reversal in magnetic storage media. To enable a proper description of finite temperature magnetisation dynamics it is vital that the thermal field strength realistically represents the temperature dependence of thermal fluctuations. The strength of the thermal field σ represents the deviation from the deterministic trajectory of the magnetisation caused by the fluctuations and σ^2 is therefore essentially the variance of the Wiener process $W(\tau)$ from which $\boldsymbol{h}_{thm}$ is derived. Since we are taking the Stratonovich interpretation we may adapt the value of σ^2 given by Brown in his derivation of the Fokker-Planck equation for a single domain particle [84]. Brown gives the second moment of $\boldsymbol{H}_{thm}$ as

$$\langle H_i(t_1)H_j(t_2)\rangle = (2k_BT\eta/V)\delta(t_2-t_1) \qquad (7.46)$$

where i, j refer to i^{th}, j^{th} components of $\boldsymbol{H}_{thm}$ respectively. Comparing our formulation of the Gilbert equation with Brown's η is given by

$$\eta = \frac{\alpha}{\gamma M_s}. \tag{7.47}$$

To give the variance of the fluctuations as

$$\begin{aligned} \sigma^2 &= \frac{2K_B T\alpha}{\gamma M_s V} s^{-1} && (7.48) \\ & && (7.49) \end{aligned}$$

7.3.2 Reduced Langevin-Gilbert equation.

Taking account of the reduced units and the $\sqrt{(dt)}$ dependence of the Wiener process discussed above we may give a concise definition of the reduced Langevin-Gilbert equation as the symbolic differential

$$\alpha(\boldsymbol{m} \times d\boldsymbol{m}) - d\boldsymbol{m} = (\boldsymbol{m} \times \boldsymbol{h}_{eff})d\tau + \sigma_r(\boldsymbol{m} \otimes d\boldsymbol{W}) \tag{7.50}$$

where σ_r is the dimensionless reduced field strength

$$\begin{aligned} \sigma_r &= \gamma\sqrt{\left(\frac{2K_B T\alpha dt}{M_s\gamma V}\right)} && (7.51) \\ &= \gamma\sqrt{\left(\frac{2K_B T\alpha d\tau}{H_k M_s \gamma^2 V}\right)} \\ &= \sqrt{\left(\frac{2K_B T\alpha d\tau}{H_k M_s V}\right)} \end{aligned}$$

where the Wiener process is now understood to have a standardized normal distribution of increments

$$dW_i \backsim N(0,1);\ i = 1,..,3 \tag{7.52}$$

7.3.3 Numerical Integration Scheme.

Previous workers on this problem [9], [92] have advocated the use of the Heun method in solving the stochastic Gilbert equation numerically. This is due to the fact that, being a form of midpoint rule, the Heun method naturally converges to the Stratonovich solution. Other schemes such as the Euler-Marayauma require the use of a so-called noise induced drift term in order to keep the magnitude of magnetisation constant during numerical integration. Rather than give a comparison of numerical schemes as has been done extensively elsewhere, we merely note here that the implicit midpoint rule outlined in the previous chapter has all the advantages of the Heun method. In fact the implicit midpoint rule converges more strongly to the Stratonovich solution giving an order of convergence which could be achieved with the predictor-corrector type Heun scheme only by iterating the predictor contribution. Applying a temporal discretization using the implicit midpoint rule we have

$$\alpha(\boldsymbol{m}^{t+1/2}) \times \Delta\boldsymbol{m}) - \Delta\boldsymbol{m} = (\boldsymbol{m}^{t+1/2} \times \boldsymbol{h}_{eff}^{t+1/2}) + \sigma_r(\boldsymbol{m}^{t+1/2} \otimes \Delta\boldsymbol{W}) \tag{7.53}$$

where $O(\Delta\tau^2)$ approximation gives

$$\begin{aligned}
\boldsymbol{m}^{t+1/2} &= \frac{\boldsymbol{m}^{t+1} + \boldsymbol{m}^{t}}{2} && (7.54)\\
\boldsymbol{h}_{eff}^{t+1/2} &= \frac{3}{2}\boldsymbol{h}_{eff}^{t} - \frac{1}{2}\boldsymbol{h}_{eff}^{t-1} && (7.55)\\
\Delta\boldsymbol{m} &= \boldsymbol{m}^{t+1} - \boldsymbol{m}^{t} && (7.56)\\
\Delta\tau &= \tau^{t+1} - \tau^{t} && (7.57)\\
\Delta\boldsymbol{W} &= \boldsymbol{W}^{t+1} - \boldsymbol{W}^{t}. && (7.58)
\end{aligned}$$

The discrete Wiener process $\bar{\boldsymbol{W}}$ again has standardized normal deviates

$$\Delta W_i \backsim N(0,1);\; i = 1,..,3 \tag{7.59}$$

scaled by the field strength constant

$$\sigma_r = \sqrt{\left(\frac{2K_B T\alpha\Delta\tau}{H_k M_s V}\right)} \tag{7.60}$$

Collecting terms in $t+1$ to the left hand side we have

$$\begin{aligned}
\alpha(\boldsymbol{m}^{t} \times \boldsymbol{m}^{t+1}) - \boldsymbol{m}^{t+1} &= -\boldsymbol{m}^{t} && (7.61)\\
-\frac{3\Delta\tau}{4}(\boldsymbol{m}^{t+1} \times \boldsymbol{h}_{eff}^{t}) &\quad +\frac{3\Delta\tau}{4}(\boldsymbol{m}^{t} \times \boldsymbol{h}_{eff}^{t})\\
+\frac{\Delta\tau}{4}(\boldsymbol{m}^{t+1} \times \boldsymbol{h}_{eff}^{t-1}) &\quad -\frac{\Delta\tau}{4}(\boldsymbol{m}^{t} \times \boldsymbol{h}_{eff}^{t-1})\\
-\frac{\sigma_r}{2}(\boldsymbol{m}^{t+1} \otimes \boldsymbol{W}) &\quad +\frac{\sigma_r}{2}(\boldsymbol{m}^{t} \otimes \boldsymbol{W}).
\end{aligned}$$

This can then by expressed as the matrix equation

$$\mathbf{A}\boldsymbol{m}^{t+1} = \mathbf{B}\boldsymbol{m}^{t} \tag{7.62}$$

where, droppping the eff subscript from components of $\boldsymbol{h}_{eff}$,

$$\begin{aligned}
A_{11} &= -1 \\
A_{12} &= -\alpha m_z^t - \frac{3\Delta\tau}{4}h_z^t + \frac{\Delta\tau}{4}h_z^{t-1} - \frac{\sigma_r}{2}\Delta W_z \\
A_{13} &= \alpha m_y^t + \frac{3\Delta\tau}{4}h_y^t - \frac{\Delta\tau}{4}h_y^{t-1} + \frac{\sigma_r}{2}\Delta W_y \\
A_{21} &= \alpha m_z^t + \frac{3\Delta\tau}{4}h_z^t - \frac{\Delta\tau}{4} + \frac{\sigma_r}{2}\Delta W_z \\
A_{22} &= -1 \\
A_{23} &= -\alpha m_x^t - \frac{3\Delta\tau}{4}h_x^t + \frac{\Delta\tau}{4}h_x^{t-1} - \frac{\sigma_r}{2}\Delta W_x \\
A_{31} &= -\alpha m_y^t - \frac{3\Delta\tau}{4}h_y^t + \frac{\Delta\tau}{4}h_y^{t-1} - \frac{\sigma_r}{2}\Delta W_y \\
A_{32} &= \alpha m_x^t + \frac{3\Delta\tau}{4}h_x^t - \frac{\Delta\tau}{4}h_x^{t-1} + \frac{\sigma_r}{2}\Delta W_z \\
A_{33} &= -1
\end{aligned} \tag{7.63}$$

$$\begin{aligned}
B_{11} &= -1 \\
B_{12} &= \frac{3\Delta\tau}{4}h_z^t - \frac{\Delta\tau}{4}h_z^{t-1} + \frac{\sigma_r}{2}\Delta W_z \\
B_{13} &= -\frac{3\Delta\tau}{4}h_y^t + \frac{\Delta\tau}{4}h_y^{t-1} - \frac{\sigma_r}{2}\Delta W_y \\
B_{21} &= -\frac{3\Delta\tau}{4}h_z^t + \frac{\Delta\tau}{4}h_z^{t-1} - \frac{\sigma_r}{2}\Delta W_z \\
B_{22} &= -1 \\
B_{23} &= \frac{3\Delta\tau}{4}h_x^t - \frac{\Delta\tau}{4}h_x^{t-1} + \frac{\sigma_r}{2}\Delta W_x \\
B_{31} &= \frac{3\Delta\tau}{4}h_y^t - \frac{\Delta\tau}{4}h_y^{t-1} + \frac{\sigma_r}{2}\Delta W_y \\
B_{32} &= -\frac{3\Delta\tau}{4}h_x^t + \frac{\Delta\tau}{4}h_x^{t-1} - \frac{\sigma_r}{2}\Delta W_x \\
B_{33} &= -1
\end{aligned} \tag{7.64}$$

and solved in the straight-forward manner

$$\begin{aligned}
\mathbf{A}^{-1}\mathbf{A}\boldsymbol{m}^{t+1} &= \mathbf{A}^{-1}\mathbf{B}\boldsymbol{m}^t \\
\boldsymbol{m}^{t+1} &= \mathbf{C}\boldsymbol{m}^t
\end{aligned} \tag{7.65}$$

where

$$C_{11} = (-1 + A_{23}A_{32} + (A_{12} + A_{13}A_{32})B_{21} \tag{7.66}$$

$$\begin{aligned}
&+(A_{13}+A_{12}*A_{23})B_{31})/D \\
C_{12} &= ((1-A_{23}A_{32})B_{12}-(A_{12}+A_{13}A_{32}) \\
&+(A_{13}+A_{12}A_{23})B_{32})/D \\
C_{13} &= ((1-A_{23}A_{32})B_{13}-(A_{13}+A_{12}A_{23}) \\
&+(A_{12}+A_{13}A_{32})B_{23})/D \\
C_{21} &= ((1-A_{31}A_{13})B_{21}-(A_{21}+A_{23}A_{31}) \\
&+(A_{23}+A_{13}A_{21})B_{31})/D \\
C_{22} &= (-1+A_{31}A_{13}+(A_{21}+A_{23}A_{31})B_{12} \\
&+(A_{23}+A_{13}A_{21})B_{32})/D \\
C_{23} &= ((1-A_{31}A_{13})B_{23}-(A_{23}+A_{13}A_{21}) \\
&+(A_{21}+A_{23}A_{31})B_{13})/D \\
C_{31} &= ((1-A_{21}A_{12})B_{31}-(A_{31}+A_{21}A_{32}) \\
&+(A_{32}+A_{12}A_{31})B_{21})/D \\
C_{32} &= ((1-A_{21}A_{12})B_{32}-(A_{32}+A_{12}A_{31}) \\
&+(A_{31}+A_{21}A_{32})B_{12})/D \\
C_{33} &= (-1+A_{21}A_{12}+(A_{31}+A_{21}A_{32})B_{13} \\
&+(A_{32}+A_{12}A_{31})B_{23})/D \\
D &= -1+A_{23}A_{32}+A_{21}A_{12}+A_{31}A_{13}+A_{21}A_{13}A_{32}+A_{31}A_{12}A_{23}
\end{aligned}$$

7.3.4 Thermal Relaxation.

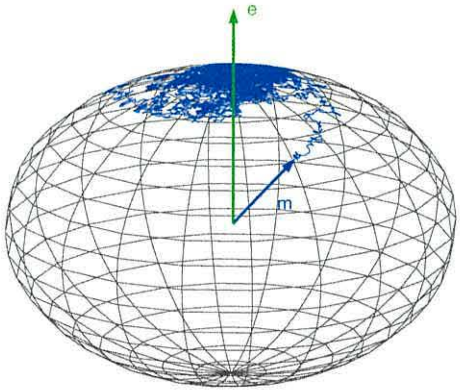

Figure 7.7: Relaxation of a Stoner-Wohlfarth particle of radius 4nm in zero field with easy-axis $\hat{e} = (0,0,1)$ and initial magnetisation $\boldsymbol{m} = (\sqrt{1/2}, 0, \sqrt{1/2})$.

A pointwise solution of the Langevin-Gilbert equation using the numerical scheme outined above may now be used to give a dynamic visualization of magnetisation reversal within a Stoner-Wohlfarth particle. We make the usual assumptions of the Stoner-Wohlfarth model, namely that magnetisation is homogeneous within the particle and that the internal magnetostatic field may be neglected due to spherical geometry. We then solve with the effective field taking contributions from anisotropy and applied field terms

$$\boldsymbol{h}_{eff} = (\boldsymbol{m} \cdot \hat{\boldsymbol{e}})\hat{\boldsymbol{e}} + \boldsymbol{h}_z. \tag{7.67}$$

The thermal field strength is given by

$$\sigma_r = \sqrt{\left(\frac{2K_B T \alpha d\tau}{H_k M_s V}\right)} \tag{7.68}$$

with the volume of the spherical particle given by $V = 4\pi r^3/3$ cm^3 and material properties for cobalt. First we consider the relaxation of magnetisation in zero applied field with initial saturation $\boldsymbol{m}_0 = (\sqrt{1/2}, 0, \sqrt{1/2})$ and $\hat{\boldsymbol{e}}$ along the z-axis at ambient temperature. Again the tiny magnitude of K_B ensures that the effect of thermal fluctuations are negligible at $T = 300$°K unless V is approaching the angstrom regime. Figure 7.7 shows the trajectory of magnetisation within a particle of radius $r = 4$nm, representing a cobalt grain of diameter 8nm which is expected to be thermally stable from experimental results [96] and is well above the superparamagnetic limit predicted by the energy barrier model. Although the magnetisation would be regarded as stable for a particle of this size the notion of an equilibrium state is shown to be naive. Once aligned with the easy-axis direction the magnetisation vector continues to be perturbed by thermal fluctuations indefinitley and can never be regarded as "at equilibrium". As the volume of the particle is reduced the deviation from the deterministic trajectory becomes more pronounced. Relaxations in zero field for particles of radius $r = 4$nm, $r = 3$nm and $r = 2$nm are summarized in figure 7.8. The plots show the magnitude of the z-component of magnetisation over a period of 1 nano-second. Defining the superparamagnetic limit as the size of particle in which spontaneous reversal can occur in zero field, we see that this occurs at a radius of somewhere between 2nm and 3nm. An increase on the prediction of direct energy minimization. As the radius decreases further the frequency of spontaneous reversals increases as shown by the plot of m_z versus time for a particle of $r = 1$nm in figure 7.9.

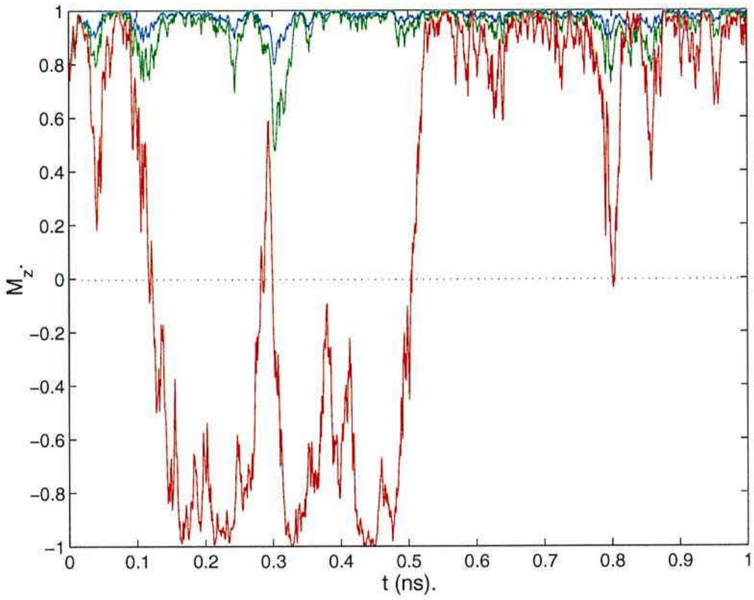

Figure 7.8: Relaxation of Stoner-Wohlfarth particles in zero field with radius 4nm (blue), 3nm (green) and 2nm (red).

7.3.5 Stochastic Resonance.

In order to consider the effect of thermal agitations on the magnetisation reversal process we repeat the simulation shown in figure 7.7 in the presence of a reverse field of $1\frac{1}{2}H_k$. To highlight the temperature dependence of the process we show the trajectory of magnetisation in figure 7.10 at (a) $T =$ 0°K, (b) $T = 150$°K and (c) $T = 300$°K. Clearly the random walk of the magnetisation vector converges in some sense to the deterministic trajectory as temperature approaches zero Kelvin. The magnitude of perturbations of the magnetisation vector around the equilibrium position also diminish with reduced temperature. Considering a slower reversal we may investigate the effect of this temperature dependence on hysteresis properties. Accordingly we apply the reversed field in steps of 6Oe, allowing the magnetisation to relax at each field step for 1ns. From the hysteresis loops shown in figure 7.11 it is clear that temperature has a profound effect on the coercivity of the particle. This phenomenon is known as stochastic resonance, it is a vital feature of the magnetisation reversal process and a crucial feature to be captured in order to perform quantitative micromagnetic modelling. As highlighted by figure 7.11 the deterministic approach cannot hope to predict coercivity of media at finite temperature. We see that in the finite temperature case the

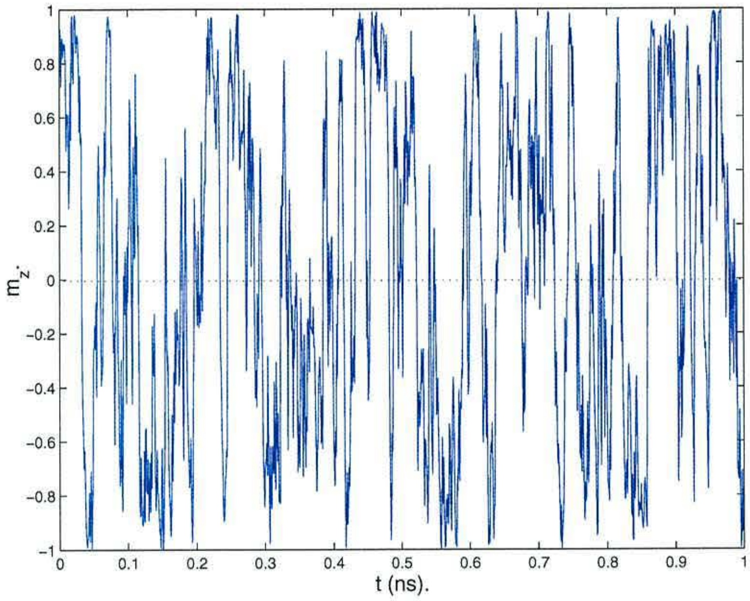

Figure 7.9: Relaxation of a Stoner-Wohlfarth particle in zero field with radius 1nm.

tails of the hysteresis curves join up at only very high and very low values of the applied field, this is again because the equilibrium position at each field step attained by the athermal system is meaningless in the finite temperature case. Finally we note that in the finite temperature case the hysteresis loop is not a uniformly changing curve but instead fluctuates about a mean path. In figure 7.12 we see that amplitude and frequency of the stochastic resonance increases with temperature.

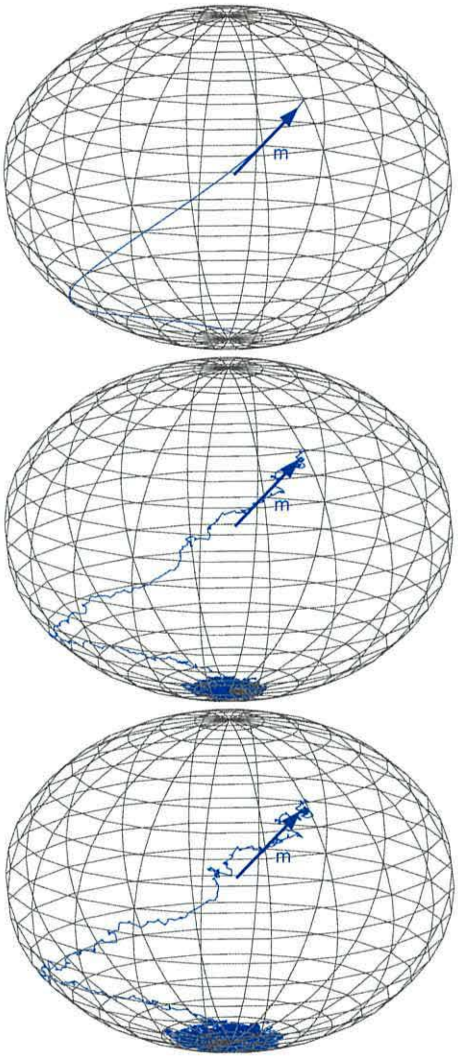

Figure 7.10: Reversal of a Stoner-Wohlfarth particle of radius 4nm for $T = 0°\mathrm{K}$ (top), $T = 150°\mathrm{K}$ (middle) and $T = 300°\mathrm{K}$ (bottom).

7.4 Finite Element Model.

Strictly speaking simulations such as those performed in the previous section should be repeated many times using different realizations of the Wiener process to obtain statistical data. However we are not concerned here with producing results on the probability of a given particle switching but rather we require a method of incorporating the effect of thermal agitations into our finite element model in a reasonably rigorous manner. It should however be

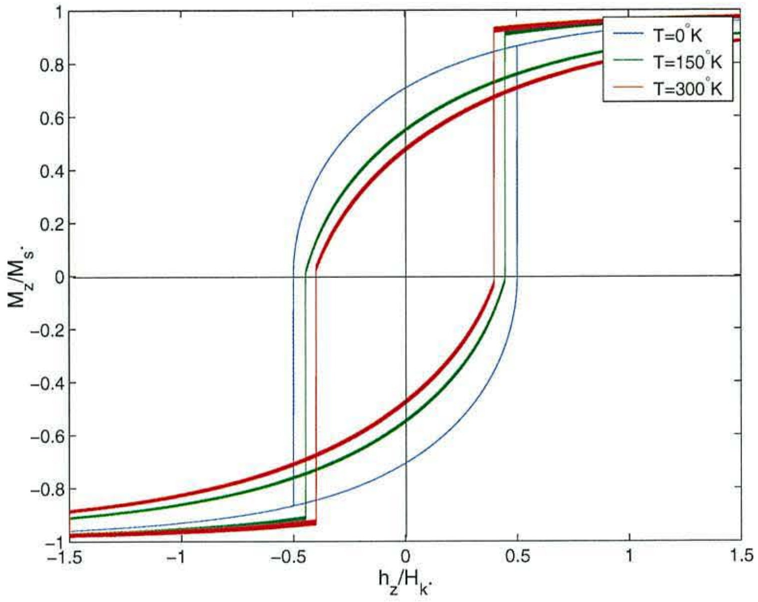

Figure 7.11: Hysteresis loops at $T = 0$°K (blue), $T = 150$°K (green) and $T = 300$°K (red).

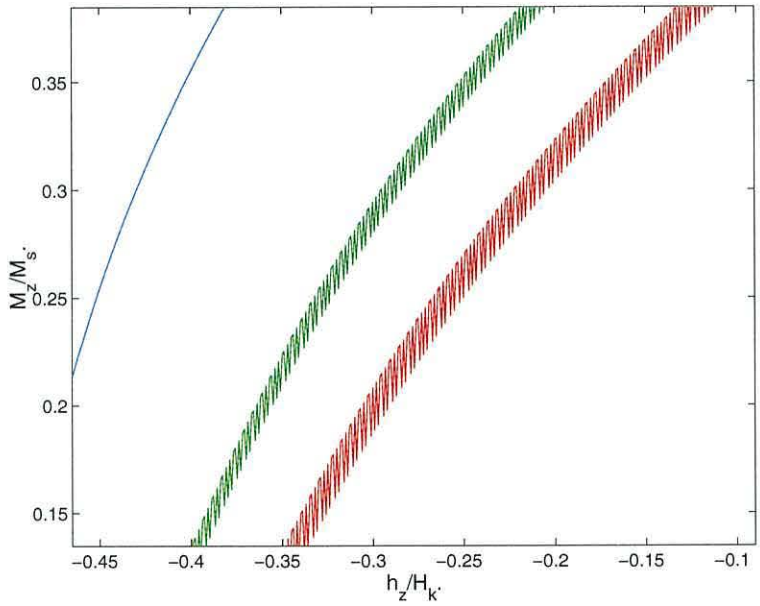

Figure 7.12: Stochastic resonance.

kept in mind that our results are only examples of a single realization of the simulated event. Although we have convergence to unique solutions for any given Wiener process, parameters such as coercivity or switching time should be understood as estimates which could form part of a sample from which to draw statistics and cannot be regarded as confident predictions. This section gives a brief overview of our finite element implementation of the stochastic time-stepping scheme followed by an example of relaxation in zero field at finite temperature. We now return to the full description of the effective field as described previously

$$\boldsymbol{h}_{eff} = \frac{A}{K}\nabla^2\boldsymbol{m} + \boldsymbol{h}_d + (\boldsymbol{m}\cdot\hat{\boldsymbol{e}})\hat{\boldsymbol{e}} + \boldsymbol{h}_z. \tag{7.69}$$

The specification of thermal field strength from Brown's work [84] makes use of the volume of the single-domain particle. In the subsequent work we follow the methods of Zhang and Fredkin [94], defining a unique thermal fluctuation over each element at each time-step. The volume used in the calculation of thermal field strength is then that of the element concerned

$$\sigma_r^e = \sqrt{\left(\frac{2K_B T\alpha d\tau}{H_k M_s V^e}\right)}. \tag{7.70}$$

7.4.1 Variational Formulation.

We now give a full spatial discretization of the problem combined with the stochastic time-stepping scheme outlined above. Following from the athermal model, the Galerkin projection of the Langevin-Gilbert equation in symbolic differential form onto the piecewise linear shape functions L_i is given by

$$\begin{aligned}\int_V L_i(\alpha(\boldsymbol{m}\times d\boldsymbol{m}) - d\boldsymbol{m})\,dV &= \int_V L_i(\boldsymbol{m}\times\boldsymbol{h}_{eff})d\tau\,dV \\ &\quad + \int_V L_i\sigma(\boldsymbol{m}\otimes d\boldsymbol{W})\,dV.\end{aligned} \tag{7.71}$$

We then employ the midpoint approximations to give

$$\begin{aligned}\int_V L_i\alpha\boldsymbol{m}^t\times\boldsymbol{m}^{t+1}\,dV - \int_V L_i\boldsymbol{m}^{t+1}\,dV \qquad & -\int_V L_i\boldsymbol{m}^t\,dV \\ -\int_V \frac{3L_i\Delta\tau}{4}\boldsymbol{m}^{t+1}\times\boldsymbol{h}_{eff}^t\,dV \quad = & +\int_V \frac{3L_i\Delta\tau}{4}\boldsymbol{m}^t\times\boldsymbol{h}_{eff}^t\,dV \\ +\int_V \frac{L_i\Delta\tau}{4}\boldsymbol{m}^{t+1}\times\boldsymbol{h}_{eff}^{t-1}\,dV \qquad & -\int_V \frac{L_i\Delta\tau}{4}\boldsymbol{m}^t\times\boldsymbol{h}_{eff}^{t-1}\,dV \\ -\int_V \frac{L_i\sigma}{2}(\boldsymbol{m}^{t+1}\otimes\Delta\boldsymbol{W})\,dV \qquad & +\int_V \frac{L_i\sigma}{2}(\boldsymbol{m}^t\otimes\Delta\boldsymbol{W})\,dV.\end{aligned} \tag{7.72}$$

Finally we interpolate $\boldsymbol{m}$ and $\boldsymbol{h}_{eff}$ in terms of the L_i to obtain a system of linear equations as before

$$\begin{aligned}\mathbf{A}_{thm}(\boldsymbol{m}^t, \boldsymbol{h}^t_{eff}, \boldsymbol{h}^{t-1}_{eff}, \Delta\boldsymbol{W})\vec{\boldsymbol{m}}^{t+1} &= \mathbf{G}_{thm}(\boldsymbol{h}^t_{eff}, \boldsymbol{h}^{t-1}_{eff}, \Delta\boldsymbol{W})\vec{\boldsymbol{m}}^{t} \\ &= \boldsymbol{G}_{thm}(\boldsymbol{m}^t, \boldsymbol{h}^t_{eff}, \boldsymbol{h}^{t-1}_{eff}, \Delta\boldsymbol{W}).\end{aligned} \quad (7.73)$$

7.4.2 Implementation.

Due to the use of the symbolic differential, $\Delta\tau$ appears in the numerator of coefficients in 7.72 instead of in the denominator as before. This was found to result in some very small entries in $\mathbf{A}_{thm}$ creating subsequent problems for the iterative solver. In practice we may divide both sides of equation 7.73 by $\Delta\tau$ so that the GMRES algorithm can minimize the residual in far fewer iterations. Since the magnitude of magnetisation is still conserved to within around 10^{-6} by the midpoint time-stepping method we may be assured that the scheme will converge to the Stratonovich solution. The incorporation of the thermal fluctuations into the finite element model was very straight forward. Computation is increased slightly as we must generate a Gaussian deviate for every interior element at each time-step.

7.4.3 Modelling Thermal Relaxation with Sub-grain Discretisation.

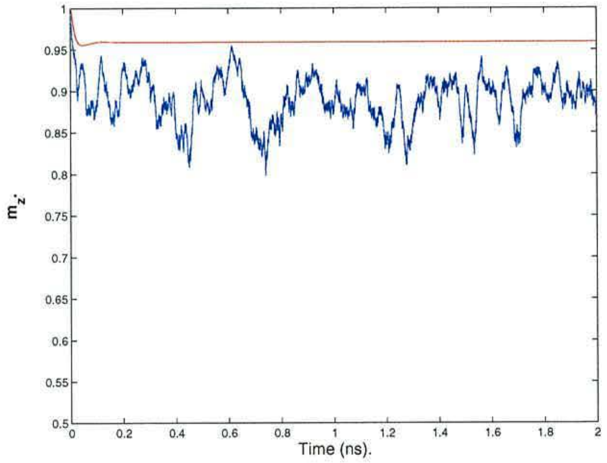

Figure 7.13: Comparison of the magnetisation component in the z-direction at 0°K and 300°K.

We may now use the finite element model to consider the relaxation in zero field of particles with arbitrary geometry. Returning to the perpendicular cobalt grain from chapter 4 consider thermal effects with sub-grain resolution. Unlike the single-spin model used earlier in this chapter we now have a non-uniform magnetisation configuration within the grain and it is more meaningful to talk of a remenance magnetisation value. In figure 7.13 we show results from a relaxation simulation of the grain at 0°K and at ambient temperature. The grain's easy-axis and initial saturation are in the out-of-plane direction as in chapter 4. At 0°K the grain reaches an equilibrium after 0.1ns and no further change occurs in the magnetisation configuration. A minimum can be seen in the relaxation curve due to precession, once in equilibrium $m_z = 0.96$ which can be regarded as a well defined remanence value m_r. In contrast at 300°K the grain never reaches an equilibrium, instead the magnetisation resonates around a value of $m_z = 0.9$. The magnetisation states of the grain after 2ns at 0°K and 300°K are compared in figure 7.14. As well as local oscillations of the magnetisation vector at 300°K which result in a more disordered system, we also see a difference in the overall configuration. In this particular snap-shot we observe an S-state. However as a function of time the magnetisation may be observed to jump between many low-energy states such as the S-state, the flower state and the C-state. Or rather their equivalents within this geometry. The effect of the thermal fluctuations is therefore twofold. The local disorder is moderated by exchange interactions and ferromagnetism is maintained. This effect could be modelled by simply considering a lattice of interacting spins at each node. In finite element analysis however it must be remembered that the magnetisation is in fact a continuous vector field which is sampled at the nodes but is also well-defined within the elements between them. Another benefit of this approach now becomes clear as we may observe frustrastion of the global

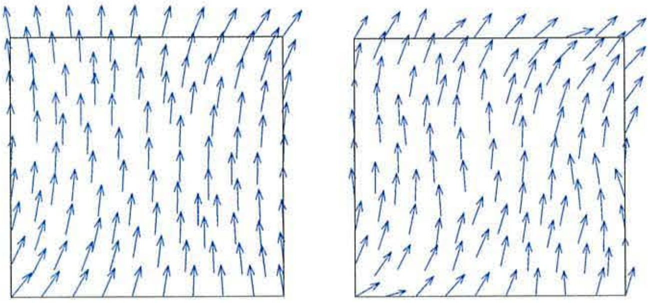

Figure 7.14: Comparison of the magnetisation states after a 2ns relaxation at 0°K (left) and 300°K (right).

magnetisation. Local fluctuations are seen to cause transitions to nearby minima in the energy surface. Since the real system is also continuous in time it is slightly misguided to think of jumps over energy barriers, instead it is more realistic to think of a constantly changing energy surface leading to the constantly varying value of m_z in figure 7.13.

These continual transitions of the minimum energy state leading to distinct changes in the global magnetisation as well as the expected local disorder have also been reported in the study of nano-scale permalloy elements [95]. Clearly as temperature is increased the increased thermal energy will lead to the annihilation of ever larger energy barriers and eventually to superparamagnetism.

We obtain a remanence value at finite temperature by averaging the value of m_z over the 2ns period of the simulation. We feel that this is a fair approximation of the value which would be macroscopically observable by experiment. Such remanence values are plotted for temperatures between 0 and 300°K is figure 7.15 where the error bars indicate the standard deviation of values taken. We can see a steady decline in m_r and by extrapolating this curve we may predict that superparamagnetism will not occur in grains of these dimensions except at impossibly high temperatures. In fact the decrease in m_r becomes more gradual as temperature increases.

Finally it should be remembered that these results refer to a single cobalt grain. Grains which are embedded within a thin film will have exchange interaction with neighbouring grains and are likely to exhibit more stable magnetisation.

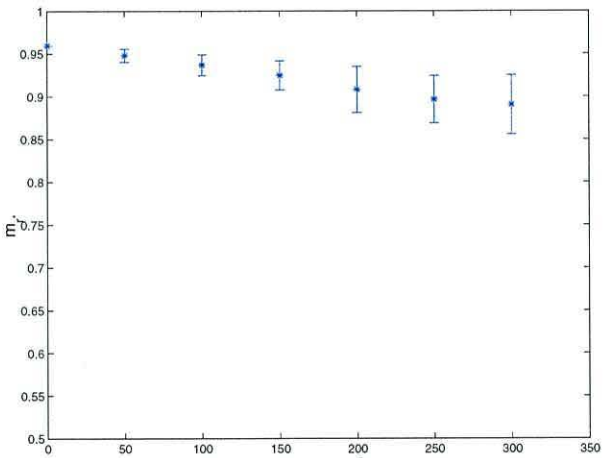

Figure 7.15: Remenance versus temperature between 0°K and 300°K.

Chapter 8

Applications.

This chapter presents some applications of the model. We have tried to present results which can only be obtained via sophisticated numerical methods in order to illustrate the usefulness of our methods. We illustrate four phenomena of nano-scale magnetism; the influence of material microstructure on magnetisation dynamics, the effects of Gilbert damping, superparamagnetism in cobalt grains and finally the temperature dependence of coercivity. All these simulations highlight the importance of sub-grain discretization since either they could not be performed at all or else they would give dubious results using a less sophisticated model. In section 8.1 we show that magnetisation dynamics and indeed coercivity values depend in a subtle way on the physical texture of cobalt nano-elements. Further we show that small deviations from a regular grain structure are enough to account for experimentally observed variation in coercivity values. Next we show that the value of the Gilbert damping parameter influences not only the reversal time but also the mode of magnetisation reversal. Indeed this work suggests the feasibility of an inverse problem to obtain the correct value or possibly the correct functional form of the damping parameter to be used in micromagnetic simulations. In considering superparamagnetism in cobalt grains we show that the superparamagnetic limit is not an abrupt transition as predicted by earlier theory but rather takes the form of a gradual reduction in remenance as grain size is reduced. Also we describe how it manifests itself as a challenge to computational modelling as well as the physical limitations it places on magnetic storage. Finally we demonstrate reduced coercivity at finite temperature due to stochastic resonance. Using the finite element model we are also able to highlight differences between the temperature dependence of longitudinal and perpendicular cobalt grains.

8.1 Influence of Material Microstructure.

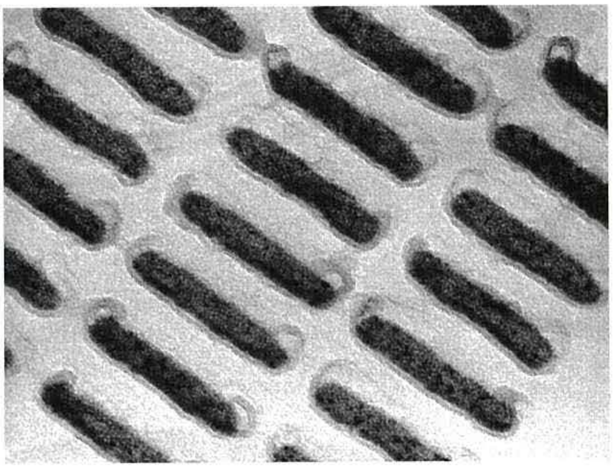

Figure 8.1: Bright-field TEM images of $200 \times 40\text{nm}^2$ cobalt nano-elements [96].

The first application of our work came at an early stage in the model development, nevertheless we were able to apply a two dimensional discretization and obtain some useful results. Nanoscale magnetic elements or nanoelements provide a unique context in which to study numerically the dependence of magnetization dynamics on material microstructure. With a bounded magnetic region it is possible to perform a rigorous calculation of magnetisation reversal which, as we have seen is currently impractical in the study of continuous media. During the first year of the work, experimental results concerning the switching of cobalt and permalloy nano-elements were published by a group at Glasgow [96], [97]. In addition to fundamental interest, arrays of such nano-elements have important applications as patterned magnetic recording media. As discussed in chapter 1, signal-to-noise ratio constraints on the minimum number of grains required per bit are eliminated. This allows patterned media to achieve a smaller bit area and therefore higher potential recording density than conventional media. Short of the superparamagnetic limit of a single grain, density is limited only by fabrication and read/write technology. The minimum feature size in lithographic fabrication techniques is now well into the nanometer regime, allowing for ever more miniaturization of nano-structured particles. We chose to investigate the switching characteristics of $200 \times 40\text{nm}^2$ rectangular nanoelements with a grain size ≥ 8nm as it was been demonstrated experimentally that these are magnetically stable in 50nm spaced arrays of mixed state [96]. However *in* *situ* magnetization reversal experiments at Glasgow revealed that the coercivity of such nanoelements can vary by up to 300Oe. This distribution has previously been attributed to the magnetostatic interactions between neighboring nanoelements which undoubtedly exist [72]. Our simulations were intended to establish that variations in coercivity from one nanoelement to another are also to be expected in the non-interacting case.

8.1.1 Experimental Comparison.

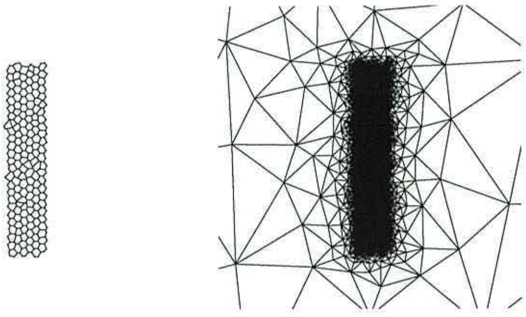

Figure 8.2: Simulated geometry of a 200 × 40nm^2 nano-element and the corresponding finite element mesh.

The predominantly hexagonal grain structure of the elements is clearly visible in the TEM image shown in figure 8.1. Accordingly we used the algorithm described in chapter 5 to obtain realistic geometries with which to construct our finite element meshes, conforming to the constraint that discretization size should be less than $l_{ex} \approx 2.8$nm for cobalt. A typical nano-element with a grain size of 8nm and the corresponding mesh is shown in figure 8.2. It has been shown that both edge roughness and end geometry have a strong effect on the reversal of such elements [99], [98]. We therefore ensured that the edge roughness ratio was simillar for all the nano-elements we investigated with excessively rough samples discarded. Also the nano-elements were defined as all grains of the Voronoi diagram which fell within in prefectly rectangular area. This ensured that nano-elements with sharply pointed ends which are known to have higher coercivity were not generated. To mimic the magnetocrystalline anisotropy of the elements a distinct randomly chosen easy-axis was assigned to each grain. We were then able to use our numerical simulation to reveal spatial resolution of the magnetization vector through incremental points in time, this gives a visualization of the reversal process which is difficult to obtain experimentally. Hysteresis simulations were performed by saturating the nano-elements along their long axis and slowly reversing the applied field, allowing the system to come to equilibrium at each of 3000 field steps from $+1.5H_k$ to $-1.5H_k$. Calculated values of coercivity were higher than those obtained experimentally but this was expected due to the absence of the strong out of plane component in the applied field which is present during *in-situ* reversal experiments [96] as well as the absense of thermal agitations in this model. The simulations allowed the mode of reversal to be observed as well as establishing how the physical grain-structure influences intermediate magnetization configurations. Figure 8.3 shows the slow magnetisation reversal of a typical nano-element of mean grain size 8nm. The corresponding hysteresis loop is shown in figure 8.4. The reversal shows the typical mechanism for elements of this grain size. At remenance (a) some magnetisation ripple can be seen, then roughly anti-symmetric vortices nucleate near the ends of the element (b). At higher field interior vortices nucleate and pass through the width of the element (c)-(d). The outer vortices migrate more slowly across the element width completing the reversal (e). Residual vortices are still present near the ends of the nano-element at the coercive field and a further increase in field is required to eliminate them. Such residual vortices are one of the origins of the so-called brown paradox, when ferromagnets are observed to switch at fields below the usual value of H_c [1], [2], [10]. If such vortices are not fully eliminated then on subsequent reversals the vortices have a "head-start" and may initiate the

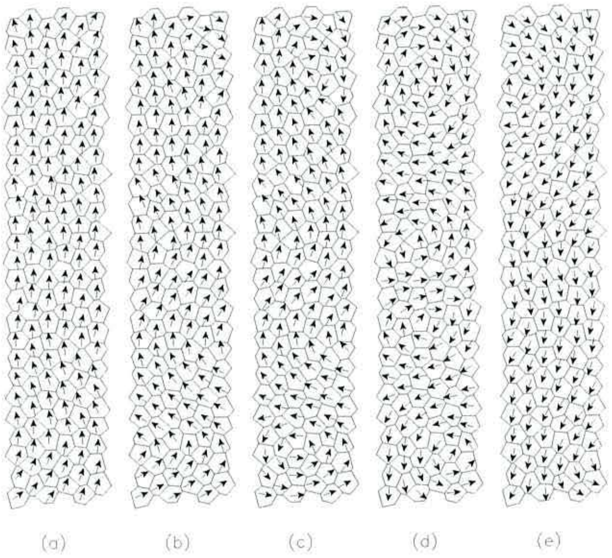

Figure 8.3: Simulated reversal of a $200 \times 40\text{nm}^2$ cobalt nano-element.

reversal of the element before the usual nucleation field is reached.

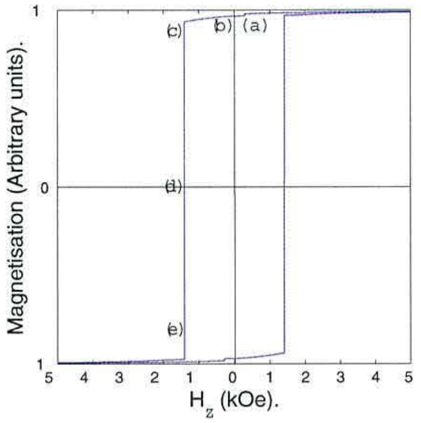

Figure 8.4: The corresponding hysteresis loop.

8.1.2 Effects of Grain Size.

To examine the grain size dependence of coercivity, we consider individual nanoelements with grain diameter of zero deviation from the mean. The hysteresis curves for three nanoelements with grain diameter 8nm, 10nm and 12nm are shown in figure 8.5. The nano-element consisting of 8nm grains exhibits strongly pinned magnetization with no significant nucleation occurring until shortly before the coercive field is reached, giving a square hysteresis curve. In larger grains we see irreversible magnetization changes at fields below the coercivity. The large Barkhausen jump in the 12nm curve corresponds to the formation of well defined end domains prior to switching. In trials with different anisotropy distributions these irreversible jumps occur at slightly different fields, but are always present in the case of larger grains and always negligible in the case of the 8nm grains. It was observed during the simulations that the magnetization within individual grains was strongly uniform in the case of the 8nm grains and less so in the larger grains. We conclude that with fixed global geometry, the relative size of the grains in the nano-elements dictates the balance between shape anisotropy and magnetocrystalline anisotropy, therefore defining the energy surface. In nanoelements of smaller grain diameter, domain motion is strongly pinned at grain boundaries. In such grains the dominant magnetocrystalline anisotropy suppresses nucleation, which is not achieved until the level of Zeeman energy is sufficient to overcome the energy barrier in each grain. As grain size increases the effects of shape anisotropy become more apparent, resulting in softer magnetic properties.

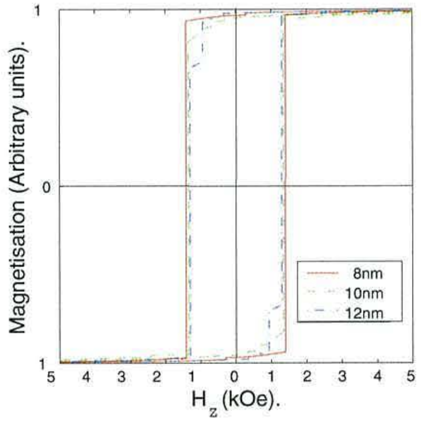

Figure 8.5: Comparison of hysteresis loops for regular nano-elements of grain size 8nm, 10nm and 12nm.

8.1.3 Effects of Grain Regularity.

We now consider the effect of grain size distribution on the reversal process. As can be seen from figure 8.6 the experimentally measured switching field is not single valued over a number of nano-elements but instead has a range of almost 300Oe. We employed our finite element simulation to test the hypothesis that differences in physical microstructure are responsible for the observed distribution of values. A sample of 100 nanoelements was generated. Each of mean grain diameter 8nm, but with standard deviation in grain area ranging from 0 to 0.3nm^2. In collaboration with the

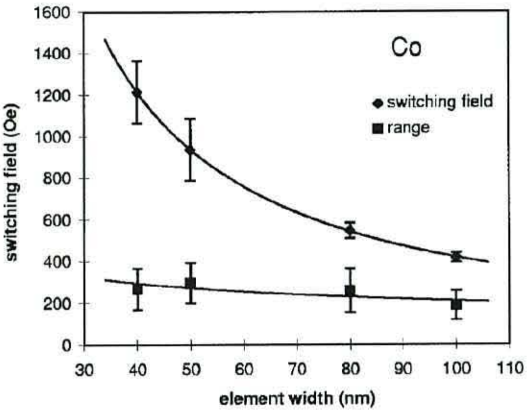

Figure 8.6: Experimentally measured coercivity values for cobalt nanoelements, [96].

Glasgow group it was decided that this gave a realistic range of grain irregularity, representative of the variation observed in TEM images. An identical easy-axis distribution was assigned to each nanoelement and hysteresis simulations were performed. The mode of reversal was qualitatively the same in all the observed simulations. In all cases magnetization ripple is observed in the remnant state with wavelength $\sim$ 100nm; this develops into vortex structures, first at the ends of the nanoelement where $\mathbf{h}_d$ is strongest, and then towards the middle. The vortices then migrate through the width of the nanoelement, aligning the magnetization with the applied field. This gives good qualitative agreement with previous numerical studies as well as with the experimental results. The coercive state during our simulations for four different nano-elements are illustrated in figure 8.7. It is clear from figure 8.7 that specific intermediate magnetization configurations are dictated by the physical microstructure. Although the magnetization configuration at coercivity is rather similar in all four cases, there are slight differences in the position and orientation of the four vortices. This can only be due to the different grain structures of each element as all other factors are identical. The distribution of the 100 calculated coercivity values is shown in figure 8.8. The range of over 200Oe accounts for much of the dispersion in experimental measurements. No strong correlation was established between coercivity and grain irregularity, indeed the nanoelement with regular grain-structure had the coercivity shown in figure 8.8, close to the mean value rather than being the maximum as expected. Specific magnetization configurations depend on the local balance between shape and magnetocrystalline anisotropy.

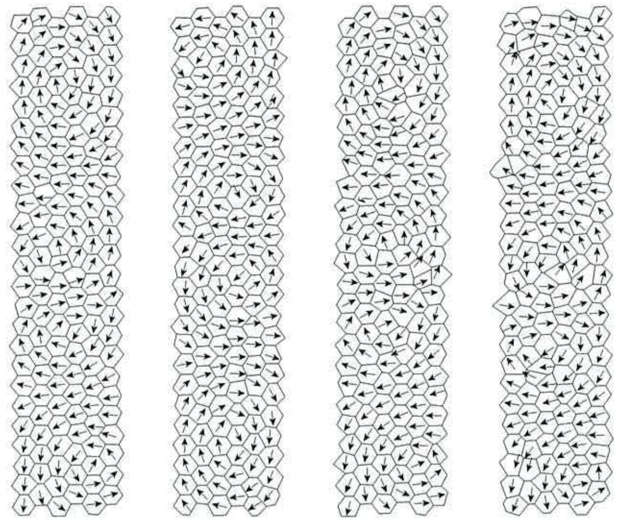

Figure 8.7: Coercive states for four irregular nano-elements of mean grain size 8nm.

Although all the 8nm grained nanoelements exhibit the same mode of reversal, different grain structures permit variations in the realized intermediate magnetization configurations during reversal due to variations in the local energy surface. This is reflected in the range of calculated coercivity values. Low correlation between coercivity and grain irregularity however indicates that the dynamics depend on a combination of grain-structure and easy-axis distribution unique to each nanoelement, reflecting a unique relationship between the physical grain-structure and the crystal lattice. Variation in the coercivity of Co nanoelements is therefore to be expected even in the absence of magnetostatic interactions from neighboring members of an array. The distribution of remnance magnetization values, M_r shown in figure 8.9 has a range of 25emu/cm^3, with most values closely packed around the mean. Interestingly the separation of the minor peak from the rest of the distribution shows that restrictions exist on the possible values of M_r. This again reflects that magnetisation is strongly pinned at grain boundaries in grains of such reduced dimensions. This apparent quantization in M_r values results from the fact that domain walls lie on or near the grain boundary, there is not a smooth transition between one magnetisation state and another with changing geometry. It is of course possible that we were unlucky enough to model almost 100 nano-elements from the lower end of the distribution and only a few from the higher end. For this reason the result was not included in our publication which discussed only the microstructure dependence of $\boldsymbol{H}_c$.

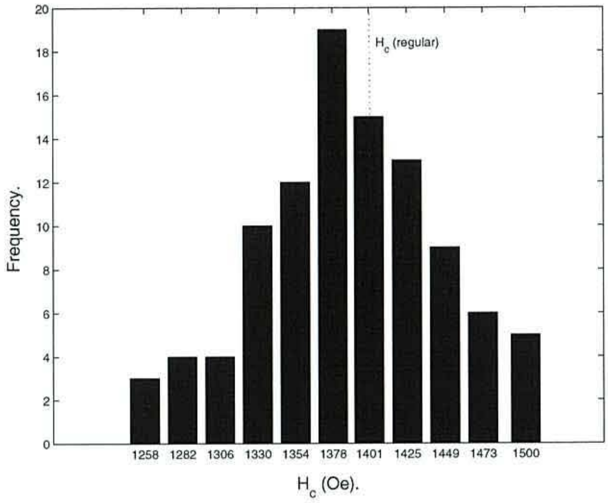

Figure 8.8: Distribution of coercivity values for 100 nano-elements of grain size 8nm.

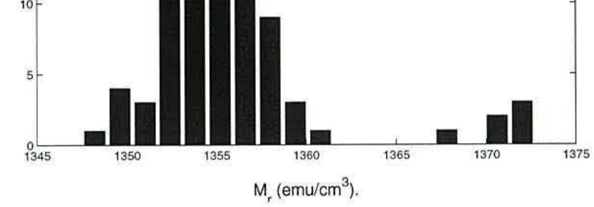

Figure 8.9: Distribution of remenance values.

8.2 Gilbert Damping in Cobalt Thin Films.

So far we have discussed the Gilbert damping parameter and the phenomena it represents briefly in chapter 2 where we proceeded to examine its influence over the motion of a single spin. The only major conclusions which can be drawn from the single spin analysis are that the length of the trajectory of magnetisation during reversal decreases with increased α and that the reversal time has a minimum with respect to α at $\alpha = 1$. These characteristics are automatically inherited by many micromagnetic models which consist essentially of ensembles of Stoner-Wohlfarth particles modified by Gilbert damping and spin to spin interactions. Hence we thought it would be an interesting and useful exercise to investigate how the damping parameter influences magnetisation dynamics in our finite element model. In all the simulations so far we have used a value of $\alpha = 1$, we have no justification for doing so other than the fact that minimum switching times and therefore minimum cpu times should result. This is defensible as until recently there was no justification for using any other value either. Until recently the contribution of damping in FMR experiments was neglected entirely and any damping in the system was included in the measured value of γ. Things have improved somewhat with the development of more rigorous FMR experiments which take account of the damping. In such experiments the FMR line width is related to the damping parameter as described in [101]. These results show a temperature dependence of α which is of course taken from the athermal Gilbert equation; this is an obvious but pertenant criticism. Also any retardation of precession due to extrinsic factors such as material defects, surface anisotropy and magnetostriction are also included in the measured value. Very recently attempts have been made to separate the intrinsic and extrinsic contributions to these measurements. With promising work at NIST [101] factoring out the contribution from the so-called two-magnon model. Although the jury is still out on exact values, the general opinion is that α is in the region of 0.01 in permalloy thin film media, however little work has been presented concerning harder magnetic materials.

8.2.1 Single grain simulations

We first employ the finite element model in the simulated reversal of a single longitudinal cobalt grain. We have already seen that the balance bewteen shape and magnetocrystalline anisotropy dictates the specific magnetisation configurations in thin films during reversal and therefore influences the coercivity. To assess the effects of damping we repeat the reversal experiment of section 4.3.1 with various values of α. We define the effective coercive state as that at which the average magnetization in the y-direction is zero during the reversals. These states are pictured in figure 8.10.

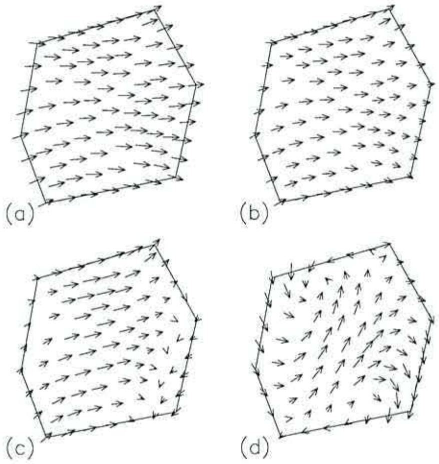

Figure 8.10: Effective coercive states for a single cobalt grain with damping parameter (a) $\alpha = 10$, (b) $\alpha = 1$, (c) $\alpha = 0.1$ and (d) $\alpha = 0.01$.

For a high damping of $\alpha = 10$ in (a) we see that the grain behaves much like a Stoner-Wohlfarth particle with almost total homogeneity of the magnetisation and the dynamics determined almost entirely by the relative orientations of $\hat{\boldsymbol{e}}$ and $\boldsymbol{h}_z$. After this coercive state has been reached the reversal continues by coherent rotation. Figure 8.10(b) shows the coercive state observed in the simulation with $\alpha = 1$ shown in section 4.3.1. As we have already noted this still results in single domain behaviour. In contrast to (a) however noticable effects of shape anisotropy are now present. Quite unexpectedly the reduction in α appears to have altered the system in favour of greater alignment with the grain surfaces, the shortened $\boldsymbol{m}$ vectors at grain boundaries indicate that a significant out of plane component is present. This is a feature we would usually identify with the minimization of magnetostatic energy. This trend continues as α is reduced to 0.1 in figure 8.10(c). Here we see that shape anisotropy becomes more important as the magnetisation has aligned with all of the grain boundaries. The reduction in magnetostatic energy achieved by this configuration must be greater than the energy taken to form the domain wall at the bottom-right edge of the grain. We can be sure of this as our athermal model will always follow the minimum energy path from its initial saturation and the saturation was the same in all four cases. In this case the reversal continues by the expansion of the reversed domain across the grain followed by coherent rotation into the applied field direction. This departure from single domain behaviour can only be interpreted as a continuing shift towards softer magnetic properties, i.e. more dominant shape anisotropy, with reduced damping. Finally in (d) we see much softer, vortices which have developed at opposite corners of the grain to minimize magnetostatic energy drive the reversal by domain motion.

These results highlight the importance of sub-grain discretization in quantitative micromagnetic modelling. Although the single-spin model is useful to visualize damping at each spin, for a full description of the magnetisation and intra-granular interactions we require sub-grain resolution. By considering the configurations shown in figure 8.10 we may see that Gilbert damping shifts the balance between shape and magnetocrystalline anisotropy within magnetic grains and does not merely dictate the reversal time, as could be inferred from the single-spin model. We see from figure 8.11 however that in agreement with the spin model we obtain a minimum switching time when $\alpha = 1$. Unlike the single spin however the increase in switching time for α much greater than 1 or much smaller than 1 is less severe.

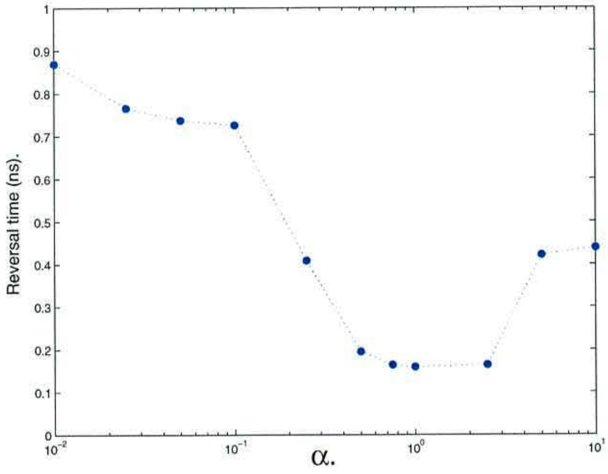

Figure 8.11: Reversal time versus α for the single cobalt grain.

8.2.2 Thin film simulations

We now apply our two dimensional finite element model to the simulation of a polycrystalline thin film. As in chapter 5 this is achieved by using implicit periodic boundary conditions. Magnetisation reversal simulations were performed on the ensemble of 48 coupled Voronoi grains with mean diameter 20nm shown previously. Again the easy-axis in each grain was chosen randomly from a uniform distribution across the half-cicle. The initial saturation

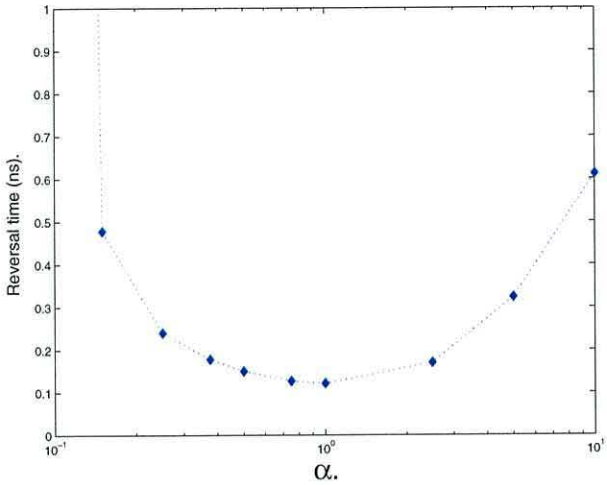

Figure 8.12: Reversal time versus α for a periodic thin film.

is allowed to relax in zero field before a reverse field of $1.5H_k$ is applied. The simulation with $\alpha = 1$ was shown in chapter 5, we now present analogous simulations with values of α less than 1. The results of these simulations are summarised in figure 8.12 to compare with the single-spin and isolated grain simulations. We see that the minimum reversal time again occurs at $\alpha = 1$, however the reversal time for $\alpha \ll 1$ is now far greater than that in either the single-spin case or the isolated grain. This must be due to the interactions between grains of different orientations which take longer to reach an equilibrium when the dynamics are negligibly damped. This is illustrated by the individual magnetisation reversal plots for various $\alpha < 1$ shown in figure 8.13. These reflect the different modes reversal. Although the magnetisation remains mostly homogeneous within individual grains at all values of the damping parameter in the coupled film, a marked difference in domain configuration was observed. As we saw in figure 5.13, for $\alpha = 1$ the reversal occurs by the motion of nucleated vortices through the system. This results in a smooth reversal curve. In contrast to this for lower damping the domain structures become more degenerate, with irregular maze-like domains dominating the the reversal. This is reflected in the many inflections in the reversal curve for $\alpha = 0.10$, presumably these are caused by more complex interaction between domains which in turn cause a slowing down of the reversal. With lower damping the reversal curves become even more structured. The effective coercive states for $\alpha = 0.1$ and $\alpha = 0.01$ are shown figures 8.14 and 8.15 respectively. At $\alpha = 0.01$ coherent magnetisation is observed only within individual grains. Returning to figure 8.13 we see that

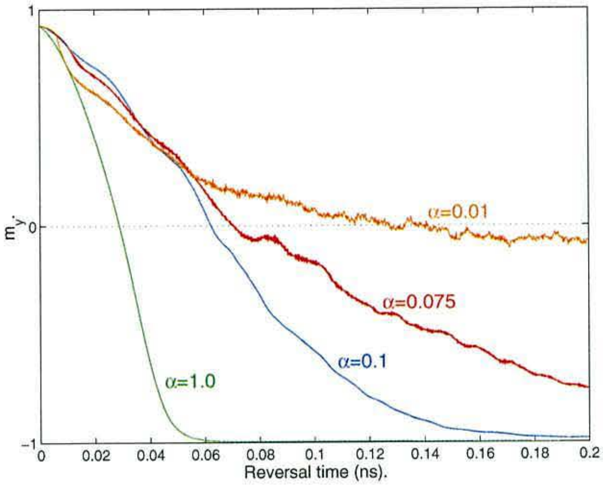

Figure 8.13: Reversal curves for the periodic thin film with $\alpha \leq 1$.

as $\alpha \rightarrow 0$ the reversal curve becomes more jagged as local energy minimisation within each grain becomes more dominant, until at $\alpha = 0.01$ no reversal occurs. Clearly such low values of α do not give a realistic representation of energy dissipation in this model, as a field of $1.5H_k$ should be sufficient to completely reverse the magnetisation in such a thin film.

8.2.3 The Nature of Energy Dissipation.

We have demonstrated that sub-grain discretization is necessary for quantitative micromagnetic modelling of polycrystalline media due to the effects of intra-granular interactions and the effect of Gilbert damping on the delicate balance between them. Although the inter-granular interactions may be incorporated into single-spin per grain models, the intra-granular interactions are not resolved. It appears that within individual grains decreased damping leads to softer magnetic properties. And within a coupled thin film reduced α leads to increased disorder in magnetisation.

The Gilbert equation is widely used to describe the dynamics of FMR experiments and the analysis often assumes that damping is negligible in such experiments. However we have seen that α plays a critical role in determining the reversal mechanism and cannot be ignored. Ideally an inverse problem can be conceived in which the value of α for a given system could be found by comparison of experimental data with the results of numerical simulations. This would provide the exact value or range of values to be used in micromagnetic models without confusion between intrinsic and extrinsic

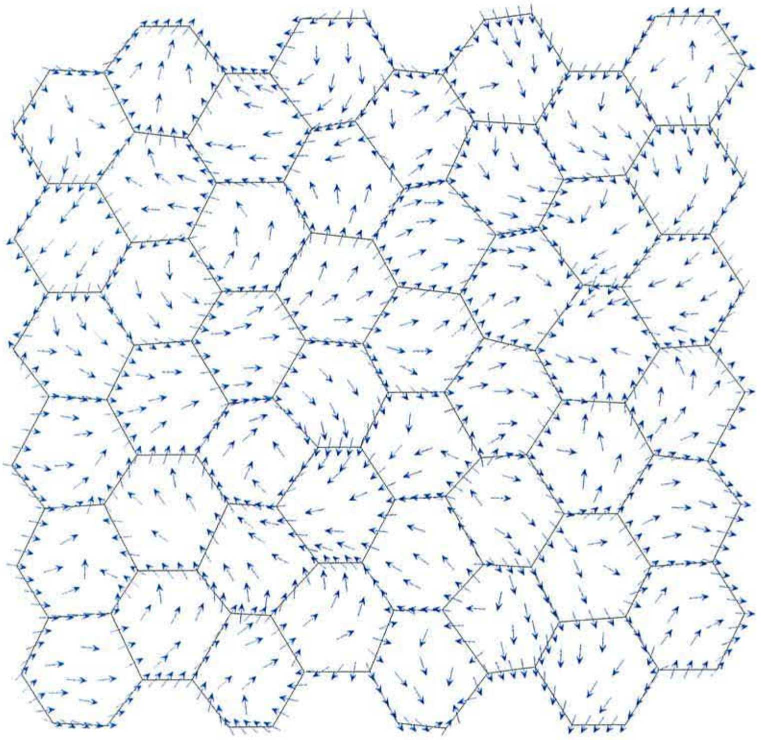

Figure 8.14: Effective coercive state of the periodic thin film with $\alpha = 0.1$.

contributions.

It is often inferred from Kikuchi [34] that a damping constant of $\alpha = 1$ is the most suitable value to use in micromagnetic simulations as this gives the minimum switching time in a single-spin system. We have seen that this is also true in both a single grain and a coupled thin film and further that $\alpha = 1$ continues to give a physically acceptable reversal time in these systems.

Originally we had concluded that α could not be as low as 0.01 since this resulted in physically unacceptable results in our model. However in light of resent experiments which confirm that α must be at least 1 or 2 orders of magnitude lower than 1 we are forced to reject this conclusion and accept that the result must be due to the periodicity in our thin film model. Intuitively if an excited spin-wave cannot ever leave the torus then we do not have a truely open magnetic region. Energy can then only be dissipated via Gilbert damping leading to the physically unacceptable result in figure 8.13. From this we must conclude that two dimensional modelling with periodic boundary conditions is not a sensible method in micromagnetics.

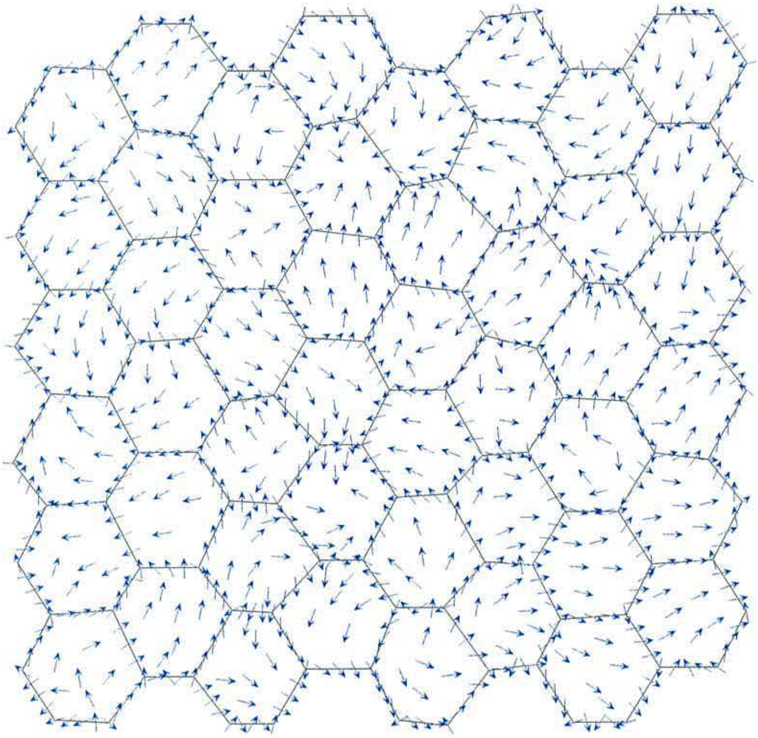

Figure 8.15: Effective coercive state of the periodic thin film with $\alpha = 0.01$.

8.3 Modelling Superparamagnetism.

We now consider the relaxation of longitudinal grains at ambient temperature and consider the effects of reducing grain size. We expect from chapter 8 that reduced grain size will eventually result in superparamagnetism. However instead of the idealized spherical grain considered previously we may now consider a realistic Voronoi grain. Again the same mesh is used for all the simulations and scaled to achieve the desired grain size. Similar results were obtained for the perpendicular grain and so to avoid repetition we present results for the longitudinal case only. In figure 8.16 we see the relaxation of the 20nm grain over a period of 2ns, as expected the magnetisation oscillates around a value which is somewhat lower than would be obtained in the athermal simulation. Nevertheless the average value of $m_y = 0.67$ is still a reasonably strong remenance value. The equivalent relaxations for grain sizes of 15, 10, 8 and 7 are shown in figures 8.17 to 8.20. Reducing the grain size to 15nm results in only a modest reduction of the average magnetisation value and the grain is resistant to thermal fluctuations. Upon reduction to 10nm the effective remenance value is reduced once more and we see fluctuations of greater amplitude in the magnetisation. Whereas at 8nm we see a large fluctuation in the magnetisation which is alsmost sufficient to switch the grain. It appears from these finite element simulations that the onset of the superparamagnetic limit is more gradual than the abrupt transition predicted by the single spin model. From the figures we see that the remenance magnetisation is reduced with reductions of grain size, accompanied by an

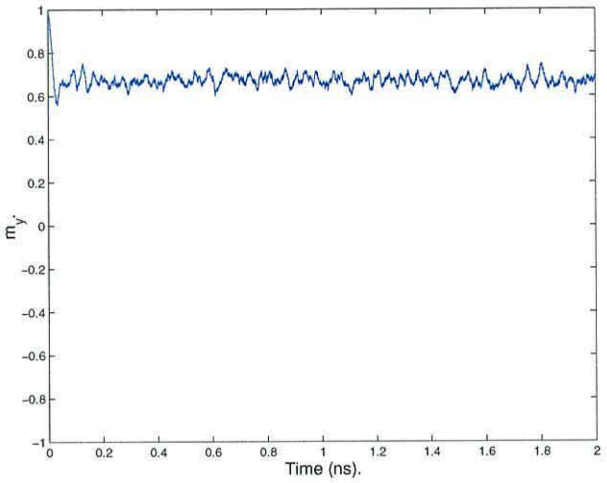

Figure 8.16: Relaxation of a 20nm longitudinal grain at 300°K.

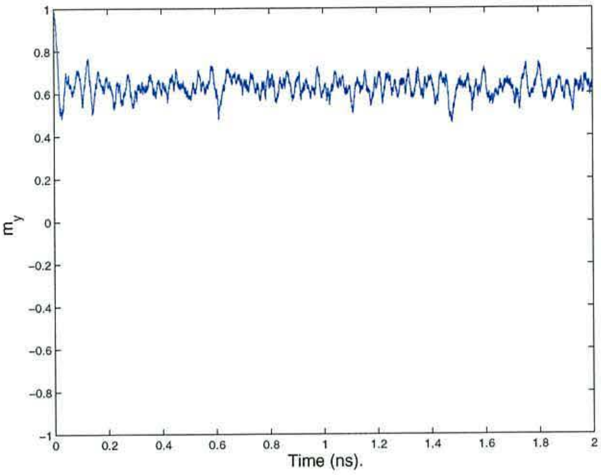

Figure 8.17: Relaxation of a 15nm longitudinal grain at 300°K.

increase in the amplitude of fluctuations. Until at 7nm the net magnetisation in the y-direction averages to zero over time. These results are summarized in figure 8.21 where m_r is defined as the average component of magnetisation in the y-direction. We should note here that during simulations of the 7nm grain the GMRES algorithm was occasionally unable to significantly reduce the residual. Upon further shrinking of the grain such errors became more and more frequent. We interpret this phenomenon as spontaneous jumps of the magnetisation to quite different low energy configurations which means that the magnetisation configuration from the previous time-step is no longer a good initial guess for the solver. On such occasions the solver simply reduces the residual as much as possible and our program proceeds to the next time-step. It would seem that this results in the magnetisation becoming stuck around low energy states with $m_y \approx 0$. This interpretation is support by noting that the trend of increased amplitude of the fluctuations with decreasing grain size is halted at 8nm which suggests that the larger fluctuations in smaller grains cannot be resolved. This requires more investigation and possibly the consideration of alternative solvers for situations in which superparamagnetism is likely to occur. No such errors occured for grains of diameter $\geq$ 8nm and we conclude that the GMRES algorithm is still the most appropriate solver for this regime.

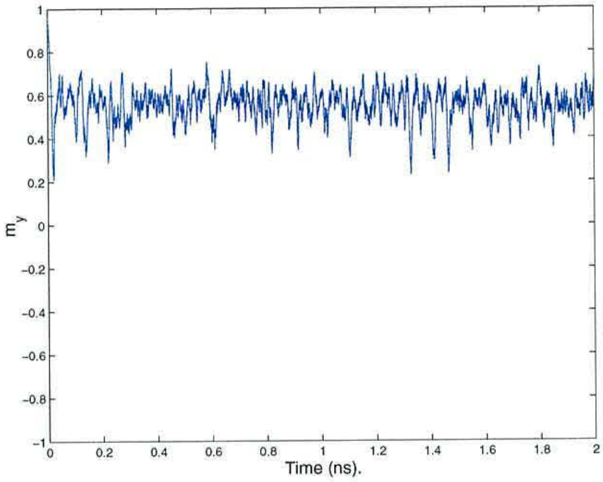

Figure 8.18: Relaxation of a 10nm longitudinal grain at 300°K.

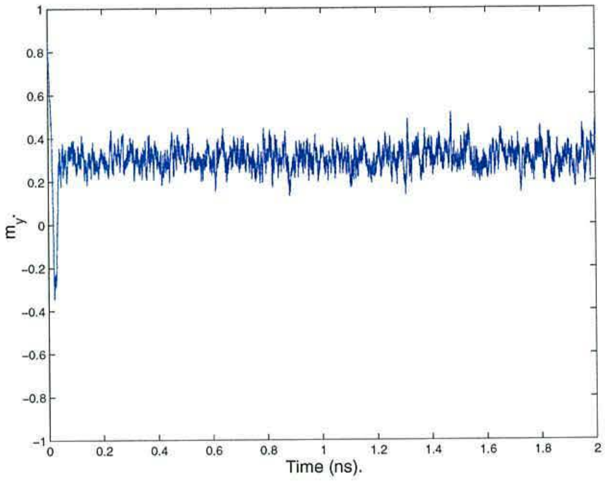

Figure 8.19: Relaxation of a 8nm longitudinal grain at 300°K.

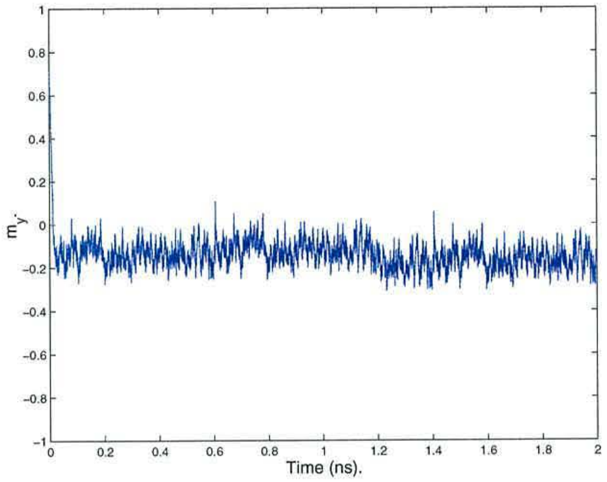

Figure 8.20: Relaxation of a 7nm longitudinal grain at 300°K.

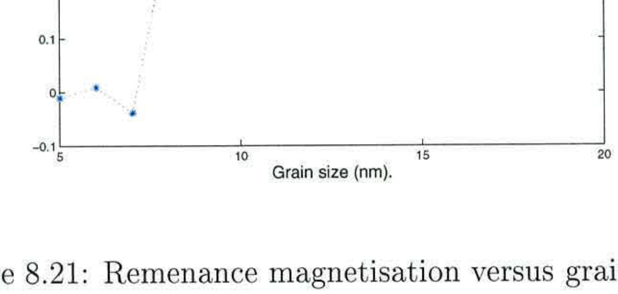

Figure 8.21: Remenance magnetisation versus grain size.

8.4 Temperature Dependence of Coercivity.

8.4.1 Longitudinal Grains.

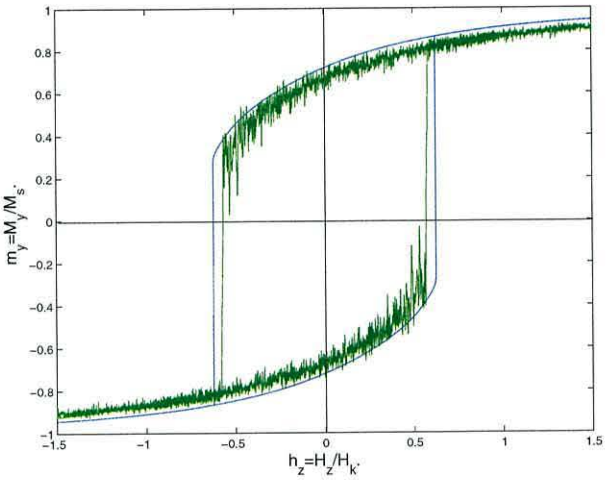

Figure 8.22: Comparison of hysteresis loops for the longitudinal grain at 0°K (blue) and 300°K (green).

To consider the effect of temperature on the coercivity of cobalt grains we repeat the simulations of section 4.3.3 using the finite temperature model. Figure 8.22 shows the hysteresis loop for the longitudinal grain at 300°K in green with the athermal curve shown in blue for reference. Immediatley we see an improvement in the quality of our results using the finite element model. With the incorporation exchange and magnetostatic interactions across the magnetisation, the abrupt jump to a reversed state which was observed for the Stoner-Wohlfarth particle does not occur. Consequently the tails of the hysteresis loop join at high and low fields as is observed experimentally. This simulation in fact gives a far deeper understanding of the reversal process. In section 7.3.5 we saw that fluctuations in the magnetisation lead to rapid oscillations of the hysteresis curve, with the amplitude of these oscillations depending only on temperature. In the Stoner-Wohlfarth model the effects of stochastic resonance are the same at all fields. In figure 8.22 on the other hand we see that the magnitude of oscillations increases with increasing magnitude of the reversing field. As more Zeeman energy is applied the effects of thermal energy are magnified. As soon as one of these oscillation results in a negative value of the average magnetisation, a Barkhausen jump occurs and the grain is switched. As expected this occurs at a field somewhat lower than that which would be required to anihilate the energy barrier at zero temperature. As expected from the previous section we obtain a remenance value of $m_r = 0.67 \pm 0.05$.

The most interesting feature of this simulation is the mechanism by which coercivity is reduced. We have already seen in chapter 7 that at elevated temperatures a frustration of the global magnetisation configuration develops. In figure 8.22 we see that this global frustration is also dependent on field. This is in contrast to earlier results which suggest that reduced coercivity at finite temperature is merely a result of increased local disorder, in analogy to the ferromagnetic-paramagnetic transition in a spin lattice. In some ways of course the analogy is good. However we may clearly see from figure 8.22 that at constant finite temperature the application of zeeman energy results in thermal fluctuations of increased magnitude, until at the critical field fluctuations become large enough to jump over the energy barrier. Finally we note that further increases in zeeman energy deepen the energy minimum corresponding to the reversed state, so that fluctuations of the magnetisation can no longer results in result in a switching event. The magnetisation therefore remains in the switched state. Magnetisation fluctuations of this magnetude are not observed in experimental hysteresis loops due to the fact that magnetisation is measured over a longer time-scale in such experiments. This results in a mean-path curve. We should also note that in the continuous thin film, intergranular interactions would tend to limit the magnitude of such fluctuations.

8.4.2 Perpendicular Grains.

In figure 8.23 we show results of a hysteresis simulation for the perpendicular grain. In this case there is only a more modest reduction in coercivity as temperature rises. Also the hysteresis curve is more disimillar from the athermal case. Here the reversal occurs over a number of field-steps at 300°K in contrast to the single Barkhausen jump observed at 0°K. Since there were no minimization problems reported from the GMRES solver during these simulations we may conclude that the system does not become artificially pinned at a specific magnetisation value over a field-step due to spontaneous jumps not being resolved. Rather we may conclude that this is in fact a feature of the finite temperature reversal in perpendicular grains and not merely an artifact of the model. This can be explained by recalling that grains are observed to jump continually over small energy barriers at finite temperature. It must be remembered that energy barriers can be small on one side corresponding to a local minima but much deeper on the other side corresponding to a state of much lower energy. Once such low-energy states

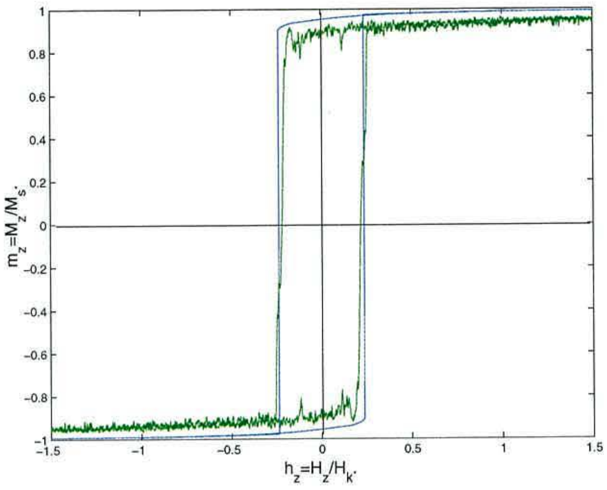

Figure 8.23: Comparison of hysteresis loops for the perpendicular grain at 0°K (blue) and 300°K (green).

have been reached the magnetisation cannot change significantly until a further increase in Zeeman energy causes a shift in the energy landscape. This phenomenon results in a sloped hysteresis loop which is in fact representative of experimental loops for perpendicular media of large grain-size. As we have seen previously some non-uniformity must exist within the magnetisation to allow alternative magnetisation configurations to be separated by small energy barriers. Notice that the slope is not curved as in the case of the longitudinal grain, this curved slope is a result of the orientaion of the easy-axis rather than of non-uniform magnetisation.

Chapter 9

Conclusions.

The aim of this project was to develop a three dimensional micromagnetic simulation using finite element methods to resolve nano-scale features in the microstructure of polycrystalline thin films. This goal has been achieved with a model that can be applied to arbitrary geometry with given material properties. We conclude that this work has brought the theory of micromagnetics one step closer to being a reliable design tool as well as giving new insight into the fundemental magnetisation reversal mechanism. We now give an evaluation of the micromagnetic model, our microstructure model and the computational simulations we have performed. We then discuss some formulation and algorithmic improvements which could be made to the code in the future as well as an outstanding physical feature which should be incorporated into the microstructure model to enable the simulation of thin film magnetic storage media. Finally we consider further technological and scientific applications in which the model could and indeed is being used to good effect.

9.1 Evaluation.

This work has consisted of three components; the development of the micromagnetic solver, the generation of realistic geometry and construction of the finite element mesh, and finally the computational simulations we have chosen to perform. These three aspects of the work will now be evaluated individually.

9.1.1 Micromagnetic Model.

We have presented a self-consistent model of magnetisation dynamics which can be applied to bounded or periodic nano-scale systems. In homogeneous material of arbitrary geometry may be considered. The model employs an unstructured finite element discretization of the Gilbert equation and associated components of the effective magnetic field. We have shown that our magnetostatic calculation converges to an analytical solution for the sphere at discretization sizes far higher than are necessary for micromagnetic calculations. We are therefore assured of a good solution for the field at each time-step in our simulations. We have employed a variational formulation of the dynamic equations which has several advantages. Most importantly the athermal model is mesh independent provided that the discretization size is smaller than the characteristic exchange length of the material. This is important because in future applications of the model Angstrom scale features such as material defects may be modelled by local refinement of the mesh without fear of mesh induced artifacts. Secondly our method allows contributions from the second order derivative of magnetisation due to exchange to be evaluated using a linear spatial basis of the magnetisation. Finally almost any conceivable term may be added to the effective field in the future. Any such terms would appear as integrands over each element; these may then be evaluated in terms of the local shape functions or indeed using Gaussian quadrature where necessary. We are therefore confident that the model is universally applicable to bounded nano-scale systems.

We have employed modern sparse matrix methods in handling the large systems of linear equations to be solved. Using a symbolic build-up of the mass matrix for a given mesh a priori we need only calculate numerical entries during the simulation with no data handling at run-time. The sparse matrix in row or column format can be passed to any external solver. At present we use the GMRES algorithm but it is not hard-wired into the code and may be supplanted by more efficient solvers should they become avalable.

As well as a model of bounded regions we have employed implicit periodic boundary conditions in order to model an infinite two dimensional region. We have peformed simulations of an extended polycrystalline thin film using this method with some success. The model captures the qualitative features of magnetisation reversal, such as the magnetisation ripple structures observed at remanence and the transition between reversal by coherent rotation and reversal by vortex motion with increasing grain size. However further work is required to establish how many grains are needed to accuratley model the quantitative characteristics of the reversal mechanism such as the coercivity. In hindsight we see that although the periodic region is infinite, the computational region will probably have to be very large in order for longitudinal magnetisation structures to develop in a realistic manner. However this constraint would seem less important in the simulation of thin films with perpendicular orientation. Indeed simillar methods with interface boundary conditions enforced in the out of plane direction have recently been successfully applied to modelling perpendicular magnetic recording media [102].

We have briefly considered the notion of geometric integration. In the context of micromagnetics a geometric method is simply any method which is quadratically invariant and therefore conserves the modulus of the magnetisation vector. We have shown that an implicit midpoint scheme which can be thought of as an average of the forward and backard Euler methods satisfies this criterion. This method was shown to be numerically stable and more efficient than normalization of a quadratically variant scheme, such as the Euler method. The method may also be implemented adaptively in time using a self-consistency control scheme. The work of Albuquerque *et al.* [82] shows that there exist other invariants of the system which are not conserved by the midpoint scheme. Investigation of geometric integration methods which preserve such invariants may further improve accuracy.

Finally we have incorporated finite temperature effects into the model via the Langevin-Gilbert equation. An implementation of our midpoint scheme is a suitable numerical method as it will naturally converge to the stratonovich solution of the stochastic differential equation. The difficulty in application of this method is that a thermal field strength must be assigned to the normally distributed Weiner process used to represent thermal fluctuations. In Browns original method he calculates a field strength inversely proportional to the volume of the single domain particle under consideration. It is unclear then how to apply his method in a multi-domain system. In line with other work [92] we have used his calculation substituting the volume of each finite element for the volume of the particle. Clearly this leads to mesh dependency and possibly an exagarated strength of the thermal field. We feel our simulations give ball-park results in the finite temperature case but that the thermal field strength should be moderated by a mesh dependent factor. The form of this factor is still an open question in our opinion [103].

9.1.2 Microstructure Model.

The Voronoi tessellation is widely accepted as the best geometric representation of polycrystalline thin films [104]. The polygonal cells accurately represent the structure of thin film grains whose boundaries straighten upon post deposition annealing. The polygonal geometry also ensures that discretisation error due to poor boundary approximation does not occur. Our algorithm for the generation of particular Voronoi constructions allows us to deform a hexagonal or indeed any other lattice to an arbitrary degree. Thus enabling arbitrary grain irregularity while maintaining the mean grain size. A realistic level of grain irregularity was decided upon in collaboration with experimental researchers. Our method has enabled us to establish the influence of material microstructure on the reversal mechanism in thin film nano-elements. At present the model is restricted to the representation of pure cobalt grains due to poor resolution of the grain boundaries. However realistic randomly oriented easy-axis can be assigned to the grains.

9.1.3 Applications.

In chapter 4 we have illustrated many types of reversal mechanism in the context of a homogeneous cobalt nano-element and went on to illustrate the most important differences between cobalt grains of longitudinal and perpendicular orientation. In chapter 8 we have presented four more interesting applications. The work on microstructural effects in cobalt nano-elements illustrates the success of both the micromagnetic and the microstructural model. With favourable comparisons to experimental results we can be sure that the solver is producing sensible results. Further the agreement with the range of coercivity values gives justification to our physical representaion. The subject of the Gilbert damping parameter is always somewhat controversial, primarily because it means different things to different people. Experimental researchers often present results which show that measured damping parameters depend on various other pheneomena, indeed even on temperature. Whereas these phenomena are almost always represented within the effective magnetic field in micromagnetic simulations and temperature effects are represented by random fluctuations in a stochastic differential equation or by Monte Carlo simulations. It is unclear then how the experimentally measured values of α should be related to the value used in computational simlations. We hope that the work shown in section 8.2 at least highlights the importance of resolving this question.

A fact which echoes through all the applications of our model is that subgrain discretization is of upmost importance in micromagnetic modelling.

We come to this conclusion simply by observing phenomena which cannot be resolved using a simple single spin model. This is due essentially to the simple energy barrier decribed by the Stoner-Wohlfarth model. Such a model cannot reflect the full complexity of the energy functional. In short the finite element method gives a continuum model which is true to our continuum hypothesis in the definition of magnetisation. In chapter 4 we saw that the distinct differences between longitudinal and perpendicular grains, as well as between grains of different sizes are due essentially to the balance between shape and magnetocrystalline anisotropy. The respective geometries can only give rise to such shape anisotropy when the grains are properly modelled. In section 8.2 we saw that Gilbert damping has a profound effect on the reversal of longitudinal grains. We have concluded that damping shifts the balance between shape and magnetocrystalline anisotropy. Again this phenomenon cannot be predicted without subgrain resolution. Finally in realistic cobalt grains the superparamagnetic limit occurs at a higher grain size than that predicted using a spherical single domain particle. Further we have shown that superparamagnetic behaviour appears gradually with reduced grain size and is not the abrupt transition which it is often perceived to be.

However as grain size decreases below the single domain limit as is the case in many applications we conclude that more useful results may be obtained using the computationally faster enhanced Stoner-Wohlfarth model. With faster simulations of this sort systems of far greater dimensions can be considered with comparable cpu time without loss of quality in the results. Indeed agreement between finite element and enhanced Stoner-Wohlfarth simulations has recently been demonstrated in the context of minute ferromagnetic particles [105]. Despite the agreement, it was also shown that the finite element model gave a deeper understanding of the reversal process. We therefore maintain that the value of information obtained from a micromagnetic simulation is proportional to the computational effort invested provided efficient methods are used. Initially sub-grain discretization is important to establish single domain behaviour, justifying the use of simpler models. Also in problems with non-uniform geometries a finite element discretization is desirable to distinguish between different types of single domain behaviour.

9.2 Model Development.

As we have already mentioned an almost arbitrary effective field may be considered using this model since terms do not have to be explicitly evaluated at a point. For example the expression for uniaxial anisotropy in the effective field could be replaced by an expression for cubic anisotropy. Incorporation of new terms could only ever be a problem if they included high order derivatives of magnetisation which could not be handled using Greens formula. Even in this case essentially the same method could be applied, requiring only a higher order basis for the magnetisation. In this section we discuss only fundemental changes which may improve the validity or efficiency of the model.

9.2.1 Grain Boundary Resolution.

The current treatment of grain boundaries in the majority of micromagnetic models is unsatisfactory. We have shown that grain size may be used to tailor magnetic properties. However at present another experimental technique which is used to increase coercivity is beyond the scope of our model. By alloying cobalt with non-magnetic substances such as chromium greater control over coercivity can be obtained. It has been shown that in such alloys the chromium segregates to the grain boundaries [104], this results in a non-magnetic grain boundary and subsequent decoupling of the magnetostatic and exchange interactions between grains. This is effective in increasing coercivity, however at 12 percent chromium the alloy becomes non-magnetic and is no longer useful as a storage medium. Therefore a greater understanding of this decoupling near the non-magnetic limit would be very useful. In our current model however the grain boundaries have zero thickness and cannot assume the properties of the chromium. Something has to be done to separate the grains, simply lowering the exchange constant at the boundary is not really acceptable. Ideally the grains should be physically separated with discretisation inside the boundary, this approach would be computationally intensive but is not unfeasible. Such a model would allow direct definition of the material properties within the grain boundary with no fudge factor.

Attempts have been made to directly incorporate atomistic effects at the grain boundary into a finite element model [106]. Here a Heisenberg model of exchange coupling between the grains was used with explicitly represented atomic moments coupled to the finite element discretisation of magnetisation within the grains. Simulations with a single grain boundary separating grains with anti-parallel magnetisations gave promising results with dramatic changes of the domain wall in the grain boundary upon a reduction of the exchange constant there. However no details of the calculation were given and it seems likely that very small elements would be required within the grains to couple with the Heisenberg model in the grain boundary. This model then suffers from the same limitations as direct discretization within the grain boundary with no foreseeable extra benefit.

Finally rather than applying a coarse-graining approach [107] we propose that the problem could be overcome using so-called mortar elements. These are used primarily to connect elements of different order in a finite element model where p-refinement rather than h-refinement is in operation. This is a common adaptive method in which the order of shape functions is increased in areas where greater resolution is required. We propose that such elements could be used to connect a pair of grains with all nodes on each ot the grain boundaries forming nodes of the mortar element. Interior nodes could then be specified at which properties such as the exchange constant differed from those in the grains. A higher order polynomial would then be used to interpolate the magnetisation across the element as in spectral element analysis [48]. These elements could then be made very thin without affecting the discretization size within the grain. Indeed they could be defined as two dimensional plates between the grains. Unfortunetly there was no time within this project to implement the idea.

9.2.2 BEM Magnetostatic Calculation.

A decision was made early in the course of this project to employ a purely finite element solution of the magnetostatic field. In this case the stiffness matrix remains sparse and computational methods for such matrices can be applied. However as discussed in chapter 3 this philosophy had several short comings. Firstly it was found that elements in the external region could not be made arbitrarily coarse without effecting the quality of the solution. This results in a large amout of computation to calculate the potential in the external region which is never explicitly used by the model. In hindsight we feel that this over-head is probably comparable to the expense of dealing with a fully populated matrix resulting from the hybrid finite element/boundary element method used by other authors [51]. The simplifications to mesh generation and processing then favour the hybrid method.

9.2.3 Preconditioning.

We have employed the GMRES matrix solver in all our simulations to date using only the default settings with the exception that the dimension of the Krylov subspace was set to the optimal value for such calculations [59]. A myriad of preconditioning schemes are now available which may well be more efficient

9.2.4 Parallelization.

Recent advances in parallel computing techniques hold interesting possibilities for micromagnetics. Such computations are carried out via two paradigms. The computational region may be split into a number of regions with each region being assigned to an individual processor. The calculation then requires overlapping layers of ghost elements between each region and a message passing interface (MPI) to couple the regions together. A scheme can be imagined in which individual processors are assigned to each grain of a thin film problem. Interior magnetisation could then be resolved subject to interactions from the other grains. This scheme would rely on a very sophisticated MPI to handle both short-ranged exchange interactions and non-local magnetostatic interactions effectively.

Alternatively parallelization may be achieved through open message passing (OpenMP). This method considers the computational region as a single entity in the same way as a serial program, here the structure of the computer program itself decomposed into modules which can be run simultaneously on different processors. For example when we loop over all elements to for a stiffness matrix or mass matrix the contributions are independent of each other and could therefore be calculated on different processors.

There are adavantages and disadvantages of both methods. MPI methods have been known to speed up calculations while still taking up the vast majority of cpu time doing the internal book-keeping. This indicates that the methos has not yet reached its full potential and will continue to improve performance as better interfaces are developed. The openMP scheme doesn't rely on domain decomposition and is often therfore more straight-forward in application. Indeed simple parallelization can be performed implicitly at compilation time. This method does have two major disadvantages; firstly it is limited in applicability and secondly it raises complicated memory management issues.

Some problems are sequential in nature over a large domain and naturally lend themselves to MPI whereas others are clearly more suited to OpenMP. Taking our model as an example it isn't clear which method would be most suitable. A rigorous comparison is required.

9.3 Further Applications.

The list of potential applications for our current model is very large and increases steadily with the refinements mentioned above. We mention only a sample of problems here that we feel illustrate the versatility of the code.

9.3.1 Magnetic Recording simulation.

In our investigations to date we have considered magnetisation dynamics due to an external field which is constant in space and time. In real appliations such as magnetic recording the head field is non-uniform in space and moves in time with respect to the media. We have accounted for these features in the model so that a full recording simulation may be performed in the future. The term

$$\int_V L_i \boldsymbol{m} \times \boldsymbol{h}_z dV \tag{9.1}$$

is evaluted over each element in the variational formulation. The applied field $\boldsymbol{h}_z$ may therefore take any functional form or may simply be defined at the nodes as required. These values may also change between time-steps. Finite element methods for head field calculations are well established. Conventional analytical calculations encounter problems when the head and media are combined in the same model, as the head should be infinitly imaged in the media and conversly the media should be infinitly imaged in the head. This is accomplished quite naturally in a finite element discretization. However we re-encounter the open-magnetic-boundary problem since periodic boundary conditions are not an appropiate means with which to resolve the head field. A first step towards a recording model is easily conceived with the media extending far enough away from the head to render edge effects neglegible when considering the reversal of a bit directly beneath the head. Such a model would require a massive number of finite elements to resolve the media at the subgrain level. However with efficient preconditioning and parallelization we feel that a micromagnetic model with essentially the same method as that outlined in this thesis could be used as a robust design tool for magnetic storage media as well as giving improved head design facilities. We accept however that in its present form the model is most useful in investigations of discrete nano-scale systems.

9.3.2 Rock Magnetism.

Such an application has recently become apparent in the form of understanding magnetisation dynamics and in particular in domain wall motion in magnetite crystals. Thermoremanent magnetisation is proposed as a cost-effective alternative to carbon dating in certain applications. This is possible because the magnetite crystals which are present in most of the earths crust in fact form the oldest known magnetic recording device. These crystals have a coercivity higher than the earths magnetic field at ambient temperature, however in periods of increased temperature it is possible for them to switch at such low fields. Combined with records of a region's thermal history, a magnetic history of the magnetite crystals can then be used to date a given rock from that region. This has prompted a need to achieve a better understanding of the micromagnetic behaviour in such crystals. Neel's relaxation time equation for thermal activation of single domain crystals over an energy barrier has been verified over extended time [108]. However in the case of multidomain particles some disagreement exists between the Neel model and observed results. The single domain limit of magnetite crystals is in the region of 100nm, therefore particle sizes of interest are well within the range of our model. We hope to perform simulations in the future in order to investigate the remanent domain configurations and thermal activation of multidomain crystals. This will however require that cubic anisotropy is incorporated into the model.

At fields as low as the earths field magnetostriction effects also become important and should be resolved. This requires the derivatives of magnetic elastic and elastic energy to be incorporated into the effective magnetic field. These energies can be found as the solution to a set of second order partial differential equations which would have to be solved at every time-step of the micromagnetic model. This work presents both a useful application and a nice numerical problem. Such a model would have further applications ranging from the investigation of mechanical damping to tribological effects in magnetic recording.

9.3.3 Superspin-glass Transition in Minute Nano-particles.

Much experimental work has been underway recently on the magnetisation dynamics of ultra-small nano-particles. In particular we note the work of J. De Tora *et al.* [109], [110] on mechanically alloyed Fe particles of only 1nm in diameter. Finite element modelling is ideally suited to modelling the interactions between such particles. Computations over many hundreds of particles employing periodic boundary conditions in three dimensions would provide the ideal complement to experimental results, particularly in the investigations of the illusive RKKY interaction. A standard micromagnetic simulation would establish whether classical interactions can account for experimentally observed behaviour. Experimental verification of the stochastic Gilbert equation could also be investigated by comparison of temperature dependent results.

Bibliography

[1] W. F. Brown.
Micromagnetics.
Wiley Interscience. (1963).

[2] A. Aharoni.
Introduction to the theory of ferromagnetism.
Oxford University Press. (1996).

[3] G. Bertotti.
Tutorial Session Notes: Micromagnetics and Non-Linear Magnetisation dynamics.
10th Biennial Conference on Electromagnetic Field Computation, Perugia. (2002).

[4] D. Jiles.
Introduction to Magnetism and Magnetic Materials.
Chapman and Hall. (1991).

[5] A. Auerbach.
Interacting Electrons and Quantum Magnetism.
Addison-Wiley.(2000).

[6] B. Cullity.
Introduction to Magnetic Materials.
Addison-Wiley Series in Metallurgy and Materials. (1972).

[7] N. Majlis.
The Quantum Theory of Magnetism.
World Scientific.(2001).

[8] S. Chikazumi.
Physics of Magnetism.
John Wiley and Sons.(1964).

[9] J. HANNAY.
Computational simulation of thermally activated magnetisation dynamics at high frequency.
PhD. Thesis: University of Wales. (2001).

[10] A. ARROT.
Plenary Lecture: Progress in Micromagnetics.
Moscow International Symposium on Magnetism, Moscow. (2002).

[11] J. ANDERSON.
Magnetism and Magnetic Materials.
Chapman and Hall. (1968).

[12] H. LORENTZ.
The theory of electrons.
B. G. Teubner, Leipzig. (1909).
Dover, New York. (1952).

[13] G. BERTOTTI.
Hysteresis in Magnetism: For Physicists, Materials Scientists and Engineers.
Academic Press.(1998).

[14] www.research.ibm.com

[15] N. BERTRAM.
Theory of Magnetic Recording.
Cambridge University Press. (1994).

[16] J. MALLINSON.
A unified View of High Density Digital Recording Theory.
IEEE Trans. Mag. 11, pp. 1166-1169.(1975)

[17] C. MEE AND E. DANIEL (EDS.).
Magnetic Recording.
McGraw-Hill. (1987).

[18] F. JORGENSEN.
The Complete Handbook of Magnetic Recording.
TAB books. (1988).

[19] J. ZHU.
Micromagnetics of Dual Spin-Valve GMR Heads.
J. App. Phys. 79, pp. 5886. (1996).

[20] D. THOMPSON AND J. BEST.
The Future of Magnetic Data Storage Technology.
IBM J. Res. Develop. 44, pp. 311-322. (2000).

[21] J. C. MAXWELL.
A Treatise on Electricity and Magnetism.
Reprinted by Dover Publications. (1954).

[22] P. WEISS.
L'Hypothese du Champ Moleculaire et de la Propriete Ferromagnetique.
J. de Phys. 6, pp. 661-690. (1907).

[23] F. BITTER.
On Inhomogeneities in the Magnetisation of Ferromagnetic Materials.
Phys. Rev. 38, pp. 1903-1905.(1931).

[24] C. KITTEL.
Theory of the Structure of Ferromagnetic Domains in Films and Small Particles.
Phys. Rev. 70, pp. 965-971.(1946).

[25] W. HEISENBERG.
Z. Physik 69, pp. 287-297.(1931).

[26] K. SIXTUS AND L. TONKS.
Phys. Rev. 37, pp. 930-958. (1931).

[27] F. BLOCH.
Z. Physik 74, pp. 295-335. (1932).

[28] L. LANDAU AND E. LIFSHITZ.
Phys. Z. Sowjet. 8, pp. 153-169 (1935).
Reprinted on pp. 101-114 of *Collected papers of L.D. Landau*, edited by D. ter Haar, Pergamon Press. (1965).

[29] L. NEEL.
Compt. Rend. 220, pp.814-815. (1945).

[30] C. KITTEL.
Rev. Mod. Phys. 21, pp. 541-583 (1949).

[31] R. BECKER AND W. DORING.
Ferromagnetismus. *Springer.* (1939).

[32] E. STONER AND E. WOHLFARTH.
A Mechanism of Magnetic Hysteresis in Heterogeneous Alloys.
Phil. Trans. 240, pp. 599-642 (1948).

[33] P. RIDLEY.
Finite Element Simulation of the Micromagnetic Behaviour of Nano-Elements.
Ph.D Thesis: University of Wales. (2000).

[34] R. KIKUCHI.
On the Minimum of Magnetization Reversal Time.
J. App. Phys. 27 (11), pp. 1352-1358. (1956).

[35] J. MALLINSON.
On Damped Gyromagnetic Precession.
IEEE Trans. Magn. 23 (4), pp. 2003-2004. (1987).

[36] T. GILBERT.
A Lagrangian Formulation of the Gyromagnetic Equation of the Magnetisation Field.
Phys. Rev. 100, pp 1243. (1955).

[37] P. PODIO-GUIDUGLI.
On Dissipation mechanisms in micromagnetics.
Eur. Phys. J. B. 19, pp. 417-424. (2001).

[38] M. BERTSCH, P. PODIO-GUIDUGLI AND V. VALENTE.
Ann. Mat. Pura. Appl. CLXXVII (2000).

[39] A. VISINTIN.
Physica B 233, pp. 619 (1997).

[40] C. BUDD.
Adaptivity and Geometric Integration.
LMS/EPSRC Short Instructional Course "New Trends in Computational Differential Equations" (2002).

[41] W. CHENEY AND D. KINCAID.
Numerical Mathematics and computing.
Brooks/Cole Publishing Company. (1999).

[42] K. TAKO.
Micromagnetic Simulation of Polycrystalline 2-D Thin Films Using the Finite Element Method.
Ph.D Thesis: University of Wales. (1997).

[43] K. ERIKSSON, D. ESTEP P. HANSBO AND C. JOHNSON.
Computational Differential equations.
Cambridge University Press. (1996).

[44] K. Atkinson.
Elementary Numerical Analysis - Secon Edition.
John Wiley and Sons. (1993).

[45] C. FRÖBERG.
Introduction to Numerical Analysis.
Addison-Wesley world student series. (1979).

[46] A. DAVIES.
The Finite Element Method : A First Approach.
Oxford Applied Mathematics and Computing Science series. (1980).

[47] O. ZIENKIEWICZ.
The Finite Element Method.
McGRAW-HILL. (1977).

[48] O. ZIENKIEWICZ AND K. MORGAN.
Finite Elements and Approximation.
Wiley-Interscience Publication. (1983).

[49] W. DAHMEN.
Multiscale and Wavelet Methods for Operator Equations.
LMS/EPSRC Short Instructional Course "New Trends in Computational Differential Equations" (2002).

[50] D. FREDKIN AND T. KOEHLER.
Numerical micromagnetics by the finite element method.
IEEE Trans. Magn. 23 (5), pp. 3385-3387. (1987).

[51] T. SCHREFL, J. FIDLER, K. KIRK AND J. CHAPMAN.
A higher order FEM-BEM method for the calculation of domain processes in magnetic nano-elements.
IEEE Trans. Magn. 33 (5), pp. 1239-1244. (1997).

[52] T. SCHREFL.
Finite elements in numerical micromagnetics.
J. Magn. Magn. Mat. 207, pp. 45. (1999).

[53] B. YANG AND D. FREDKIN.
Dynamical micromagnetics by the finite element method.
IEEE Trans. Magn. 34 (6), pp. 3842-3852. (1998).

[54] Peter N. Brown and A. C. Hindmarsh.
Reduced Storage Matrix Methods in Stiff ODE Systems.
Lawrence Livermore National Laboratory Report UCRL-95088. (1987).

[55] S. Pissanetzky.
Sparse Matrix Technology.
Academic Press. (1984).
viewable at http://www.ceaspub.eas.asu.edu/PowerZone/SparseVisual

[56] D. Braess.
Finite Elements - Theory, fast solvers, and applications in solid mechanics.
Cambridge University Press. (1997).

[57] E. Kreyszig.
Introductory Functional Analysis with Applications.
John Wiley and Sons. (1978).

[58] P. N. Brown, G. D. Byrne and A. C. Hindmarsh.
SIAM J. Sci. Stat. Comput. **10**, *1038.* (1989).

[59] V. Tsiantos, T. Schrefl, J. Fidler, A. Bratsos.
Cost-effective way to speed up micromagnetic simulations in granular media.
App. Numer. Math. 39, pp. 191-204. (2001).

[60] www.cs.cmu.edu/ quake/triangle.html

[61] www.endo.sandia.gov/SEACAS/cubit/cubit.html

[62] N. Parthasarathy.
A comparison of tetrahedron quality measures.
Finite Element Analysis Des. 15, pp. 255-261. (1993).

[63] P. Knupp.
Achieving finite element mesh quality via optimizaton of the Jacobian matrix norm and associated quantities.
Intl. J. Numer. Meth. Engng. 48, pp. 1165-1185. (2000).

[64] P. Ridley, G. Roberts, M. Wongsam and R. Chantrell.
Finite element modelling of nanoelements.
J. Magn. Magn. Mat. 193, pp. 423-426. (1999).

[65] R. HERTEL AND H. KRONMüLLER.
Micromagnetic simulation of the domain structure of a flat rectangular permalloy prism.
J. App. Phys. 85 (8), pp. 6190-6192. (1999).

[66] D. SUESS, T. SCHREFL AND J. FIDLER.
Reversal modes, thermal stability and exchange length in perpendicular recording media.
Intermag/MMM 2001 paper FA-10.

[67] G. JONES, M. JACKSON AND K. O'GRADY.
Determination of grain size distribution in thin films.
J. Magn. Magn. Mat. 193, pp. 75-78. (1999).

[68] D. STOYAN, W. KENDALL AND J. MECKE.
Stochastic Geometry and its Applications.
John Wiley and Sons.(1987).

[69] A. OKABE.
Spatial Tessellations : Concepts and Applications of Voronoi Diagrams.
John Wiley and Sons. (1992).

[70] J. XUE AND R. VICTORA.
Micromagnetic calculation for superlattice magnetic recording media.
J. App. Phys. 87 (9), pp. 6361-6363. (2000).

[71] A.W. SPARGO, P.H.W. RIDLEY, G.W. ROBERTS AND R.W. CHANTRELL.
Influence of microstructure on the magnetisation reversal in Co nanoelements.
J. App. Phys. **91**, *pp. 6923-6925.* (2002).

[72] T. SCHREFL, J. FIDLER, K. KIRK AND J. CHAPMAN.
Simulation of magnetization reversal in polycrystalline patterned Co elements.
J. App. Phys. 85 (8), pp. 6169-6171. (1999).

[73] P. BETTES.
Finite element modelling of exterior electromagnetic problems.
IEEE Trans. Magn. 24 (1). (1988).

[74] C. EMSON.
Methods for the solution of open-boundary electromagnetic field problems.
IEE Proc. 135A (3). (1988).

[75] X. BRUNOTTE AND G. IMHOFF.
Finite element modeling of unbounded problems using transformations: A rigorous, powerful and easy solution.
IEEE Trans. Magn. 28 (2), pp. 1663-1666. (1992).

[76] B. NATH AND J. JAMSHIDI.
The w-plane finite element method for the solution of scalar field problems in two dimensions.
Int. J. Numer. Meth. Eng. 15 pp. 361-379. (1980).

[77] D. LAMBETH.
Modern hard disk media issues.
Proc. NATO ASI: Magnetic storage systems beyond 2000. (2000).

[78] B. MIDDLETON AND J. MILES.
Fast switching and coercivity in thin-film media.
J. App. Phys. 89 (11), pp. 6997-6999. (2001).

[79] G. HERZER.
Grain size dependence of coercivity and permeability in nano-crystalline ferromagnets.
IEEE. Trans. Magn. 26 (5), pp. 1397-1402. (1990).

[80] C. BUDD AND M. PIGGOT.
Geometric Integration and its applications.
LMS/EPSRC Short Instructional Course "New Trends in Computational Differential Equations" (2002).
Viewable at:
http://www.bath.ac.uk/~mascjb/revnew9.ps.gz

[81] C. SERPICO, I.D. MAYERGOYZ AND G. BERTOTTI.
Numerical Technique for Integration of the Landau-Lifshitz Equation.
J. App. Phys. 89, pp. 6991-6993. (2001).

[82] G. ALBUQUERQUE, J. MILTAT AND A. THIAVILLE.
Self-consistency based control scheme for magnetization dynamics.
J. App. Phys. 89, pp. 6719-6721. (2001).

[83] L. LANDAU AND E. LIFSHITZ.
Statistical physics.
Pergamon Press, London, chapter 12 (1958).

[84] W. Brown.
Thermal fluctuations of a single-domain particle.
Phys. Rev. 130 (5), pp. 1677-1686 (1963).

[85] K. Ito.
On stochastic differential equations.
Memoirs, Amer. Math. Soc. 4 (1951).

[86] I. Gikhman and A. Skorokhad.
Stochastic differential equations.
Springer (1972).

[87] R. Stratonovich.
A new representation for stochastic integrals and equations.
SIAM J. Control 4, pp. 362-371 (1966).

[88] P. Kloeden and E. Platen.
Numerical solution of stochastic differential equations.
Springer-Verlag, Berlin (1992).

[89] W. Press, S. Teukolsky, W. Vetterling and B. Flannery.
Numerical recipes in Fortran 90
Cambridge University Press (1996).
www.library.cornell.edu/nr/bookf90pdf/chap7f9.pdf

[90] P. Langevin.
Sur la theorie du mouvement Brownien.
C.R. Acad. Sci., Paris 146 pp. 530-533 (1908).

[91] L. Arnold.
Stochastic differential equations: Theory and applications.
John Wiley and Sons. (1974).

[92] W. Scholz.
Micromagnetic simulation of thermally activated switching in fine particles.
Diplomarbeit: Univertsity of Vienna (1999).

[93] H. Callen, M. Barasch and J. Jackson.
Phys. Rev. 88, pp. 1382 (1952).

[94] K. Zhang and D. Fredkin.
Stochastic Dynamic Micromagnetic Study of Fine Particles.
J. App. Phys. 85, pp. 5208-5210 (1999)

[95] V. Tsiantos, T. Schrefl, W. Scholz and J. Fidler.
Thermal magnetisation noise in submicron spin valve sensors.
47th Conference on Magnetism and magnetic materials, paper HC-04 (2002).

[96] K. Kirk.
Nanomagnets for sensors and data storage.
Contemporary Physics 41 (2), pp. 61-78. (2000).

[97] K. Kirk, J. Chapman, S. McVitie, P. Aitchison, C. Wilkinson.
Switching of nanoscale magnetic elements.
App. Phys. Lett. 75 (23), pp. 3683-3685. (1994).

[98] M. Herrmann, S. McVitie and J. Chapman.
Investigation of the influence of edge structure on the micromagnetic behavior of small magnetic elements.
J. App. Phys. 87 (6), pp. 2994-2999. (2000).

[99] J. Gadbois and J. Zhu.
Effect of edge roughness in nano-scale Magnetic bar switching.
IEEE Trans. Magn. 31 (6), pp. 3802-3804. (1995).

[100] P. Ridley, G. Roberts and R. Chantrell.
Investigation of magnetization behavior in nanoelements using the finite element method.
J. App. Phys. 87 (9), pp. 5523-5525. (2000).

[101] D. Twisselmann, R. McMichael, A. Chen, W. Egelhoff and S. Russek.
Intrinsic damping and intentional ferromagnetic resonance broadening in thin permalloy films.
47th Conference on Magnetism and magnetic materials, paper BH-01 (2002).

[102] T. Schrefl, M. Schabes and B. Lengsfield.
Fast reversal dynamics in perpendicular magnetic recording media with soft underlayer.
J. App. Phys. 91 (10), pp. 8662-8664 (2002).

[103] J. Deak.
Finite temperature micromagnetics and magnetic measurements of submicron patterned permalloy thin films.
47th Conference on Magnetism and magnetic materials, paper BC-07 (2002).

[104] K. KRISHNAN.
Magnetism and Microstructure.
Proc. NATO ASI: Magnetic storage systems beyond 2000. (2000).

[105] D. SUESS, T. SCHREFL, W. SCHOLZ AND T. FIDLER.
Micromagnetic Calculation of Coercivity and Remanence of Self-Assembled FePt Nanoparticle Arrays.
47th Conference on Magnetism and magnetic materials, paper CC-04 (2002).

[106] H. KRONMULLER, R. FISCHER, R. HERTEL AND T LEINEWEBER.
Micromagnetism and the Microstructure in Nanocrystalline Materials.
J. Magn. Magn. Mater. 175, pp. 177-192 (1997)

[107] X. FENG AND P. VISSCHER.
Coarse-graining Landau-Lifshitz damping.
J. App. Phys. 89 (11), pp. 6988-6990. (1999).

[108] D. DUNLOP.
Rock Magnetism, Fundamentals and Frontiers.
47th Conference on Magnetism and magnetic materials, paper FZ-04 (2002).

[109] J. DE TORA, M. LOPEZ DE LA TORRE AND J. RIVEIRO.
Mossbauer study of the superspin glass transition in nanogranular $Al_{49}Fe_{30}Cu_{21}$.
Phys. Rev. B 64. (2002).

[110] J. DE TORA, M. LOPEZ DE LA TORRE, M. ARRANZ AND J. RIVEIRO.
Nonequilibrium magnetic dynamics in mechanically alloyed materials.
Phys. Rev. B 64. (2002).